Microstructural Characterization of Ferroelectric $(Na_{1/2}Bi_{1/2})TiO_3$-$BaTiO_3$ Ceramics via Transmission Electron Microscopy

Mikrostrukturelle Charakterisierung von ferroelektrischen $(Na_{1/2}Bi_{1/2})TiO_3$-$BaTiO_3$ Keramiken via Transmissionselektronenmikroskopie

Genehmigte Dissertation zur Erlangung des Grades eines
Doktors der Naturwissenschaften (Dr. rer. nat.)

von Ann-Katrin Fetzer geboren in Schwäbisch Gmünd

Erstgutachter: Prof. Dr. Hans-Joachim Kleebe
Zweitgutachter: Prof. Dr. Jürgen Rödel

Technische Universität Darmstadt, 2023

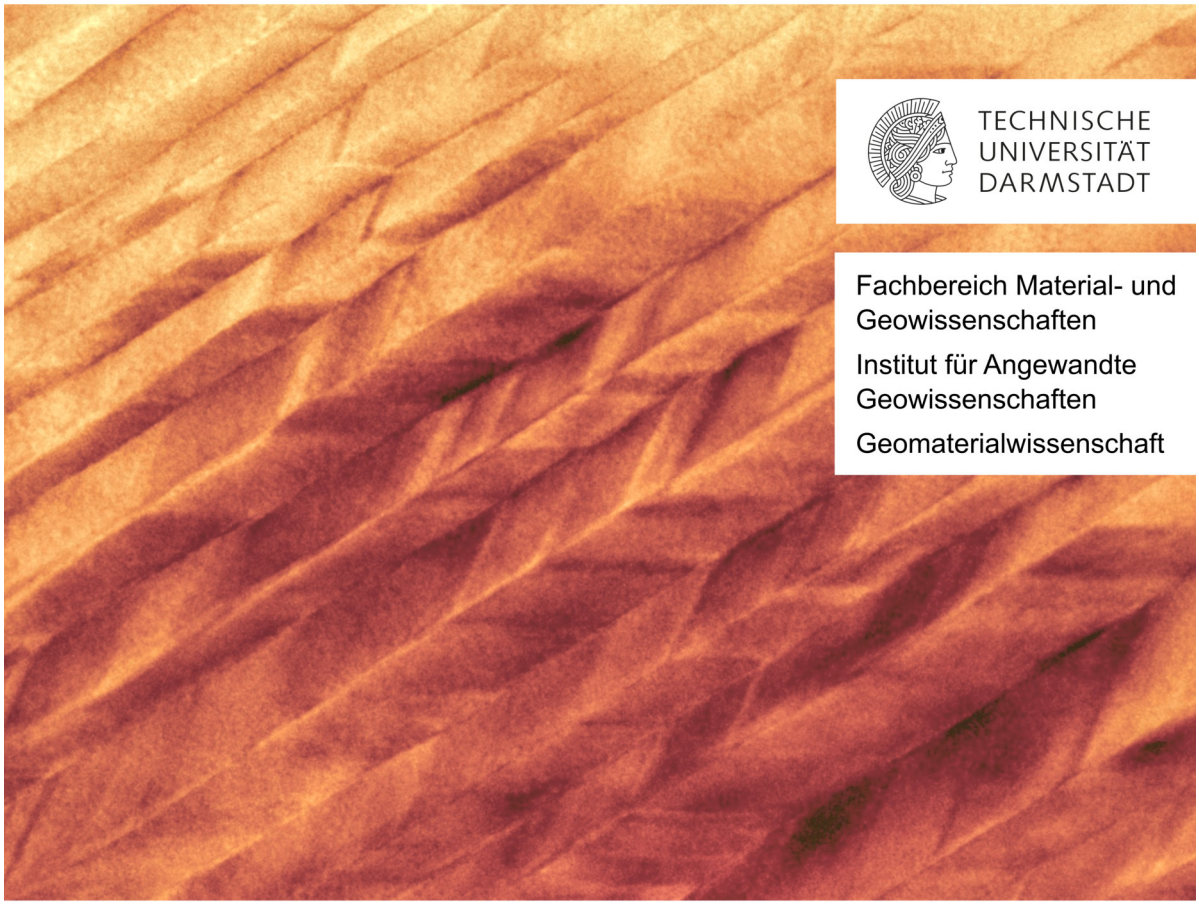

Microstructural Characterization of Ferroelectric $(Na_{1/2}Bi_{1/2})TiO_3$-$BaTiO_3$ Ceramics via Transmission Electron Microscopy

Mikrostrukturelle Charakterisierung von ferroelektrischen $(Na_{1/2}Bi_{1/2})TiO_3$-$BaTiO_3$ Keramiken via Transmissionselektronenmikroskopie

Genehmigte Dissertation von Ann-Katrin Fetzer geboren in Schwäbisch Gmünd

Tag der Einreichung: 31. Oktober 2022
Tag der Prüfung: 10. Januar 2023

Darmstadt, Technische Universität Darmstadt

Erklärungen laut Promotionsordnung

§ 8 Abs. 1 lit. c PromO

Ich versichere hiermit, dass die elektronische Version meiner Dissertation mit der schriftlichen Version übereinstimmt.

§ 8 Abs. 1 lit. d PromO

Ich versichere hiermit, dass zu einem vorherigen Zeitpunkt noch keine Promotion versucht wurde. In diesem Fall sind nähere Angaben über Zeitpunkt, Hochschule, Dissertationsthema und Ergebnis dieses Versuchs mitzuteilen.

§ 9 Abs. 1 PromO

Ich versichere hiermit, dass die vorliegende Dissertation selbstständig und nur unter Verwendung der angegebenen Quellen verfasst wurde.

§ 9 Abs. 2 PromO

Die Arbeit hat bisher noch nicht zu Prüfungszwecken gedient.

Darmstadt, 31. Oktober 2022

Ann-Katrin Fetzer

Content

Abbreviations & Symbols

Abbreviations

AFE	Antiferroelectric
AC	Alternating current
BCZT	$(Ba,Ca)(Zr,Ti)O_3$
BF	Bright-field
BFO	$BiFeO_3$
BSE	Back-scattered electron
BT	$BaTiO_3$
c	Cubic
DF	Dark-field
DW(s)	Domain wall(s)
EDS	Energy-dispersive X-ray spectroscopy
EELS	Electron energy-loss spectroscopy
ELNES	Energy-loss near edge structure
EU	European Union
FC	Furnace cooled
FE	Ferroelectric
FFT	Fast Fourier transform
GTF	Goldschmidt tolerance factor
HAADF	High-angle annular dark-field
HR	High-resolution
HRTEM	High-resolution transmission electron microscopy
HRSTEM	High-resolution scanning transmission electron microscopy
KNN	$(K_{0.5}Na_{0.5})NbO_3$
M	Monoclinic
MPB	Morphotropic phase boundary
NBT	$(Na_{1/2}Bi_{1/2})TiO_3$
NBT-BT	$(1-x)(Na_{1/2}Bi_{1/2})TiO_3$-$x$$BaTiO_3$
NMR	Nuclear magnetic resonance
pc	Pseudocubic
PFM	Piezoresponse force microscopy

PMN	$Pb(Mg_{1/3}Nb_{2/3})O_3$
PNR(s)	Polar nanoregion(s)
PT	$PbTiO_3$
PZT	$Pb(Zr_xTi_{1-x})O_3$
Q	Quenched
R	Rhombohedral
RoHS	Restriction of Hazardous Substances
SE	Secondary electron
SEM	Scanning electron microscopy
SR(s)	Superlattice reflection(s)
STEM	Scanning transmission electron microscopy
T	Tetragonal
TEM	Transmission electron microscopy
WBDF	Weak-beam dark field
XRD	X-ray diffraction

Symbols

A	Cation in the cuboctahedral cage site of the perovskite structure
A_{AC}	Amplitude (alternating current)
A_0	Maximum amplitude
$A_{1\omega}$	Vibration amplitude
ABX_3	Generic perovskite structure
$A'_xA''_{(1-x)}B'_yB''_{(1-y)}O_3$	Generic perovskite oxide structure with two A- and B-site cations
a, b, c	Lattice parameters along the crystallographic [100], [010] and [001] axes
a_{pc}, b_{pc}, c_{pc}	Pseudocubic lattice parameters
a_0	Lattice parameter of the cubic perovskite structure
$a^0a^0a^0$	Glazer notation for non-tilted perovskite structure
$a^0a^0c^+$	Glazer notation for octahedral in-phase tilting with tilt axis [001]
$a^0a^0c^-$	Glazer notation for octahedral anti-phase tilting with tilt axis [001]
$a^-a^-a^-$	Glazer notation for octahedral anti-phase tilting with tilt axis [111]
α, β, γ	Angle of oxygen octahedral tilt around the [100], [010] and [001] axis
α in $90° - \alpha$	Angle in the rhombohedral unit cell
B	Cation in the central octahedral position of the perovskite structure
C	Curie constant
C_c	Chromatic aberration
C_s	Spherical aberration
χ_{ij}	Dielectric susceptibility
d	Lattice spacing
d_f	Defocus of the objective lens

D_i	Dielectric displacement
d_{ijk}	Piezoelectric coefficient
d_{33}	Longitudinal piezoelectric coefficient
d_{33}^{*}	Large-signal piezoelectric coefficient
d_{33}^{eff}	Effective piezoelectric coefficient
d_{31}	Transverse piezoelectric coefficient
d_{15}	Shear piezoelectric coefficient
d_s	Disc diameter for the spherical aberration
d_c	Disc diameter for the chromatic aberration
e'	Electron (Kröger-Vink notation)
E, E_0	Energy, energy of the incident electron beam
E_a	Activation energy
E_d	Depolarization field
E_c	Coercive field
E_i	Electric field
ε_{ij}	Dielectric permittivity
ε_r	Relative permittivity
ε'_{ij}, ε'	Real part of the permittivity
ε''_{ij}, ε''	Imaginary part of the permittivity
ε_0	Permittivity of vacuum
f, f_0	Frequency, cut-off frequency
G	Reciprocal diffraction spot
g, g_{hkl}	Reciprocal lattice vector
hkl	Miller indices
$[hkl]$	Specific crystallographic direction
$\langle hkl \rangle$	Set of symmetrically equivalent crystallographic directions
(hkl)	Specific crystallographic plane
$\{hkl\}$	Set of symmetrically equivalent crystallographic planes
I_B	Background intensity
I_{hkl}	Intensity of hkl reflection
I_{SR}	Intensity of superlattice reflection
K	Scattering vector
k_b	Boltzmann constant
k_d	Vector of diffracted wave
k_i	Vector of incident wave
k_{ij}	Electromechanical coupling factor
k_p	Planar electromechanical coupling factor
k_t	Thickness electromechanical coupling factor
λ	Electron wavelength

n	Integer number
ω	Angular frequency
p_i	Pyroelectric coefficient
P_i	Polarization
P_{max}	Maximum polarization
P_S	Spontaneous polarization
P_r	Remanent polarization
r_A, r_B, r_X	Radius of *A*-site cation, *B*-site cation and anion in the perovskite structure
s, s_g	Excitation error for a reciprocal lattice vector
S_{jk}	Elastic strain
S_{max}	Maximum strain
S_r	Remanent strain
σ_{jk}	Mechanical stress
t	Time
T	Temperature
T_C	Curie temperature
T_B	Burns temperature
T_d	Depolarization temperature
$T_{F\text{-}R}$	Ferroelectric-to-relaxor transition temperature
T_m	Temperature of the permittivity maximum
T_{VF}	Vogel-Fulcher temperature
$tan\delta$	Dielectric loss
θ	Diffraction angle
Θ	Rotation angle of two 90° domains
ϕ_g	Amplitude of diffracted beam
ϕ_0	Amplitude of direct beam
τ	Collection semi-angle
φ	Phase difference
V, V_0	Driving voltage, maximum (amplitude) of voltage
$V_O^{\bullet\bullet}$	Twice positively charged oxygen vacancy (Kröger-Vink notation)
W	Fringe distance
w_{tot}	Total energy density
X	Anion in the perovskite structure
ξ_0, ξ_g	Extinction distance for the direct and diffracted beam, respectively
Z	Atomic number
z	Distance (thickness)
$[001]_{pc}$, $[001]_T$	[001] direction in the pseudocubic and tetragonal phase, respectively
$\frac{1}{2}\{ooo\}$, $\frac{1}{2}\{ooe\}$	Superlattice reflections on half-integral reciprocal positions with odd (o) and even (e) hkl indices

Abstract

Lead-free ferroelectrics increasingly gain significance as replacement for lead-containing ceramic materials in electronic devices. A main focus lies in modifying their functional properties in order to meet industry demands. Quenching of the lead-free relaxor ferroelectric solid solution $(1-x)(Na_{1/2}Bi_{1/2})TiO_3$-$xBaTiO_3$ (NBT-BT) was developed as a procedure for increasing the material's low depolarization temperature (T_d), which strongly limits the application range. Quenching also increases the lattice distortion and affects the temperature-dependent permittivity response. However, there is a lack of clear understanding about the interrelation of such characteristics and the local microstructure. This work investigates the compositional range of $(1-x)$NBT-xBT ceramics ($0.03 \leq x \leq 0.12$), primarily using transmission electron microscopy (TEM) and scanning transmission electron microscopy (STEM). It sheds light on the relaxor ferroelectric micro- and nanostructural features and examines the microstructure-structure-property correlation upon quenching.

Di- and piezoelectric properties of NBT-BT ceramics vary profoundly, dependent on the composition. Close to the morphotropic phase boundary (MPB) of $x \approx 0.06$, the relaxor behavior reflects in the presence of short-range polar structures (nanodomains/polar nanoregions) and the coexistence of rhombohedral and tetragonal symmetries. The stabilization of a more ferroelectric character upon quenching is accompanied by a shift in the phase assemblage towards the formation of abundant lamellar tetragonal (*P*4*mm*) and rhombohedral (*R*3*c*) domains, coexisting with the relaxor *P*4*bm* phase. Quenching thus promotes a spontaneous onset of ferroelectric order in unpoled relaxor compositions, where the increased non-cubic lattice distortions manifest in an enforced formation of lamellar ferroelastic domains in order to accommodate the corresponding strain.

In-situ TEM analyses illustrate the temperature-dependent evolution of the domain and phase assemblage and investigate on the stability of the quenched structural features with increasing temperature. The depolarization of the material (T_d) is strongly linked to the disintegration of the ferroelectric domain structure. The lamellar *P*4*mm* domains in the quenched MPB composition exhibit a partial stability up to elevated temperatures (∼300 °C), which benefits a delayed depolarization and relates to the overall increase in T_d. The reversibility of the temperature-dependent structural transitions is furthermore investigated.

TEM dark-field imaging using superlattice reflections visualizes the relaxor nanostructure of *P*4*bm* and *R*3*c* nanodomains. High-resolution STEM investigations display a heterogeneous cation displacement with nanometer-sized polar fluctuations, which are denoted as polar nanoregions (PNRs) and relate to the relaxor behavior. In BT-rich compositions, a complex hierarchical domain configuration is revealed, where a reduced population of *P*4*bm* and *R*3*c* nanodomains prevails embedded within the lamellar *P*4*mm* domain structure. The findings demonstrate that TEM constitutes a viable tool for unravelling the complex nanostructure of multi-phase relaxor ferroelectric systems.

1 Introduction

1.1 Motivation

Ferroelectrics represent an important class of functional materials. They are characterized by a spontaneous and switchable electric polarization (P_S), but also exhibit various useful di-, pyro- and piezoelectric properties. While ferroelectric materials are manifold, perovskite oxides are most widely studied and find versatile applications. The beginning of the electroceramic industry during the 1940s is connected to the commercial use of $BaTiO_3$ in ceramic capacitors [1]. Nowadays, ferroelectric ceramics are widely deployed in sensor and actuator technologies, transducers, resonators, as well as sonar and ultrasonic systems [2]. Such applications do not necessarily exploit the ferroelectricity itself, but rather make use of the superior piezoelectric properties [3]. During the late 1980s, ferroelectric thin-films became important as components in micro-electromechanical systems (MEMS) [4].

Since 2002, focus of the scientific research has been shifted towards the development of lead-free ferroelectrics, based on the European Union (EU) directive for the Restriction of Hazardous Substances (RoHS). Until today, $Pb(Zr_xTi_{1-x})O_3$ (PZT) and related Pb-containing materials are among the most widely used electroceramics. While there is no universal replacement for PZT, various lead-free materials are suited for specific applications [5]. They comprise $(Na_{1/2}Bi_{1/2})TiO_3$ (NBT)-based, $(K_{0.5}Na_{0.5})NbO_3$ (KNN)-based, $BaTiO_3$ (BT)-based and $BiFeO_3$ (BFO)-based ceramics. In more recent years, tailoring and tuning the electrical and structural properties in order to meet specific requirements plays an important role in the development of lead-free materials.

The lead-free $(Na_{1/2}Bi_{1/2})TiO_3$-$BaTiO_3$ (NBT-BT) system is a solid solution between the relaxor ferroelectric NBT and the classical ferroelectric BT. The latter exhibits ferroelectric domains, which are regions with a consistent polarization direction. Relaxor ferroelectrics feature more complex nano-and mesoscale polar structures, such as polar nanoregions (PNRs) and nanodomains [6, 7]. The unique structural characteristics give rise to a high permittivity and an enhanced electromechanical response [8, 9]. Di-and piezoelectric properties of the relaxor ferroelectric solid solution peak at its morphotropic phase boundary (MPB) [10]. While NBT-BT is specially suited for high-frequency and high-power applications, such as required for ultrasonic devices [11, 12], the low depolarization temperature (T_d), where piezoelectric properties disappear, limits the temperature range of possible applications.

In order to overcome this limitation, the procedure of air-quenching NBT-based ceramics from sintering temperatures has been established [13, 14]. Quenching NBT-BT compositions close to the MPB results in an increase in T_d and an enhanced lattice distortion, as well as a decrease in permittivity; all suggesting a stabilization of the ferroelectric order [15]. Therefore, a detailed microscopic investigation in order to correlate the quenching-induced property changes to the microstructural characteristics is important.

Transmission electron microscopy (TEM) is a widely applied method for examining the microstructure of ferroelectric materials. TEM offers a combination of various imaging methods such as bright-field (BF) and dark-field (DF) imaging, electron diffraction, in-situ techniques and high-resolution (HR) imaging down to the atomic level, which are well suited for analyzing domain configurations, local symmetries and other microstructural features. While many studies on NBT-BT focus on the long-range average structure, TEM allows for a detailed, locally resolved analysis.

1.2 Objective & Concept

Quenching lead-free ceramics can tailor specific application-relevant characteristics without significantly impairing the piezoelectric and electromechanical properties. However, little is known about quenching-induced changes on a microstructural level. Therefore, this work addresses the following three questions:

- How does quenching affect the domain structure?
- How does quenching-induced microstructural changes correlate with the phase assemblage?
- How does the temperature-dependent evolution of the domain structure and phase assemblage correlate to the increased depolarization temperature upon quenching?

In order to determine and assess the structural changes upon quenching, the conventionally furnace cooled structure requires a detailed identification. Domain features and phases strongly differ in the composition-dependent relaxor and ferroelectric states, which are characterized via TEM. Subsequently, alterations in the domain structure and phase assemblage upon quenching are investigated in detail. The qualitative phase fractions before and after quenching are compared. Complementary imaging techniques, such as SEM and PFM append information about the domain structure. In addition to the unpoled state, the quenched structure in poled MPB compositions is investigated. Correlations between the microstructure and average structure are drawn, which in turn influence the relaxor/ferroelectric behavior. Mechanisms for the quenching-induced structural changes are discussed. In-situ TEM analysis comparatively investigates on the temperature-dependent development of the domain structure, the phase assemblage and the reversibility of the phase transitions in furnace cooled and quenched MPB compositions.

In order to better understand the complex nature of relaxor ferroelectric ceramics, a detailed and highly resolved examination of the NBT-BT nanostructure is executed. It emphasizes the following two major questions:

- How can nanostructural characteristics, such as the spatial distribution and morphology of coexisting symmetries be linked to the relaxor/ferroelectric behavior?
- How are relaxor and ferroelectric structural features associated in the relaxor-to-ferroelectric transition of the solid solution?

Using DF imaging in TEM, nanometer-sized domains of different symmetries and octahedral tilt systems can be displayed. Their morphology and association is investigated, which provides direct experimental evidence for the nanoscale relaxor structure. High-resolution scanning transmission electron microscopy (HRSTEM) investigations on the local polar displacement are performed. The relaxor-to-ferroelectric transition is analyzed with increasing BT content, starting from the MPB, revealing the association of nanoscale and large-scale ferroelectric structures.

2 Theory & Literature Review

2.1 Ferroelectrics

2.1.1 From Di- over Piezo- to Pyroelectrics

Ferroelectric materials are per definition characterized by the existence of a spontaneous and permanent electric polarization (P_S), which exhibits a reversibility under the application of an external electric field [16]. Ferroelectricity is a property inherent to certain dielectric materials. Dielectrics can be classified in a hierarchical way into the subgroups of piezo-, pyro- and ferroelectrics (Fig. 2.1). Detailed information on dielectric properties in polar oxides and electroceramics can be found in Refs. 17–19.

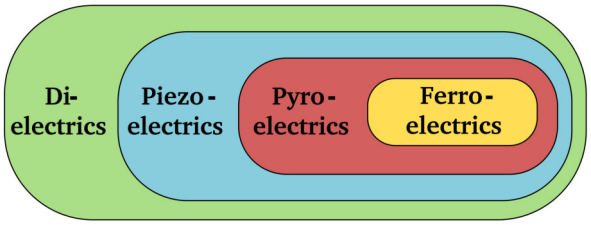

Figure 2.1: Hierarchical classification of dielectrics and their subgroups.

Dielectrics are insulating materials. Opposed to electrical conductors, they do not enable the flow of electric charges [20]. However, dielectrics can be polarized in an external electric field (E_i). In response to the stimulus of the electric field, charges are displaced over short distances along the electrical field vector, creating dipole moments and a dielectric polarization (P_i) within the material. Several mechanisms (Fig. 2.2) can contribute to the net polarization and the dielectric response [17, 18]. Electronic polarization, common to all dielectrics, describes the shift of negative electron shells against the positive atom cores. Ionic polarization refers to the displacement of anions and cations in an ionic crystal lattice. If the material consists of molecules with permanent dipole moments, they can realign under an electric field (orientation polarization). Space charge polarization describes the displacement of mobile charge carriers up to a potential barrier, e.g., a grain boundary. In a ferroelectric crystal, ionic polarization is the major contributor to the net polarization [16], which is also termed lattice polarization, since it describes the relative displacement of the respective sublattices.

The dielectric displacement of a material, D_i [C/m^2], depends on the applied electric field, E_i [V/m], and the induced macroscopic polarization, P_i [C/m^2], according to [21]:

$$D_i = \varepsilon_0 E_i + P_i \tag{2.1}$$

with ε_0 as the electric permittivity of vacuum, which has a value of 8.854 x 10^{-12} F/m. The

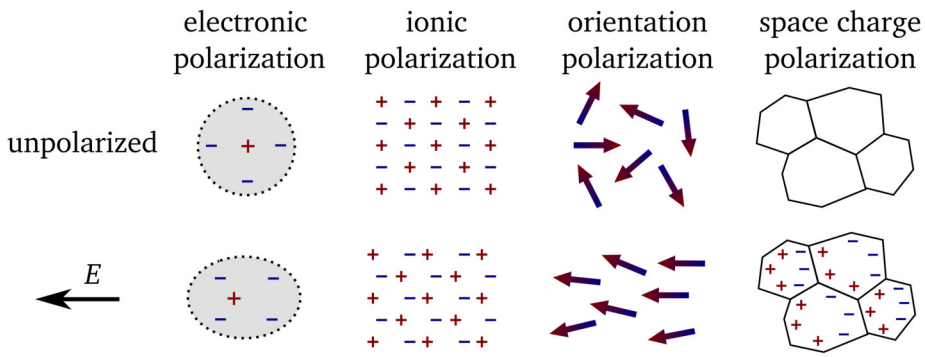

Figure 2.2: Different polarization mechanisms arising in dielectrics upon application of an external electric field (redrawn after Ref. 18).

polarization, P_i, induced by the electric field, is defined as:

$$P_i = \varepsilon_0 \chi_{ij} E_j \tag{2.2}$$

The electric susceptibility, χ_{ij}, is a quantitative measure of the materials ability to be polarized in an electric field. From Equations 2.1 and 2.2 follows that D_i can be expressed as:

$$D_i = \varepsilon_0 E_i + P_i = \varepsilon_0 (1 + \chi_{ij}) E_j = \varepsilon_0 \varepsilon_r E_j \tag{2.3}$$

with $\varepsilon_r = (1 + \chi_{ij})$ as the relative permittivity (or also termed dielectric constant). The permittivity of a certain material, ε_{ij}, is the product of ε_0 and ε_r, a property describing the capacity of the insulating material to store electric energy. In alternating electric fields, the dielectric permittivity comprises a real part, ε'_{ij}, and an imaginary part, ε''_{ij}:

$$\varepsilon_{ij} = \varepsilon'_{ij} - i\varepsilon''_{ij} \tag{2.4}$$

with i being the imaginary number $i = \sqrt{-1}$. The ratio of ε''_{ij} and ε'_{ij} results in the dielectric loss, $tan\delta$, which is another important measure for the dielectric quality of the material. The dielectric loss is the dissipation factor of the electric energy. For materials with a small loss, $tan\delta$ is close to 0.

Regarding crystal structures, dielectric behavior comprises all 32 crystallographic point groups, while piezoelectricity is demonstrated only in non-centrosymmetric crystal structures, which leaves 20 point groups [22]. In piezoelectrics, polarization can not only be induced by the application of an external electric field, but also by applying mechanical stress [21]. The direct piezoelectric effect describes the formation of a polarization (P_i or D_i) when applying pressure to the material, creating a potential difference and thus electric charges at the outer surfaces of the crystal. The direct piezoelectric effect is mathematically expressed as:

$$P_i = d_{ijk} \sigma_{jk} \tag{2.5}$$

with d_{ijk} [pC/N] as the piezoelectric coefficient and σ_{jk} [N/m^2] as the applied stress. In contrast, the converse piezoelectric effect describes the deformation of the material upon the application of an electric field. The field-induced strain, S_{jk}, is defined as:

$$S_{jk} = d_{ijk} E_i \tag{2.6}$$

Here, d_{ijk} has the unit pm/V. The piezoelectric coefficient is a third rank tensor, but can be expressed

in reduced matrix notation, d_{ij}, with i denoting the direction of the electrical component and j representing the direction of the mechanical component [23]. The longitudinal piezoelectric coefficient, d_{33}, applies for the strain (deformation) in direction of the electric field and polarization vector [18]. The transverse piezoelectric coefficient, d_{31}, relates to the strain perpendicular to the polarization axis and the field, while d_{15} describes the shear component. Concerning electroceramics, d_{33} is an important property since it connects the mechanical strain to the applied electric field. Large d_{33} values are therefore related to large mechanical displacements in the material.

Another important parameter of piezoelectrics is the electromechanical coupling factor, k_{ij}. It describes the ratio between the stored mechanical energy and the applied electrical energy in % [2]. When assessing the quality and performance of piezo- and ferroelectrics, properties like the relative permittivity (ε_r), the d_{33} coefficient, the dielectric loss ($tan\delta$) and the coupling factor (k_{ij}) are descriptive parameters. It needs to be noted that these properties can also be strongly temperature dependent.

Among the 20 non-centrosymmetric point groups which give rise to piezoelectric properties, 10 possess a unique polar axis and are characterized by the existence of a spontaneous polarization, P_S. The lattice exhibits a permanent electric dipole moment [21] and P_S is also present, when no external electric field is applied. Such materials are known as pyroelectrics. The name arises from the temperature-dependency of P_S. The pyroelectric effect relates to a change in P_S with changing temperature according to:

$$\Delta P_{S,i} = p_i \Delta T \tag{2.7}$$

where $\Delta P_{S,i}$ is the induced polarization upon the temperature difference ΔT [K] and p_i [$Cm^{-2}K^{-1}$] denotes the pyroelectric coefficient.

2.1.2 Ferroelectric Characteristics

In ferroelectrics, the spontaneous polarization (P_S) has the ability to switch its direction when an external electric field is applied. Ferroelectrics are therefore always pyro- and piezoelectric, but not vice versa. The spontaneous polarization arises from the ionic displacement within the unit cells (Fig. 2.3). When the cations and/or anions are displaced, the centers of positive and negative charges become separated, leading to the creation of a polarization vector along the displacement. Therefore, ferroelectrics possess at least two equivalent orientations for the polarization [21].

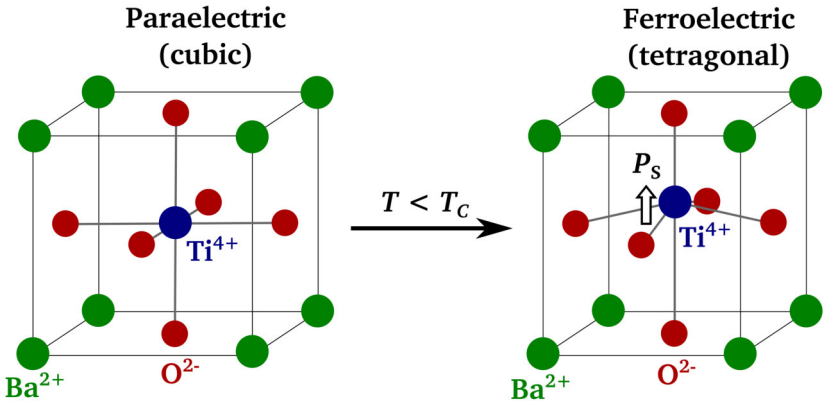

Figure 2.3: Schematic of the $BaTiO_3$ unit cell in the paraelectric and ferroelectric state. Below T_C (120 °C), a spontaneous polarization (P_S) emerges from the ionic displacement.

Switching can also occur under the application of mechanical stress. Such a behavior is denoted as ferroelastic and a material can both be ferroelectric and ferroelastic.

Perovskite oxides form the major group among ferroelectric ceramics with a technological significance [24]. Ferroelectric perovskites with a ABO_3 structure usually undergo several symmetry changes with temperature. The high-temperature phase is always cubic and hence centrosymmetric; so no ferroelectricity occurs. This state is referred to as the paraelectric state. When cooled down, a transition to a low symmetry ferroelectric phase takes place at the Curie temperature, T_C. A classical ferroelectric ceramic is $BaTiO_3$ (BT). Since the discovery of its ferroelectric properties in the mid-1940s, it has been widely studied [25–27]. Below T_C, the displacement of Ti^{4+} along the $[001]_{pc}$ direction is accompanied by a tetragonal distortion of the structure, giving rise to the formation of the permanent spontaneous polarization (Fig. 2.3). It should be noted that in BT, the O^{2-} anions are slightly displaced as well [27]. The succession of temperature-dependent symmetry changes in BT is [27, 28]:

Cubic ($Pm\bar{3}m$) $\xrightarrow{120\ °C}$ Tetragonal ($P4mm$) $\xrightarrow{5\ °C}$ Orthorhombic ($Amm2$) $\xrightarrow{-90\ °C}$ Rhombohedral ($R3m$).

In the rhombohedral symmetry, the cation displacement is along $\langle 111 \rangle_{pc}$, while it is along $\langle 110 \rangle_{pc}$ in the orthorhombic phase. The polarization and relative permittivity change upon a phase transition, as does the dimension of the unit cell, as illustrated in Fig. 2.4. The phase transitions in BT are first order transitions, featuring a sharp discontinuity of the above mentioned properties. A slight thermal

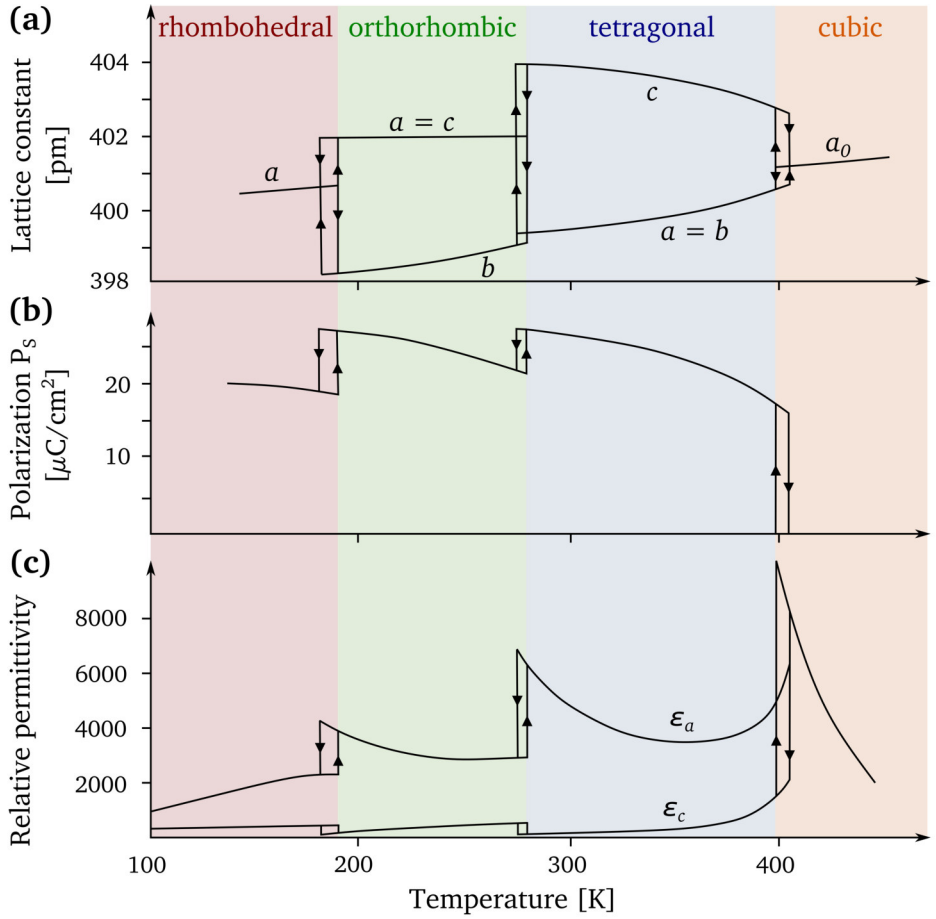

Figure 2.4: Temperature-dependent phase transitions in $BaTiO_3$ and corresponding changes in (a) the lattice constants, (b) the spontaneous polarization, P_S, and (c) the relative permittivity, ε_r (redrawn after Ref. 17).

hysteresis occurs, which can be due to various factors, e.g., the temperature rate or an intrinsic inhomogeneity [17]. The transition to the ferroelectric phases is associated with the formation of ferroelectric domains (discussed in more detail in section 2.2). The relative permittivity (ε_r) exhibits a sharp peak at T_C. Above T_C, the temperature dependence of ε_r follows the Curie-Weiss law ($\varepsilon_r = C/(T - T_0)$ with C as the Curie constant and T_0 as the extrapolated Curie temperature) [29].

A descriptive feature of ferroelectrics is the hysteresis character of polarization and strain, obtained from field-dependent macroscopic measurements. The relation between the polarization and the applied electric field (P-E loop) and between the strain and the electric field (S-E loop) is schematically displayed in Figs. 2.5(a) and (b), respectively. In a polycrystalline material, the polarization vectors are statistically equally distributed between possible directions. Hence, on a macroscopic level they cancel each other out and the overall polarization is zero. When an electric field is applied, the polarization of an initial unpoled material increases from zero until a saturated state is reached and the polarization vectors are aligned along the field. The realignment is closely related to domain reorientation (see section 2.2.3). The intersection of the linear extrapolation of the saturated polarization, P_{max}, with $E = 0$ determines the value for the spontaneous polarization, P_S. When the electric field is turned off, a certain amount of dipoles will switch back and a stable state will adjust itself with a remanent polarization, P_r. When the field is increased in the opposite direction, a coercive field, E_c, has to be reached in order to overcome the potential barrier for reorienting the dipoles and switching the net polarization to the other direction. Then again a saturated state is reached. Returning the electric field to zero will leave a remanent polarization with negative value. Single crystals exhibit more rectangular P-E loops with square shoulders, while polycrystalline materials often show rotated and round loops. The finer the grain size, the thinner the P-E loop. Ferroelectrics which require a high coercive field for switching are called 'hard' ferroelectrics, while 'soft' ferroelectrics can be more easily poled. The strain hysteresis is mainly determined by the converse piezoelectric effect. The S-E loop typically exhibits a butterfly shape (Fig. 2.5(b)). Analogous to the polarization, a saturated value, S_{max}, and a remanent strain, S_r, is reached.

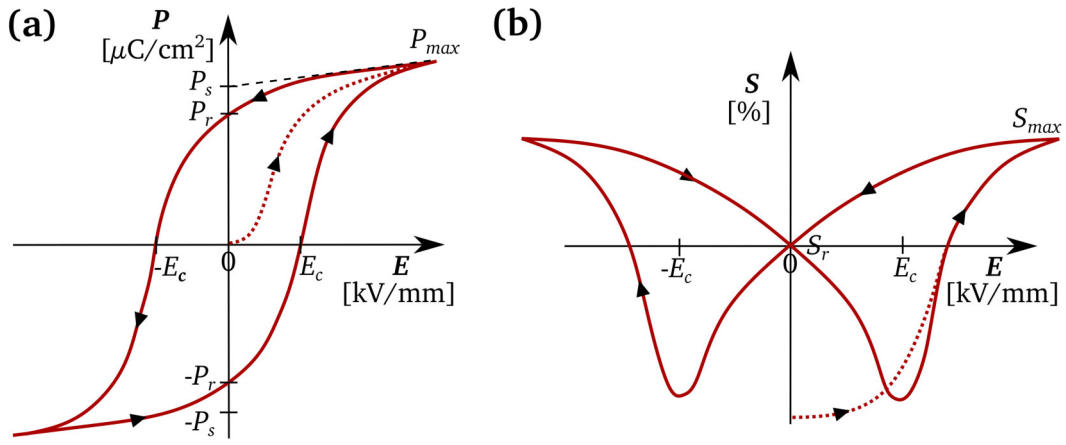

Figure 2.5: (a) Schematic field-dependent polarization (P-E) hysteresis loop and (b) strain (S-E) hysteresis loop of a ferroelectric ceramic. The dotted lines relate to the curves starting from the unpoled state (modified after Ref. 30).

In contrast to normal ferroelectrics, where adjacent dipoles are oriented in the same direction, antiferroelectric materials exhibit an antiparallel dipolar displacement. Within the crystal structure, a line of ions is shifted in one direction, while the ions in the neighboring line are shifted in the opposite direction [31]. On a macroscopic level, the antiparallel dipoles cancel each other out. When an electric field is applied, one set of the dipoles is switched and the material is transferred from the antiferroelectric (AFE) to a ferroelectric (FE) state [32] (Fig. 2.6(a)). Upon removal of the field, the material transforms back to the AFE state, showing no remanent polarization. If the field is reversed, the switching process is reversed as well, leading to double P-E loops (Fig. 2.6(b)), which are a typical characteristic of antiferroelectrics [20].

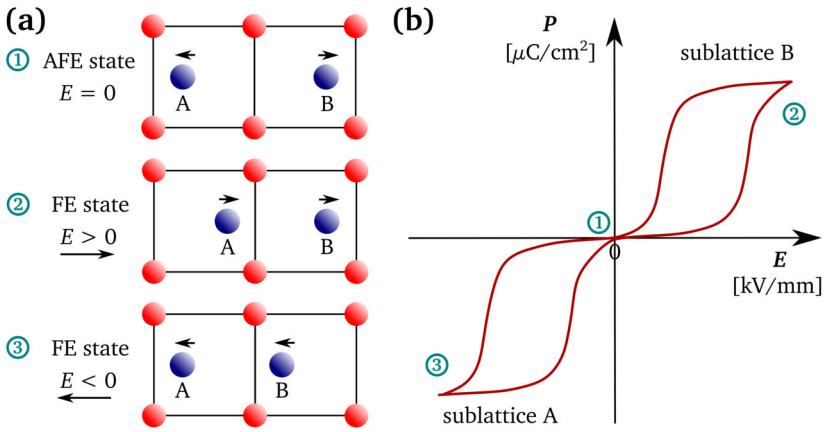

Figure 2.6: (a) Schematic illustrating the anti-parallel ionic displacement within the unit cells of an antiferroelectric at zero electric field. One set of ions (A) is switched under a positive electric field, while the other set of ions (B) is switched under a negative electric field. (b) Schematic double hysteresis P-E curve of an antiferroelectric. No remanent polarization state is present (modified after Ref. 32).

2.1.3 Morphotropic Phase Boundary

In ferroelectric materials, superior dielectric and piezoelectric properties are often found in compositions close to a MPB. In a solid solution with two (or more) end members, a MPB relates to the composition-dependent transition between two phases of different symmetry. A MPB is usually not a sharp line, but rather a transition area where several phases coexist. At the MPB, the polarizability of the material is enhanced due to the interplay of phases with equivalent energy/polarization states [33]. This enables a facilitated dipole (domain) reorientation upon poling. The classical example of a ferroelectric material with a MPB is found in lead zirconate titanate. PZT is a solid solution of $PbTiO_3$ and $PbZrO_3$ and has a MPB at $x = 0.52$, where rhombohedral (R) and tetragonal (T) phases occur [22]. At the MPB, properties such as ε_r, d_{33} and k_p exhibit very high values, arising from the increased polarizability between R and T polar directions via an intermediate local monoclinic phase, serving as a bridging link [34, 35]. A flattening of Gibbs free energy profiles is present, allowing for easy polarization reversal [36, 37]. The complexity of the local structure at the MPB plays a significant role in achieving a high piezoelectric response [38, 39].

2.1.4 Lead-Free Ferroelectrics

In the past two decades, the development of lead-free ferroelectrics has been an important research topic in order to replace lead-containing materials. The extensive implementation of PZT and related

Pb-containing systems is owed to their superior dielectric and piezoelectric properties. An easy processing and availability of precursors, as well as low cost, are further advantages of PZT-based materials [40]. Lead, however, is toxic to the human body and causes various environmental issues. The World Health Organization states lead poisoning as a high health risk, since the cumulative toxin is distributed to the liver, kidney and bones and damages the brain and central nerve system during physical development [41]. Concerning PZT-based electroceramics, the health risks for end-users is relatively low, since the Pb-containing units are usually installed in devices where they cannot be accessed easily [42]. However, PZT-containing devices include a chain of manufacturing processes where the risk of lead poisoning is enhanced, especially in developing countries, where no strict work safety regulations apply. During sintering and processing, lead can evaporate in the form of toxic PbO [43, 44]. Recycling of lead-containing products plays another big role in the release of lead to the environment. Based on the EU's RoHS directive of 2002 and its revisions (RoHS-2 in 2011 and RoHS-3 in 2019), the content of lead and other toxic substances in electronic equipment has been restricted to 0.1 wt. % [45]. However, there are numerous exemptions in the regulation for areas where lead-free replacements are not yet available, including piezoelectric materials. The EU Commission extended the exemptions for the use of lead in electroceramics to July 2021. Requests for a renewal of the exemptions have been surveyed and new recommendations including a further extension period were published in December 2021 [46]. Currently, the exemptions remain in force until a new decision is reached by the EU Commission.

Most promising lead-free material groups are $(Na_{1/2}Bi_{1/2})TiO_3$ (NBT)-based, $(K_{0.5}\ Na_{0.5})NbO_3$ (KNN)-based, $BaTiO_3$ (BT)-based, $(Ba,Ca)(Zr,Ti)O_3$ (BCZT)-based and $BiFeO_3$ (BFO)-based ceramics. Since PZT exhibits a MPB-related property enhancement, lead-free solid solutions inherent of a MPB are especially of interest. Comprehensive overviews of the development of lead-free electroceramics have been covered in multiple reviews [47–52]. Fig. 2.7 underlines that there is no single lead-free substitute for all PZT applications [5]. However, different materials can be considered as replacement for certain requirements, such as for high piezoelectricity and strain, or a high temperature stability of piezoelectric properties.

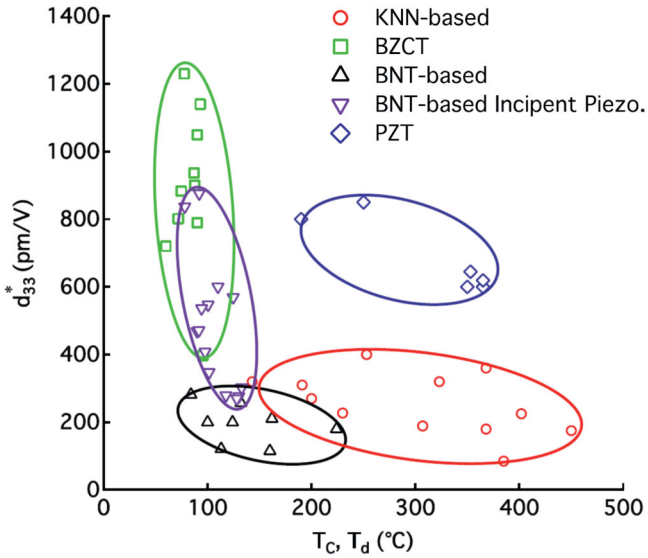

Figure 2.7: The large-signal piezoelectric coefficient d^*_{33} as function of depolarization temperature for different lead-free materials and PZT (reprinted from Ref. 5 with permission from Elsevier).

Bi-based materials are of interest, because Bi^{3+} and Pb^{2+} display a similar behavior in the perovskite structure, since they feature the same outermost electron shell. The $6s^2$ lone pair of Pb^{2+} is known to cause large structural distortions from the cubic symmetry [53]. The off-centering of the Bi^{3+} ion from its cation site due to its $6s^2$ lone pair hybridization with the oxygen *p*-orbitals also promotes the stabilization of a distorted perovskite structure [54, 55]. Bi-containing NBT features a high remanent polarization, but is limited by a high coercive field and conductivity. Therefore, solid solutions with improved properties of MPB compositions were developed, e.g., with BT or $K_{0.5}Bi_{0.5}TiO_3$ (KBT). Ternary systems, such as NBT-BT-KNN or NBT-KBT-KNN, which also form solid solutions, allow for further complex compositions with enhanced properties. NBT-BT-KNN ceramics were found to display an extremely large strain (0.45 %) [56] and are therefore well suited for electromechanical applications. Pure KNN has some processing disadvantages concerning the preparation of dense ceramics [57]. However, KNN-based ceramics doped with elements such as Li or Ta achieve high d_{33} values comparable to PZT [58]. BCZT has excellent piezoelectric properties near the crystallographic (phase) triple point [59], but only at low temperatures. BFO has the unique property of being both ferroelectric and ferromagnetic. BFO-BT solid solutions are promising candidates for high temperature applications [60].

More recently, emphasize is laid on bringing lead-free ferroelectrics into application and tailoring material properties in order to comply with specific requirements [5]. Besides piezoelectric properties, life cycle assessment, cost-benefit, reproducibility, mechanical and thermal properties and fatigue behavior are crucial parameters for replacing a lead-based with a lead-free material [44, 50]. Recent industrial developments of lead-free products and prototype devices include, e.g., transducers with a NBT-based piezoceramic for fabrication of an ultrasonic cleaner by Honda Electronics Co., Ltd. (Japan) [11]. KNN-based actuator materials and NBT-based ultrasonic transducers for sonar and hydrophonic applications were developed by PI Ceramic GmbH (Germany) [61, 62]. Further application examples, such as a KNN-based ring-type ultrasonic motor for auto-focusing in digital cameras, are given in Refs. 51 and 63 and are displayed in Fig. 2.8.

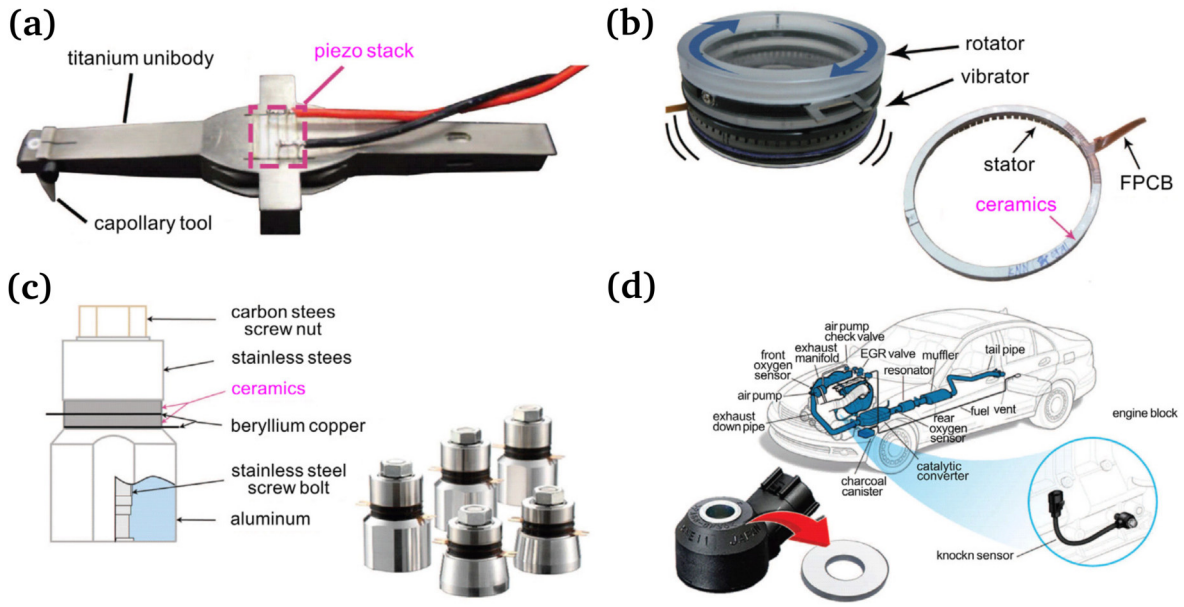

Figure 2.8: Devices with lead-free piezoceramics. (a) Transducer with a NBT ceramic, (b) KNN-based ring-type ultrasonic motor for cameras, (c) NBT-based bolt-clamped Langevin-type transducer for ultrasonic cleaning and (d) knock sensor for car engines (reprinted from Ref. 51 under Creative Commons License CC BY-NC-ND 4.0).

2.2 Ferroelectric Domains

2.2.1 Domain Formation

The characteristic microstructural feature of ferroelectric ceramics are ferroelectric domains. A domain is an area which exhibits the same direction of spontaneous polarization. The interface which separates areas of different polarization directions is called domain wall. The width of the domain wall spans few unit cells over which the ionic displacement changes direction (Fig. 2.9). A 180° domain wall separates two neighboring domains, where the polarization direction is orientated in opposite direction (Fig. 2.9(a)). A non-180° domain wall separates two domains, where the polarization directions are not anti-parallel but, e.g., oriented perpendicular to each other as in 90° domains (Fig. 2.9(b)).

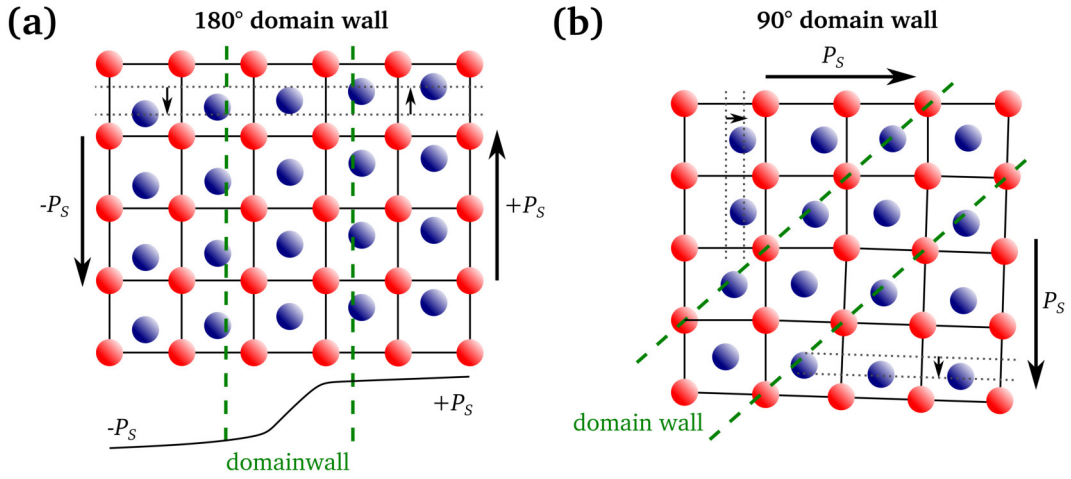

Figure 2.9: Schematic of the ionic displacement and spontaneous polarization (P_S) near a 180° domain wall (a) and a 90° domain wall (b) in a tetragonal ferroelectric structure (redrawn after Ref. 21).

The creation of P_S during the transition from the paraelectric to the ferroelectric phase leads to the formation of bound charges which in turn create a depolarization field, E_d, within the material. Bound charges can appear as surface charges on the outside of the sample, or in the bulk ceramic when P_S is heterogeneous [64]. In order to minimize the electric energy associated with E_d, domains with opposite polarization are created by the formation of 180° domain walls [65]. While they are solely ferroelectric, reducing the electric energy, non-180° domain walls are both ferroelectric and ferroelastic. At the phase transition from the cubic to the ferroelectric state, strain emerges due to the change of the lattice dimensions. However, in a polycrystalline material, the grains cannot deform freely since space is restricted by their neighboring grains. They are forced to maintain their shape which leads to high internal stress [66]. The stress can be compensated by the formation of ferroelastic domains minimizing the elastic energy, however not by 180° domain walls. The formation of ferroelastic domains can be regarded analogues to crystal twinning [66]. Ferroelastic domains can also form under the application of external stress. Note that the term 'ferroelectric domains' used in this work refers to both ferroelectric and ferroelastic domains.

The total energy density (w_{tot}) of the ferroelectric system consists of the sum of the elastic energy, the electric energy, the domain wall energy and the surface energy [66]. In ferroelectric bulk ceramics, the elastic and domain wall energy mainly determine the process of domain formation, while the electric and surface energy are rather small. In order to minimize w_{tot}, the elastic (and

electric) energy is reduced at the expense of the domain wall energy. The number of domain walls (and the domain size) thus reflects the equilibrium state between the domain wall energy and the energies arising during the phase transition [67].

2.2.2 Domain Wall Orientation

Non-180° domain walls are oriented on crystallographic planes, which depend on the symmetry of the ferroelectric upon the phase transition. The point group of the ferroelectric phase is always a subgroup of the paraelectric phase. Mirror planes form permissible domain walls, which are missing in the ferroelectric phase [68]. Along those planes, conditions of both orientation states show mechanical compatibility so that the spontaneous strain arising within two adjacent domains matches each other [69]. Regarding BT, the polarization direction in the tetragonal phase is aligned along one of the six energetically equivalent $\langle 001 \rangle_{pc}$ directions. During the cubic $P\frac{4}{m}\bar{3}\frac{2}{m}$ to tetragonal $P4mm$ transition upon cooling, four of the six $\{101\}_{pc}$ mirror planes present in the cubic phase are lost (the third viewing direction in the cubic system comprises the six [011], [01$\bar{1}$], [101], [$\bar{1}$01], [110] and [1$\bar{1}$0] directions). Two of the $\{101\}_{pc}$ mirror planes remain in $P4mm$, where the third viewing direction in the tetragonal system comprises the [110] and [1$\bar{1}$0] directions. The lost $\{101\}_{pc}$ mirror planes can then act as 90° domain walls. When taking all six $\langle 001 \rangle_{pc}$ polarization directions within the tetragonal phase into account, six 90° domain wall orientations are possible, which form three orientation types with two perpendicular planes each [67, 68], illustrated in Fig. 2.10(a). Across the 90° domain wall, the polarization vectors are arranged in a head-to-tail configuration in order to reduce the local charge at the interface [70].

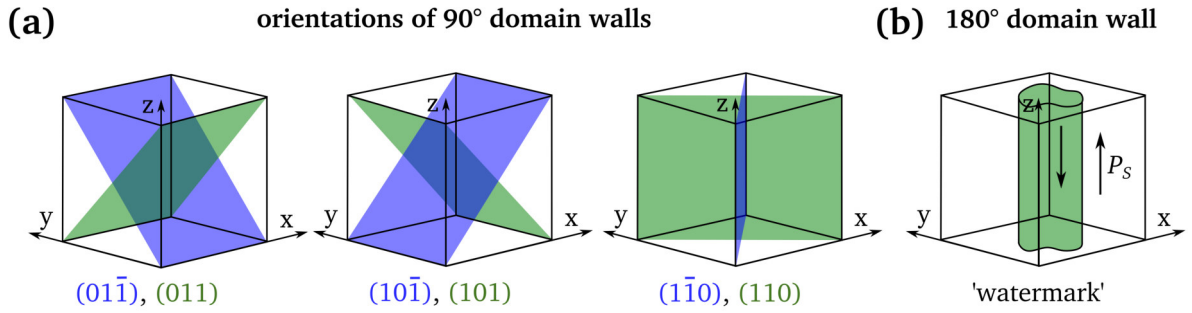

Figure 2.10: Domain wall orientations in a tetragonal perovskite. (a) The six orientations for 90° domain walls. (b) Wavy 180° domain wall, called 'watermark' (redrawn after Ref. 67).

In the tetragonal phase, 180° domain walls can lie on $\{001\}_{pc}$ planes. In BT, they are found to be crisscrossing lamellar 90° domains [71]. However, 180° domain walls often exhibit a wavy shape and do not follow a specific crystallographic direction [70, 72, 73]. Due to their irregular rounded shape, they are denoted as 'watermarks' (Fig. 2.10(b)). Their wavy form is a result of electrostatic energy minimization, since 180° domain walls do not possess a head-to-tail orientation of the polarization vectors [74]. In contrast to uncharged domain walls, charged domain walls exhibit an accumulation of positive or negative charges at the wall boundary. In charged 180° domain walls, the polarization direction either points towards the domain wall in a head-to-head configuration, or away from it in a tail-to-tail configuration [75].

Depending on the orientation of the a and c axes with respect to the image plane, it can be distinguished between a-a, a-c and c-c domains [70] (Fig. 2.11). 90° a-a and a-c domains are structurally identical, only viewed from different directions. For a 90° a-a domain, both polarization

vectors (and with that the tetragonal c_T axes) lie in the image plane, while for a 90° a-c domain, one polarization vector is perpendicular to the image plane. The notations 'a' and 'c' should not be confused with the actual lattice parameters. 180° a-a and c-c domains are also structurally identical. The former exhibit polarization vectors parallel to the image plane, while they are perpendicular to the image plane in the latter configuration.

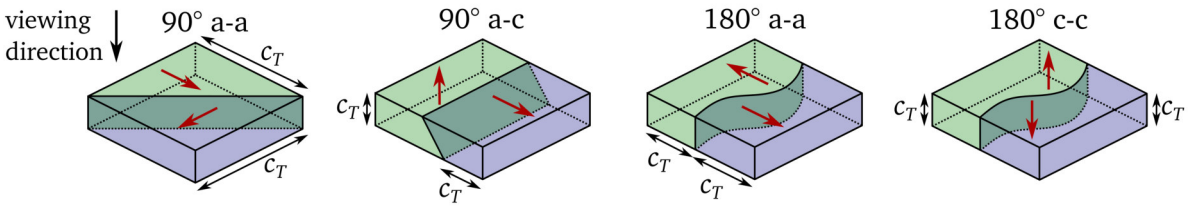

Figure 2.11: Domain configurations in a tetragonal ferroelectric, dependent on the viewing direction. Polarization vectors are depicted as red arrows (modified after Ref. 70).

In a rhombohedral ferroelectric phase, 180° domain walls can lie on $\{111\}_{pc}$ planes, parallel to the $\langle 111\rangle_{pc}$ polarization orientation [76]. Ferroelastic domain walls lie on $\{110\}_{pc}$ and $\{100\}_{pc}$ planes, which are permissible twin boundaries [68, 77]. In the transition from $P\frac{4}{m}\bar{3}\frac{2}{m}$ to $R3m$, all $\{100\}_{pc}$ mirror planes (first cubic viewing direction) and three of the $\{110\}_{pc}$ mirror planes are lost, while three remain (second viewing direction in the trigonal system: $[1\bar{1}0]$, $[01\bar{1}]$, $[\bar{1}01]$).

The orientation states on both sides of ferroelastic domain walls in the rhombohedral phase can form an angle of 109° and 71°. Initially, it was postulated that 71° walls lie on $\{100\}_{pc}$ planes, while 109° walls lie on $\{110\}_{pc}$ planes [76, 78]. Schierholz [79] and Wang et al. [80] suggested to turn the nomenclature around and showed that for $\{100\}_{pc}$ walls the mathematical angle between the polarization vectors is 109° (Fig. 2.12(a)), while it is 71° for $\{110\}_{pc}$ walls (Fig. 2.12(b)). In an orthorhombic ferroelectric, the polarization vectors are oriented along $\langle 110\rangle_{pc}$ directions and 180°, 90°, 60° and 120° domain walls can occur [81, 82].

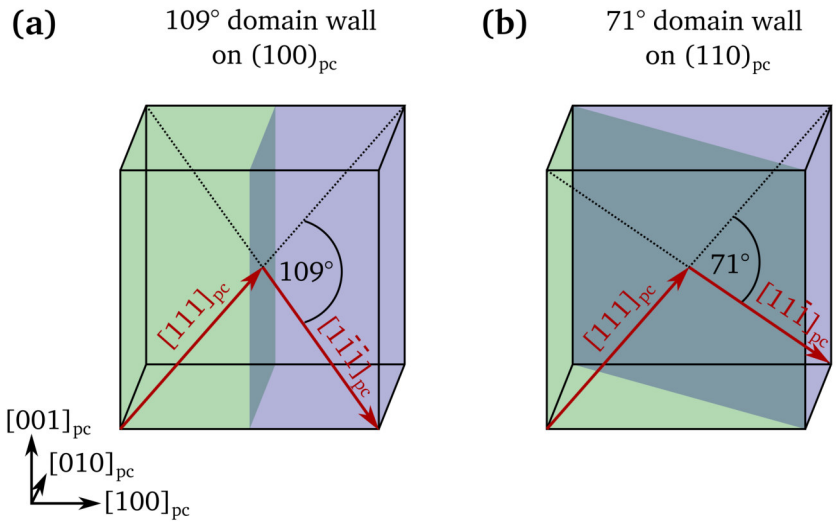

Figure 2.12: Ferroelastic domain walls in a rhombohedral ferroelectric. (a) 109° domain wall on a $(100)_{pc}$ plane. (b) 71° domain wall on a $(110)_{pc}$ plane. The polarization directions are depicted as red arrows (redrawn after Ref. 79).

In polycrystalline ceramics, the domain formation is dependent on the grain size. In a very fine-grained material, lamellar two dimensional twins are formed, while twinning with a more complex three dimensional structure takes place in coarse grained ceramics, in order to accommodate the phase transition strain [66]. Arlt & Sasko [67] observed a herringbone pattern in BT, built of $\{101\}_{pc}$ and $\{001\}_{pc}$ domain walls (Fig. 2.13). The herringbone pattern is not only a common domain configuration in tetragonal ferroelectrics. It also appears in rhombohedral NBT [83, 84], in rhombohedral PZT with near-MPB composition [38, 76, 85] and in orthorhombic KNN [73]. It has to be noted that an ideal domain configuration can be interrupted by intrinsic defects, pores or compositional variations.

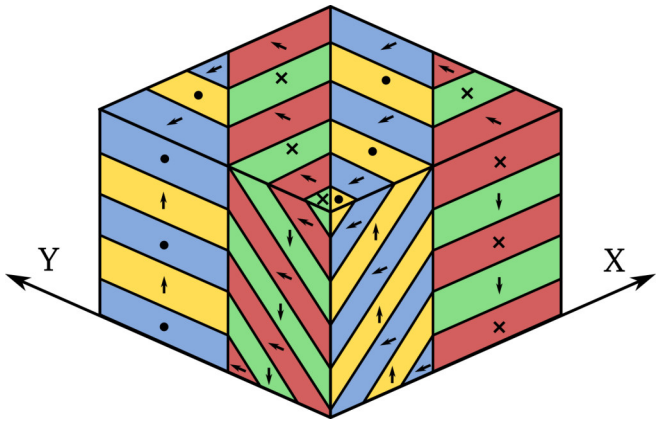

Figure 2.13: Schematic of the herringbone domain configuration. Colors represent domains with identical polarization directions, indicated with arrows. Polarization vectors pointing out and into the viewing plane are denoted with • and ×, respectively (redrawn after Ref. 67).

2.2.3 Poling of Domains

By applying an external electric field, ferroelectric ceramics are brought to a poled state (compare P-E loop in Fig. 2.5(a) on page 7). Poling is thus associated with a reorientation of the domains in the direction of the applied electric field vector. The switching of 90° domains also produces a measurable strain (elongation) oriented along the polarization direction. The alignment of domains upon poling depends on the possible polarization states within the structure. Since crystallites in a ceramic are randomly oriented, a high number of potential polarization orientations allows for a more feasible domain reorientation. In consequence, the polarizability of a material is increased in compositions, where different symmetries account for an increase in possible orientation states. Ideally, upon poling, the material develops a single-domain state, which can be observed in single crystals when the poling direction is along one of the polar axes of the crystal [86]. However, the grains in a polycrystalline material exhibit complex combinations of internal electric fields and stresses, which do not allow for all domains to be reoriented [21]. Upon removal of the field, some domains may switch back and a remanent macroscopic polarization (P_r) and a residual change of dimensions (S_r) remains (Fig. 2.14).

Mechanisms such as domain wall motion and domain nucleation enable the reorientation of polarization during the poling process. Domains with an energetically favored polarization orientation in relation to the poling field can expand while unfavorable domain orientations diminish. Energetically favored domains grow and increase in number. The formation and reorientation of domains can be demonstrated on ferroelectric thin films, where anti-parallel wedge-shaped domains appear

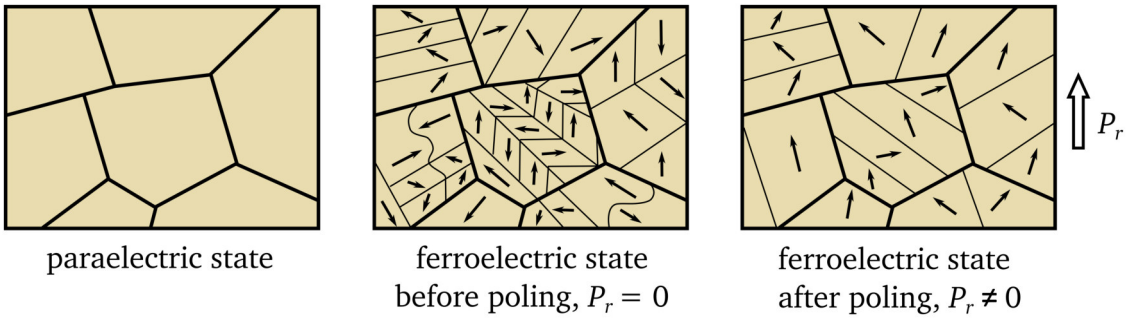

Figure 2.14: Schematic of a polycrystalline ceramic in the paraelectric state, the unpoled ferroelectric state and the poled ferroelectric state with a remanent macroscopic polarization (P_r).

once an electric field is applied in opposite direction of the polarization state [87]. The domains grow forward and coalesce into larger domains or adopt a sideways expansion and sideways domain wall motion [88, 89] (Fig. 2.15). The velocity of the domain wall motion depends on the applied electric field strength [90, 91]. Motion of ferroelastic domain walls can be dictated by a stop-and-go pinning at lattice defects [92]. With increasing field strength, pinned domain walls can proceed further. The effect of domain wall pinning can be reduced by poling the ceramics at high temperatures [93].

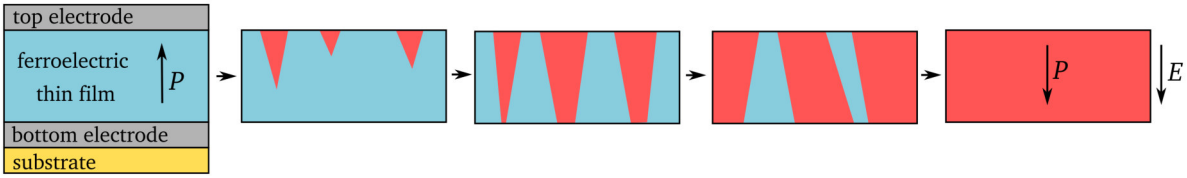

Figure 2.15: Sequence of polarization switching in a ferroelectric thin film. Upon application of an electric field (E) domains start to nucleate and grow, then expand sideways until the entire specimen is poled along the electric field vector (modified after Ref. 89).

2.3 Tilt Systems in Perovskite Oxides

The general formula of the perovskite structure, which comprises the major group of ferroelectric ceramics, is defined as ABX_3. Perovskites are ionic compounds build up by BX_6 octahedra and usually large A-site cations ($r_A > r_B$) situated in the cuboctahedral cage site [94] (Fig.2.16(a)). In perovskite oxides, X is occupied by oxygen forming a corner-connected oxygen octahedra network (Fig. 2.16(b)). The aristotype for perovskites is $SrTiO_3$, which is cubic at room temperature. It has the ideal perovskite structure and a Goldschmidt tolerance factor (GTF) of 1. The GTF is a measure for the stability of the perovskite structure. It depends on the chemical formula and the ionic radii r_A, r_B and r_X of the A, B and X ions [94, 95]:

$$\mathrm{GTF} = \frac{r_A + r_X}{\sqrt{2}(r_B + r_X)} \tag{2.8}$$

If the GTF is between 0.9 and 1.0, the cubic perovskite structure is likely to form. When the GTF is between 0.71 and 0.9, lower symmetries occur. A change in composition can therefore be accompanied by a change in lattice parameters and hence in symmetry. The perovskite structure can host a great number of different ions. Thus, physical properties of perovskites can be manifold

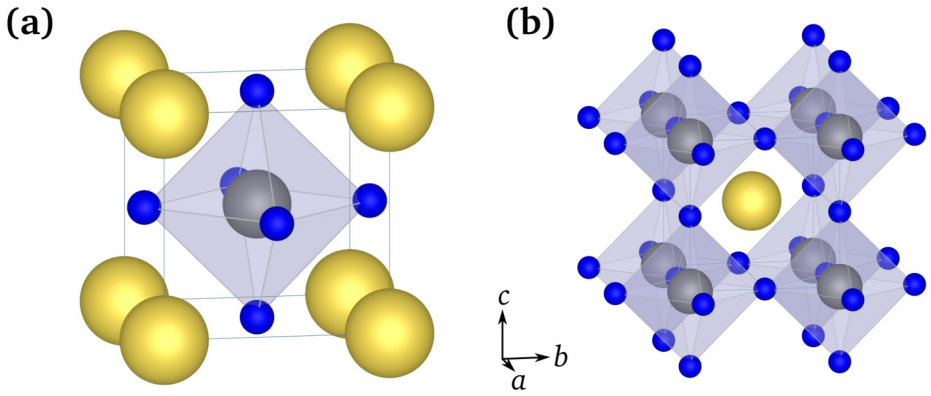

Figure 2.16: (a) Generic perovskite structure (oxygen = blue, *A*-site cations = yellow, *B*-site cations = gray). (b) Different representation showing corner-connected BO_6 octahedra (structure created with Vesta [97]).

[96]. Substitution often occurs at the *A* site, but is also possible at the *B* site. The occupation of one site by several atoms can be random or ordered.

Structural distortions of perovskite oxides are mainly attributed to three different mechanisms [96]: tilting of the BO_6 octahedra, distortion of the BO_6 octahedra and cation displacement on the *A* and *B* site. Cation displacement is the fundamental mechanism for creating a spontaneous polarization and is therefore essential to the resulting ferroelectric properties.

Oxygen octahedral tilting is the most common distortion mechanism in perovskite oxides. It always produces a symmetry lower than the cubic aristotype [98]. The BO_6 octahedra are tilted while maintaining their corner connectivity. Tilting of one octahedron always provokes tilting of its neighboring octahedra in the opposite sense. Octahedral tilting occurs, when the *A*-site cation is too small for the *A*-site interstice. By tilting the oxygen octahedra, the volume of the *A*-site interstice is reduced, forming a more energetically efficient structure [99, 100]. Tilting therefore allows for a larger variety in the elemental occupancy on the *A* site, while the surrounding of the *B* site is left unaltered [98].

Glazer [101] established a classification and nomenclature for octahedral tilting in perovskites. The Glazer notation consist of a set of three letters a, b and c, which refer to the tetrad axes [100], [010] and [001]. If tilting is equal along two or three axes, the letter is repeated. As example, aac refers to equal tilts about [100] and [010] and a different tilt about [001]. A superscript is added, to specify the sense of tilting of two adjacent perovskite layers, which can be in-phase (+) or anti-phase (−). For in-phase tilting, octahedra are tilted in the same direction around the tilt axis, while for anti-phase tilting, octahedra in adjacent layers are tilted in opposite direction around the tilt axis. If no tilting is present, the superscript 0 is used. An ideal perovskite structure without tilting has the Glazer notation $a^0a^0a^0$. In-phase and anti-phase tilted perovskites, where the c axis is the tilt axis, have the notation $a^0a^0c^+$ and $a^0a^0c^-$, respectively (Fig. 2.17(a)). Since the corners of the octahedra remain connected, tilting along one axis decreases the distance between octahedra centers perpendicular to the tilt axis. Denoting the angle of tilt (α, β and γ) to each of the tetrad axes, the pseudocubic (pc) axial lengths (a_{pc}, b_{pc} and c_{pc}) can be derived [102]:

$$\begin{aligned} a_{pc} &= a_0 * cos\beta * cos\gamma \\ b_{pc} &= a_0 * cos\alpha * cos\gamma \\ c_{pc} &= a_0 * cos\alpha * cos\beta \end{aligned} \tag{2.9}$$

with a_0 being the lattice parameter of the non-tilted perovskite structure. The same tilt about all three axes ($a^+a^+a^+$) results in $a_{pc} = b_{pc} = c_{pc}$ with $\langle 111 \rangle_{pc}$ being the rotation axis [101]. In total, 23 different tilt systems are possible. They are listed by Glazer with their corresponding notation, unit cell parameters and space group [101] .

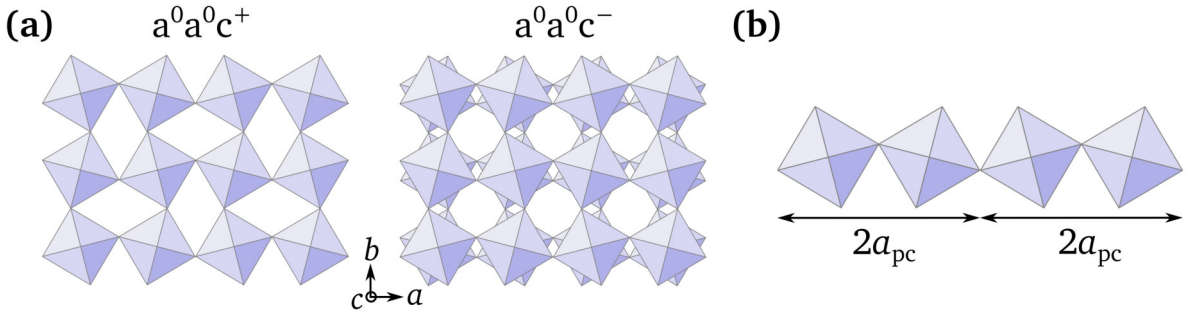

Figure 2.17: (a) In-phase $a^0a^0c^+$ tilt system, where adjacent oxygen octahedra layers are tilted in the same sense around the c axis and anti-phase $a^0a^0c^-$ tilt system, where the layers are tilted in an opposite sense. (b) The repeat distance of lattice parameters perpendicular to the tilt axis is doubled ($2a_{pc}$); (modified after Refs. 96 and 102).

From the illustration in Fig. 2.17(b) it becomes apparent that the repeat distances along the a_{pc} and b_{pc} axes, perpendicular to the tilt axis, are doubled ($2a_{pc}$). Regarding diffraction patterns, the doubling of the unit-cell parameters causes reflections that lie on half-integral reciprocal distances [102]. While the main reflections have integer hkl, the superlattice reflections (SRs) have $\frac{1}{2}\{hkl\}$ indices. Howard & Stokes [98] derived group-subgroup relationships between the different tilt systems. While Glazer's 23 tilt systems are partly in the same space group, their analyses led to 15 distinct tilt patterns with distinct space groups. The group-subgroup relations are shown in Fig. 2.18. All known perovskite structures (except one that requires octahedral distortion) fall within these 15 tilt systems.

In ferroelectric perovskites, octahedral tilting and cation displacement often become superimposed [103]. The combination of both can therefore lead to changes in the symmetry. When the cation displacement is anti-parallel, the structure is centrosymmetric and the space group stays the same as defined by the tilt system. If cation displacement is parallel, the structure becomes non-centrosymmetric and the space group is a subgroup of the group defined by the tilt system [102]. As an example, rhombohedral NBT-BT exhibits the tilt system $a^-a^-a^-$ ($R\bar{3}c$) and additionally parallel cation displacement along $\langle 111 \rangle_{pc}$. Due to the parallel displacement, $R\bar{3}c$ becomes $R3c$ since the inversion centre is lost. A similar reduction in symmetry occurs in the tetragonal phase, which exhibits $a^0a^0c^+$ tilting and parallel cation displacement along $[001]_T$. Due to the cation shift, the mirror plane perpendicular to the c axis in $P\frac{4}{m}bm$ is lost, resulting in the $P4bm$ space group. It has to be noted that cation displacement itself can also produce superlattice reflections analogous to octahedral tilting, however, only if the displacement is anti-parallel [102]. Chemical ordering of ions can also result in superlattice reflections. Chemical ordering generates reflections of $\frac{1}{y}\{hkl\}$, where y is the number of planes in the repeat distance [100]. Exemplary, ordering of 2:1 results in $y = 3$. As long as $y \neq 2$, such SRs can be distinguished from the SRs caused by oxygen octahedral tilting, where y always equals 2.

Generally, the scattering from oxygen atoms is considered weaker than the scattering from the cations in the lattice [100]. A clear advantage of electron diffraction is the possibility to image weak SRs, while other X-ray techniques may be insensitive to monitoring such reflections. Woodward & Reaney [100] simulated electron diffraction patterns for all known perovskite structures, based on

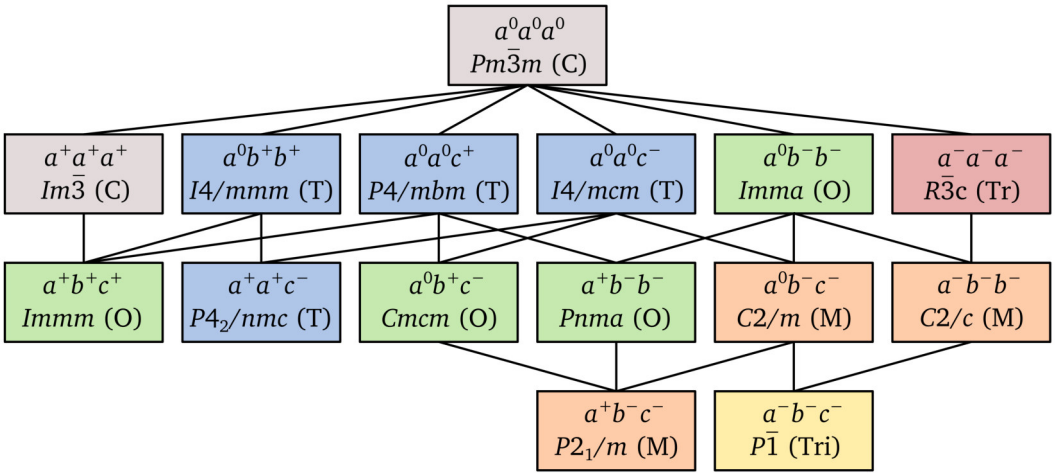

Figure 2.18: (a) Group-subgroup relations of the allowed space groups by the 15 possible tilt systems. C = cubic, T = tetragonal, Tr = trigonal, O = orthorhombic, M = monoclinic, Tri = triclinic (redrawn after Ref. 98).

ideal kinematical assumptions, which regard only a single scattering event. Allowed SRs underlie specific *hkl* conditions. However, usually no perfectly kinematical scattering is present, but multiple scattering events occur (dynamical theory). As a result, reflections can arise in positions where they are kinematically absent.

Anti-phase tilting results in SRs of the type $\frac{1}{2}\{ooo\}$, where '*o*' stands for odd *hkl* indices. They occur in $\langle 110\rangle_{pc}$ zone axes [100]. Kinematically, the $\frac{1}{2}\{ooo\}$ SRs are absent from $\langle 110\rangle_{pc}$ zone axes that are perpendicular to the tilt axis. For $a^-a^-a^-$ with its tilt axis $\langle 111\rangle_{pc}$, six of the possible twelve $\langle 110\rangle_{pc}$ zone axes do not contain SRs. A clear differentiation of the anti-phase tilt systems $a^0a^0c^-$, $a^0b^-b^-$ and $a^-a^-a^-$ under kinematical assumptions is only theoretically possible by analyzing all $\langle 110\rangle_{pc}$ electron diffraction patterns (which is practically unfeasible due to the restricted tilting range in the TEM and dynamical scattering). In-phase tilting results in SRs of the type $\frac{1}{2}\{ooe\}$, where '*e*' denotes even *hkl* indices. For the single tilt $a^0a^0c^+$, SRs occur in $\langle 100\rangle_{pc}$ zone axes parallel to the tilt axis and in all $\langle 111\rangle_{pc}$ zone axes. When more than one axis is tilted in-phase, all variants of $\frac{1}{2}\{ooe\}$ SRs occur in $\langle 100\rangle_{pc}$, $\langle 110\rangle_{pc}$ and $\langle 111\rangle_{pc}$. The $a^0a^0c^+$ tilt system can thus clearly be distinguished from the other in-phase tilt systems by the absence of SRs in $\langle 110\rangle_{pc}$. Mixed tilt systems exhibit both $\frac{1}{2}\{ooo\}$ and $\frac{1}{2}\{ooe\}$ SRs, as well as additional reflections of the type $\frac{1}{2}\{oee\}$ [100].

In ferroelectric ceramics, such as NBT-BT, where the deviation in the unit cell from the cubic symmetry is very small, electron diffraction patterns appear pseudocubic. The occurrence of superlattice reflections is therefore crucial for identifying the present phases and tilt systems, as executed in this work.

2.4 Relaxor Ferroelectrics

Relaxor ferroelectrics (or relaxors) are ferroelectric-like materials that exhibit some of the largest known values of piezoelectric coefficients and strain [104]. Besides the strong electromechanical response, they also show a large dielectric permittivity, which led to their broad industrial application as capacitors and actuators [9]. The reason for their enhanced properties lies in their complex and dynamic nanoscale polar structure, which differs profoundly from a conventional ferroelectric

domain structure. A classical relaxor ferroelectric is $Pb(Mg_{1/3}Nb_{2/3})O_3$ (PMN) and its solid solutions, which have been extensively studied [6, 105, 106]. Due to the legislative constraints for Pb-containing materials, lead-free relaxors gained considerable attention [8, 107]. Still, despite decades of research, understanding the structural origins of relaxor behavior remains a challenging quest [108]. As stated by Cohen, while being fascinating materials, relaxor ferroelectrics seem to be 'heterogeneous and hopeless messes' [109].

2.4.1 Relaxor vs. Ferroelectric Characteristics

Unlike classical ferroelectrics, relaxors with a perovskite structure possess a random distribution of different atoms at either or both the A and B site in the ABO_3 lattice. If both the A and B sublattice is occupied by two different cations, the chemical formula is $A'_xA''_{(1-x)}B'_yB''_{(1-y)}O_3$ [6]. The A' and A'' ions (respectively B' and B'') can have different charges, however x and y are defined to maintain an overall charge neutrality.

One of the most prominent dielectric features of relaxors, which distinguishes them from a normal ferroelectric, is a broad and diffuse maximum of the temperature-dependent permittivity [111]. The curve of the permittivity further exhibits a strong frequency dependence, whose dispersion is broadened for temperatures below the temperature of the maximum of permittivity, T_m [110]. Fig. 2.19(a) compares the temperature-dependent permittivity of a normal ferroelectric, showing a sharp transition at T_C, and a relaxor displaying a diffuse transition over T_m. With higher frequency of the probing field, T_m is moved to higher temperatures. Unlike in ferroelectrics, above T_m, relaxors do not obey the Curie-Weiss law [6, 110]. T_m therefore does not correspond to the phase transition from the ferroelectric to paraelectric state, as does T_C. This is due to the presence of polar nanoregions (PNRs) which persist well above T_m [112]. The transformation to a non-polar paraelectric phase occurs only at higher temperature, the so-called Burns temperature, T_B [110]. At T_B, no PNRs are present any more (Fig. 2.19(b)). The transformation at T_B, however, is no structural phase transition in the classical sense, because it is not accompanied by a macroscopic

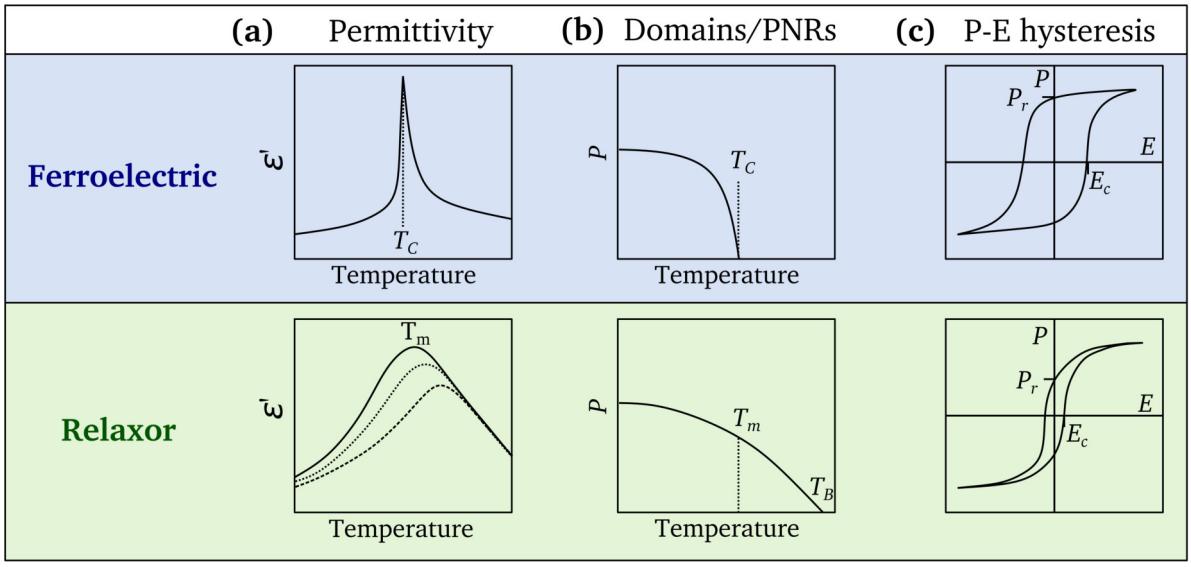

Figure 2.19: Characteristics of a normal ferroelectric vs. a relaxor. (a) Sharp peak of ε' at T_C vs. dispersive and broad maximum at T_m. (b) No ferroelectric domains and macroscopic polarization above T_C vs. PNRs present up to T_B. (c) Broad P-E loop with high P_r vs. slim P-E loop and low P_r (redrawn and modified after Ref. 110).

change in crystal symmetry [7]. In contrast to ferroelectrics, relaxors show slim hysteresis loops with a small remanent polarization, P_r (Fig. 2.19(c)). The reason lies in a swift reversion of PNRs to their random orientation after the electric field is removed [110]. Such relaxors are denoted as ergodic and do not exhibit a remanent ferroelectric state once the electric field in removed. Non-ergodic relaxors, however, are irreversibly transformed into a ferroelectric upon poling and exhibit more square-shaped P-E loops with a higher remanent polarization.

2.4.2 Polar Nanoregions and Relaxor Models

There is no uniform definition for PNRs in literature. The term generally describes nanometer-sized polar regions (dynamic or static) [108]. Unlike ferroelectric domains, which are large and uniform, PNRs are nanoregions with a short-range polar order. The terms 'PNRs' and 'nanodomains' sometimes refer to the same structural feature. It reflects that the terminology for polar regions with a short correlation length has a certain ambiguity. PNRs form below T_B, where they are assumed to be mobile and dynamic (ergodic). Their polar axis is thermally fluctuating between equivalent states of polarization [113]. PNRs are assumed to grow in size with decreasing temperature [111]. Their temperature-dependent evolution is schematically illustrated in Fig. 2.20.

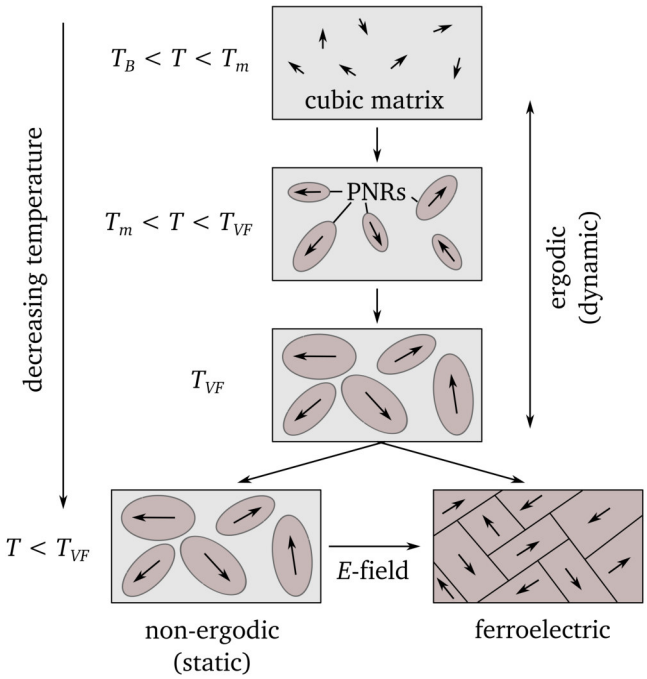

Figure 2.20: Schematic illustrating the evolution of the relaxor nanostructure with decreasing temperature (redrawn after Ref. 114).

In a canonical relaxor, the dynamics of PNRs slow down until a critical freezing temperature (T_{VF}) is reached, where they are transferred into a 'frozen' state. Such behavior is known from dipole glass phases. Therefore, slowing down and freezing of PNR dynamics is considered under the dipolar glass model [115]. Macroscopically, the polarization is zero, since the PNR dipoles are randomly distributed and the average symmetry appears pseudocubic [8]. A non-ergodic relaxor can irreversibly be transformed into a ferroelectric state when an electrical field is applied [116]. Only when heated, the ferroelectric state is transformed back to the relaxor state at the ferroelectric-

to-relaxor transition temperature, $T_{F\text{-}R}$ [117]. This transition is represented by an anomaly in the permittivity when crossing from the non-dispersive to the dispersive region of the permittivity curve [118, 119]. In non-canonical relaxors, the ergodic state is directly transformed into a ferroelectric state upon cooling by a spontaneous phase transition and vice versa [7].

Relaxors derive their name from the dielectric relaxation response. Dielectric relaxation is considered as the delayed and gradual response of polarization in a dielectric material to an external stimulus, a small-signal electric field [111]. In relaxors, the relaxational dynamics reflect in the frequency dependence of the permittivity and its maximum. The dielectric relaxation time, which increases with decreasing temperature, is believed to originate from the reorientation of the PNR dipoles [112]. The relaxational freezing temperature of PNRs, T_{VF}, is considered under the Vogel-Fulcher relation [113, 120, 121]:

$$f = f_0 \, exp\left[\frac{-E_a}{k_b(T_m'' - T_{VF})}\right] \tag{2.10}$$

with the frequency, f, the cut-off frequency of the distribution of relaxation time, f_0, the activation energy, E_a, the Boltzmann constant, k_b, and the temperature maximum of the imaginary part of the permittivity, T_m''.

Most interpretations for relaxor properties are subdivided into two underlying concepts: the already mentioned dipolar glass model and the random-field model. A comparative overview of further relaxor models is given by Ahn et al. [122]. In the dipolar glass model, PNRs are considered as nanometer-sized phase fluctuations located within a non-polar cubic matrix [7] (Fig. 2.21(a)). The PNRs can grow in size, but their percolation into large ferroelectric domains is prevented by chemical disorder and random electric fields [123]. The random-field model [124–126] advocates the assumption that the relaxor microstructure is build up by polar nanodomains separated by small domain walls (Fig. 2.21(b)). The symmetry transition applies to the entire crystal and no cubic matrix is present. The structure is broken up into ferroelectric nanodomains, which stay in their small size due to constraint of random electric fields which originate from charged compositional disorder [125]. The concept of PNRs is controversial, as illustrated by Hlinka [127], who makes a clear distinction between PNRs and ferroelectric nanodomains. While the mechanisms of PNR formation are not yet conclusively resolved, they are believed to be the central element for the relaxor behavior. The occurrence of PNRs has been confirmed by a variety of analytical techniques, including neutron diffraction [128, 129], nuclear magnetic resonance (NMR) spectroscopy [130] and visualization via piezoresponse force microscopy (PFM) [131] and TEM [132].

Models describing PNR formation are manifold. Some earlier explanations relate to the disordered distribution of the different ions in the relaxor perovskite structure. Below T_B, polarization develops in regions of several unit cells in size that are richer in one cation (e.g. B' or B'') and grow in size with

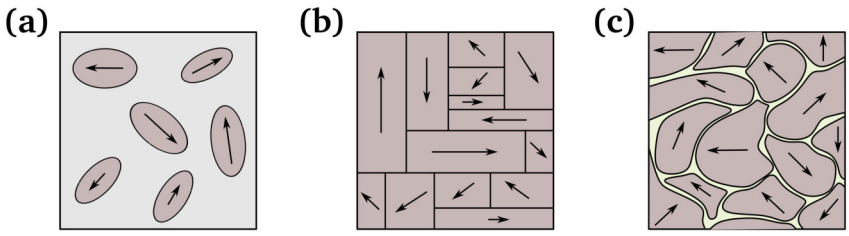

Figure 2.21: Models for the relaxor microstructure. (a) PNRs embedded in a cubic matrix and (b) PNRs/nanodomains separated by domain walls (redrawn after Ref. 7). (c) Slush-like state with PNRs of different symmetries (redrawn after Ref. 133).

decreasing temperature [134]. PNRs were also related to small areas of chemical ordering within a disordered matrix. These ordered regions with short coherency are suggested as the nucleation site of localized polar clusters [135]. Here, ordering of the cations constitutes a relaxation process via diffusion, which can be quite fast at elevated temperatures. However, it needs to be noted that these deductions were made from TEM diffraction studies, where superlattice reflections were assigned to cation ordering, while such reflections can likewise be created by oxygen octahedral tilting. Opposed to chemical short-range ordering, it could be shown for doped BT relaxor ferroelectrics that PNRs arise from Ti and O off-center displacement induced by the dopant ions, which cause random local strain fields suppressing a ferroelectric long-range order [136]. More recent molecular dynamics simulations on the solid solution of PMN with $PbTiO_3$ (PMN-PT) suggest a multi-domain state of domains being 2-10 nm in size (comparable to the slush state of water), rejecting the presence of a cubic matrix [137]. For KNN-based ceramics, a slush-like multiphase coexistence of polar nanoregions (Fig. 2.21(c)) was demonstrated [133]. Observations of a dynamic nature of diffuse scattering opposes the concept of static PNRs [138, 139]. The multitude of scientific works illustrates that solving the questions concerning the complex microstructure of relaxor ferroelectrics and the formation of PNRs still remains challenging. This is also owed to the wide variety of different relaxor materials, rendering the adoption of one single descriptive model inapplicable.

Chemical substitution in solid solutions allows mixing of relaxors with classical ferroelectrics, which display a crossover from relaxor to ferroelectric properties dependent on their composition. Such systems include, e.g., PMN-PT, but also numerous lead-free materials, such as BT-, KNN- and NBT-based solid solutions. Among them is NBT-BT, which is surveyed in detail in the following section.

2.5 The NBT-BT System

$(1-x)Na_{1/2}Bi_{1/2}TiO_3$-$xBaTiO_3$ (NBT-BT) is a well-investigated lead-free material system which exhibits relaxor behavior close to its MPB and close to the NBT end member. Takenaka et al. [10] firstly described the enhancement of piezoelectric properties at the MPB for $x \approx 0.06$, where rhombohedral and tetragonal phases coexist. NBT is a relaxor, where the *A* site is occupied by Na^+ and Bi^{3+} in equivalent amounts, while BT is a classical ferroelectric. In the relaxor-ferroelectric solid solution with perovskite structure, Na^+, Bi^{3+} and Ba^{2+} all occupy the *A* site.

2.5.1 Potential of NBT-BT Ceramics

Compared to pure NBT, which exhibits a relatively high coercive field (E_c), conductivity and electrical loss [140], all being disadvantageous for the poling process, NBT-BT ceramics allow for an easier poling. While NBT-BT exhibits lower piezoelectric and electromechanical coupling coefficients (d_{33} and planar electromechanical coupling factor, k_p) compared to other promising lead-free materials, such as KNN-based systems [141], it has the advantage of enabling an easy preparation of dense ceramics [13, 142]. Furthermore, NBT-BT shows a high electric field induced strain response (∼0.4 %) [143], which makes it interesting for the application as actuator material. The high mechanical strength and large k_t/k_p ratio (with k_t being the thickness coupling coefficient) makes NBT-BT suitable for high-frequency and high-power applications [10, 12, 144]. Superior high-power and high-frequency properties are especially promising for ultrasonic techniques, such as ultrasonic cleaning devices. Tou et al. [11] could demonstrate that NBT-BT-based ceramics

display a higher mechanical quality factor compared to PZT at high vibration velocities. Transducers with a NBT-BT-based ceramic installed in an ultrasonic cleaning device (displayed in Fig. 2.8(c) on page 10) show a higher vibration velocity and lower power loss compared to the same transducer with a PZT ceramic [11]. However, the drawback of the NBT-BT system is its comparably low depolarization temperature, T_d, where piezoelectric properties disappear [145, 146]. A low T_d limits the range of potential operating temperatures for NBT-BT ceramics.

2.5.2 Di- and Piezoelectric Properties & Phase Diagrams

Piezoelectric properties of NBT-BT ceramics peak at the MPB (x = 0.05-0.08) [10, 12, 147–151]. The MPB is no sharp transition, but a transition region with coexisting phases. Different ranges of the MPB are reported in literature, with the electromechanical properties demonstrating a maximum around x = 0.06-0.07. Room temperature values for a d_{33} of 167 pC/N [152] and a high k_p of 29 % [12, 152] are reported for x = 0.06-0.07. The dielectric loss ($tan\delta$) is reduced to 0.04 (for x = 0.07) [153]. For x = 0.06, T_d decreases and exhibits the lowest value of ∼100 °C [145, 154]. T_d is most accurately obtained from the decrease of the piezoelectric coefficient, d_{33}, as a function of temperature [155]. It is argued that at the MPB, poling-induced domains align more easily from the nanoscale relaxor structure and in turn can be more easily disintegrated by temperature, thus reducing the thermal stability of domains and resulting in a low T_d [156]. Others argue that the phase mixture at the MPB increases lattice incompatibilities, resulting in less temperature-stable domain structures [152].

In unpoled samples, the non-ergodic relaxor behavior at the MPB is characterized by a diffuse phase transition with a broad peak over T_m and a frequency dispersion of the temperature-dependent permittivity (ε') on the low temperature side (Fig. 2.22(a)), relating to the coexistence of rhombohedral *R*3*c* and tetragonal *P*4*bm* PNRs [157]. At higher BT fraction ($x > 0.10$), the frequency

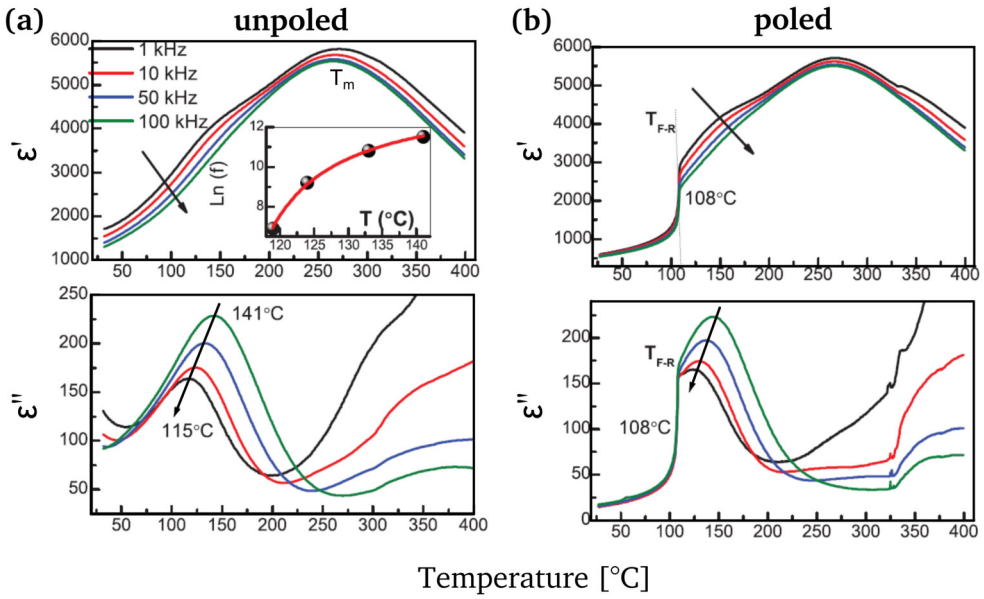

Figure 2.22: Temperature-dependent real (ε') and imaginary (ε'') part of the relative permittivity at different frequencies in unpoled (a) and poled (b) NBT-6BT (with 6 mol % BT). Arrows indicate the increasing frequency. The inset in (a) displays the Vogel-Fulcher fitting of the dielectric data (reprinted from Ref. 121 with permission of the American Physical Society).

dispersion at lower temperatures strongly decreases, indicating ferroelectric behavior at room temperature. For compositions left to the MPB there is a certain discrepancy in published permittivity data. The absence of a frequency dispersion suggesting a ferroelectric character was observed for $x = 0.04$ [158], while pure NBT displays a relaxor-typical frequency dispersion [159].

Permittivity measurements of poled specimens vary profoundly from unpoled samples. When poling MPB compositions at high electric field, the room temperature non-ergodic relaxor state can be converted into a ferroelectric state. Here, the low-temperature frequency dispersion of permittivity is lost [121] (Fig. 2.22(b)). When heated, the ferroelectric state is transformed back to the relaxor state, manifested in the sharp transition at $T_{F\text{-}R}$, where the induced ferroelectric domains lose their macroscopic texture and piezoelectricity disappears [118]. Subsequently, a disintegration into nanoscale PNRs takes place.

The NBT-BT system was initially believed to undergo a transition from a FE to an AFE state at elevated temperatures, deduced from anomalies in the permittivity and a doubled P-E hysteresis loop [10, 141, 143, 153, 160]. Fig. 2.23 shows the temperature-dependent polarization hysteresis of NBT-6BT (with 6 mol % BT), where a constriction appears at 85-100 °C [157]. The AFE state was believed to persist between T_d and T_m and then transform into the paraelectric state at higher temperature. However, this subject experienced a lot of controversy. A constriction of the P-E loop can also arise due to other mechanisms, such as the field-induced relaxor-ferroelectric transition [157], or domain wall pinning at defects and formation of internal bias fields [21]. Raman scattering studies could not confirm any indications for a structural phase boundary in the compositional range of $0.00 < x < 0.09$, which would be expected for a FE-AFE transition [161, 162]. Due to missing structural and thermal characteristics, the FE-AFE transition was consequently omitted [157].

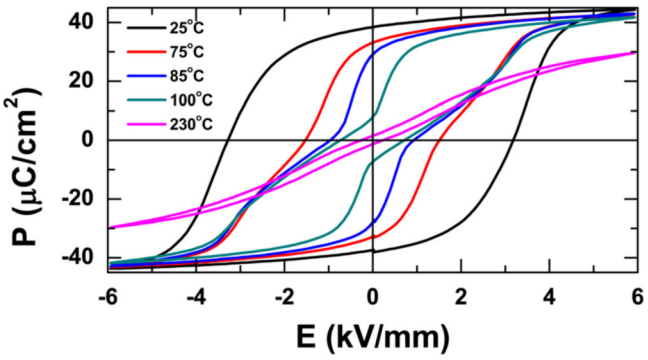

Figure 2.23: P-E hysteresis of the MPB composition NBT-6BT at different temperatures (reprinted from Ref. 157 with permission of AIP Publishing).

Ma & Tan [160] published a structural phase diagram for unpoled NBT-BT based on in-situ temperature-dependent TEM investigations (Fig. 2.24). In addition to the MPB of coexisting *R*3*c* + *P*4*bm* phases, they identified a second MPB for $x \approx 0.11$, where *P*4*bm* nanodomains and large ferroelectric *P*4*mm* domains coexist. Ferroelectric domains start to disappear when reaching T_d and all compositions subsequently exhibit the nanoscale *P*4*bm* structure. The transition to the paraelectric cubic phase takes place in a large temperature range well above T_m. Subsequently, a further MPB on the NBT-rich side for $x = 0.03$-0.04 was introduced, separating a *Cc* from a *R*3*c* phase field [163]. Another setup with two MPBs, one showing a *R*3*c*-to-*R*3*m* transition for $x = 0.05$ and a *R*3*m*-to-*P*4*mm* transition for $x = 0.11$ was proposed based on in-situ synchrotron diffraction [164].

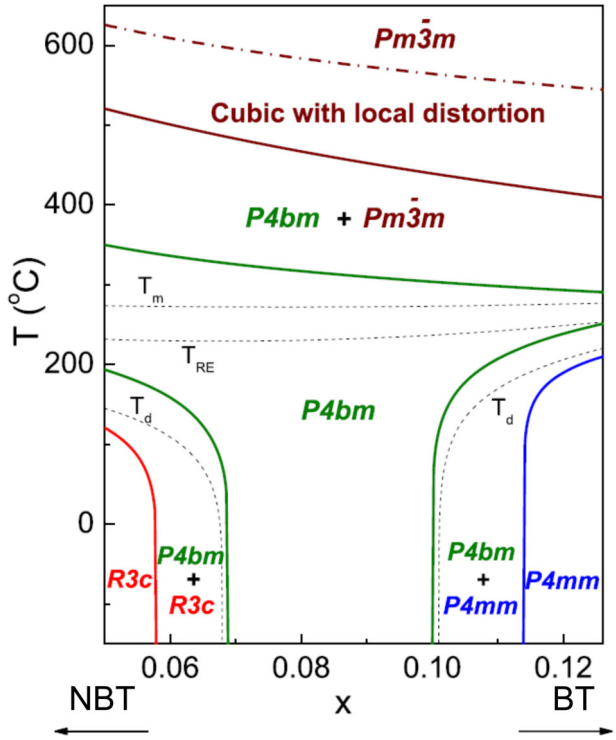

Figure 2.24: Structural phase diagram of unpoled $(1-x)$NBT-xBT. Dotted lines indicate temperatures derived from anomalies in the permittivity response. T_{RE} denotes the vanishing of the frequency dispersion (reprinted from Ref. 160 with permission of John Wiley and Sons).

While the structural phase diagram in Fig. 2.24 is mainly based on TEM investigations, Adhikary et al. [150] lately presented an updated phase diagram for unpoled (Fig. 2.25(a)), as well as for poled NBT-BT (Fig. 2.25(b)), based on temperature-dependent X-ray and neutron powder diffraction. In unpoled specimens, the *R*3*c* + *P*4*bm* MPB spans the compositional range of $0.03 < x < 0.065$ and develops into a coexisting phase field of *P*4*bm* + *P*4*mm* for $x > 0.065$. In contrast to Fig. 2.24, a single *P*4*bm* phase field is absent. The *P*4*mm* + *P*4*bm* coexistence spans over a wide compositional range up to $x = 0.18$. The distinction between an ordered and disordered *P*4*bm* phase is made based on an accurate fit of the *P*4*bm* structural model for the superlattice reflections. In the structural phase diagram of poled NBT-BT (Fig. 2.25(b)), a *Cc* + *R*3*c* MPB is absent. The coexisting phase field of *R*3*c* + *P*4*bm* only exists at higher temperatures between 150 and 300 °C. Compositions are rhombohedral for $x < 0.065$ and tetragonal (*P*4*mm* + *P*4*bm*) for $x > 0.065$. Structural characteristics of unpoled and poled NBT-BT are further discussed in section 2.5.4 and 2.5.5, respectively.

2.5.3 The End Members NBT and BT

The properties of NBT-BT are strongly linked to the complex structural characteristics of the relaxor ferroelectric end member NBT. Its temperature-dependent phase transition from $Pm\bar{3}m$ to *P*4*bm* takes place at ~500-540 °C [165]. The *P*4*bm* phase exhibits in-phase $a^0a^0c^+$ octahedral tilting and cation displacement along the polar $[001]_{pc}$ axis [166]. *P*4*bm* transforms into rhombohedral *R*3*c* at 250-400 °C, exhibiting anti-phase $a^-a^-a^-$ octahedral tilting and cation displacement along $[111]_{pc}$ [165]. However, the structure of NBT at room temperature is debated [167]. Besides being described with a *R*3*c* symmetry, high-resolution X-ray diffraction showed that the average structure of NBT can

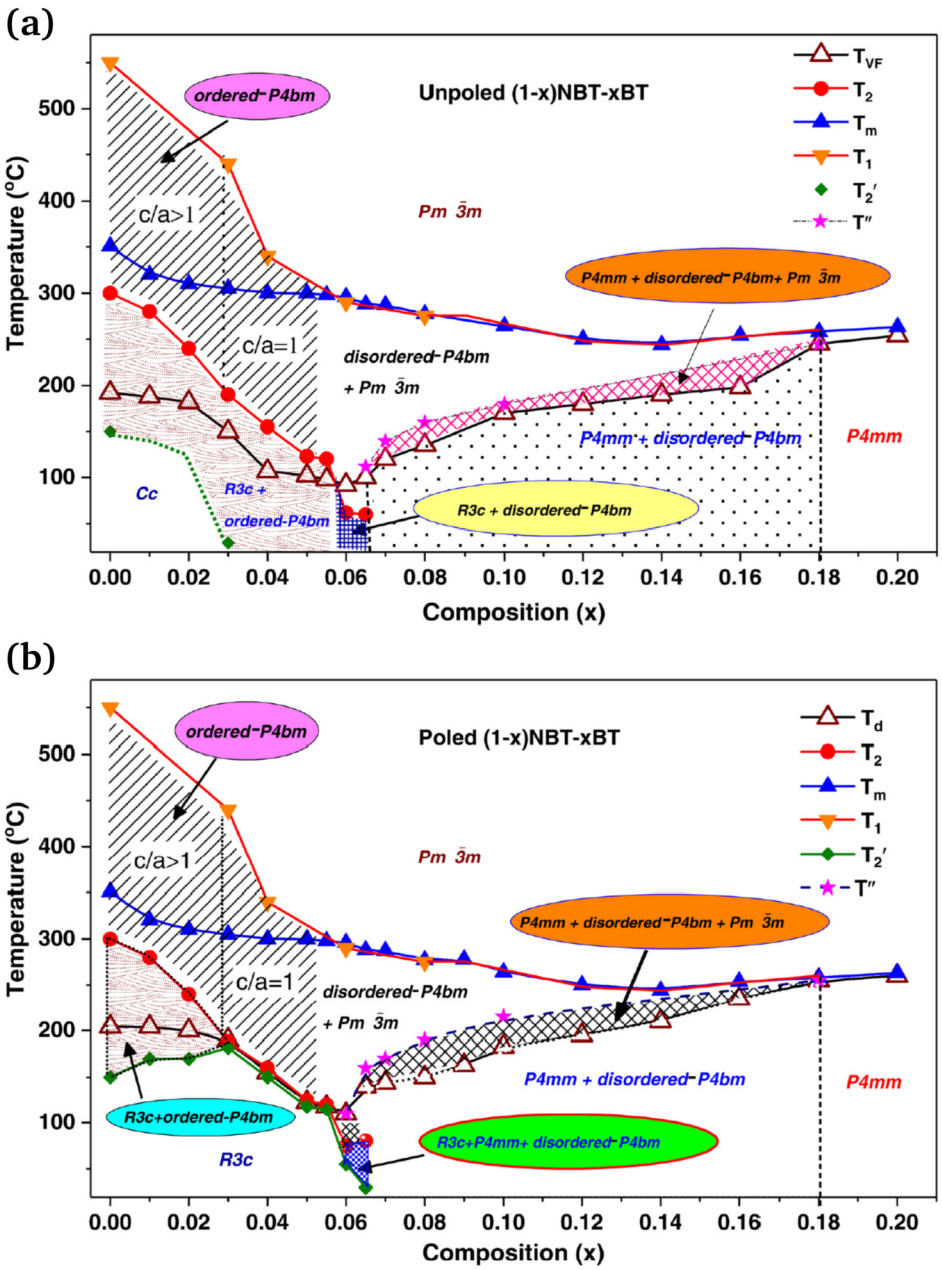

Figure 2.25: Structural phase diagram of unpoled (a) and poled (b) $(1-x)$NBT-xBT. Besides T_{VF} (unpoled), T_d (poled) and T_m, the *R*3*c*-to-*P*4*bm* transition temperature, T_2, the *P*4*bm*-to-*Pm*$\bar{3}$*m* transition temperature, T_1, the temperature for the onset of in-phase octahedral tilting, T_2', and the *P*4*mm*-to-*Pm*$\bar{3}$*m* transition temperature, T'', is given (reprinted from Ref. 150 with permission of the American Physical Society).

also be fitted with the monoclinic *Cc* space group, comprising $a^-a^-c^-$ octahedral tilting [168, 169]. A coexistence of *R*3*c* + *Cc* is also reported [170], which transforms to pure *R*3*c* upon poling [171, 172]. Concerning the domain structure, Dorcet & Trolliard [84] observed lamellar needle-shaped domains lying in $\{110\}_{pc}$ and $\{100\}_{pc}$ planes, a cross pattern of orientations and a herringbone-type structure. NBT ceramics investigated by Otoničar et al. [83] show differently oriented domains forming a uniform complex domain pattern (Figs. 2.26(a) and (b)) and a triangular shaped pattern of three directions when viewed along the $\langle 111\rangle_{pc}$ zone axes (Fig. 2.26(c)). NBT single crystals exhibit similar domain configurations [173, 174].

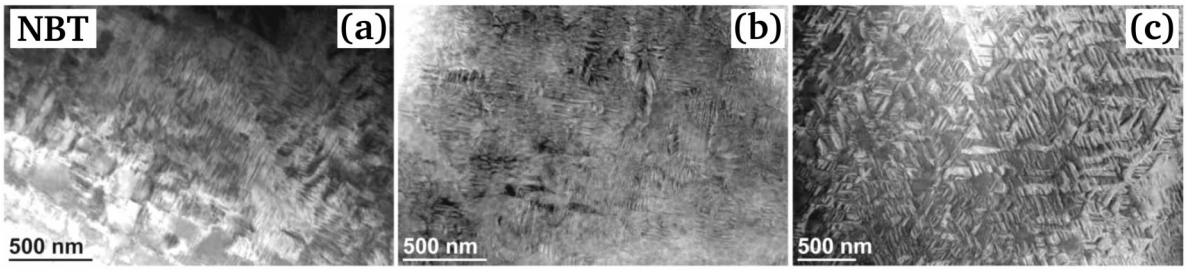

Figure 2.26: TEM micrographs of the domain patterns in pure NBT. (a) Needle-shaped domains, which form a square-net pattern in (b) and a triangular pattern in (c) (reprinted with permission from Ref. 83, copyright 2011 IEEE).

In electron diffraction, elongated $\frac{1}{2}$ $\{ooe\}$ SRs indicate the presence of small tetragonal *P*4*bm* platelets lying in $\{100\}_{pc}$ planes within the *R*3*c* matrix [84]. The platelets are interpreted as remnants of the high temperature *P*4*bm* phase. Levin & Reaney [175] proposed an even more complex model comprising three plate-like orthorhombic variants with short-range $a^-a^-c^+$ tilting, resulting in an average pseudorhombohedral or pseudomonoclinic structure for scale lengths larger than 10 nm. Furthermore, local orthorhombic octahedral tilting within a rhombohedral matrix due to an easy $a^-a^-a^-$ to $a^-a^-c^+$ tilt transition is considered as nucleation site for PNRs [176]. An intermediate orthorhombic phase was further suggested to bridge the rhombohedral to tetragonal phase transition between 230 and 300 °C [177, 178]. The occupancy of the *A* site by different cations causes varying *A*-O bonding environments and local structural deviations [179]. Structural distortion of the octahedra is further enhanced by the hybridization of the Bi^{3+} lone pairs with the oxygen's *p*-orbitals [54]. Lines of diffuse intensity in selected area electron diffraction (SAED) patterns were attributed to a locally correlated cation displacement along $\langle 111 \rangle_{pc}$ and $\langle 100 \rangle_{pc}$ chains [175]. No direct evidence of *A*-site cation ordering could be observed via scanning transmission electron microscopy (STEM), suggesting a random distribution of Bi^{3+} and Na^+ ions [175]. Nevertheless, the possibility of local short-range cation ordering can be considered [180, 181]. Gröting et al. [182] investigated the Bi/Na-order in NBT and found that short-range ordering is plausible. They argue that these locally order areas can induce PNR formation, giving rise to the relaxor behavior of NBT.

In contrast, the end member BT is a classical ferroelectric perovskite. The domain structure (Fig. 2.27) displays long-range ferroelectric 90° domains with a herringbone-type domain configuration [67], sometimes also termed zig-zag domains [72]. The temperature-dependent phase transitions

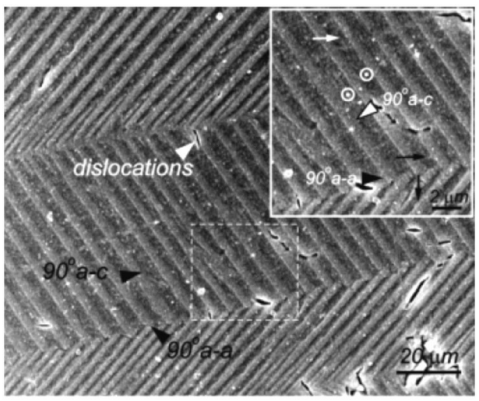

Figure 2.27: Scanning electron microscopy (SEM) micrograph of ferroelectric lamellar 90° a-a and a-c domains in a chemically etched BT ceramic displaying a herringbone-type domain configuration (reprinted from Ref. 72 with permission of John Wiley and Sons).

in BT were already addressed in section 2.1.2. At room temperature, BT is of tetragonal *P*4*mm* symmetry, where the Ti^{4+} cations are displaced along $[001]_{pc}$. Reported lattice constants are $a = 3.9998$ Å and $c = 4.0180$ Å [183].

2.5.4 Structure of Unpoled NBT-BT

As already illustrated, there is a lot of discussion about the structure of NBT-BT at room temperature, the phase transitions and the compositional range of the MPB. Varying results may arise from differences in the synthesis and especially in the conducted structural characterization methods [142]. NBT-BT has a near cubic structure and distortions from the cubic unit cell are small and sometimes hard to detect or leave room for interpretation. The observed average structure therefore can vary from the actual local structure.

The long-range order at the MPB is often described as pseudocubic, based on X-ray diffraction analysis. A transition from a rhombohedral to a pseudocubic phase at $x = 0.055$ is reported [184]. For $x > 0.06$, an average tetragonal symmetry develops [152, 154]. High-resolution neutron diffraction showed the presence of two types of superlattice reflections, $\frac{1}{2}\{ooo\}$ ($a^-a^-a^-$ tilt system) and $\frac{1}{2}\{ooe\}$ ($a^0a^0c^+$ tilt system), confirming the coexistence of pseudocubic phases with tetragonal and rhombohedral distortions at the MPB [185]. While Jo et al. [164] assigned the range of $0.06 < x < 0.10$ to space group *R*3*m*, another X-ray study suggests a transition from *R*3*c* to *P*4*mm* with coexisting phases for $0.06 < x < 0.07$ [186]. Here, it has to be noted that weak SRs may not be observable with X-ray techniques, influencing the phase assignment.

The existence of a monoclinic (M) phase alongside the R and T phases at the MPB (analogous to the PZT system) is debated. A monoclinic phase would allow a continuous and easy change of polarization between $\langle 001\rangle_{pc}$ and $\langle 111\rangle_{pc}$ directions and could explain high electromechanical coupling at the MPB [187]. While one synchrotron X-ray study on NBT-BT single crystals reports a *Cc* + *P*4*bm* MPB [188], no direct evidence of a M phase was found by others [187]. They argue that, if monoclinic distortions exist, they must be related to only local short correlation lengths. A comprehensive study by Garg et al. [121] assigned the range of $0 < x < 0.05$ to a phase coexistence of *R*3*c* + *Cc*. However, they assumed that the *Cc* phase does not play a role in the piezoelectric response, since it disappears upon poling when the structure turns into a single *R*3*c* phase.

Streaking of SRs observed in diffuse scattering experiments on NBT-4BT confirmed the presence of planar tetragonal regions within the *R*3*c* symmetry [189]. The streaking is reduced in poled samples, indicating the removal of the tetragonal platelets and growth of the rhombohedral domains [189]. In NBT-3.6BT, the thickness of tetragonal platelets, separated from the rhombohedral phase by an intermediate cubic phase, increases with temperature and thus shows a clear correlation with the change in permittivity [190]. L-shaped streaking in neutron diffuse scattering along two $\langle 001\rangle_{pc}$ directions is assigned to an enhanced Bi^{3+} displacement along $\langle 001\rangle_{pc}$, forming PNRs [191]. Increasing the BT amount changes the shape of streaking to a $\langle 011\rangle_{pc}$ orientation, which is related to a change in cation displacement and corroborates a higher PNR mobility and enhanced relaxor properties at the MPB [191, 192]. It should be noted that all diffuse scattering experiments have been conducted on single crystals.

While some earlier works consider chemical *A*-site ordering in MPB compositions [193, 194], a more profound investigation by Kling et al. [195] simulated NBT-6BT structures with different *A*-site occupation and compared them to experimental high-resolution TEM images. No evidence for chemical ordering could be found. Broad Raman bands also suggest the existence of disorder

on the *A* site [196]. The random distribution of Na^+, Bi^{3+} and Ba^{2+} facilitates the appearance of relaxor characteristics and the diffuse phase transition at T_m [154]. Local displacive order of *A*- and *B*-site cations in an disordered matrix is discussed by Guo et al. [141]. Diffuse streaking in SAED patterns of MPB compositions are assigned to 1-D correlated off-center displacements of the *A* and *B* ions along $\langle 001 \rangle_{pc}$ chains. In NBT-10BT, lines of diffuse intensity indicate off-center displacement along $\langle 111 \rangle_{pc}$ direction. The 1-D chains are not correlated with each other and Ba^{2+} disrupts a long-range order, giving rise to only nanoscale ordered regions (PNRs).

A systematic TEM study of the domain morphology in unpoled NBT-BT ceramics was conducted by Ma et al. [158]. NBT-4BT shows a complex structure with domains of 100 nm in length (Fig. 2.28(a)). They exhibit the *R*3*c* symmetry with $a^-a^-a^-$ octahedral tilting, which is evident from the presence of $\frac{1}{2}$ $\{ooo\}$ SRs. With increasing BT fraction, a transition towards a nanodomain structure was observed. The NBT-6BT composition exhibits a two-phase mixture which is represented by a complex domain structure in the center of the grains, surrounded by a faint nanodomain contrast [158] (Fig. 2.28(b)). The core still exhibits *R*3*c* symmetry, while the nanodomains show $\frac{1}{2}$ $\{ooe\}$ SRs and are thus of *P*4*bm* symmetry with $a^0a^0c^+$ octahedral tilting. Other TEM studies on NBT-6BT display a similar diffuse and 'grainy' or even homogeneous contrast, indicating the nanoscale structure at the MPB [157, 197, 198]. From the elongation of $\frac{1}{2}$ $\{ooe\}$ SRs, it can be inferred that the *P*4*bm* nanoregions are platelets with a thickness of only few nanometers [157]. A similar coexistence of phases is also known from TEM studies on NBT-BT-KNN, where small *P*4*bm* platelets and *R*3*c* domains can be found in the same grain [199]. The *P*4*bm* phase with its nanometer-sized polar regions is often denoted as the relaxor phase, being responsible for the strong frequency dispersion of ε_r [148, 158]. In the NBT-9BT composition, Ma et al. [158] solely observed the *P*4*bm* phase (Fig. 2.28(c)). In NBT-11BT, lamellar ferroelectric domains of tetragonal *P*4*mm* symmetry lying on $\{101\}_{pc}$ planes occur (Fig. 2.28(d)), while small remaining areas of *P*4*bm* symmetry are still present.

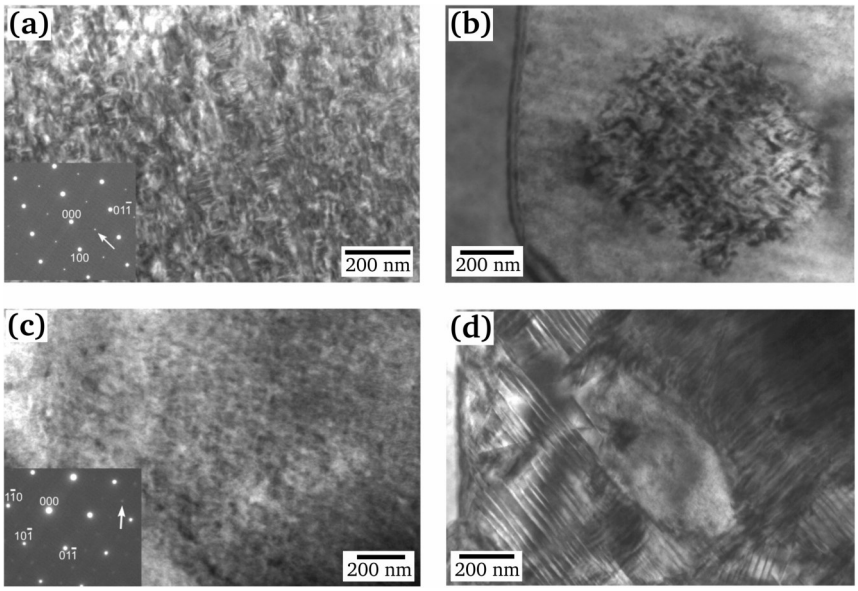

Figure 2.28: TEM-BF images of the domain structures in NBT-BT. (a) NBT-4BT with a complex domain configuration and SAED pattern with $\frac{1}{2}$ $\{ooo\}$ SRs (*R*3*c*). (b) NBT-6BT with *R*3*c* domains surrounded by *P*4*bm* nanodomains, (c) NBT-9BT with nanodomains and SAED pattern with $\frac{1}{2}$ $\{ooe\}$ SRs (*P*4*bm*). (d) NBT-11BT with lamellar ferroelectric *P*4*mm* domains and a remaining central area of *P*4*bm* symmetry (reprinted from Ref. 158 with permission of AIP publishing).

In NBT-6BT ceramics prepared from hydrothermally synthesized nanoparticles, tetragonal PNRs in the size of 3-5 nm embedded within a rhombohedral matrix are reported [200]. In TEM-related studies on NBT-BT single crystals, nanodomains with tetragonal symmetry were observed as well [201], indicating an increased volume fraction close to the MPB by intensified $\frac{1}{2}$ $\{ooe\}$ SRs [202].

In-situ heating TEM experiments on NBT-6BT show that the complex *R*3*c* domains disappear with increasing temperature and that the *P*4*bm* fraction increases until it occupies the entire grain at 170 °C [160]. In NBT-11BT, the ferroelectric *P*4*mm* domains start to disappear at 170 °C. The dissolution of the domain structure and transition to the *P*4*bm* phase is believed to correspond with T_d. Gradual weakening of the $\frac{1}{2}$ $\{ooe\}$ SRs starts at 335 °C, indicating the beginning transition from the tetragonal to the paraelectric cubic phase. The temperatures where the dielectric frequency dispersion vanishes (∼240 °C) and the permittivity peaks (T_m, ∼280 °C) do not seem to correspond to any structural phase transitions, since no structural changes were observed in the TEM study in this temperature range [160].

In summary, reports about the coexistence of *R*3*c* ($a^-a^-a^-$ tilting) and *P*4*bm* ($a^0a^0c^+$ tilting) phases in MPB compositions are numerous. It is comprehensively argued that the nanodomains/PNRs enable low energy barriers for dipole switching and hence contribute to enhanced piezoelectric properties and relaxor behavior at the MPB.

2.5.5 Structure of Poled NBT-BT

Relaxor NBT-BT compositions can be transformed into a ferroelectric by the application of an external electric field. A systematic comparison of poled and unpoled NBT-BT ceramics with 0-20 mol % BT revealed significant differences in unit cell parameters [203]. Upon poling, the lattice distortion for both the T and R phase is increased. In NBT-7B, the field-induced transition from a pseudocubic to a tetragonal phase increases the tetragonal volume fraction [203, 204]. The field-induced strain is correlated to a textured ferroelectric domain structure, where the *c* axis of the tetragonal phase is predominately aligned with the electric field [204]. A transformation from the pseudocubic to a predominantly rhombohedral structure was reported for NBT-6BT [185]. Both $a^0a^0c^+$ and $a^-a^-a^-$ tilt systems are present in the unpoled state and transform to solely $a^-a^-a^-$ tilting upon poling, implying a *P*4*bm*-to-*R*3*c* transformation. Diffuse scattering from structural short-range ordering disappears upon poling, indicating a field-induced transformation to a long-range ferroelectric order [205]. The transition is irreversible, having a remanent ferroelectric state upon field removal [185, 189, 206]. Interestingly, the phase stability at the MPB upon poling seems to be also dependent on the direction of the applied electric field [207]. In NBT-5.6BT single crystals, a transition from pseudocubic to tetragonal was observed when the electric field was parallel to $[001]_{pc}$, whereas a rhombohedral phase was established in the very same composition, when the electric field was parallel to $[111]_{pc}$. The development of the cubic phase fraction upon poling and annealing was examined via ^{23}Na NMR analysis [130]. The fraction of the cubic phase is diminished in poled samples, suggesting that PNRs grow and percolate throughout the structure. The cubic phase fraction rises again when samples are annealed and the ferroelectric state is transformed back to the relaxor state.

Ma et al. [149] investigated the field-induced transitions by in-situ *E*-field-dependent TEM analyses and observed the formation and degradation of MPBs during the poling process. They summarized the results in a *E*-field-composition phase diagram (Fig. 2.29). For $x = 0.55$, the *P*4*bm* + *R*3*c* mixture transforms to pure *R*3*c*. For $x = 0.06$, the phase transitions with increasing field strength can be described as: *R*3*c* + *P*4*bm* → *R*3*c* + *P*4*mm* → *R*3*c*. For $x = 0.07$, *P*4*bm* nanodomains firstly transform

to *P*4*mm* lamellar domains, then also enter the MPB phase field with *P*4*mm* + *R*3*c*. Hence, poling not only causes a relaxor-to-ferroelectric transition, but also a ferroelectric-to-ferroelectric phase transition. The piezoelectric coefficient (d_{33}) increases, once the relaxor *P*4*bm* phase is transformed into a ferroelectric domain structure. In-situ *E*-field TEM analysis on the related NBT-BT-KNN system also showed that grains with tetragonal nanoregions can be transformed into long-range ferroelectric domains of rhombohedral symmetry [208]. TEM imaging of the fatigue remanent state after electric cycling shows a strong rhombohedral and weak tetragonal distortion in cycled NBT-6BT, while it is vice versa in NBT-7BT [198].

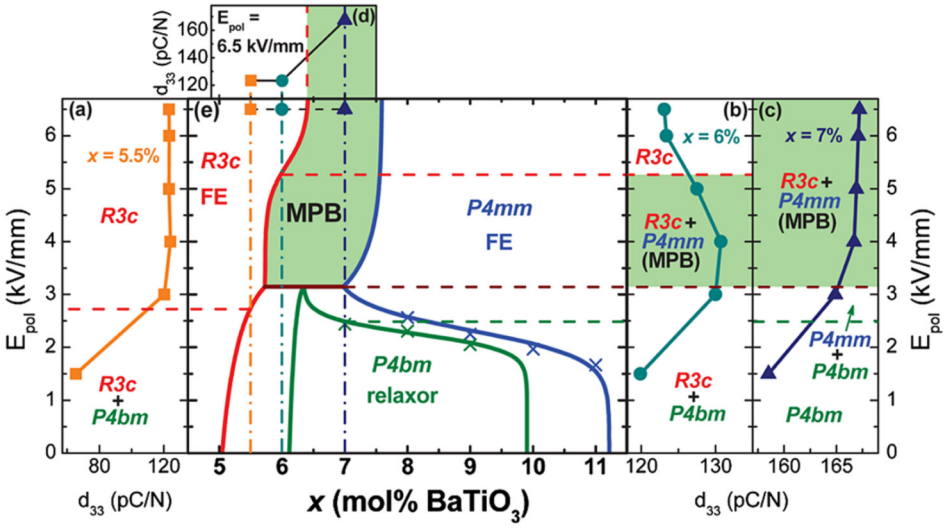

Figure 2.29: *E*-field-composition phase diagram and d_{33} of NBT-BT. (a)-(c) display the d_{33} values for NBT-5.5BT, NBT-6BT and NBT-7BT, respectively. (e) illustrates the E_{pol} vs. phase diagram. The *R*3*c* + *P*4*mm* MBP region is colored in green (reprinted from Ref. 149 with permission of the American Physical Society).

2.5.6 Quenching of NBT-BT-Based Ceramics

Improving the performance of NBT-based ceramics has been a central research goal in more recent years. So far, the low T_d of ~100 °C at the MPB [15, 145] was seen as a major drawback. This issue has been approached by different methods. The formation of composites, where an additional phase is introduced, such as ZnO [209–211] or Al_2O_3 [212], defers the thermal depolarization. The incorporation of ZnO effects mechanical hardening and leads to a stabilization of the induced ferroelectric state [213, 214]. With 20 mol % ZnO in NBT-6BT, T_d could be increased up to 150 °C [209]. The formation of new solid solutions, such as NBT-BFO [215], as well as the introduction of oxygen vacancies through chemical substitution with $BaAlO_{2.5}$ [216] proves as alternative ways in overcoming existing temperature limits.

The procedure of quenching constitutes another effective tool for deferring T_d to higher temperatures while retaining the desired piezoelectric properties. Quenching of NBT-6BT was firstly reported under the aspect of aging, where samples were furnace cooled to 400-600 °C and then quenched in water, suppressing the integrated aging process (permittivity degradation) of furnace cooled samples [217]. First quenching experiments demonstrating an increased T_d were conducted on NBT, Li-doped NBT and Li-doped NBT-BT (BNLBT) samples [13, 14]. Quenched samples were removed from the furnace at 600-1100 °C and cooled in air with a fan. A maximum increase in T_d of 60-80 °C was achieved for quenching from 1100 °C [14]. Quenching from below 800 °C resulted in

negligible changes [13] (Fig. 2.30(a)). The quenching process stabilizes the rhombohedral phase in pure NBT [218] and on the NBT-rich side of the MPB, where the rhombohedrality (given as $90° - \alpha$) increases. The tetragonality (c/a ratio) increases for compositions on the BT-rich side of the MPB [14] (Fig. 2.30(b)). The increased lattice distortion is related to the enhanced off-centering of the Bi^{3+} cation in the cubic phase at high temperatures [14]. Nagata et al. [219] could demonstrate that Bi^{3+} ions are frozen in stronger off-centered positions with a more ordered structure upon quenching compared to furnace cooled specimens.

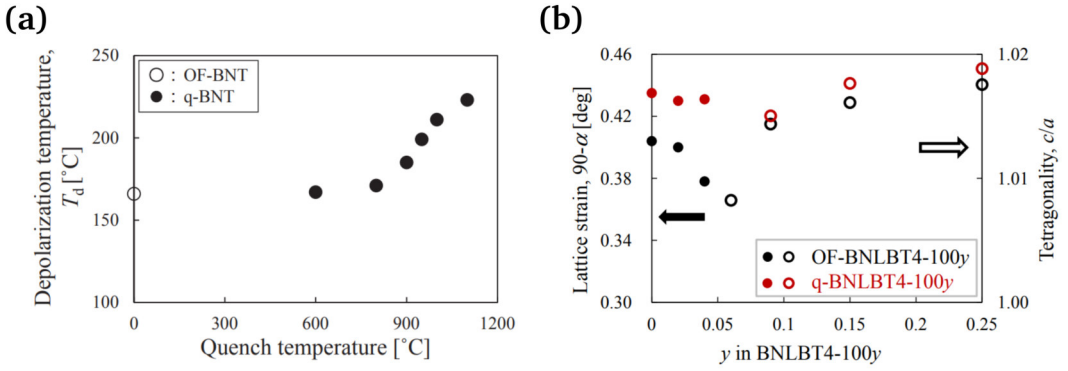

Figure 2.30: Quenching-induced property changes in NBT-based ceramics. (a) In NBT, T_d increases when quenched over 800 °C (reprinted from Ref. 13 with permission of IOP Publishing, Ltd). (b) Rhombohedral ($90° - \alpha$) and tetragonal (c/a) distortion in furnace cooled (OF) and quenched (q) Li-substituted NBT-BT (BNLBT4-100y) as a function of the BT content, y (reprinted from Ref. 14 with permission of IOP Publishing, Ltd).

Investigations on NBT-6BT and -9BT ceramics conducted by Lalitha K. V. et al. [15] confirmed the above findings of an increased lattice distortion upon quenching. Since enhanced lattice distortion is usually observed close to the field-induced relaxor-to-ferroelectric transition, one can conclude that quenching stabilizes the ferroelectric order [15]. Furthermore, the permittivity in quenched samples is lower compared to their furnace cooled counterpart, which is also the case for ferroelectrics compared to relaxors. T_d exhibits a value of 140 °C for quenched NBT-6BT (increase by 40 °C) and 200 °C for NBT-9BT (increase by 60 °C) as illustrated in Fig.2.31(a) [15].

$T_{F\text{-}R}$ of poled samples is likewise shifted to higher temperatures upon quenching (Fig. 2.31(b)). Noticeably, a spontaneous relaxor-to-ferroelectric transition can be observed in unpoled and quenched NBT-9BT (Fig. 2.31(b)). This implies that the stabilization of ferroelectric order upon quenching is strong enough to induce a spontaneous transformation. When quenched samples were annealed at 800 °C, $T_{F\text{-}R}$ shifts back to the value of the furnace cooled samples and NBT-9BT reverts back to the relaxor state [15, 220].

The quenching procedure itself has been proven to be feasible without causing mechanical deterioration of the ceramics [221]. However, this only applies for quenching in air with moderate quenching rates and not for quenching in water or oil. Air-quenching NBT with a quenching rate of 3.85 °C/s in the 1100-800 °C temperature range results in a similar bending strength as obtained for furnace cooled NBT, while the bending strength is decreased for faster quenching rates [222].

Quenching has been adopted as a tool to related Bi-based systems and opens new pathways for the modification and improvement of ferroelectric perovskites [223]. Quenched BFO-BT ceramics with Mn exhibit improved piezoelectric properties, such as a decrease in the dielectric loss and an increase in the remanent polarization [224]. The ternary system of NBT, BT and $AgNbO_3$ (NBT-6BT-3AN) transforms from an ergodic to a non-ergodic relaxor upon quenching [225].

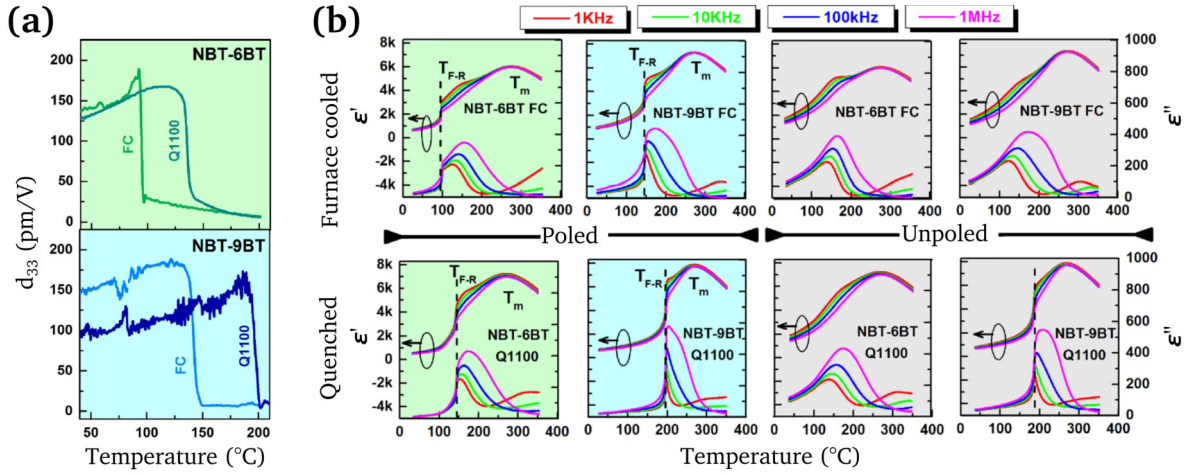

Figure 2.31: (a) Temperature-dependent d_{33} of furnace cooled (FC) and quenched (Q1100) NBT-6BT and NBT-9BT. (b) Temperature-dependent permittivity of poled and unpoled furnace cooled and quenched NBT-6BT and -9BT at different frequencies. $T_{F\text{-}R}$ marks the ferroelectric-to-relaxor transition temperature of poled specimens (reprinted from Ref. [15] with permission of AIP Publishing).

Besides the off-centering of Bi^{3+}, point defects like oxygen vacancies might play an important role in the stabilization of the ferroelectric order upon quenching [15, 226]. Quenched La-doped BT and SnO_2 ceramics show an increase in oxygen vacancies [227, 228], which generate easily at high temperatures. Quenching can freeze-in the high-temperature vacancy distribution and prohibit vacancy annealing and ordering [229]. Furthermore, quenched and poled NBT-BT-KBT samples show a more irregular domain morphology compared to the furnace cooled state [230]. Here, an increased defect concentration is believed to pin the domains, thereby impeding the domain mobility and domain switching during poling. While the conductivity increase in quenched NBT-BT suggests an increased oxygen vacancy concentration, annealing in oxygen atmosphere, however, leaves the conductivity unaltered [220]. Alternatively, residual stress from the quenching procedure may also be beneficial for stabilizing a ferroelectric phase and increasing T_d. Stress states, which cannot be released by microcracking may cause local stress fields, inducing a pseudocubic-to-rhombohedral phase transition in NBT-6BT [231].

3 Materials & Methods

3.1 Specimen Preparation

3.1.1 Ceramic Pellet Sintering

NBT-BT ceramics with varying stoichiometric amounts of BT were prepared via solid state synthesis route in the research group Nonmetallic-Inorganic Materials by Andreas Wohninsland. The four compositions with 3, 6, 9 and 12 mol % BT are denoted as NBT-3BT, NBT-6BT, NBT-9BT and NBT-12BT, respectively. As initial raw powders (all by Alfa Aesar, Kandel, Germany), Na_2CO_3 (99.5 %), $BaCO_3$ (99.8 %), Bi_2O_3 (99.975 %) and TiO_2 (99.6 %) were used. Their respective purities are given in parenthesis. The raw powders were dried at 100 °C in a drying cabinet for 24 h in order to evaporate residual water. Afterwards, they were weighed in stoichiometric amounts. The powder blends were immersed in ethanol and milled in a planetary mill (250 rpm) for 24 h. The powders were then dried and ground in an agate mortar. Successively, calcination was conducted at 900 °C for 3 h, which was followed by a second milling step. Subsequently, the powders were sieved with a 160 µm sieve and compacted to pellets. Sintering was conducted with a heating rate of 5 K/min at 1150 °C and a dwell time of 3 h. The green bodies were placed in sacrificial powder during sintering in order to avoid the loss of volatile elements, such as Na and Bi. The reference samples were cooled down in the furnace and are denoted with 'FC' for 'furnace cooled'. The quenched samples, denoted with 'Q', were quickly removed from the furnace after the sintering dwell time at 1150 °C and cooled in air with an conventional air fan.

3.1.2 TEM Specimen Preparation

TEM analysis generally requires the preparation of an electron transparent specimen, where sample thicknesses are usually in the range of 20 to 100 nm. For the NBT-BT ceramics, several TEM preparation routes were adopted (Fig. 3.1), governed by the sample requirement and the conducted TEM technique.

For investigations on unpoled ceramics, plane-parallel TEM specimens were prepared. Discs with a diameter of 3 mm were cut from the ceramic pellets with an ultrasonic disc cutter Model 601 (Gatan, Pleasanton, USA) in order to comply to the standardized TEM specimen geometry. Each disc was ground and polished on both sides with a MultiPrep™ sample preparation grinding and polishing machine (Allied High Tech Products Inc., Rancho Dominguez, USA). For this procedure, the ceramic disc was mounted onto a sample holder with a mounting adhesive (Crystalbond™ 509-3, Aremco Products Inc., New York, USA) by heating both on a heating plate to ∼160 °C, at which the mounting adhesive becomes liquid. Diamond lapping films (Allied High Tech Products Inc., Rancho Dominguez, USA) with grain sizes of 15, 9, 6, 3 and 1 µm were used successively for polishing each sample side. The rotation of the MultiPrep™ plate was reduced with smaller

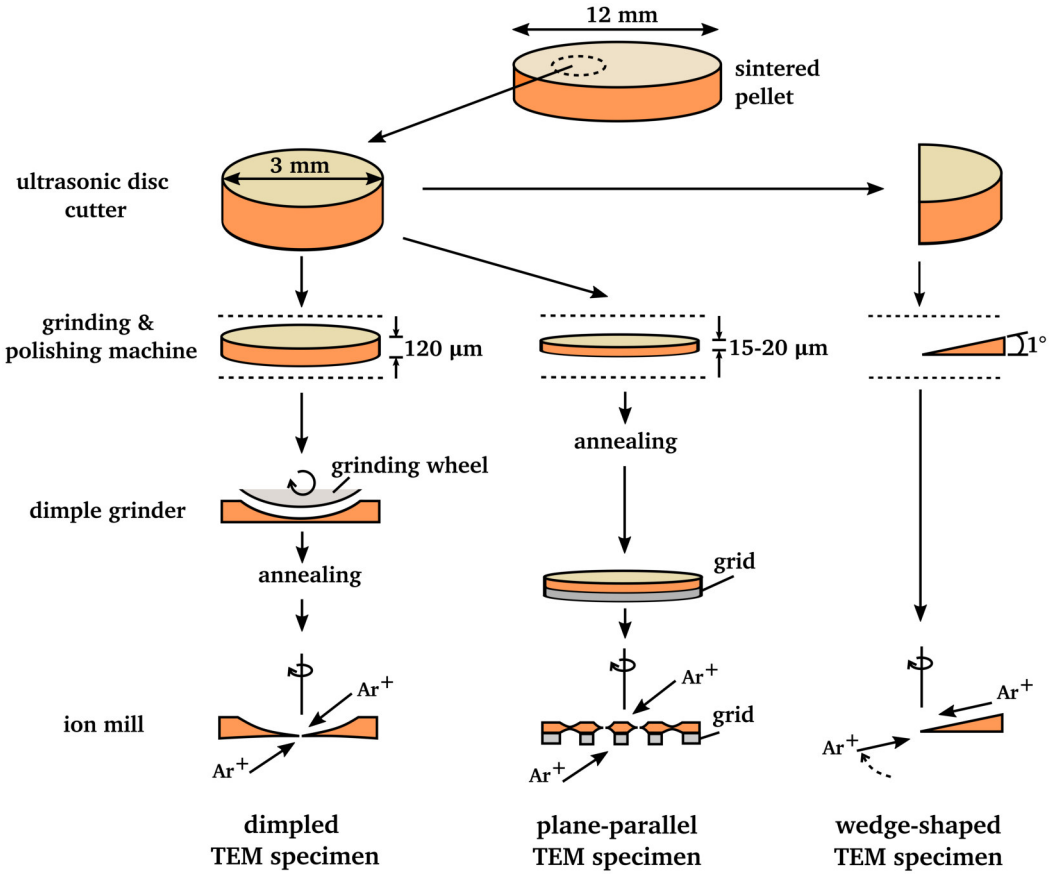

Figure 3.1: Schematic illustrating the preparation steps for obtaining a dimpled, a plane-parallel and a wedge-shaped TEM specimen.

polishing grain size from 60 rpm to 35 rmp. During the final 1 µm polishing step, a mixture of 50 % hexylene glycol and 50 % water was used as lubricant. The thickness of the sample foils after polishing was in the range of 15-20 µm. Samples were then annealed in a furnace at 400 °C with a heating rate of 1 °C/min and a holding time of 30 min, in order to compensate and relieve mechanically induced stress from grinding and polishing. After cooling in the furnace, the sample foils were then glued onto a molybdenum TEM grid for support with a two-component adhesive. Successively, the TEM specimens were Ar^+-ion thinned from both sides in a DuoMill 600 (Gatan, Pleasanton, USA). An angle of 14° between the rotating sample and the Ar^+-ion beam and a current voltage of 4 kV was applied. Ion thinning was carried out for several hours until perforations appeared in the specimen (compare Fig. 3.2(a)). At the edges of the perforations, the specimen is thin enough to be examined in the TEM. A last cleaning step with a low angle of 12° and a voltage of 2.5 kV was conducted in the Ar^+-ion mill for approx. 10 min, in order to reduce the amorphous surface layer on the specimen, which develops during thinning by the invasive influence of the Ar^+-ion beam. Before investigating the specimens in the TEM, they were sputtered with a thin carbon layer using a MED 010 deposition system (Balzers Union, Balzers, Liechtenstein) in order to avoid charging in the microscope by the incident electron beam.

For TEM investigations on poled compositions, the ceramic pellets were electroded with silver paste and poled at room temperature in silicone oil with an electric field amplitude of 6 kV/mm for 20 min (conducted by A. Wohninsland). In order to verify a successful poling process, the d_{33} value was recorded. Subsequently, wedge-shaped TEM foils were prepared (Fig. 3.2(b)). Since

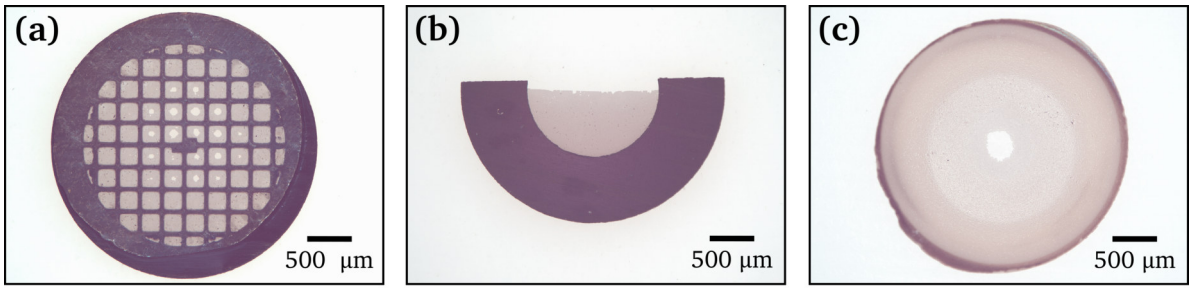

Figure 3.2: Different types of TEM specimens prepared from the NBT-BT ceramics. (a) Plane-parallel specimen glued to a carrier TEM grid, (b) wedge-shaped specimen on half of a pinhole aperture, (c) self-supporting dimpled specimen.

poled NBT-6BT is known to depolarize at ∼100 °C, thermal treatment of the poled specimens had to be avoided during sample preparation. Therefore, a different sample preparation technique was adopted. The 3 mm ceramic discs were halved using a diamond cutting saw and one semicircular piece was mounted to the sampler holder of the MultiPrep^{TM} at room temperature with the help of a low viscous superglue (Sico Met 40, Henkel, Düsseldorf, Germany). One side of the semicircular sample was polished plane-parallel. For polishing the other side, the sample holder was tilted by 1° with respect to the polishing plate, in order to obtain a wedge-shaped geometry. For a smooth sample surface, diamond lapping films of 0.5 and 0.1 µm grain size were used as last polishing steps on both sides. The wedge tip of the sample ought to be as thin as possible, which in turn rendered it very fragile, so cautious polishing with minimal load on the sample was required. When the wedge tip was thin enough, colored interference lines running parallel to the edge became visible under the light microscope (Fig. 3.3).

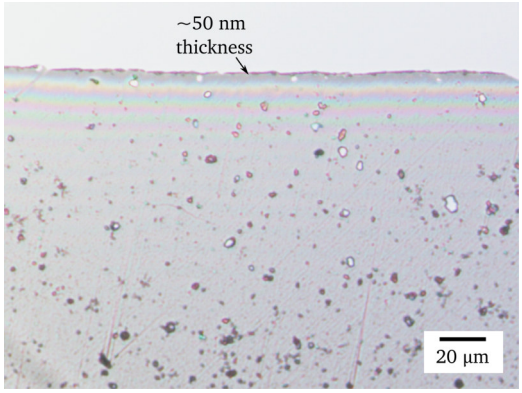

Figure 3.3: Micrograph of a wedge-shaped TEM foil of poled NBT-6BT. Colored interference lines running parallel to the tip of the wedge indicate electron transparency (dark spots are pores within the ceramic specimen).

The specimen was then glued onto a semicircular pinhole aperture serving as sample support analogous to a TEM grid. Consequently, the annealing step at 400 °C was omitted for all poled samples. Since the tip of the wedge-shaped samples was already close to the desired sample thickness, only a short thinning time in the Ar^+-ion mill was required. The thinning process was conducted under liquid nitrogen cooling, in order to avoid heating of the sample under the influence of the ion beam. After allowing enough time for the entire sample stage of the DuoMill 600 to cool down (∼45 min), the wedge-shaped samples were thinned in three intervals of 10 min with a 10 min break in between to minimize heating of the specimen. A low thinning angle of 12° and a reduced voltage of 3 kV was used. When the interference lines on the sample tip ranged towards an alternating black and white color, the sample was suited for TEM microscopy.

Poled specimens of NBT-6BT FC and Q, which were used for in-situ heating experiments were prepared in the above described wedge-shaped geometry. However, no sample-supporting pinhole aperture was used in order to avoid applying the two-component adhesive, which might decompose under high temperature and vacuum in the TEM. Instead, the free-standing wedge-shaped specimens were directly placed into the TEM heating holder.

For the in-situ heating experiments on unpoled NBT-6BT, specimens were prepared via the conventional dimpling method (compare Fig. 3.1). A dimpled sample is self-supporting and thus, gluing of the sample onto a grid can be avoided. Firstly, a 3 mm disc was ground to a thickness of 120 µm. One side was polished with diamond lapping films down to a 1 µm polish. An indentation was then ground into the other side of the sample with a dimple grinder Model 656 (Gatan, Pleasanton, USA). During dimpling, abrasive diamond paste of 9, 6, 3 and 1 µm was successively applied onto the dimpling wheel until a final thickness of 20 µm in the center of the indentation was reached. The sample was then thinned in the Ar^+-ion mill under the same conditions used for plane-parallel specimens. The thinning process was carried out until a single perforation emerged in the center of the sample (Fig. 3.2(c)).

3.1.3 SEM and PFM Specimen Preparation

Sample preparation for SEM analyses on chemically etched surfaces of NBT-BT ceramics was conducted by Andreas Wohninsland. The pellets were polished with 15, 6, 3, 1 and 0.25 µm diamond paste. Poled specimens were electroded with silver paint and poled in a silicon oil bath at 6 kV/mm for 20 min at room temperature. The specimens were chemically etched by immersing them into a solution of 4 % HCl, 2 % HF and 94 % distilled water. The dwell time in the etching solution was between 30 s and 60 s.

For PFM analyses, 3 mm sample discs were polished with 15, 9, 6, 3 and 1 µm diamond lapping films and successively with 1 and 0.25 µm diamond paste. For improving the final surface finish, vibration polishing was conducted for 10 h in a suspension of distilled water and colloidal silica with a 50 nm particle size. The samples were then annealed at 400 °C for 30 min with a heating rate of 5 °C/min in order to relieve mechanically induces stresses. Poling was conducted as described above.

3.2 Conventional Transmission Electron Microscopy (TEM)

Conventional TEM investigations were carried out with a JEM-2100F microscope (JEOL, Tokyo, Japan), equipped with a field emission electron gun operating at 200 kV. A double-tilt beryllium sample holder (JEOL, Tokyo, Japan) allowed for a theoretical tilting of the specimen by +/- 25° in two direction, which is crucial for grain orientation along zone axes of interest. Images were recorded with a UltraScan® 1000 charge-coupled device (CCD) camera (Gatan, Pleasanton, USA). Image acquisition was carried out via the Gatan Microscopy Suit® software. SAED patterns were either indexed by hand or with PIEP [232], a program for interpreting electron diffraction patterns. The SAED patterns in this work were color inverted for a better visibility of weak reflections. The JEM-2100F microscope is further equipped with a TEM 250 SDD energy-dispersive X-ray spectroscopy (EDS) detector and the corresponding INCA Energy software (both Oxford Instruments, Abingdon, UK) for the acquisition of EDS data in TEM and STEM mode.

3.2.1 Theoretical Aspects of TEM

TEM combines a row of versatile characterization techniques for solid materials, especially for those of crystalline nature. Since this work is primarily based on investigations conducted via conventional TEM, the most important theoretical aspects and techniques are briefly outlined. A more detailed introduction to TEM is given in Ref. 233.

In the TEM, image contrast arises by the interaction of electrons with the specimen volume. The electron beam is generated in the gun, accelerated (100-300 kV) and passes the column of the TEM, which comprises various electromagnetic lens systems [234–236]. From top to bottom, the usual succession in a TEM column starts with the condenser lens system for adjusting the spot size and focusing or opening the beam. The sample is situated right inside the objective lens, which is split in an upper and lower polepiece. Below, the intermediate lens system is used to switch between imaging and diffraction mode by either selecting the image plane of the objective lens or its back focal plane, where the diffraction pattern is formed. The projector lens system allows the adjustment of the desired magnification of the image displayed on the fluorescent viewing screen. Figs. 3.4(a) and (b) schematically illustrate the ray path in a TEM in imaging and diffraction mode, respectively.

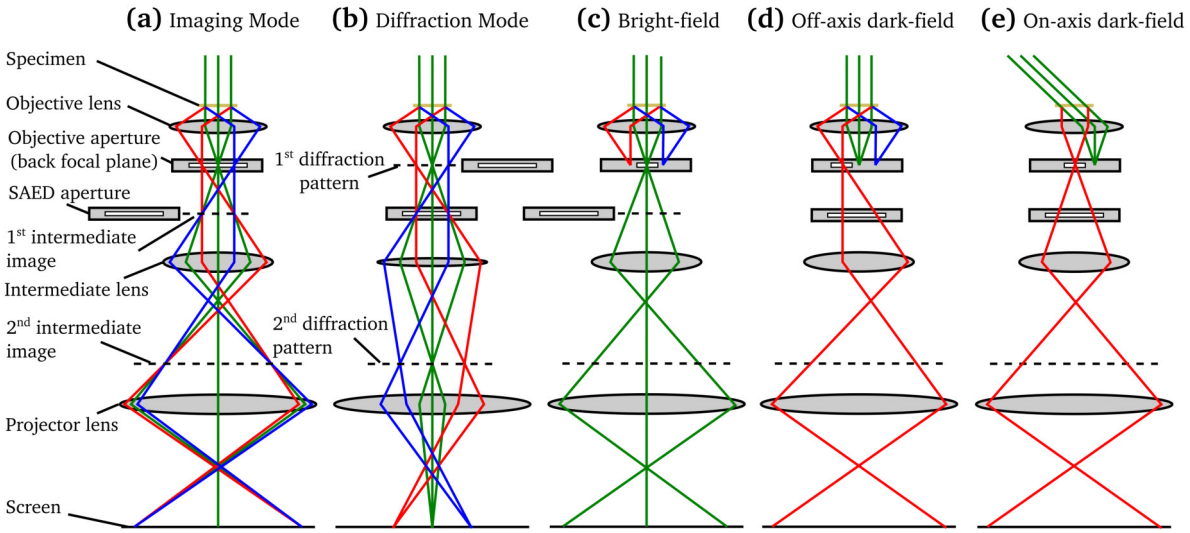

Figure 3.4: Schematic ray path within a TEM column for (a) imaging mode, (b) diffraction mode, (c) bright-field, (d) off-axis dark-field and (e) on-axis dark-field imaging.

In electron (and optical light) microscopy, the resolution limit is directly linked to the wavelength (λ) of the light source [234]. Using electrons as the radiation source ($\lambda = 0.0025$ nm for the JEM-2100F microscope) allows for the HR capacity of TEMs, since the wavelength of the source has to be smaller than the structural features, which need to be resolved. However, the theoretical resolution is limited by lens aberrations, caused by non-perfect conditions of the electromagnetic lenses [237]. The most relevant aberrations are the spherical aberration and the chromatic aberration [238]. The spherical abberation is based on the stronger deflection of rays passing the outer rim of the lenses. A point source is thus imaged as a disc with the diameter $d_s = \frac{1}{2} C_s \tau^3$ (with the spherical aberration coefficient, C_s, and the collection semi-angle of the lens, τ) [239]. The chromatic aberration is caused by a certain energy spread, ΔE, in the emitted electron beam and can similary be expressed by a disc diameter $d_c = C_c \tau \frac{\Delta E}{E_0}$, with the chromatic aberration coefficient, C_c, and the energy of

the incident beam, E_0 [239]. Modern TEMs and high voltage instruments can achieve a resolution limit of 1 Å. When the machine is C_s- and C_c-corrected, a resolution down to 0.5 Å can be reached.

When the electron beam interacts with the specimen, elastic scattering is the main process generating the image contrast [240, 241]. The beam-specimen interaction also causes other signals, such as Auger electrons, secondary and backscattered electrons or X-rays, which can be used for e.g. chemical analyses via EDS. Inelastically scattered electrons can be exploited by electron energy-loss spectroscopy (EELS, see section 3.5).

When the electron wave is scattered elastically within the specimen volume, it can change both its amplitude and phase. Both mechanisms result in image contrast. Amplitude contrast is crucial for lower and intermediate magnifications and phase contrast becomes important for high-resolution TEM (HRTEM) imaging [234, 240]. Amplitude contrast can be divided into mass-thickness contrast (by incoherent elastic scattering) and diffraction contrast (by coherent elastic scattering under Bragg condition). The first is dependent on the atomic number, Z, and the thickness of the specimen. Areas with heavier atoms cause stronger scattering and will appear darker in BF images. In BF mode, the primary beam on the optical axis is selected via the objective aperture and strongly scattered beams are blocked and do not contribute to the image forming process (Fig. 3.4(c)). Diffraction contrast is crucial for crystalline specimens. Diffraction on lattice planes in the crystalline material occurs according to Bragg's law ($n\lambda = 2dsin\theta$ with d as the lattice spacing, θ as the diffraction angle, n as the diffraction order and λ as the electron wavelength). Diffraction contrast thus highly depends on the crystal orientation towards the incident beam, defining the lattice planes which are in Bragg condition. By choosing a small objective aperture, more diffracted beams are excluded from the image forming process, which leads to an overall increase in the BF image contrast. Opposed to BF imaging, DF imaging excludes the direct beam. Here, usually one diffracted beam is chosen with a small objective aperture in the SAED pattern and hence only areas in the specimen which contribute to this specific beam under Bragg condition appear bright, while the rest of the sample remains dark. It can further be distinguished between off-axis dark-field (Fig. 3.4(d)), wherein the direct beam is kept on the optical axis and on-axis dark-field (Fig. 3.4(e)), wherein the chosen diffracted beam is tilted to the optical axis by deflection coils in the TEM column, thus reducing the impact of the spherical aberration.

The switching between imaging and diffraction mode allows the simultaneous recording of BF/DF images and diffraction patterns of specific sample regions. A SAED pattern (Fig. 3.5(a)) is formed by defining the region of interest with a SAED aperture, usually a single crystalline grain. The corresponding diffraction pattern can be observed and analyzed in reciprocal space, where discrete diffraction spots correspond to specific lattice spacings, d_{hkl}, of the analyzed crystallite. The lattice spacing is equal to the inverse length of the reciprocal lattice vector, g_{hkl} ($d_{hkl} = 1/|g_{hkl}|$) [234]. In order to record an SAED pattern, the grain has to be oriented along a crystallographic zone axis. This can be achieved by deploying Kikuchi lines. These lines are formed due to inelastically scattered electrons, which are then diffracted by a set of lattice planes in Bragg condition [240]. Two diffraction cones (Kossel cones) arise corresponding to hkl and $\overline{hkl}$, forming a Kikuchi band. A crystal is oriented along a specific zone axis, when the Kikuchi bands all cross at the center of the optical axis (Fig. 3.5(b)). In order to carry out this procedure, the sample has to be tilted while being illuminated with a convergent electron beam in diffraction mode.

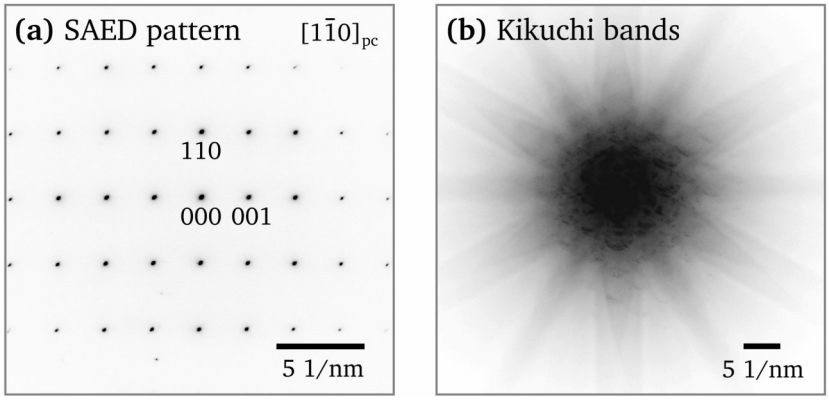

Figure 3.5: (a) SAED pattern of a NBT-BT grain displaying discrete diffraction spots. (b) According Kikuchi bands under convergent illumination settings in diffraction mode. The bands cross at the center, indicating precise orientation along the $[1\bar{1}0]_{pc}$ zone axis.

In order to demonstrate the relationship between the reciprocal lattice and the wave vectors of the incident and diffracted beam (Fig. 3.6), the Ewald sphere construction is used [235]. The incident wave is represented by a wave vector (k_i), which length is equal to the reciprocal electron wavelength and thus defines the radius of the Ewald sphere ($|k_i| = 1/\lambda$). If a reciprocal lattice point is cut by the Ewald sphere, the Laue criterion and Bragg's law is fulfilled. The diffracted wave vector (k_d) points towards that lattice point. Since the radius of the Ewald sphere is very large (generating an approximated flat surface), several lattice points in the Zero Order Laue Zone are intersected, yielding the material and symmetry specific diffraction pattern. Is has to be noted that also diffraction spots are imaged, which deviated from the exact Bragg condition to a small degree and slightly lie inside or outside of the Ewald sphere. Here, the excitation error (s) serves as a measure for the deviation from the exact Bragg condition. The scattering vector (K) is then the sum of the reciprocal lattice vector (g) and s. The excitation error can be positive or negative, depending on the location of the diffraction spot (G) with respect to the Ewald sphere.

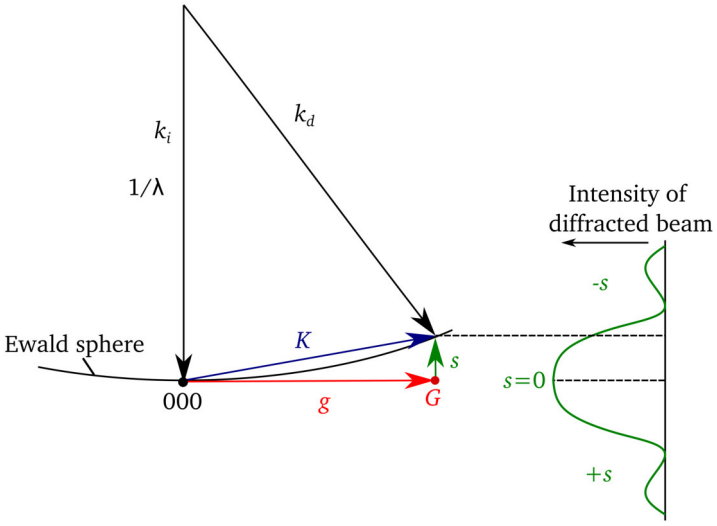

Figure 3.6: Ewald sphere construction showing the incident wave vector (k_i), the diffracted wave vector (k_d), the reciprocal lattice vector (g) and the scattering vector (K). The intensity of the diffracted beam depends on the excitation error, s (redrawn after Ref. 233).

For magnifications higher than 150 000 x, phase contrast becomes the dominating image forming process in the TEM [234, 242]. Contrast arises from the phase shift introduced by the scattering of the wave on the atomic column with respect to the incident wave. Both waves interfere and intensity variations arise which can be interpreted as lattice spacing contrast. However, an additional phase shift can also be introduced by the spherical aberration and the defocus of the objective lens, which contributes to the final image. For optimal resolution, defocusing of the objective lens can slightly compensate for the spherical aberration (Scherzer defocus [237]). The contrast of the HRTEM image also depends on the sample thickness and atom type. In consequence, the actual location of the atom columns cannot be directly derived from the contrast in the HRTEM image. Image simulations are required to interpret experimentally recorded HRTEM images.

3.2.2 Ferroelectric Domain Imaging in TEM

Imaging of domains in TEM is a widely deployed method for analyzing the micro- and nanostructure and domain patterns of crystalline ferroelectric materials. Imaging of non-180° domain walls in the TEM is based on diffraction contrast. If, for example, 90° domain walls in the tetragonal ferroelectric phase are viewed 'edge-on' (aligned parallel to the incident electron beam), no strong domain wall contrast is visible. When the domain wall is inclined with respect to the electron beam, stronger diffraction contrast can be observed. As the wave of the electron beam propagates along the domain wall, a phase shift is induced which reflects in the appearance of fringes [244]. These alternating bright and dark lines propagate parallel to the intersection of the domain wall and sample surface (Fig. 3.7(a)). Their appearance is analogous to thickness fringes, which can typically be observed in TEM, when a sample thins out at the edge and its thickness (z) changes. It is apparent from Fig. 3.7(a) that both domains on each side of the 90° domain wall exhibit a wedge shape when the domain wall is inclined towards the viewing direction. The alternating bright and dark contrast lines can be explained with the help of the Howie-Whelan equations, which describe the coupling and oscillating intensity of the direct and diffracted beam as function of the specimen thickness, z, in beam direction [234]:

$$\frac{d\phi_g}{dz} = \frac{\pi i}{\xi_g}\phi_0 e^{-2\pi i s z} + \frac{\pi i}{\xi_0}\phi_g \quad \text{and} \quad \frac{d\phi_0}{dz} = \frac{\pi i}{\xi_0}\phi_0 + \frac{\pi i}{\xi_g}\phi_g e^{2\pi i s z} \tag{3.11}$$

with the amplitude of the direct (ϕ_0) and diffracted (ϕ_g) beam, the excitation error (s) and the

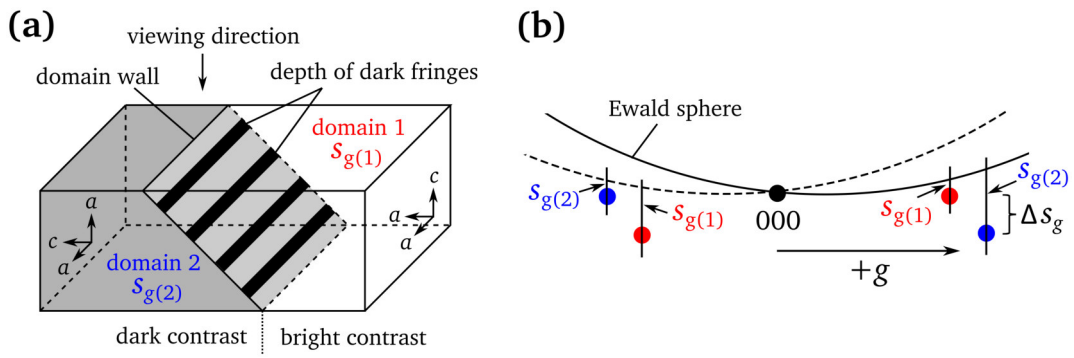

Figure 3.7: (a) Schematic of inclined 90° domain wall exhibiting alternating bright and dark fringes. The different orientations in both domains results in a contrast difference. (b) The Ewald sphere construction illustrates the difference in the excitation error, Δs_g, between domain 1 and domain 2 (redrawn after Ref. 243).

extinction distance for the direct (ξ_0) and diffracted (ξ_g) beam, which constitutes the distance that is needed to transfer the intensity of the direct beam to the diffracted beam. ξ_g depends on the atomic number, the scattering angle, the lattice parameters and the electron wavelength [234].

The difference in the unit cell orientation of two neighboring 90° domains, given by the 90° rotation of the polarization direction, results in slightly different diffraction conditions for each side of the domain wall. As a consequence, the excitation error (s) varies for both domains and they can thus exhibit an alternating bright (domain 1) and dark (domain 2) contrast, as depicted in Fig. 3.7(a) [243]. The difference between both excitation errors, $s_{g(1)}$ and $s_{g(2)}$, for a specific reciprocal lattice vector (g) is illustrated by the Ewald sphere construction in Fig. 3.7(b).

For purely 180° domains, no domain wall contrast is visible in BF imaging. Since both domains on each side of the wall are related by an inversion symmetry, there is no difference in lattice parameters and Friedel's law is obeyed [70, 245]. According to Friedel's law, a diffraction pattern is always centrosymmetrical and the intensity of the hkl reflection is identical to the intensity of the $\overline{hkl}$ reflection ($I_{hkl} = I_{\overline{hkl}}$). 180° domain walls can however be visible in DF imaging, because for non-centrosymmetric crystals (as for non-cubic perovskites) Friedel's law holds for the transmitted 000 beam but not necessarily for diffracted beams [70, 246]. Therefore, 180° domain walls can only be imaged in TEM in DF mode, or in BF mode when a larger aperture is used also including some diffracted beams.

A typical feature of twin planes and lamellar domains is the occurrence of spot splitting in electron diffraction patterns (Fig. 3.8(a)). When the domain wall is aligned parallel to the electron beam (edge-on), splitting of reflection spots can be observed in reciprocal space along the direction which is perpendicular to the domain wall [76, 245]. The term 'spot splitting' is slightly misleading, since it is actually an image of two overlapping diffraction patterns, one from each side of the twin boundary. In Fig. 3.8(a), the diffraction pattern is viewed from the $[001]_{pc}$ direction. One row of unsplit spots is present along the $[110]_{pc}$ direction passing through the direct beam. Due to $(110)_{pc}$ twin planes (domain walls), reflection splitting can be observed in $[110]_{pc}$ direction in the rows that are further away from the center of the diffraction pattern. Since the a and c lattice constants in the tetragonal structure slightly differ from each other, the unit cells on both sides of the 90° domain wall are slightly rotated towards each other, due to the mirrored orientation relationship of the a and c axes in both domains [70, 247] (Fig. 3.8(b)). As a result, the angle between the $[001]_T$ directions in two adjacent domains is in fact not exactly 90°, but slightly smaller [244].

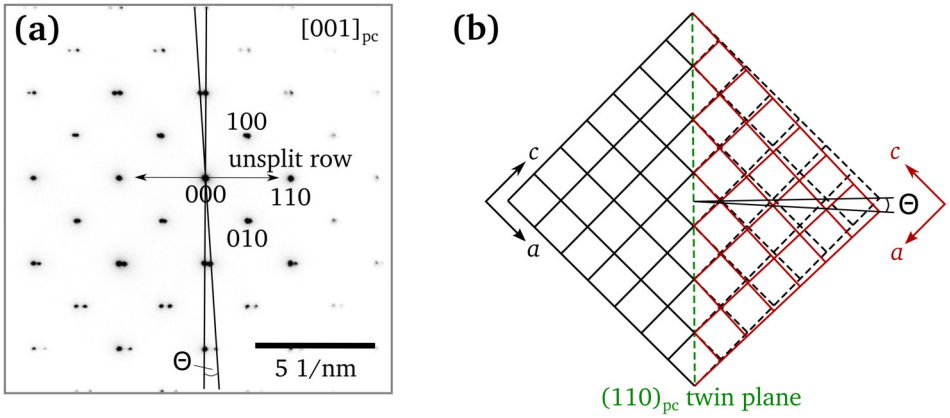

Figure 3.8: (a) SAED pattern of a tetragonal PZT grain with 90° twin domains. Splitting of reflections occurs along the $[110]_{pc}$ direction and is due to $(110)_{pc}$ oriented domain walls. (b) Illustration of the unit cell orientation on both sides of the $(110)_{pc}$ twin boundary, which is slightly rotated towards each other (redrawn after Ref. 247).

3.3 In-Situ Hot-Stage TEM

For in-situ heating experiments conducted with the JEM-2100F microscope, an in-situ heating holder Model 652 (Gatan, Pleasanton, USA) with a tantalum furnace was utilized, which allowed tilting of the specimen in two directions. The sample was clamped between two tantalum washers for optimal heat conductivity. For monitoring the temperature, a Model 901 SmartSet Hot Stage Controller (Gatan, Pleasanton, USA) was used, which allowed to specify the heating rates and holding times. Fig. 3.9(a) shows a free-standing poled NBT-BT wedge-shaped sample located in the furnace of the heating holder.

The samples were heated with a heating rate of 15 °C/min. The temperature was held at points of interest for ∼10 min to allow for stabilization of the temperature reading. Then, images and diffraction patterns were recorded. This approach resulted in a stepwise heating of the sample up to a maximum temperature of 400 °C. The cooling of the specimen was conducted in a similar stepwise manner and controlled manually, since the device does not allow to apply a cooling rate. Figure 3.9(b) schematically illustrates the temperature profile as function of time for a heated and cooled NBT-BT specimen.

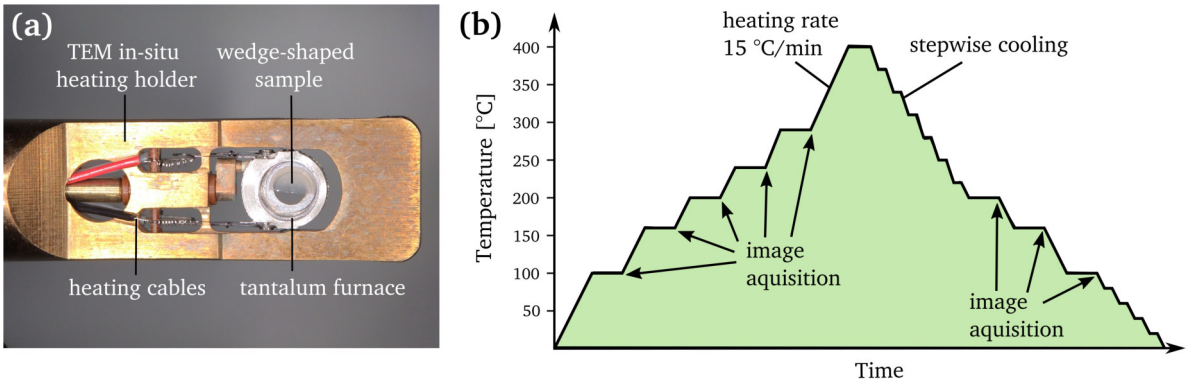

Figure 3.9: (a) TEM in-situ heating holder with a wedge-shaped NBT-BT sample. (b) Schematic temperature profile as a function of time for a TEM heating experiment.

For illustrating the changing intensity of superlattice reflections as function of the applied heating temperature (depicted in Fig. 4.36 on page 93), the intensities were determined from the SAED patterns recorded at each respective temperature. An intensity line profile with a width of 2.5 $\frac{1}{nm}$ and a length of 4 $\frac{1}{nm}$ was drawn over a main reflection and one neighboring $\frac{1}{2}$ $\{ooe\}$ and $\frac{1}{2}$ $\{ooo\}$ SR. The intensity of the background between the reflections was averaged over a distance of 0.4 $\frac{1}{nm}$. Subsequently, the ratio between the maximum intensity value of each superlattice reflection (I_{SR}) and the determined background value (I_B) was calculated and plotted.

3.4 Scanning Transmission Electron Microscopy (STEM)

STEM analyses were performed with a C_s-corrected JEM ARM 200F microscope (Jeol, Tokyo, Japan) operating at 200 kV and allowing for a resolution of 0.8 Å in STEM mode. In STEM, the beam is focused to a fine spot and scans over the specimen area in a raster pattern. The signals arising from the beam-specimen interaction are correlated with the beam position and therefore with each location in the image. Detailed descriptions relating to STEM analysis can be found in Pennycook

& Nellist [248]. BF images were recorded with a 3 mm BF aperture corresponding to an angle detection range of 0-23 mrad. For high-angle annular dark-field (HAADF) images, a camera length of 6 cm was used, resulting in an inner detector acceptance angle of 90 mrad and an outer angle of 370 mrad, while annular bright-field (ABF) imaging corresponds to a detector range of 10-23 mrad. In a BF image, which includes the transmitted beam, atoms appear dark on a bright background, while the contrast is reversed for a HAADF image. The HAADF technique produces a dark-field image formed from incoherently scattered electrons under very high angles [249]. The technique is very sensitive to the atomic number (Z) of the analyzed material. Elements with a higher Z value result in a stronger interaction of the electron beam and atomic nucleus, leading to stronger scattering of electrons under high angles. Heavy atoms therefore appear brighter than lighter atoms, which is useful in identifying elements in an atomically resolved HAADF image. Since the signal strongly depends on the atomic number, very light atoms ($Z < 8$) are usually not imaged by HAADF. In contrast, ABF images are formed from weakly scattered electrons and have the advantage of being more sensitive to light elements (e.g. oxygen), which can simultaneously be displayed with the more heavy atoms [250].

Atomically resolved HAADF images obtained along $\langle 001 \rangle_{pc}$ zone axes were used for subsequent analyses of the cation displacement. HAADF images were recorded with a resolution of 2048x2048 px, which resulted in a pixel size of 0.055 Å for a x20 Mio. magnified image. In order to minimize the

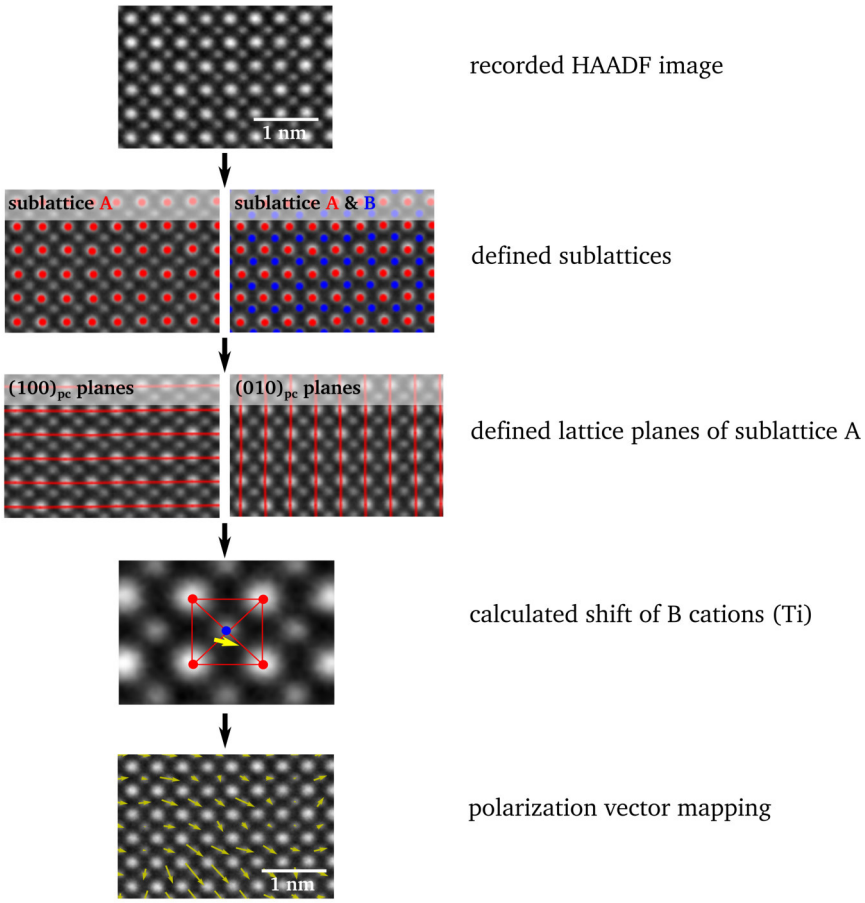

Figure 3.10: Workflow for analyzing a HAADF image with the Atomap and TEMUL Toolkit [251, 252]. After defining the atomic positions, sublattices and groups of lattice planes, the polar displacement (yellow arrows) of the B cation site can be mapped.

impact of image drift, a sequential imaging tool was used. Five images with a pixel scan time of 3 µs were successively recorded and then stacked and corrected for the image drift. Subsequently, the HAADF images were used for analyses with the freely available software tools Atomap [251] and TEMUL Toolkit [252], in order to map the local polar displacement. The tools comprise a Python-based script library for analyzing atomically resolved STEM images. The work flow for analyzing a HAADF image of NBT-BT is illustrated in Fig. 3.10. Since the *A* cation site is occupied by Na^{+}, Bi^{3+} and Ba^{2+} and the *B* cation site by Ti^{4+}, two sublattices have to be defined. Both *A* and *B* sublattices are identified by locating and refining the positions of the atomic columns. Firstly, the center of mass for refining the atom positions is used, then a 2D-Gaussian fitting [251]. Once both sublattices are defined, groups of lattice planes can be constructed. The Ti^{4+} atom shift with reference to the *A* sublattice can then be calculated [252]. The polar displacement is displayed as yellow arrows showing the direction and magnitude of the shift. By convention, the displacement vectors point towards the negative center of charge (so opposite to the Ti^{4+} displacement direction).

3.5 Electron Energy-Loss Spectroscopy (EELS)

EELS analyses were carried out on the JEM ARM 200F microscope, which is equipped with an Enfina EELS Spectrometer (Gatan, Pleasanton, USA). A dispersion of 0.05 eV and 0.1 eV was used for the measurements, allowing a high energy resolution. EELS extracts information from inelastically scattered electrons, which lose energy while they interact with the specimen [253]. The energy loss is then measured by the EELS detector. Electron energy-loss can arise from ionization of inner atom shells of the elements present in the specimen. Thus, chemical information can be gained from the high-loss spectrum (> 50 eV), which contains the characteristic ionization edges of the present elements [253, 254], the so called energy-loss near edge structure (ELNES). The low-loss spectrum (< 50 eV) contains the zero-loss peak at 0 eV and the plasmon peaks (Fig. 3.11). EELS can not only give chemical information about atoms, but also information about their bonding states, coordination number and local environment. The ELNES thus provides details about the electronic structure of an element. The $L_{3,2}$-edges of transition metals such as Ti^{4+} can, for example, give conclusions about the valence state and site coordination [255]. Compared to EDS, EELS allows elemental identification of nanometer-sized areas, a high energy resolution and more sensitivity to lighter elements. A low specimen thickness is crucial for a high peak-to-background ratio, so very thin NBT-BT grains were used for the analyses.

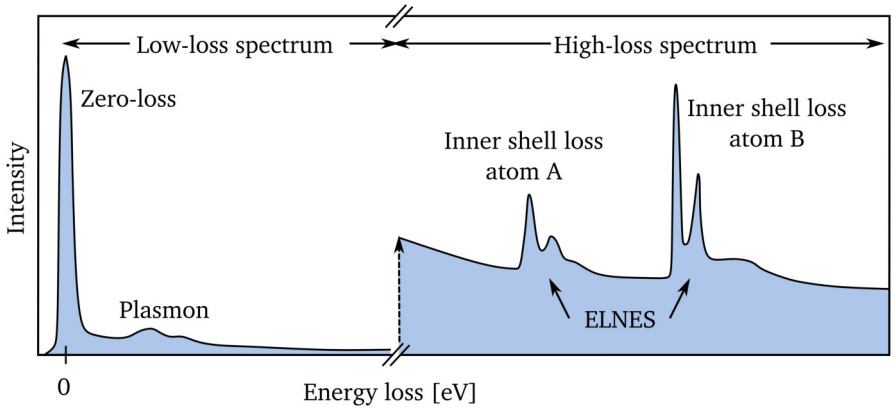

Figure 3.11: Schematic EELS spectrum showing the low-loss region and the high-loss region with the ELNES of atom A and B (modified after Ref. 253).

3.6 Scanning Electron Microscopy (SEM)

SEM analyses were carried out with a JSM-7600F microscope (Jeol, Tokyo, Japan), equipped with an X-Max80 EDS detector (Oxford Instruments, Abingdon, UK). Chemically etched NBT-BT samples were coated with a thin carbon layer prior to the analyses, in order to prevent charging in the SEM. Images were obtained with an acceleration voltage of 15 kV in back-scattered electron (BSE) mode. With increasing atomic number, Z, atoms in the specimen backscatter incident electrons more strongly due to stronger interaction with the heavier atom nuclei. Hence, the BSE signal strength and with that the contrast in the image is very sensitive to the elemental composition of the sample [256]. Since backscattered electrons can emerge from deeper areas of the samples excitation volume, BSE images show a lower resolution than surface sensitive secondary electron (SE) images. The BSE image contrast is not only influenced by the atomic number of the analyzed elements, but also by the surface topography of the specimen [257]. Inclined surface areas can, for example, cause shadowing effects. Etched domain structures of ceramic specimens relate to variations in the surface topography due to varying etching conditions for different domains and can thus be imaged in BSE mode.

3.7 Piezoresponse Force Microscopy (PFM)

PFM measurements were conducted with the assistance of Dr. Fangping Zhuo. A Cypher atomic force microscope (Asylum Research, Santa Barbara, USA) was utilized in vector PFM mode to collect the piezoresponse signal in vertical and lateral direction. Conductive cantilevers with a platinum and chromium coating, a tip with an apex curvature radius of 25 nm and a resonance frequency of 75 kHz were used (ElectriMulti75-G, Budget Sensors, Sofia, Bulgaria). The cantilever was tuned with a starting contact resonance frequency of 350 kHz for the vertical and 800 kHz for the lateral component. PFM images with a scan size of 4x4 μm^2 and a resolution of 512x512 px were acquired. The image area was scanned with a 0.5 Hz scan rate. An AC driving voltage of 1-2 V was applied to the cantilever.

PFM analysis makes use of the electromechanical coupling of a material. Through the conductive cantilever tip, an electric current is conducted to the sample surface, which results in a mechanical displacement according to the converse piezoelectric effect. The local surface deformation causes the cantilever to deflect, which is tracked via a reflected laser beam [258]. The deflection of the cantilever, while scanning over the sample, can be vertical (out-of-plane) or lateral (in-plane) to the surface, relating to vertical and lateral components of the piezoelectric deformation. The ability to record displacements in the picometer-range has rendered PFM a widely applied method for mapping ferroelectric domains [259]. By applying a AC driving voltage ($V = V_0 cos(\omega t)$), the sample surface expands and contracts periodically, which is translated in the vertical vibration of the cantilever [260], where the first harmonic component of the oscillation is given by the amplitude A_{AC} [261, 262]:

$$A_{AC} = A_0 + A_{1\omega} cos(\omega t + \varphi) \tag{3.12}$$

A_0 is the static surface displacement induced by the applied voltage, ω the driving frequeny and φ the phase difference between the driving voltage and the voltage-induced piezoresponse of the sample surface. The vibration amplitude of the cantilever, $A_{1\omega}$, directly relates to the converse

piezoelectric effect and thus to the piezoelectric response of the sample surface. $A_{1\omega}$ represents the surface displacement and can be expressed as $A_{1\omega} = d_{33}^{eff} V_0$, with the effective piezoelectric coefficient $d_{33}^{eff} \approx d_{33}$ for ferroelectric c-domains, where the polarization direction is aligned vertical to the sample surface [260]. Both amplitude ($A_{1\omega}$) and phase (φ) can be recorded as PFM images. The phase gives information about the polarization direction. When the polarization vector is oriented downwards (positive c-domain), the surface expands and vibrates in phase with the applied voltage, so $\varphi = 0°$ (Fig. 3.12(a)). For an upwards pointing polarization vector (negative c-domain), $\varphi = 180°$ and the local surface contracts (Fig. 3.12(b)). In a-domains, where the polarization direction is parallel to the sample surface, an in-plane displacement is induced by the electrical field, which results in a torsional motion of the cantilever [258] (Figs. 3.12(c) and (d)).

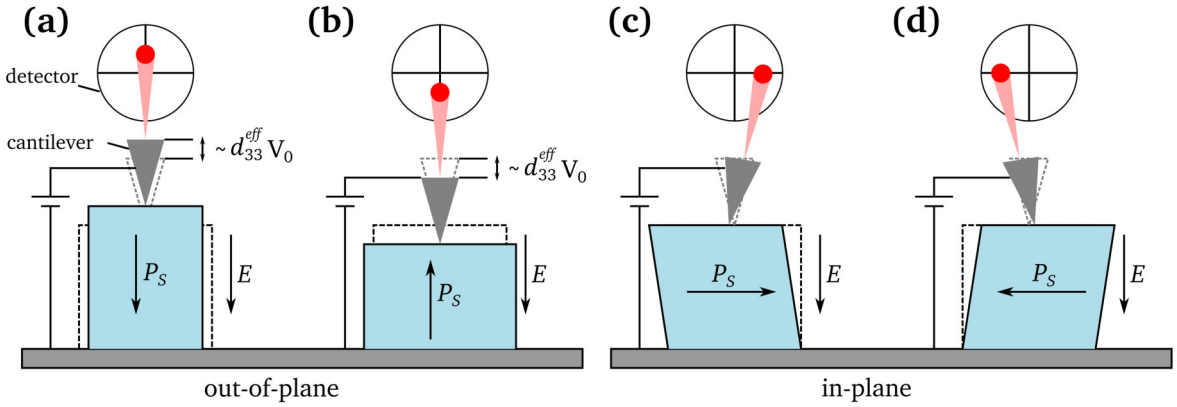

Figure 3.12: Piezoelectric response in a ferroelectric by PFM analysis. The parallel (a) or anti-parallel (b) alignment of the electric field (E) and the spontaneous polarization (P_S) results in vertical (out-of-plane) displacement of the sample and cantilever, which is proportional to $d_{33}^{eff} V_0$. (c), (d) When the applied field is perpendicular to P_s, a shear deformation results, which leads to a horizontal (in-plane) deflection of the signal (redrawn after Refs. 258 and 262).

4 Results & Discussion

4.1 Composition-Dependent Domain Structure and Phase Assemblage

Four NBT-BT compositions with a BT content spanning over a wide compositional range were examined. NBT-3BT is located on the rhombohedral NBT-rich side, NBT-6BT represents a MPB composition, NBT-9BT a near-MPB and NBT-12BT a tetragonal BT-rich composition. Accordingly, the four furnace cooled specimens exhibit variations in the domain structure, as well as in the phase assemblage. Fig. 4.1 depicts comparable grains viewed along the $[\bar{1}10]_{pc}$ zone axis. A complex and irregular domain configuration is present in NBT-3BT (Fig. 4.1(a)). NBT-6BT, on the other hand, is

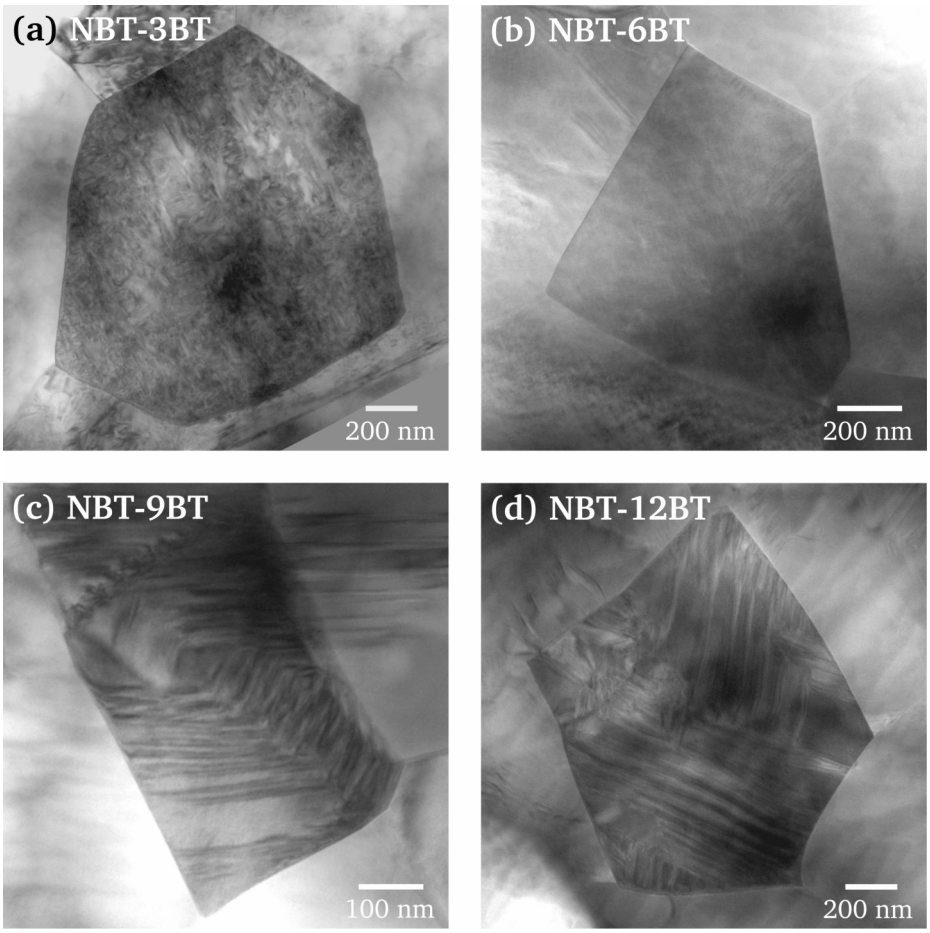

Figure 4.1: TEM-BF micrographs of the furnace cooled NBT-BT compositions (all viewed along the $[\bar{1}10]_{pc}$ zone axis). (a) NBT-3BT, (b) NBT-6BT, (c) NBT-9BT and (d) NBT-12BT.

characterized by the absence of a distinct domain contrast (Fig. 4.1(b)), while NBT-9BT and -12BT both exhibit lamellar domains (Figs. 4.1(c) and (d)). Grain sizes range from approx. 500 nm up to 3-4 µm, while smaller grains are predominately found in the BT-rich compositions. This is in agreement with other observations of sintered NBT-BT ceramics, where the grain size decreases with increasing BT content [151, 152, 154].

The correct assignment of phases is complicated by the rather small deviations of both rhombohedral and tetragonal symmetries from the cubic perovskite structure. Indexing simply the main reflections in SAED patterns is not applicable, since they appear pseudocubic. However, the structural symmetry can be derived from superlattice reflections (SRs), arising from the different oxygen octahedral tilt systems inherent to the rhombohedral *R*3*c* and tetragonal *P*4*bm* structure. Table 4.1 illustrates an overview of SRs occurring in different zone axes in the four compositions. Anti-phase octahedral tilting results in $\frac{1}{2}\{ooo\}$ SRs [100], which are present in $\langle 110\rangle_{pc}$ zone axes and can be assigned to the rhombohedral *R*3*c* phase ($a^-a^-a^-$ tilt system). In-phase octahedral tilting causes the formation of $\frac{1}{2}\{ooe\}$ SRs, which are absent from the $\langle 110\rangle_{pc}$ zone axes and present in the $\langle 001\rangle_{pc}$ and $\langle 111\rangle_{pc}$ viewing directions. They can be assigned to the tetragonal *P*4*bm* phase ($a^0a^0c^+$ tilt system). SRs are also present in zones axes of lower symmetry, while some of them can display both types of SRs, such as $\langle 112\rangle_{pc}$, $\langle 103\rangle_{pc}$ and $\langle 213\rangle_{pc}$. In Table 4.1, the observed SRs are marked with a color coding, indicating the reflection intensity from strong to very weak (or only occasional appearance). Fig. 4.2 exemplarily depicts the SAED patterns of the eight zone axes listed in Table 4.1. The location of $\frac{1}{2}\{ooo\}$ and $\frac{1}{2}\{ooe\}$ SRs on half-integral reciprocal positions is marked. The transition from a solely rhombohedral *R*3*c* symmetry to a phase coexistence of *R*3*c* + *P*4*bm* in

Table 4.1: Different zone axes and possible and observed superlattice reflections (SRs) in the four NBT-BT compositions. The $\frac{1}{2}\{ooo\}$ SRs can be associated to *R*3*c* and the $\frac{1}{2}\{ooe\}$ SRs to *P*4*bm*.

Zone axis	**Possible superlattice reflections**	**Observed superlattice reflections**			
		NBT-3BT	**NBT-6BT**	**NBT-9BT**	**NBT-12BT**
$\langle 001\rangle_{pc}$	$\frac{1}{2}\{ooe\}$	-	$\frac{1}{2}\{ooe\}$	$\frac{1}{2}\{ooe\}$	$\frac{1}{2}\{ooe\}$
$\langle 110\rangle_{pc}$	$\frac{1}{2}\{ooo\}$	$\frac{1}{2}\{ooo\}$	$\frac{1}{2}\{ooo\}$	$\frac{1}{2}\{ooo\}$	$\frac{1}{2}\{ooo\}$
$\langle 111\rangle_{pc}$	$\frac{1}{2}\{ooe\}$	-	$\frac{1}{2}\{ooe\}$	$\frac{1}{2}\{ooe\}$	$\frac{1}{2}\{ooe\}$
$\langle 102\rangle_{pc}$	$\frac{1}{2}\{ooe\}$	-	$\frac{1}{2}\{ooe\}$	$\frac{1}{2}\{ooe\}$	$\frac{1}{2}\{ooe\}$
$\langle 112\rangle_{pc}$	$\frac{1}{2}\{ooe\}$, $\frac{1}{2}\{ooo\}$	$\frac{1}{2}\{ooo\}$	$\frac{1}{2}\{ooe\}$, $\frac{1}{2}\{ooo\}$	$\frac{1}{2}\{ooe\}$, $\frac{1}{2}\{ooo\}$	$\frac{1}{2}\{ooe\}$
$\langle 103\rangle_{pc}$	$\frac{1}{2}\{ooe\}$, $\frac{1}{2}\{ooo\}$	$\frac{1}{2}\{ooo\}$	$\frac{1}{2}\{ooe\}$, $\frac{1}{2}\{ooo\}$	$\frac{1}{2}\{ooe\}$, $\frac{1}{2}\{ooo\}$	$\frac{1}{2}\{ooe\}$, $\frac{1}{2}\{ooo\}$
$\langle 113\rangle_{pc}$	$\frac{1}{2}\{ooe\}$	-	$\frac{1}{2}\{ooe\}$	$\frac{1}{2}\{ooe\}$	$\frac{1}{2}\{ooe\}$
$\langle 213\rangle_{pc}$	$\frac{1}{2}\{ooe\}$, $\frac{1}{2}\{ooo\}$	$\frac{1}{2}\{ooo\}$	$\frac{1}{2}\{ooe\}$, $\frac{1}{2}\{ooo\}$	$\frac{1}{2}\{ooe\}$	$\frac{1}{2}\{ooe\}$
Intensity of SRs:		strong	weak	very weak	- none

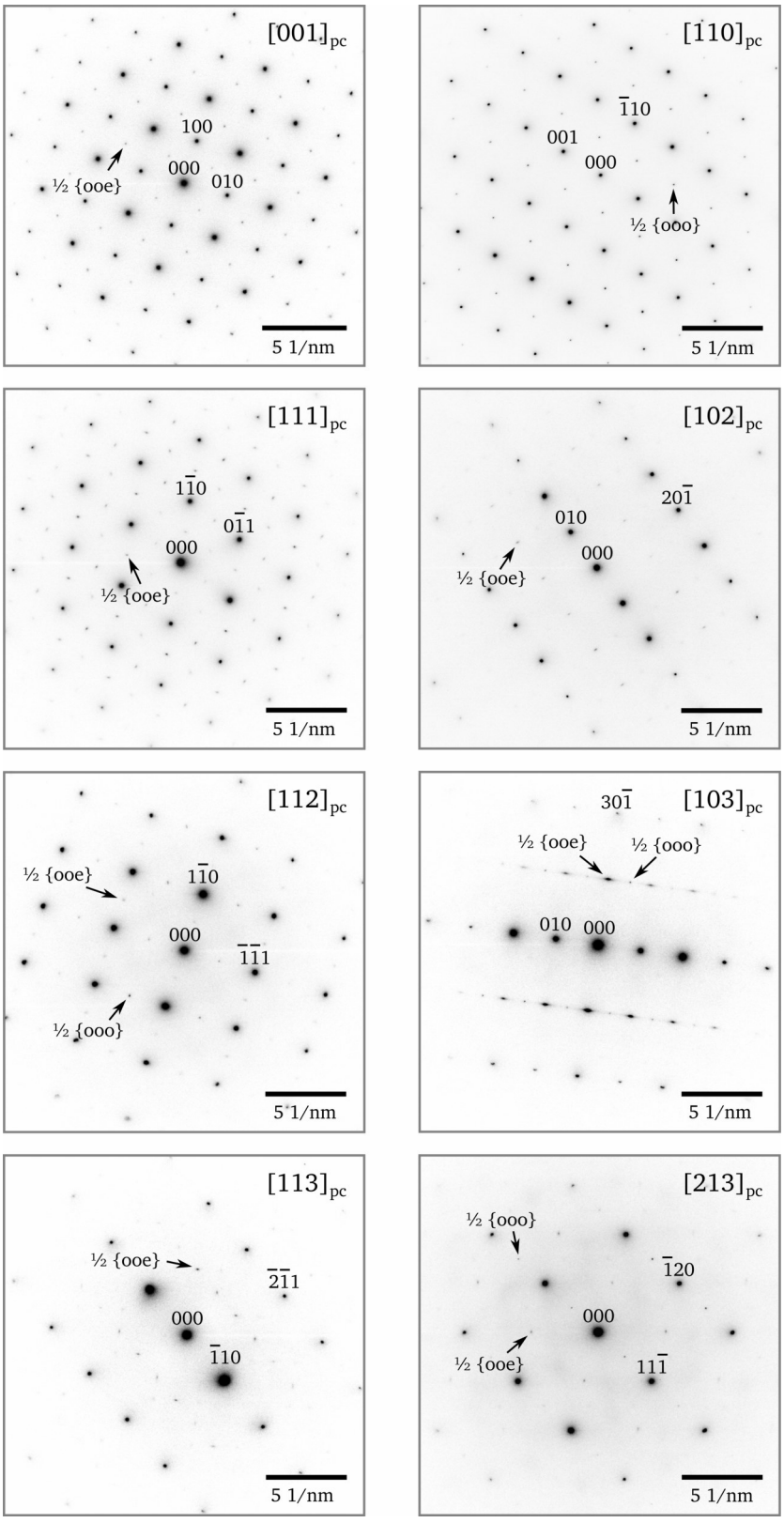

Figure 4.2: SAED patterns of the eight zone axes listed in Table 4.1, exemplarily shown for NBT-6BT FC. The locations of $\frac{1}{2}$ $\{ooo\}$ and $\frac{1}{2}$ $\{ooe\}$ SRs are marked with arrows.

MPB-close compositions towards a predominantly tetragonal symmetry is illustrated with increasing BT content. Note that the tetragonal *P*4*mm* phase, which is present in BT-rich compositions, does not feature oxygen octahedral tilting and hence no SRs. In the following, a detailed examination of the phase assemblage and domain structure of each composition is given.

4.1.1 NBT-Rich Composition (NBT-3BT)

The complex domain configuration in NBT-3BT comprises small and irregularly shaped domains of up to 150 nm in length. Partially, these domains can have a lamellar character. A square-net pattern with two dominating perpendicular directions becomes visible along the $[1\bar{3}1]_{pc}$ zone axis (Fig. 4.3(a)). No $\frac{1}{2}$ $\{ooe\}$ SRs occur in the corresponding SAED pattern (Fig. 4.3(b)). However, in the $\langle 110\rangle_{pc}$ zone axes, strong $\frac{1}{2}$ $\{ooo\}$ SRs (*R*3*c*) can be observed (Fig. 4.3(c)). The corresponding BF image displays a faint domain wall contrast (Fig. 4.3(d)). In the DF image obtained from the 001 main reflection (encircled in (c)), the irregular and detailed domain features are more clearly visible (Fig. 4.3(e)). Wavy structures indicated by the arrow are likely related to 180° domain walls. The complex domain configuration in NBT-3BT is comparable to observations made in pure NBT ceramics [83]. DF imaging of the $\frac{1}{2}$ $\{ooo\}$ SRs gives information about the grain areas which exhibit the $a^-a^-a^-$ oxygen octahedral tilt system. Fig. 4.3(f) displays a DF image obtained from the $\frac{1}{2}$ $(11\bar{1})$ SR (marked in (c)). Intensity arises from the whole grain, indicating its *R*3*c* symmetry. However, small dark areas of ∼100 nm in size appear as well (indicated by arrows). A certain degree of tilt disorder can be inferred, disrupting coherent anti-phase tilting.

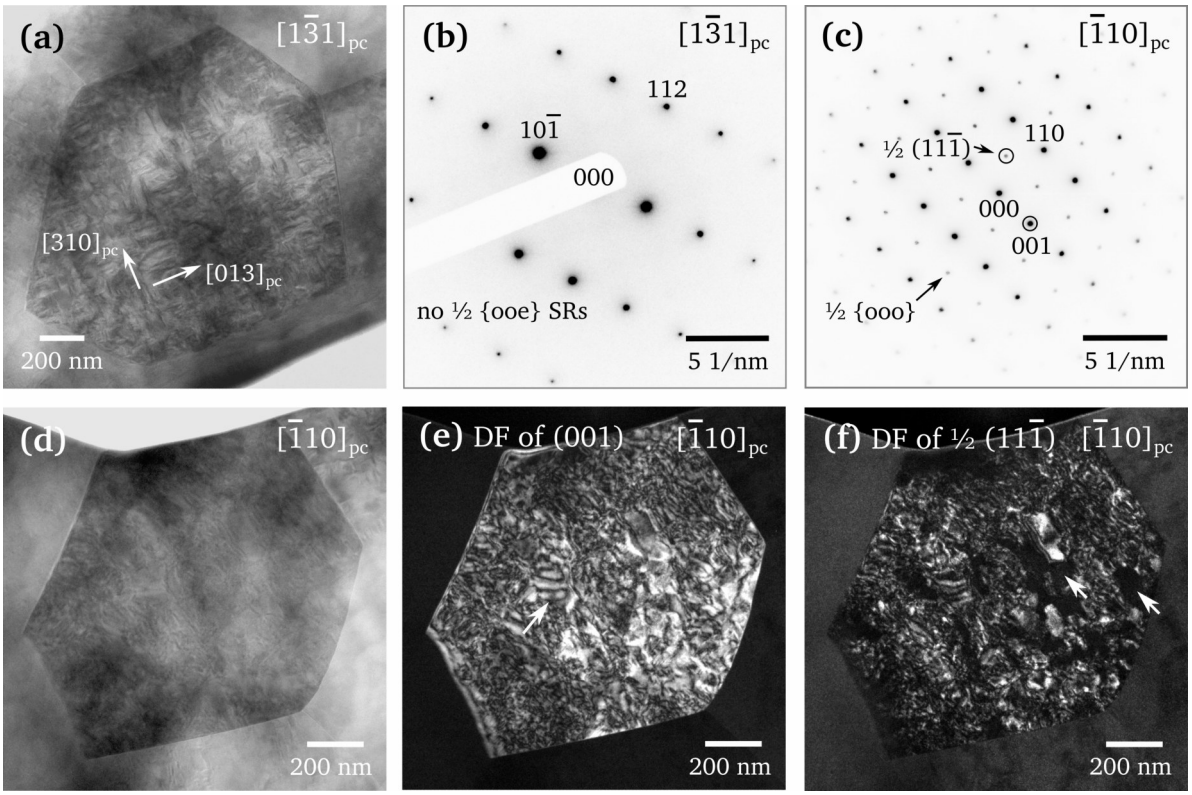

Figure 4.3: TEM images of NBT-3BT FC. (a) A grain with square-net pattern viewed along $[1\bar{3}1]_{pc}$ and corresponding SAED pattern (b). (c) SAED pattern of the $[\bar{1}10]_{pc}$ zone axis, depicting $\frac{1}{2}$ $\{ooo\}$ SRs (*R*3*c*) and corresponding grain in BF mode in (d), in DF mode obtained from the main 001 reflection in (e) and from the $\frac{1}{2}$ $(11\bar{1})$ SR in (f).

4.1.2 Relaxor MPB Composition (NBT-6BT)

In NBT-6BT, large domain structures are mostly absent. Many grains appear completely homogeneous. On a closer look, a nanoscale contrast is present, illustrated in an enlarged grain section in Fig. 4.4(a). Small lamellar nanodomains with a length of up to approx. 40 nm can occasionally be observed (indicated with arrows). Predominantly, the nanoscale contrast has a 'grainy' character without any orientation preference. A small fraction of grains displays few lamellar domains. Grains can show roundish areas of enhanced contrast embedded within the more homogeneous grain matrix, as shown in Fig. 4.4(b). The latter, to which the nanodomain contrast is inherent, exhibits $\frac{1}{2}$ $\{ooe\}$ SRs and the *P*4*bm* symmetry (Fig. 4.4(c)). In the SAED pattern from the small circular area (marked as (d)), $\frac{1}{2}$ $\{ooe\}$ SRs are absent, indicating a different symmetry (Fig. 4.4(d)).

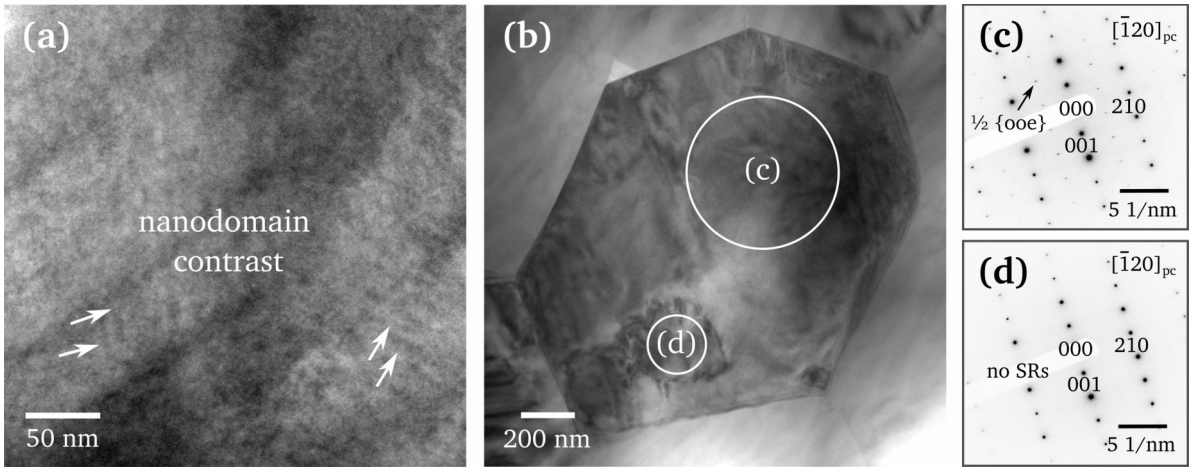

Figure 4.4: TEM micrographs of NBT-6BT FC. (a) The *P*4*bm* phase can show nanometer-sized domains (indicated by arrows). (b) A grain with a circular area (d), where $\frac{1}{2}$ $\{ooe\}$ SRs are absent from the corresponding SAED pattern, while they are present in the rest of the grain indicating the *P*4*bm* symmetry (c). The position of the SAED aperture for (c) and (d) is marked in (b).

Such grain areas are in fact of *R*3*c* symmetry. This can be illustrated by choosing a zone axis, where both types of SRs can be observed, such as the $[103]_{pc}$ axis in Fig. 4.5. The SAED pattern exhibits $\frac{1}{2}$ $\{ooe\}$ SRs, which are elongated along the $[010]_{pc}$ direction and show a strong intensity. Circular $\frac{1}{2}$ $\{ooo\}$ SRs are present in the same reflection row, showing a weaker intensity. A SR of each type encircled in Fig. 4.5(a) is chosen for DF imaging in order to illustrate the morphology and location of the *R*3*c* and *P*4*bm* phase, respectively. A BF image of an enlarged grain section is displayed in Fig. 4.5(b). The corresponding DF image of the $\frac{1}{2}$ $\{ooo\}$ SR (Fig. 4.5(c)) reveals that the lamellar domains on the bottom right side are of *R*3*c* symmetry. The R phase manifests in a coherent area separated from the rest of the grain. Here, it verges on the grain boundary, while it can also be located within the grain completely surrounded by the *P*4*bm* phase. The DF image of the $\frac{1}{2}$ $\{ooe\}$ SR displays thin and elongated bright entities, which have a length of 10-35 nm and a thickness of up to 5 nm (Fig. 4.5(d)). Thus, the *P*4*bm* phase consists of a dense population of plate-like nanodomains. Their elongation direction is perpendicular to the $[010]_{pc}$ stretching direction of the SRs in reciprocal space. Hence, they are oriented along $(010)_{pc}$ planes. The plate-like nanoscale morphology of *P*4*bm* is in accordance with other TEM studies [160, 199]. Their terminological description ranges from tetragonal 'platelets' or 'nanodomains' to 'nanoregions' or 'PNRs'. In this work, the nanoscale *P*4*bm* regions observed in DF imaging are referred to as 'nanodomains'. They

are commonly related to the relaxor behavior of NBT-BT and *P4bm* is thus denoted as the relaxor phase [150, 158, 200]. It appears likely that the nanodomains observed in the DF image relate to the nanodomain contrast observed in BF imaging (compare Fig. 4.4(a)), also corroborated by the similarity in correlation length. Interestingly, the lamellar domains on the left side in Fig. 4.5(b) are not of rhombohedral symmetry. Instead, a reduced population of *P4bm* nanodomains is present among those larger domains (4.5(d)). This configuration is discussed in a separate chapter (see section 4.4.3) relating to the nanostructural characteristics of NBT-BT.

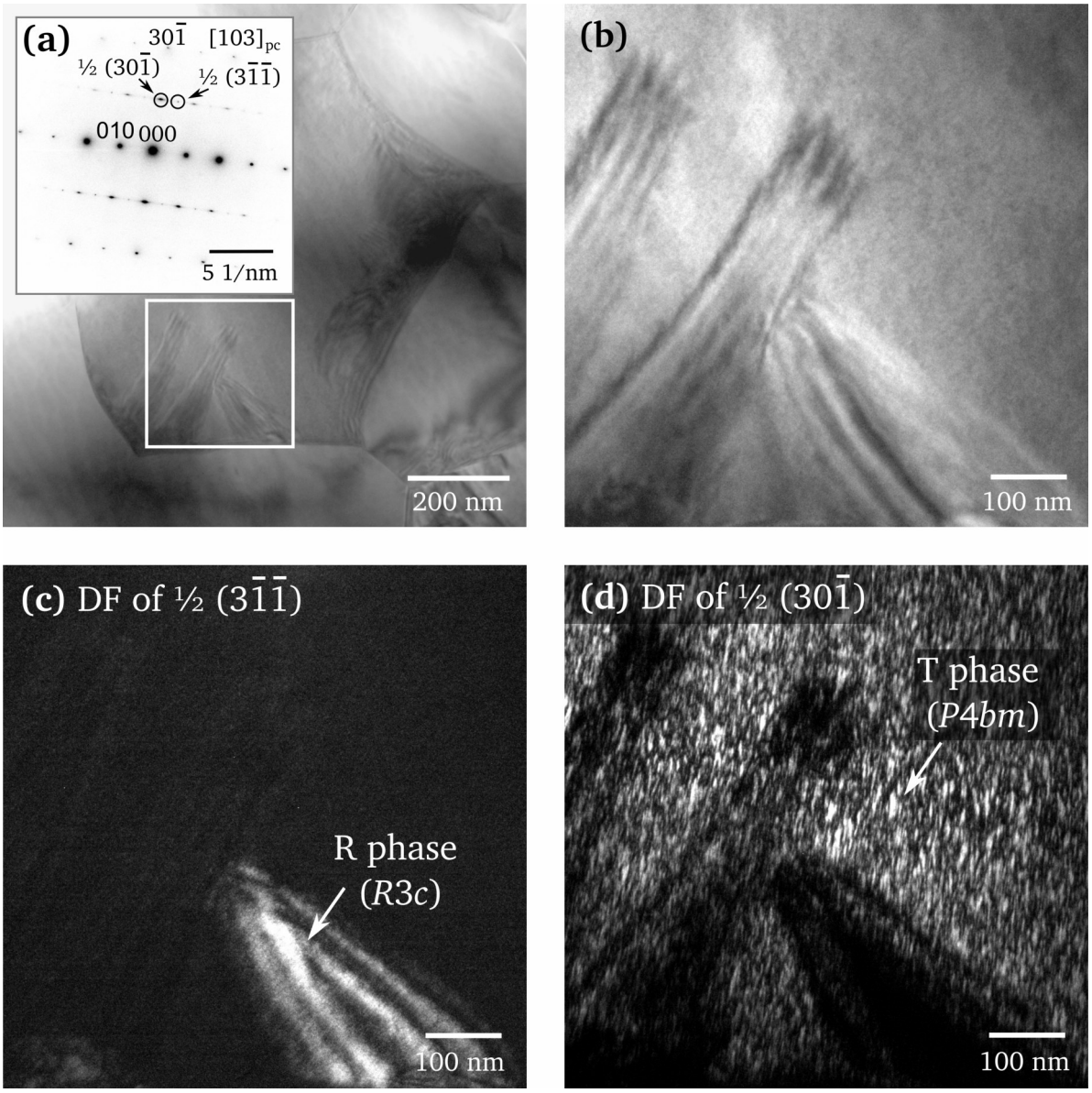

Figure 4.5: (a) TEM-BF image of a grain in NBT-6BT FC and corresponding $[103]_{pc}$ SAED pattern as inset where both $\frac{1}{2}$ $\{ooo\}$ and $\frac{1}{2}$ $\{ooe\}$ SRs occur. The area framed in white is enlarged in (b), displaying some lamellar domains. (c) Corresponding DF image obtained from the encircled $\frac{1}{2}$ $(3\bar{1}\bar{1})$ SR showing the *R*3*c* phase. (d) DF image obtained from the encircled $\frac{1}{2}$ $(30\bar{1})$ SR, depicting plate-like *P4bm* nanodomains.

4.1.3 Near-MPB Composition (NBT-9BT)

The domain structure in the NBT-9BT composition differs strongly from NBT-6BT and is characterized by an abundance of long-range ferroelectric domains. These lamellar domains show a width of 20-40 nm. Many grains also exhibit smaller grain areas, where no domains are present (Fig. 4.6(a)), while others are fully occupied by lamellar domains. Since NBT-9BT is located on the BT-rich tetragonal side of the MPB, the occurrence of lamellar domains can be associated with the tetragonal *P*4*mm* phase. However, weak $\frac{1}{2}$ {*ooe*} SRs can still be found throughout this composition in all grains (Fig. 4.6(b)), indicating that a coexistence of both tetragonal phases *P*4*mm* and *P*4*bm* is prevalent in NBT-9BT. Additionally, weak $\frac{1}{2}$ {*ooo*} SRs were observed in some grains in $\langle 110 \rangle_{pc}$ zone axes (Fig. 4.6(d)). In the corresponding DF image in Fig. 4.6(c), the R phase comprises only several small regions in the central area of the grain. The volume fraction of *R*3*c* within the grains is thus strongly reduced compared to NBT-6BT and -3BT.

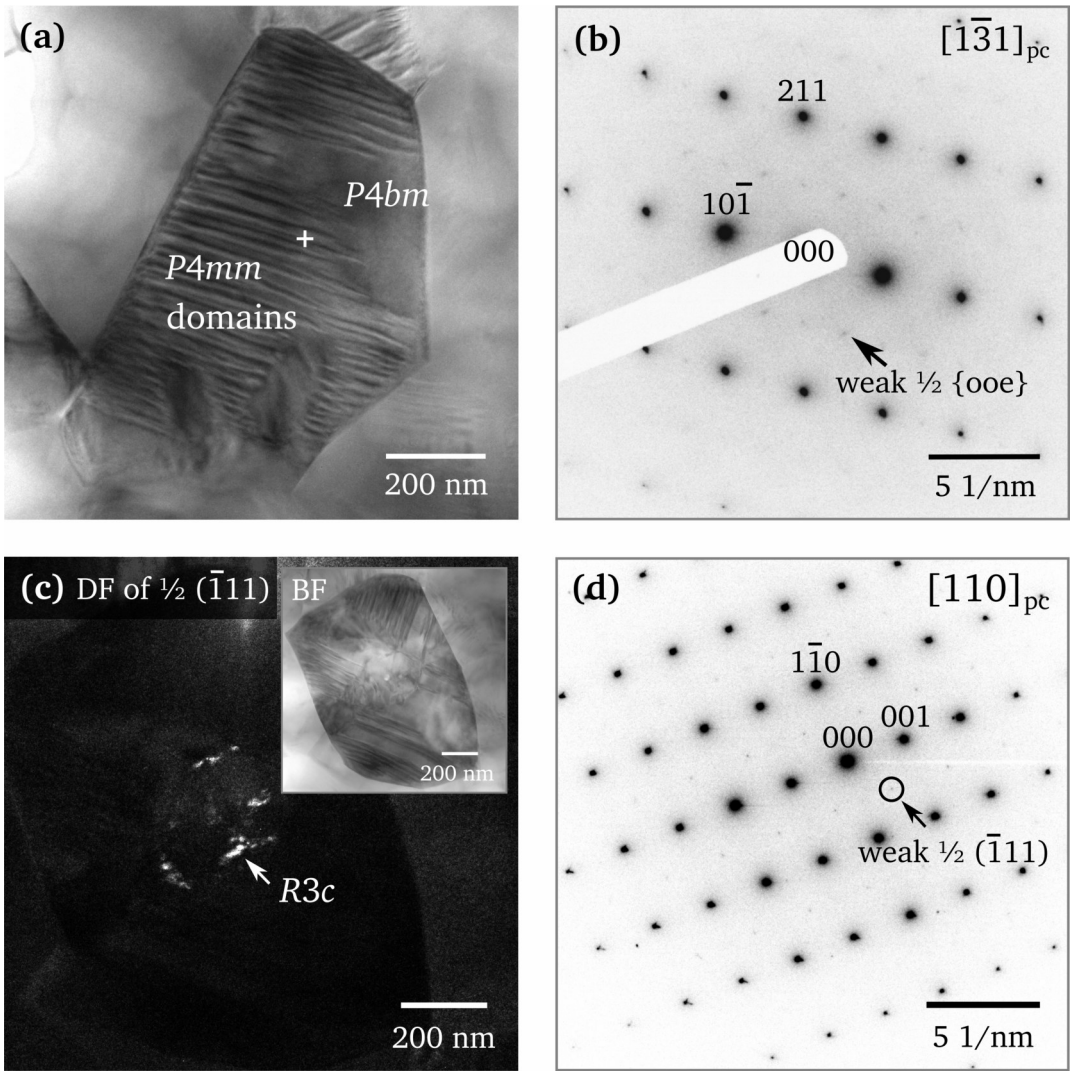

Figure 4.6: TEM micrographs of NBT-9BT FC. (a) A grain with lamellar domains (*P*4*mm*) and small areas, where domains are absent (*P*4*bm*). (b) The corresponding SAED pattern exhibits weak $\frac{1}{2}$ {*ooe*} SRs. (c) DF image of another grain with small *R*3*c* areas (BF image as inset), obtained from a weak $\frac{1}{2}$ {*ooo*} SR marked in the SAED pattern in (d).

4.1.4 BT-Rich Composition (NBT-12BT)

The domain structure of the NBT-12BT composition is largely comparable to NBT-9BT, featuring predominantly long-range lamellar domains, as displayed in Fig. 4.7(a). Here, the grain is viewed along a $\langle 001 \rangle_{pc}$ direction, where the domain walls are oriented edge-on. Thus, they appear as narrow lines with reduced contrast. From this viewing direction, the location of the domain wall planes can be inferred by comparing the BF image with the SAED pattern (inset in Fig. 4.7(a)). The two sets of lamellar domain walls are located on $(011)_{pc}$ and $(01\bar{1})_{pc}$ planes. $\{101\}_{pc}$ planes are permissible 90° domain walls in the tetragonal ferroelectric phase (compare section 2.2.2). Both sets of $(011)_{pc}$ and $(01\bar{1})_{pc}$ domain walls form a perpendicular plane pair as depicted in Fig. 2.10(a) (page 12). This further confirms that the lamellar domains are of tetragonal *P*4*mm* symmetry. The appearance of weak $\frac{1}{2}$ $\{ooe\}$ SRs in the $[100]_{pc}$ SAED pattern (Fig. 4.7(a)) points towards a minor volume fraction of in-phase tilted *P*4*bm* regions. Comparable to NBT-9BT, some grains exhibit minor homogeneous regions where domains are absent, as in Fig. 4.7(b). The $[110]_{pc}$ SAED pattern of the homogeneous region reveals very weak $\frac{1}{2}$ $\{ooo\}$ SRs (Fig. 4.7(c)), while they are absent from areas with strong domain contrast (Fig. 4.7(d)). The *R*3*c* symmetry with $a^-a^-a^-$ oxygen octahedral tilting is thus present to a minor degree, probably only on a very local length scale, similar to NBT-9BT.

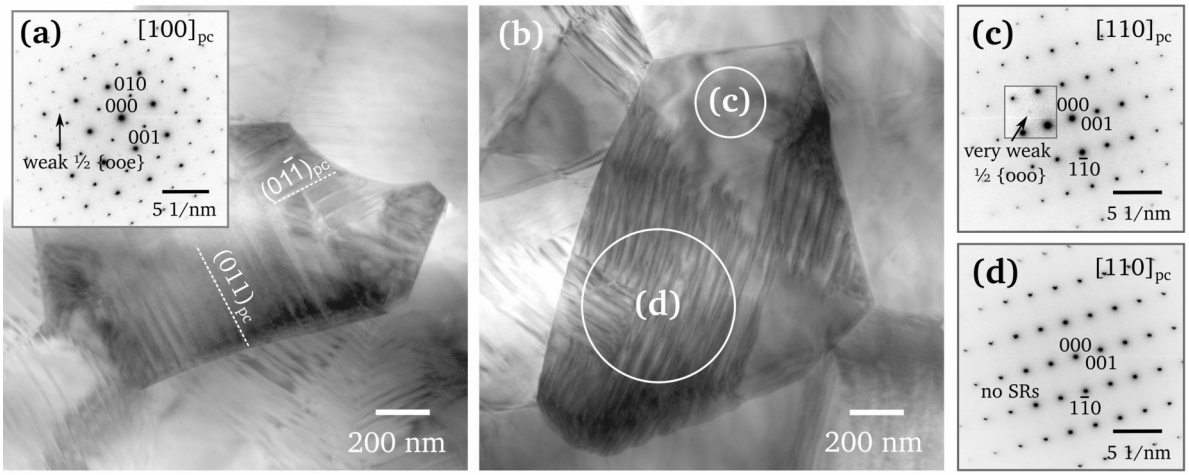

Figure 4.7: (a) TEM image of a grain in NBT-12BT FC depicted along the $[100]_{pc}$ zone axis (SAED pattern as inset). The $(011)_{pc}$ and $(01\bar{1})_{pc}$ domain walls are oriented edge-on and indicated with dashed lines. (b) Another grain, where the homogeneous region shows very weak $\frac{1}{2}$ $\{ooo\}$ SRs associated to *R*3*c* in the $[110]_{pc}$ SAED pattern (c), while they are absent in the SAED pattern of the lamellar domains (d).

4.1.5 Secondary Phase and Grain Boundaries

In all NBT-BT specimens, a secondary phase was observed, located at multi-grain junctions. In order to estimate its abundance, 150 multi-grain junctions in each composition have been inspected via TEM. Only 15-30 % displayed the presence of an additional phase. The majority of multi-grain junctions (70-85 %) did not show any indications for the presence of a secondary phase.

In Fig. 4.8(a), a non-wetted triple-grain junction is displayed. Grain 1 and grain 2 are aligned along the $[111]_{pc}$ and $[110]_{pc}$ zone axis, respectively. Lattice fringes reflecting the respective symmetry orientation can be seen in both grains in HRTEM (Fig. 4.8(b)). The third adjacent grain is not oriented along a low-indexed zone axis (grain 3), hence no lattice fringes appear here. The boundary

between the grains is inconspicuous and not coherent, which reflects the general appearance of grain boundaries in the NBT-BT ceramics. No secondary phase is present in the triple-grain junction.

In contrast, Fig. 4.8(c) depicts a triple-grain junction with a secondary phase. Its amorphous nature becomes apparent from the HRTEM image in Fig. 4.8(d). In the fast Fourier transform (FFT) image, only an amorphous-characteristic halo ring pattern is present and reflection spots are absent. The secondary phase exhibits a vesicular appearance. Under a focused electron beam in the TEM, which increases the energy density and local specimen temperature, bubbles were observed to form within the amorphous phase. A low melting point and the separation of a gaseous compound can be inferred. The secondary phase thus likely forms as a melting phase during sintering, which collects at pores and grain junctions and transforms into an amorphous solid glassy phase upon cooling. EDS analysis reveals a high barium content, as well as a noticeable phosphorus and silicon peak (inset in Fig. 4.8(c)). The raw powders used for preparing the ceramics have been analyzed by EDS and a small P and Si peak was observed in the TiO_2 starting powder (99.6 % purity), likely being the source of the impurities.

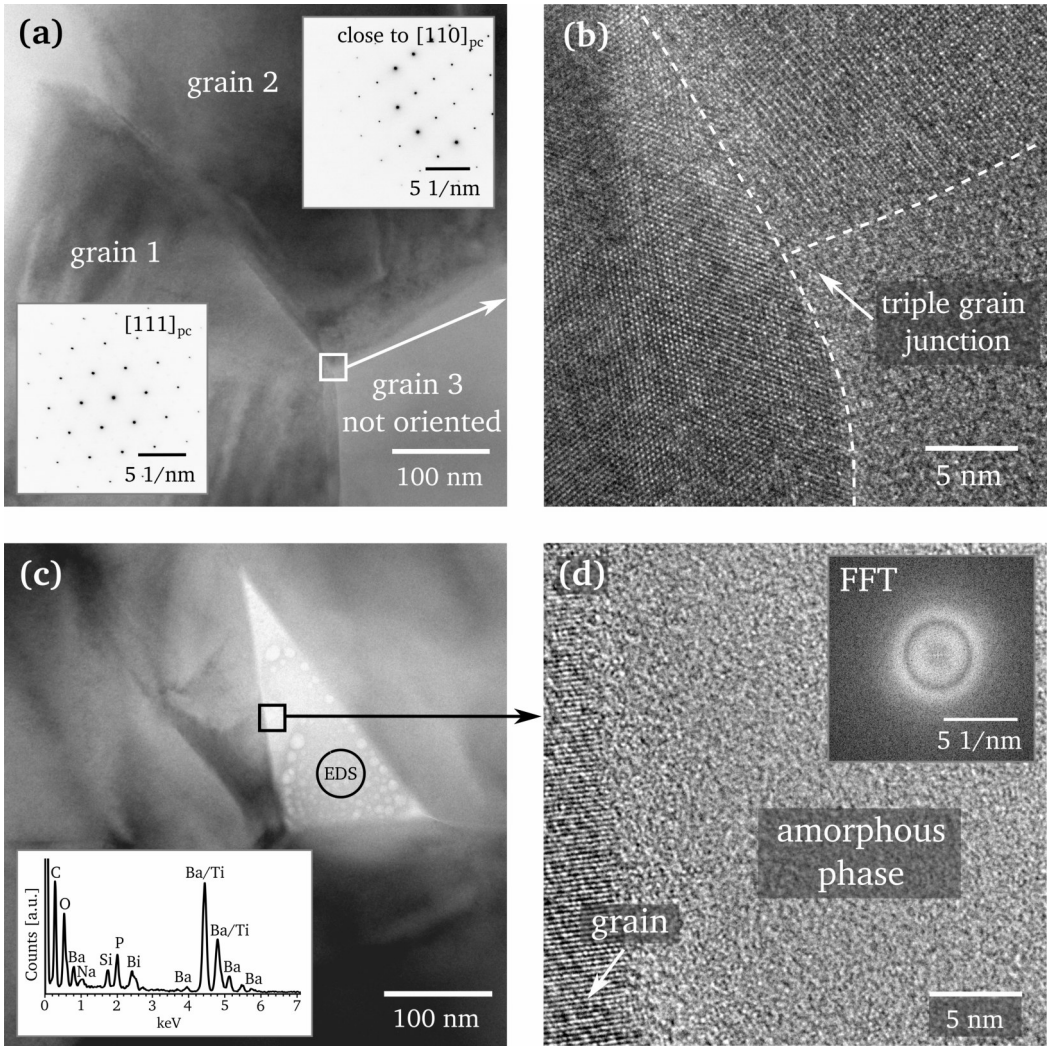

Figure 4.8: TEM micrographs of triple-grain junctions in NBT-9BT FC. (a) Non-wetted grain junction (SAED patterns of grain 1 and 2 as insets) and (b) corresponding HRTEM image. (c) Triple-grain junction with secondary phase (EDS spectrum as inset). (d) HRTEM image and FFT (inset) showing the amorphous nature of the secondary phase.

Only one out of five grain boundaries, which adjoins a multi-grain junction with a secondary phase, shows indications for the presence of an amorphous interface layer. This implies that overall only approx. 3-6 % of all grain boundaries in NBT-BT are wetted. A defocus imaging series in TEM can be executed, in order to measure the thickness of the amorphous film between two grains (Fig. 4.9). The defocus Fresnel fringe imaging technique makes use of the appearance of dark and bright contrast fringes in under- and overfocused images, respectively, which originate from the interface of the grain and the amorphous film [263, 264]. Changing from the focused image (Fig. 4.9(c)) towards negative defocus (d_f) values, leads to the appearance of two dark contrast lines (Fresnel fringes) and a central bright line (Fig. 4.9(b)). The two dark fringes propagate further away from each other with decreasing d_f. For positive defocus values, the contrast is vice versa (Fig. 4.9(d)). By drawing intensity profiles perpendicular to the grain boundary and measuring the distance between the two intensity minima or maxima, respectively, the fringe distance is determined. Plotting the fringe distance as function of the defocus value results in a V-shaped dependency (Fig. 4.9(a)). Extrapolating the curves to $d_f = 0$ gives the thickness of the film, which

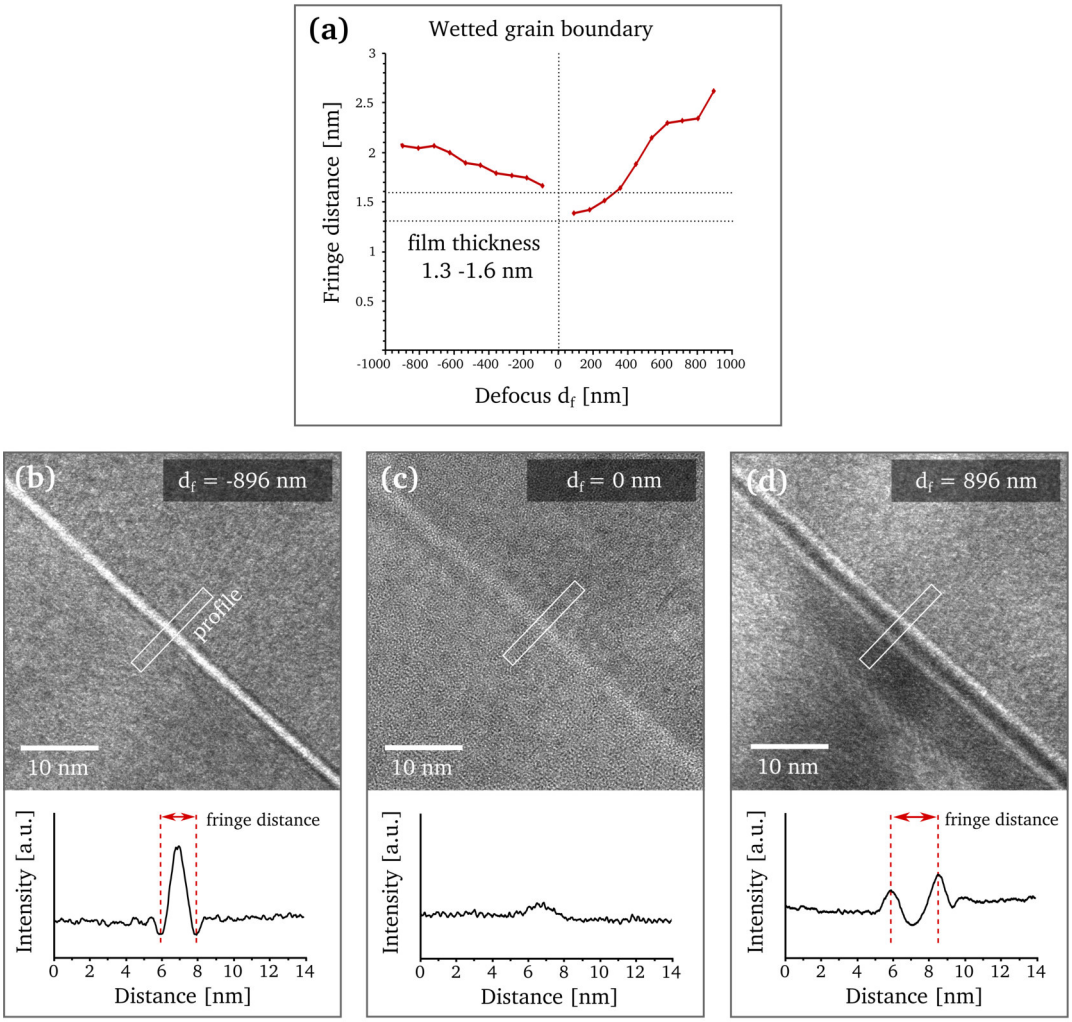

Figure 4.9: Film thickness determination of a wetted grain boundary in NBT-3BT FC. The graph in (a) is obtained by measuring fringe distances at different defocus values. (b) BF image of the grain boundary at a negative defocus value (d_f). The fringe distance is measured in the corresponding intensity profile. (c) The grain boundary in focus and (d) at a positive defocus value.

is 1.3-1.6 nm (1.3 nm for the overfocused series and 1.6 nm for the underfocused series). Cinibulk et al. [263] showed that the film thickness (z) and the fringe distance (W) follow a dependency according to $z = W - (3\lambda\Delta d_f)^{\frac{1}{2}}$, with the electron wavelength, λ, and the defocus distance, Δd_f. The indirect method of defocus Fresnel fringe imaging usually yields a 20-35 % wider film thickness as measured in a comparable HRTEM image [263].

Wetting of grain boundaries can occur in order to minimize the interface surface energy of adjacent grains. If the surface energy between solid grains is smaller than the surface energy of a grain-liquid interface, grain boundaries are non-wetted and the wetting angle of isolated melt pockets in triple-grain junctions is larger than 60° [265]. This is the case for the majority of wetting angles in the NBT-BT ceramics. Secondary phases can generally have an influence on the ceramics properties, such as the conductivity. This is especially the case, when grains are surrounded by an interconnected network of a secondary phase. In the four NBT-BT compositions, however, 94-97 % of all examined grain boundaries are non-wetted. Therefore, no relevant influences on the electrical properties can be assumed.

The incorporation of Ba in the secondary phase needs to be considered critically, since it may influence the stoichiometry within the grains. Therefore, several grains in each composition have been analyzed by EDS in TEM. Measuring spots located within central regions of the grains have been chosen, excluding grain boundaries or grain junctions. An exemplary EDS spectra of a grain in NBT-6BT is displayed in Fig. 4.10(a). Note that the Mo peak is due to the Mo TEM grid, on which the sample is mounted. Since the Ba $L_{\alpha 1}$ and $L_{\beta 1}$ lines overlap with Ti, the intensity increase of

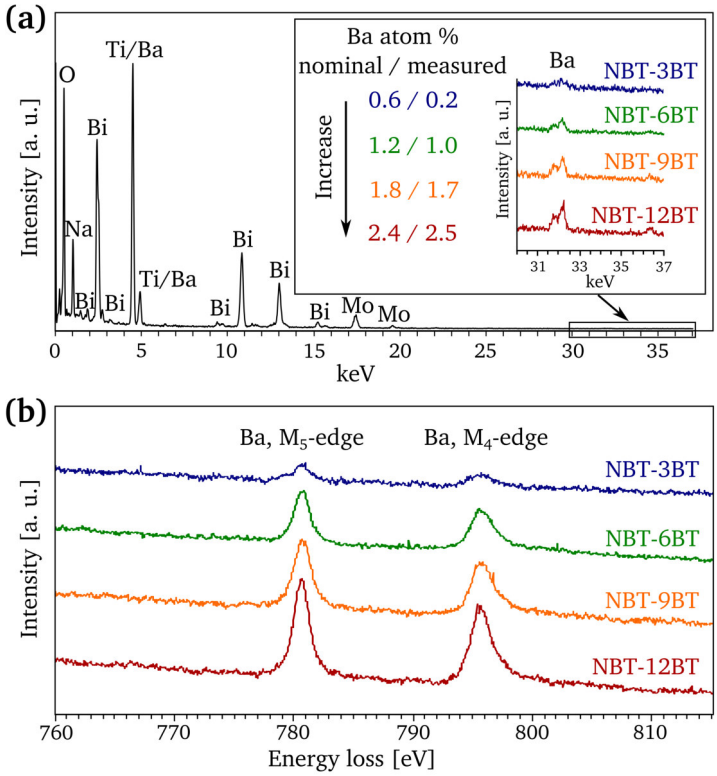

Figure 4.10: Ba content determined in the four NBT-BT FC compositions. (a) Exemplary EDS spectrum of a grain in NBT-6BT FC. The inset depicts the Ba $K_{\alpha 1}$ and $K_{\alpha 2}$ peaks and stoichiometric (nominal) and measured Ba atom % values of the four compositions. (b) EELS spectra displaying the Ba M_5- and M_4-edges, which exhibit an increasing peak intensity with increasing Ba content.

the Ba $K_{\alpha 1}$ and $K_{\alpha 2}$ peaks at 32.2 and 31.8 keV is illustrated for comparison. The stoichiometric (nominal) and measured Ba atom % of each composition is given in the inset of Fig. 4.10(a). A clear trend towards an increasing Ba content, which is close to the stoichiometric value, was determined in the four compositions. Via EELS analysis, an increasing intensity of the Ba M_5- and M_4-edges with increasing BT content could also be verified (Fig. 4.10(b)). The amount of Ba incorporated in the secondary phase can therefore be considered as negligible.

4.1.6 Discussion of Composition-Dependent Domain and Phase Evolution

TEM investigations on the unpoled NBT-BT specimens show a composition-dependent transition from a complex domain pattern (*R*3*c*) over a predominantly nanoscale structure (*P*4*bm*) towards a lamellar ferroelectric domain configuration (*P*4*mm*). Reported values for the *R*3*c* + *P*4*bm* MPB vary from a narrow range between 6-7 mol % [10] to a wider range of 6-10 mol % BT [152]. In the present study, the NBT-6BT, -9BT and -12BT specimens all display a phase coexistence, which is inferred from the presence of different SRs and regions of varying domain contrast within single grains. However, the three compositions show very different phase proportions, thereby influencing the appearance of the overall domain structure. Fig. 4.11 illustrates the qualitative phase fractions deduced from the TEM study in the compositional range between 3 and 12 mol % BT and the characteristic domain structure of each phase.

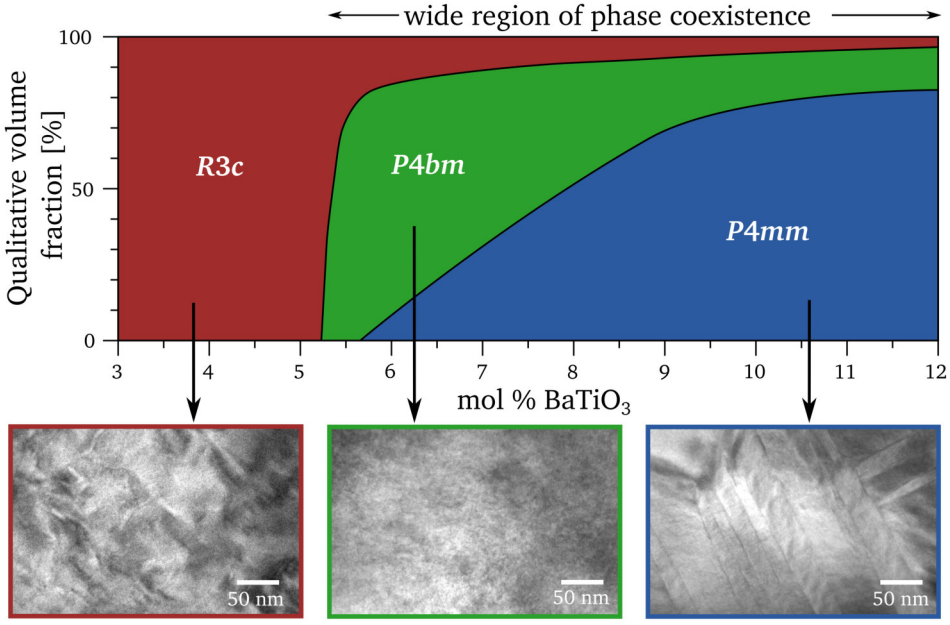

Figure 4.11: Qualitative volume fractions of the phase assemblage in the compositional range between 3 and 12 mol % BT deduced from the TEM study. The characteristic domain/nanodomain features of each phase are illustrated in the TEM-BF images.

The *P*4*bm* phase is known to initially occur at ~5 mol % BT, so that the transition between the *R*3*c* and *P*4*bm* phase can be assumed to be rather sharp. In NBT-6BT, the relaxor *P*4*bm* phase with its plate-like nanodomains is the dominant feature. Areas of *R*3*c* symmetry constitute a minor volume fraction. Few lamellar domains in NBT-6BT, which are not rhombohedral (compare Fig. 4.5), hint towards a minor fraction of tetragonal *P*4*mm* domains. While the TEM study by Ma et al. [158] shows a similar domain and phase assemblage for NBT-6BT, results strongly vary for the

compositions with higher BT content. In their study, NBT-9BT is of pure *P*4*bm* and NBT-11BT of *P*4*bm* + *P*4*mm* symmetry. These observations lead to the postulation of a second *P*4*bm* + *P*4*mm* MPB between 10 and 11.5 mol % BT and a single-phase-field of *P*4*bm* between the two MPBs (compare the phase diagram given in Fig. 2.24 on page 25). The results here, however, show a strong lamellar domain contrast in NBT-9BT, attributed to a dominating *P*4*mm* symmetry, while minor *P*4*bm* and *R*3*c* fractions are present as well. This also holds true for NBT-12BT, which strongly resembles NBT-9BT in domain configuration and phase assemblage. The minor amounts of *P*4*bm* and *R*3*c* decline only gradually with increasing BT content. The results thus illustrate that a wide region of phase coexistence is present, comprising not only *R*3*c* and *P*4*bm*, but in fact all three phases (*R*3*c* + *P*4*bm* + *P*4*mm*).

As a solid solution of a relaxor and a ferroelectric, NBT-BT displays a transition between relaxor and ferroelectric properties, which also manifests in the composition-dependent change in domain configuration. The relaxor characteristics, such as a strong frequency dispersion of the temperature-dependent permittivity, a diffuse phase transition (T_m) and high permittivity values in general were observed in compositions close to the MPB [10, 153]. Enhanced piezoelectric properties, such as high d_{33} and k_p values [12, 152] are linked to the R and T phase coexistence, providing an enhanced polarizability due to an increase in equivalent polarization orientations with low energy barriers [33]. The relaxor characteristics in NBT-BT relate to the appearance of *P*4*bm*, its nanoscale structure and coexistence with *R*3*c* [148], which can be confirmed by the present TEM study. The observed absence of larger domains corresponds to the reported pseudocubic nature [184] of the NBT-6BT composition. A profound lamellar domain formation is usually accompanied by a notable non-cubic lattice distortion, which is absent in NBT-6BT. Instead, nanoscale regions (nanodomains, PNRs) are abundant. The thermal evolution of PNRs, comprising a dynamic and fluctuating nature at elevated temperatures, has been correlated to the frequency-dependent permittivity response [148, 157]. In contrast, lamellar ferroelectric domains correspond to a pronounced reduction in the frequency dependence [158]. The TEM results illustrate the short coherence length of *P*4*bm* nanodomains in NBT-6BT, opposed to lamellar long-range domains observed in NBT-12BT, relating to the relaxor-to-ferroelectric transition with increasing BT content.

NBT-3BT is assigned to a single-phase composition of *R*3*c* symmetry. Note that the occurrence of $\frac{1}{2}$ $\{ooo\}$ SRs is not necessarily a clear evidence for the $a^-a^-a^-$ (*R*3*c*) oxygen octahedral tilt system. Other anti-phase tilt systems, such as $a^-a^-c^-$ (*Cc*), produce the same type of superlattice reflections. The existence of a local monoclinic phase at the MPB, serving as a bridging link between R and T phases, was debated [121, 187]. However, several studies on pure NBT prefer an average monoclinic (*Cc*) over the rhombohedral (*R*3*c*) structure [168, 169]. This led to the establishment of a further MPB, separating *Cc* on the NBT-side from *R*3*c* with a coexisting region ranging from 3 to 4 mol % BT [163] (compare also with the phase diagram in Fig. 2.25(a) on page 26). The distinction between *Cc* and *R*3*c* can theoretically be made based on the occurrence of $\frac{1}{2}$ $\{ooo\}$ SRs in the $\langle 101 \rangle_{pc}$ zone axes. For a domain wall lying on $\{010\}_{pc}$, SRs are absent when the $\langle 111 \rangle_{pc}$ tilt axis of both adjacent domains is perpendicular to the $\langle 101 \rangle_{pc}$ viewing axis [100]. For *R*3*c*, this is the case for one of the two adjacent $\langle 101 \rangle_{pc}$ zone axes. For *Cc*, only one of the three possible $\{010\}_{pc}$ domain wall configurations fulfills the same requirement, resulting in a lower extinction probability for the SRs [163]. However, tilting to both $\langle 101 \rangle_{pc}$ axes in order to discern between both symmetries requires a tilting range of ± 45°, which a conventional TEM sample holder (as used in the present study) cannot provide. Ma et al. [163] observed different domain regions within single NBT-3.5BT grains and assigned them to *R*3*c* and *Cc*. In the present study, the NBT-3BT composition did not display such distinct regions. A continuous complex domain configuration is present throughout the

grains suggesting a single phase. High-resolution XRD studies on powder samples obtained from the same sample batch as used for the TEM characterization show that the NBT-3BT composition can be refined with the rhombohedral *R*3*c* phase and an only minor cubic phase fraction [266]. It is therefore concluded that the $\frac{1}{2}$ $\{ooo\}$ SRs are most plausibly assigned to *R*3*c* with its $a^-a^-a^-$ oxygen octahedral tilt system.

Short Summary

The domain structure and phase assemblage in unpoled NBT-BT ceramics strongly varies with the BT content. NBT-3BT exhibits a complex domain pattern and strong $\frac{1}{2}$ $\{ooo\}$ SRs ($a^-a^-a^-$ tilting), attributed to the *R*3*c* phase. In NBT-6BT, the major volume fraction is characterized by nanodomains of *P*4*bm* symmetry with $\frac{1}{2}$ $\{ooe\}$ SRs ($a^0a^0c^+$ tilting). The prevalence of the *P*4*bm* phase and wide absence of a ferroelectric domain contrast reflects in the relaxor behavior and pseudocubic average structure of the MPB composition. However, a minor volume fraction of *R*3*c* and *P*4*mm* domains occur. The phase coexistence spans over a large compositional range, while the SR intensity declines with increasing BT content. Both NBT-9BT and -12BT are predominantly characterized by a lamellar ferroelectric *P*4*mm* domain structure. In all ceramics, an amorphous secondary phase is present at multi-grain junctions. However, grain boundaries are largely non-wetted, suggesting no significant influence on the electrical properties.

4.2 Quenching-Induced Domain Structure and Phase Assemblage

4.2.1 Domains and Phase Mixture in Quenched NBT-3BT

Comparing NBT-3BT FC with its quenched (Q) counterpart reveals a striking change in the domain structure. All NBT-3BT Q grains exhibit lamellar domains, opposed to the irregular and complex domain configuration in the FC specimen (Fig. 4.12). The lamellar domains in NBT-3BT Q show a width of 10-40 nm and domain walls are located on $\{001\}_{pc}$ and $\{110\}_{pc}$ planes. Twin boundaries are present, along which the lamellar domain structure is mirrored (dashed lines in Fig. 4.12(b)). Along the twin boundary, domains on both sides are coherent.

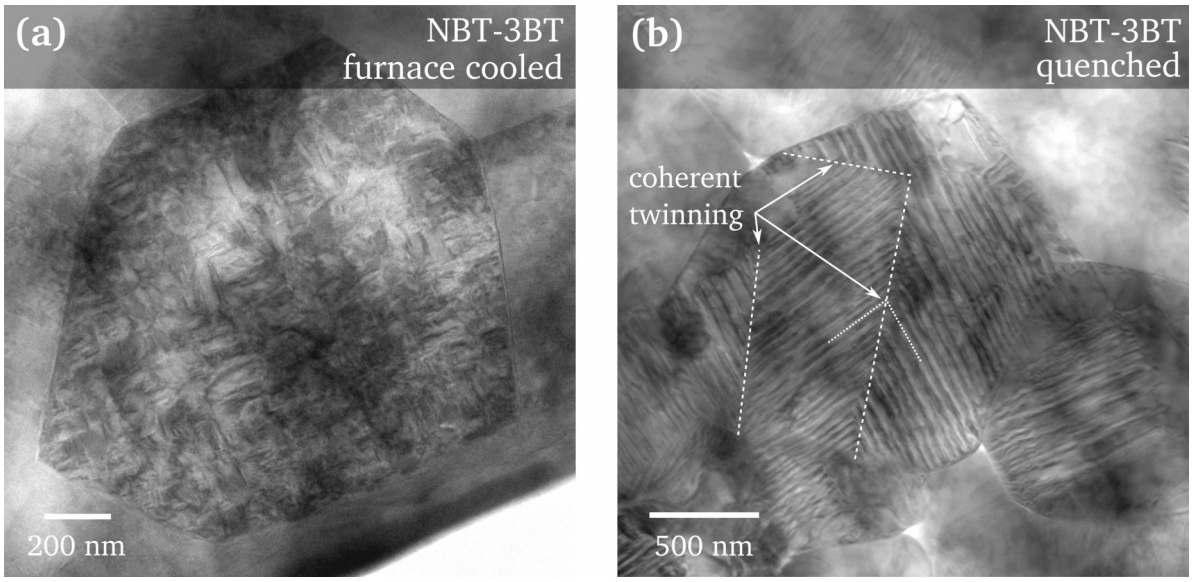

Figure 4.12: TEM-BF images comparing NBT-3BT FC and Q (both viewed along the $[1\bar{3}1]_{pc}$ zone axis). A complex domain structure is present in NBT-3BT FC (a), while the Q specimen exhibits a lamellar domain structure (b).

Furthermore, a change in the phase assemblage was observed. While $\frac{1}{2}$ $\{ooo\}$ SRs are present throughout NBT-3BT FC, they occur only in certain grain regions in NBT-3BT Q. Fig. 4.13(a) displays a grain in the Q specimen, where the corresponding SAED pattern (Fig. 4.13(b)) clearly shows $\frac{1}{2}$ $\{ooo\}$ SRs. However, forming a DF image from the $\frac{1}{2}$ (111) SR reveals that only the lower left grain section contributes to the SR formation (Fig. 4.13(c)). In the DF image, this section appears bright, while the rest of the grain remains dark. It can be concluded that only the bright area is of *R*3*c* symmetry and exhibits $a^-a^-a^-$ oxygen octahedral tilting. This grain section also differs in domain structure. Here, domains show a more irregular lamellar appearance, while the rest of the grain exhibits very straight lamellar domains with a herringbone-type configuration (Fig. 4.13(d)).

Within the herringbone structure, no superlattice reflections occur (Fig. 4.14(a)), therefore, no oxygen octahedral tilting is present. Since NBT-3BT Q is of rhombohedral symmetry, as evidenced by X-ray structural analyses [266, 267], *R*3*m* can be deduced as the space group of the herringbone-type domains. *R*3*m* is a well know rhombohedral ferroelectric phase of perovskite structures, where oxygen octahedral tilting is in fact absent [102, 268]. The presence of $\{001\}_{pc}$ and $\{110\}_{pc}$ domain walls within the herringbone structure supports this presumption, since both planes are permissible domain walls in a rhombohedral ferroelectric phase.

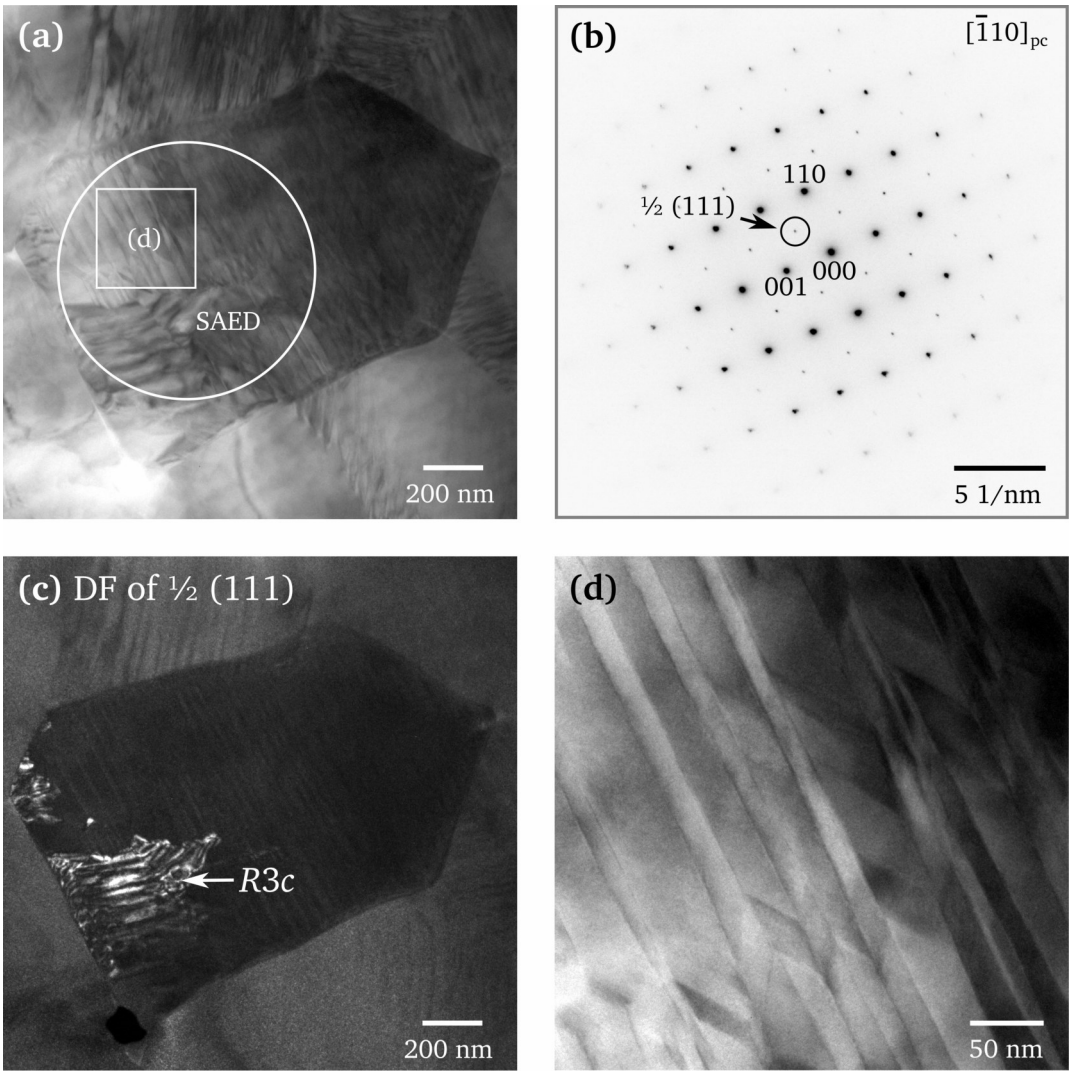

Figure 4.13: TEM micrographs of NBT-3BT Q. (a) BF image of a grain viewed along $[\bar{1}10]_{pc}$. The position of the SAED aperture is indicated and the SAED pattern is displayed in (b). The encircled $\frac{1}{2}$ (111) SR was used to obtain the DF image in (c), where only the lower left grain section appears bright and is of *R*3*c* symmetry. The rest of the grain depicts a herringbone-type domain configuration as illustrated in (d) with *R*3*m* symmetry.

Viewed along the $[\bar{1}10]_{pc}$ zone axis, the long lamellar domain walls in the herringbone pattern appear edge-on and lie on $(001)_{pc}$ planes (Fig. 4.14(a)). Short domain walls of up to 50 nm in length coherently cross the $(001)_{pc}$ domain walls in a zigzag-pattern. These $\{110\}_{pc}$ domain walls appear as broader lines, since they are inclined towards the viewing direction. When considering the distinct $\{110\}_{pc}$ planes, on which these domain walls are located, two variants are possible. The domain walls can either lie on $(0\bar{1}1)_{pc}$ and $(011)_{pc}$ or on $(\bar{1}01)_{pc}$ and $(101)_{pc}$ planes. The two possible variants are schematically illustrated in Fig. 4.14(b) for the $(0\bar{1}1)_{pc}$ / $(011)_{pc}$ and in Fig. 4.14(c) for the $(\bar{1}01)_{pc}$ / $(101)_{pc}$ pair of planes. The respective left schematic illustrates the orientation of the pair of planes (green and blue) and the $(001)_{pc}$ plane (red) within the unit cell. The schematic in the middle shows the same configuration, only with the $(\bar{1}10)_{pc}$ viewing plane as solid grey plane, thus indicating the intersection lines of the plane pairs with the viewing plane. Both domain wall plane pairs form an angle of 90° towards each other, which is centrally

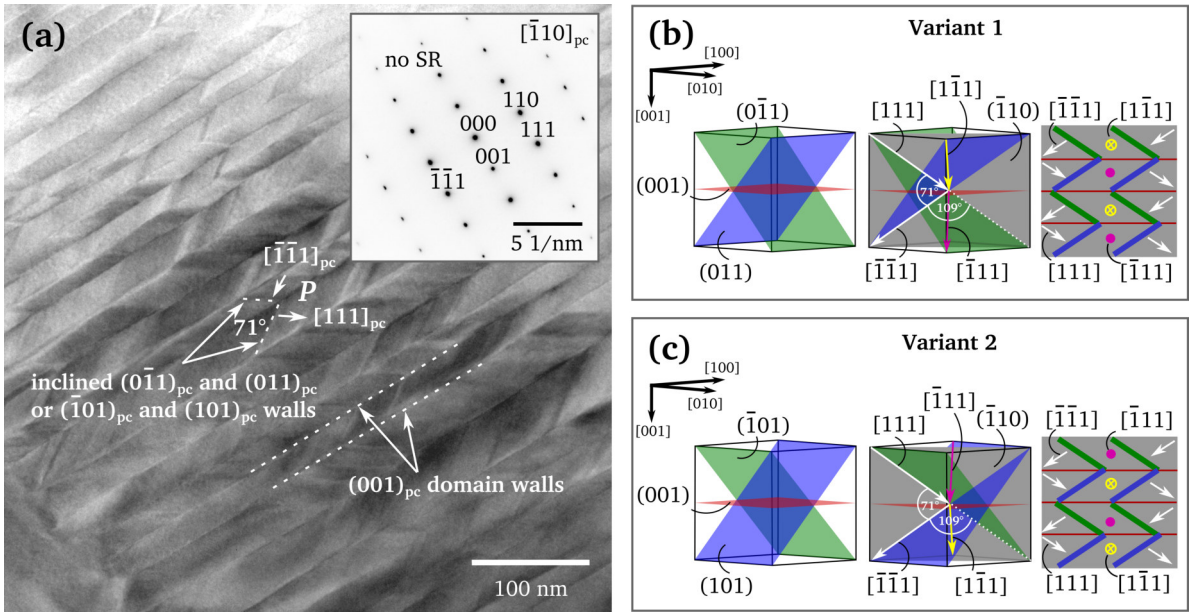

Figure 4.14: (a) TEM-BF image of the herringbone structure in NBT-3BT Q. Domain walls are indicated as dashed lines and the polarization (P) with arrows. The corresponding $[\bar{1}10]_{pc}$ SAED pattern, where $\frac{1}{2}$ $\{ooo\}$ SRs are absent, is depicted in the inset. (b) and (c) illustrate unit cell schematics of the two possible $\{110\}_{pc}$ domain wall orientations and polarization directions. (b) In the left schematic, the $(0\bar{1}1)$ / (011) plane pair is given in green and blue and the (001) plane in red. In the middle schematic, the $(\bar{1}10)$ viewing plane (gray), the [111] and $[\bar{1}\bar{1}1]$ polarization directions (white arrows), the $[\bar{1}11]$ (pink arrow) and $[1\bar{1}1]$ (yellow arrow) polarization directions are shown. The schematic on the right illustrates the polarization in the domains of the herringbone pattern. Domain walls are shown as lines and polarization directions as arrows in the respective color (• for pointing out of the viewing plane and ⊗ for pointing into the viewing plane). The same description as for (b) applies for the $(\bar{1}01)$ / (101) plane pair in (c).

intercepted by the $(001)_{pc}$ plane. However, due to being tilted to the $[\bar{1}10]_{pc}$ viewing direction, this angle appears as 71° in the image plane (indicated in the schematic and also measurable in the TEM image in (a)).

For a rhombohedral ferroelectric, Schierholz [79] illustrated that 109° walls lie on $\{001\}_{pc}$ planes and 71° walls on $\{110\}_{pc}$ planes (compare Fig. 2.12 on page 13). The present configuration agrees with this description. The polarization vector in the rhombohedral phase is oriented along the threefold $\langle 111\rangle_{pc}$ axis. Two distinct directions lie in the viewing plane in Fig. 4.14: $[111]_{pc}$ and $[\bar{1}\bar{1}1]_{pc}$. These two polarization directions are indicated by the white arrows in the TEM image and the schematics (Figs. 4.14(a)-(c)) and correspond with the 109° configuration illustrated in Fig. 2.12(a). The $(001)_{pc}$ planes, over which the two polarization directions are correlated, thus represent the 109° domain walls. Consequently, the $\{110\}_{pc}$ planes are the 71° domain walls. For variant 1 (Fig. 4.14(b)), the $[111]_{pc}$ polarization direction correlates with the $[\bar{1}11]_{pc}$ polarization direction (pink arrow) over the $(011)_{pc}$ plane (blue). The $[\bar{1}\bar{1}1]_{pc}$ polarization direction correlates with the $[1\bar{1}1]_{pc}$ polarization direction (yellow arrow) over the $(0\bar{1}1)_{pc}$ plane (green). The domain walls and polarization directions in the herringbone pattern are illustrated in the schematic on the very right with the respective color (Fig. 4.14(b)). Note that the $[1\bar{1}1]_{pc}$ polarization direction (yellow arrow) points into the viewing plane (marked with ⊗), while the $[\bar{1}11]_{pc}$ direction (pink arrow) points out of the viewing plane (marked with •). For variant 2 in Fig. 4.14(c), the correlation is reversed: $[111]_{pc}$ correlates with $[1\bar{1}1]_{pc}$ (yellow arrow) over the $(101)_{pc}$ plane (blue), while $[\bar{1}\bar{1}1]_{pc}$ correlates with $[\bar{1}11]_{pc}$ (pink arrow) over the $(\bar{1}01)_{pc}$ plane (green). The above considerations

show that the herringbone-type domain pattern can be nicely explained by the allowed domain wall orientations and polarization directions in a rhombohedral ferroelectric phase. Since a direct symmetry assignment in TEM is complicated by the pseudocubic nature of the SAED patterns, identifying the specific locations of the domain walls affirms the allocation of the herringbone structure to the rhombohedral *R*3*m* symmetry.

4.2.2 Lamellar Domain Contrast in Quenched NBT-6BT

Similar to the NBT-3BT Q specimen, an increased lamellar domain contrast is visible in NBT-6BT Q. Compared to the widely homogeneous contrast in NBT-6BT FC (Fig. 4.15(a)) with only very few lamellar domains, NBT-6BT Q displays a pronounced increase in lamellar domains upon quenching (Fig. 4.15(b)). A wide variety in the domain width is present, ranging from 50 nm in large lamellae, down to very fine domain structures. Nanometer-sized domains and domain walls lying on $\{101\}_{pc}$ planes have been observed.

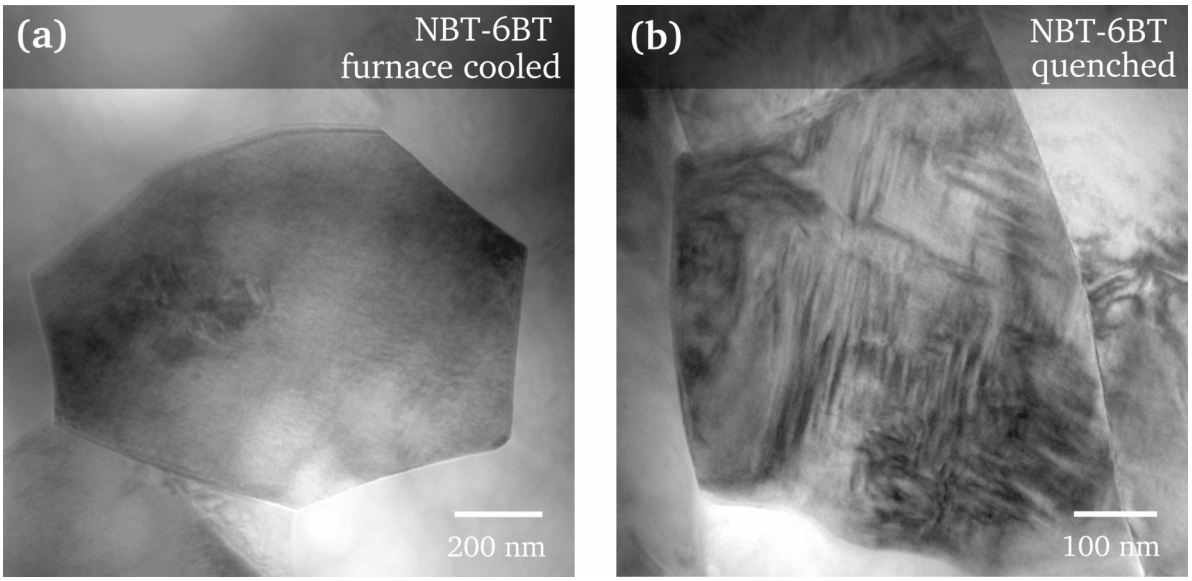

Figure 4.15: TEM-BF images comparing NBT-6BT FC and Q. (a) A grain with homogeneous contrast in NBT-6BT FC. (b) A grain with enhanced lamellar domain contrast in NBT-6BT Q. Both grains are viewed along the $[110]_{pc}$ direction.

Since both rhombohedral and tetragonal phases are present in NBT-6BT FC, the question arises, whether the increased domain contrast upon quenching can be assigned to an increase in rhombohedral or tetragonal domains. Inspecting a grain along the $[1\bar{2}1]_{pc}$ zone axis reveals strong $\frac{1}{2}\{ooo\}$ SRs alongside weaker $\frac{1}{2}\{ooe\}$ SRs, indicating both *R*3*c* and *P*4*bm* (Fig. 4.16(a)). A DF image formed with the $\frac{1}{2}(1\bar{1}\bar{3})$ SR illustrates that the *R*3*c* phase accounts for the majority of the lamellar domains (Fig. 4.16(b)). Tetragonal areas can be surrounded by *R*3*c*, indicated by the dark irregular patches in the DF image. The lamellar *R*3*c* domains show a slightly irregular appearance and therefore differ from the very uniformly arranged domain structure of the *R*3*m* phase in NBT-3BT Q. Furthermore, no herringbone-type domain configuration was observed in the *R*3*c* phase. Compared to the FC specimen, where the *R*3*c* phase only occurs in smaller grain regions, it can be concluded that its volume fraction is significantly increased by the quenching process.

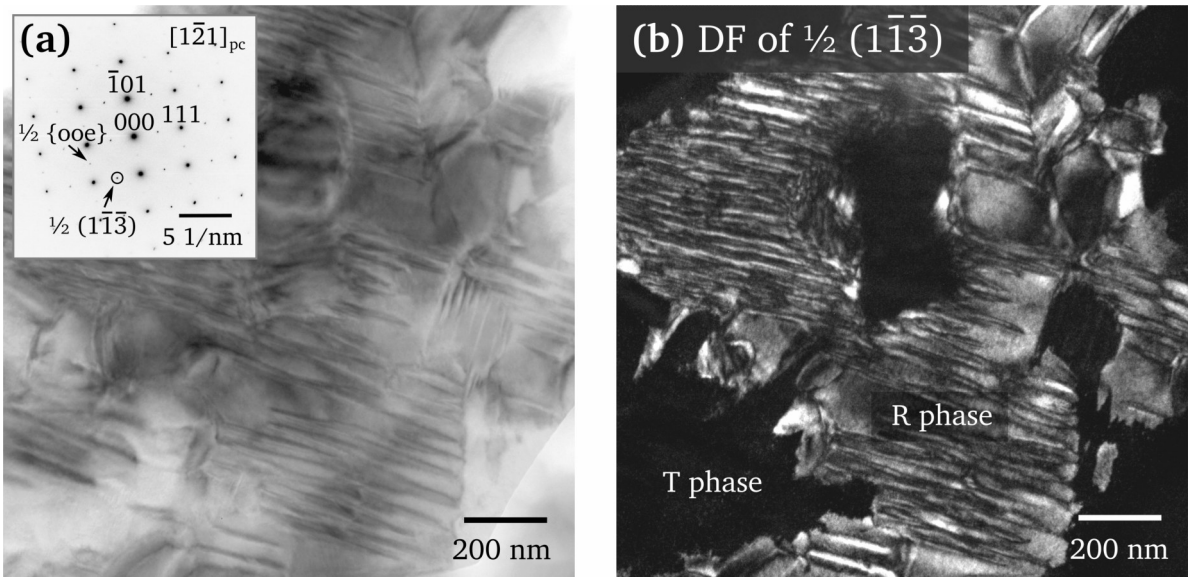

Figure 4.16: (a) TEM-BF image of a grain with strong lamellar domain contrast viewed along $[1\bar{2}1]_{pc}$. Both types of SRs appear in the SAED pattern (inset). (b) DF image formed with the encircled $\frac{1}{2}$ $(1\bar{1}\bar{3})$ SR showing a large volume fraction of the *R*3*c* phase.

The lamellar domains in NBT-6BT Q, however, are not solely attributed to *R*3*c*, but can also be assigned to the presence of tetragonal domains, as illustrated in Fig. 4.17. The BF image shows a strong domain contrast and both types of SRs occur in the corresponding $[112]_{pc}$ SAED pattern (Figs. 4.17(a) and (b)). The DF image in Fig. 4.17(c) illustrates the location of the *R*3*c* phase in two separated grain regions, showing a lamellar domain morphology. However, the grain section which remains dark also clearly exhibits lamellar domains of another orientation, as visible in the BF image in (a). The DF image using a $\frac{1}{2}$ $\{ooe\}$ SR shows that *P*4*bm* nanodomains are dispersed among those domains (Fig. 4.17(d)). It can be concluded that long-range lamellar domains of tetragonal *P*4*mm* symmetry are present, which coexist with nanoscale regions of *P*4*bm* symmetry. The T phase is thus composed of both *P*4*mm* and *P*4*bm* structures. Conclusively, the increased lamellar domain contrast in NBT-6BT upon quenching can be assigned to both *R*3*c* and *P*4*mm* domains.

In addition to the conventionally air-quenched sample, a water-quenched NBT-6BT specimen was also analyzed by TEM. It revealed a comparable significant increase in lamellar domain contrast (see Fig. A.1 in Appendix on page 145). However, the high cooling rates of water-quenching result in fracturing of the ceramic pellets, rendering the procedure unfavorable from an application point of view. Furthermore, in order to examine whether there is a gradient in domain structure within the ceramic pellet, NBT-6BT FC and Q specimens were additionally prepared from the near-surface area of the sintered ceramic. Conventionally, TEM specimens were obtained from the central area of the ceramic pellets by grinding the ceramic discs from both sides. Both near-surface samples show the same characteristics as the conventionally obtained TEM specimens (see Fig. A.2 in Appendix on page 145). Hence, it appears insignificant from which area of the pellet the TEM specimen is produced. Moreover, omitting the annealing step at 400 °C after grinding and polishing did not reveal any observable deviation from the above described domain structure and phase assemblage of a conventionally prepared NBT-6BT Q sample (see Fig. A.3 in Appendix on page 146). This conclusion is relevant with regard to the poled specimens, where the annealing step had to be omitted, in order to avoid annealing of the poling-induced domain structure.

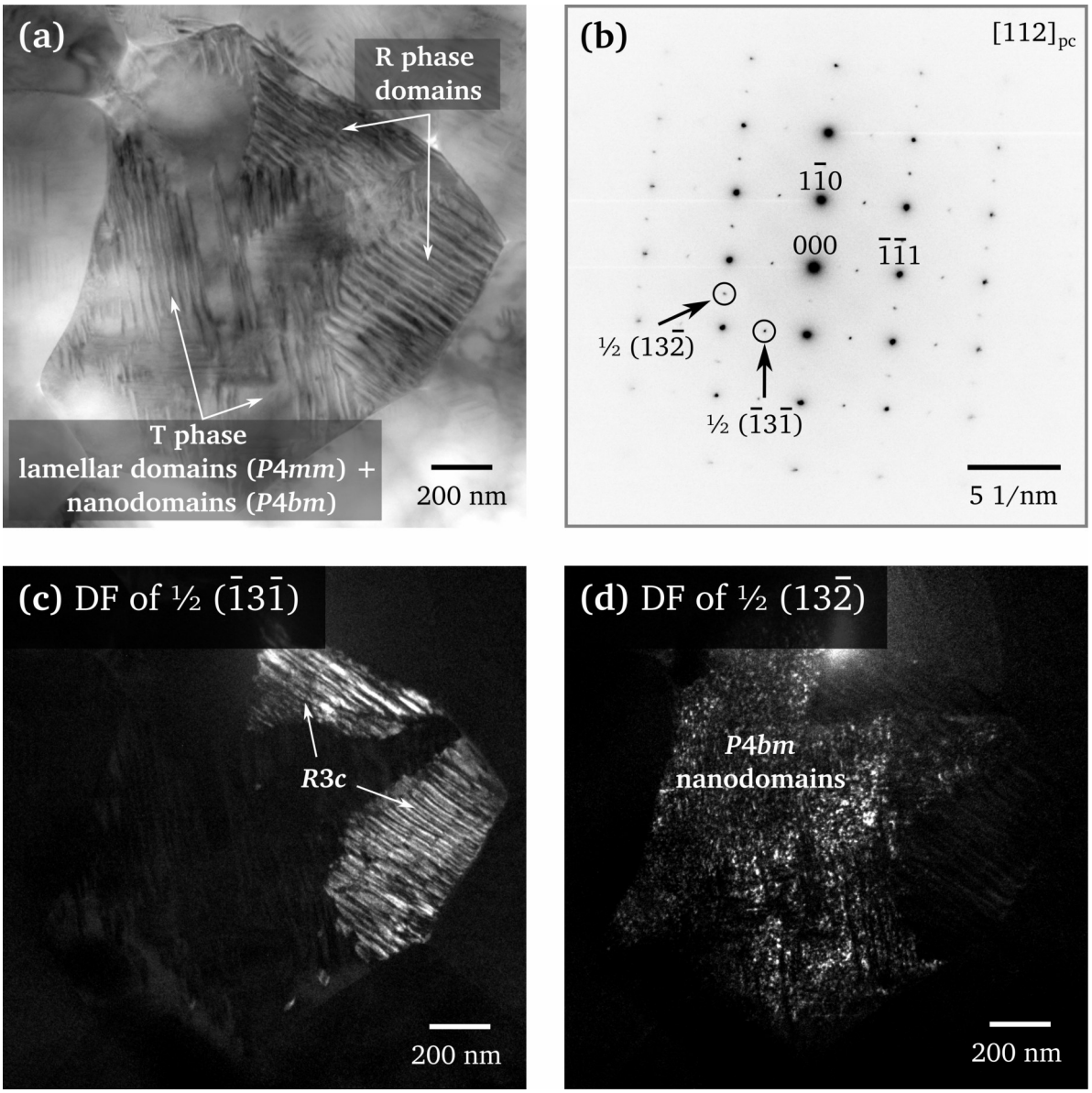

Figure 4.17: (a) TEM-BF image of a grain in NBT-6BT Q showing R and T lamellar domains. (b) Corresponding SAED pattern of the $[112]_{pc}$ zone axis where $\frac{1}{2}$ {*ooo*} and $\frac{1}{2}$ {*ooe*} SRs are visible. (c) DF image of the encircled $\frac{1}{2}$ ($\bar{1}3\bar{1}$) SR showing the *R*3*c* domains. (d) DF image of the encircled $\frac{1}{2}$ ($13\bar{2}$) SR showing the *P*4*bm* nanodomains, which coexist with *P*4*mm* lamellar domains.

4.2.3 Quenching of BT-Rich Compositions

Comparing FC and Q specimens of the NBT-9BT composition does not reveal any distinct difference in the domain structure or phase assemblage. Lamellar domains assigned to *P*4*mm* dominate this composition (Fig. 4.18(a) and (b)). Smaller regions where domains are absent and $\frac{1}{2}$ {*ooe*} SRs occur indicate the presence of *P*4*bm*. Small volume fractions of the *R*3*c* phase can still be found in some grains in NBT-9BT Q as well, as it is the case in the FC specimen (compare Fig. 4.6(c)). It can be concluded that quenching the NBT-9BT composition does not result in any significant change of the local structure observable via TEM. In contrast, a transition from a relaxor to a

ferroelectric-like behavior was observed for the temperature-dependent permittivity response upon quenching (compare Fig. 4.32 on page 86 and according discussion).

Likewise, no differences could be identified in terms of domain structure and phase assemblage in NBT-12BT when comparing FC and Q specimens (Fig. 4.18(c) and (d)). Both display a pronounced formation of tetragonal lamellar domains lying on $\{101\}_{pc}$ planes. Weak $\frac{1}{2}$ $\{ooe\}$ and occasionally weak $\frac{1}{2}$ $\{ooo\}$ SRs are present in NBT-12BT Q, indicating a minor fraction of *P4bm* and *R3c*. Small *R3c* regions are observable in some grains as indicated in the inset of Fig. 4.18(d). From the TEM perspective, quenching does not affect the existing phase assemblage. Additional information can be gained from large scale analyses (such as XRD), which give complementary information about quenching-induced changes in the average phase fractions.

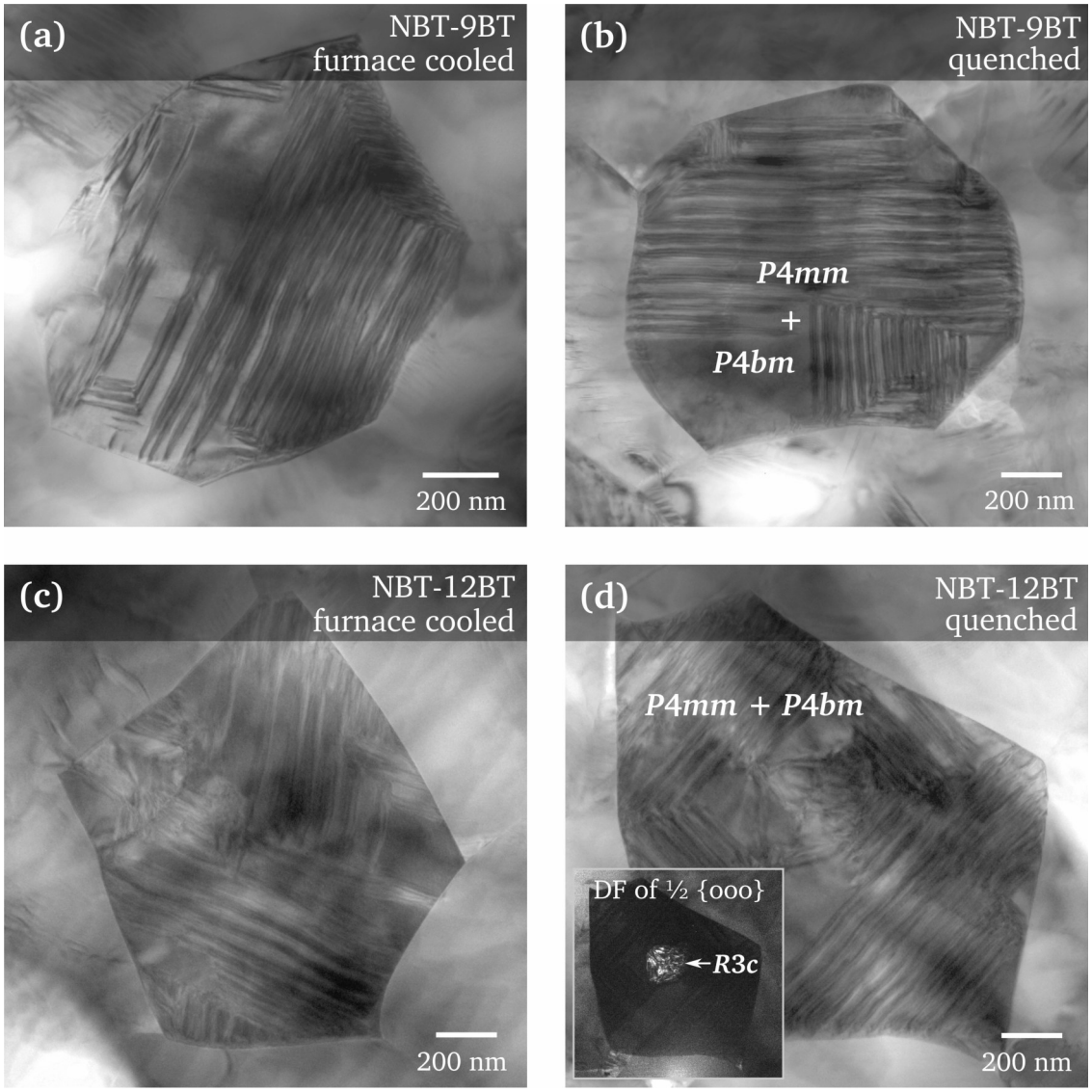

Figure 4.18: BF images of NBT-9BT FC (a) and Q (b), showing a comparable domain contrast. Both grains are viewed along the $[120]_{pc}$ zone axis. NBT-12BT FC (c) and Q (d) also show comparable lamellar domain configurations. Both grains are depicted from the $[110]_{pc}$ zone axis. The inset in (d) shows a corresponding DF image of a residual *R3c* phase obtained employing a $\frac{1}{2}$ $\{ooo\}$ SR.

4.2.4 Tilt Series of Tetragonal Domains

The tetragonal compositions with its abundant lamellar domains can be used to demonstrate a tilt series in the TEM (Fig. 4.19). In general, the observable diffraction contrast of 90° domains is highly influenced by the orientation of the grain with respect to the viewing direction. An enhanced domain contrast arises when the domain walls are tilted against the viewing direction, as it is the case in Fig. 4.19(a). Here, the grain is aligned along the $[\bar{1}20]_{pc}$ zone axis (Fig. 4.19(b)). Fringes running parallel to the domain walls become visible (magnified in the inset in Fig. 4.19(a)). The fringes arise from the oscillating intensity of the direct and diffracted beam when propagating along the domain wall (compare section 3.2.2, Howie-Whelan equation, Eq. 3.11, and Fig. 3.7 on page 42). Both domains on each side of the inclined domain wall can be regarded as complementary wedges. Each wedge (domain) produces a set of fringes and the observable fringe pattern results from the superimposition of the fringes arising from both domain areas [269].

When tilting the grain to the $[010]_{pc}$ zone axis, the 90° domain walls are viewed edge-on (Fig. 4.19(c)). The domain walls become narrow lines and an alternating bright and dark contrast is visible resulting in a stripe-like pattern, where one set of domains appears brighter than the other. These variations originate from the two alternating unit cell orientations within the 90° domains. Both domain orientations have slightly different diffraction conditions and a varying excitation error, s (also compare section 3.2.2). From the SAED pattern, it can be inferred that the edge-on 90° domain walls lie on $(\bar{1}01)_{pc}$ and $(101)_{pc}$ planes. Reflection splitting along the $[101]_{pc}$ direction is visible (Fig. 4.19(d)). The splitting is more pronounced in rows further away from the center of the diffraction pattern (as magnified in the inset). It arises from the slightly rotated tetragonal unit cells of the two domain orientations, creating two overlapping diffraction patterns (compare Fig. 3.8 on page 43). The angle (Θ) between two split diffraction spots amounts to 1.9°. This implies that there is a true angle of 88.1° between the $[001]_T$ directions of two adjacent 90° domains. Furthermore, it should be noted that the intensity of the $\frac{1}{2}$ $\{ooe\}$ SRs is stronger in the SAED pattern of the high-symmetry $[010]_{pc}$ zone axis compared to their weak intensity in the low-indexed zone axes in (b) and (f).

In certain areas of the grain, the stripe-like bright and dark domain contrast is reversed along a boundary crossing the lamellar domains in a zigzag-manner (inset in Fig. 4.19(c)). These boundaries are 180° domain walls. Interestingly, they also become visible in BF imaging when viewed along the $[\bar{1}3\bar{1}]_{pc}$ zone axis (Fig. 4.19(e) and (f)). The zigzag-shaped 180° domain walls marked with arrows in the inset of Fig. 4.19(e) are most likely located on alternating $(001)_{pc}$ and $(100)_{pc}$ planes. 180° domain walls often occur as wavy watermarks, but can also be located on $\{001\}_{pc}$ planes in the tetragonal phase (see section 2.2.2). Usually, 180° domain walls can not be observed in BF imaging. However, due to a breaking of Friedel's law ($I_{hkl} = I_{\overline{hkl}}$) for the diffracted beams, it can be possible to observe a weak fringe contrast in TEM-BF, when not only the direct beam but also diffracted beams are involved in the image forming process. Furthermore, the contrast of the $(\bar{1}01)_{pc}$ 90° domain walls has almost completely vanished, while the contrast of the $(101)_{pc}$ 90° walls becomes very strong (Fig. 4.19(e)). This can be explained by their respective orientation towards the viewing direction, which is edge-on for the $(\bar{1}01)_{pc}$ planes, while the $(101)_{pc}$ planes are strongly inclined towards the viewing plane.

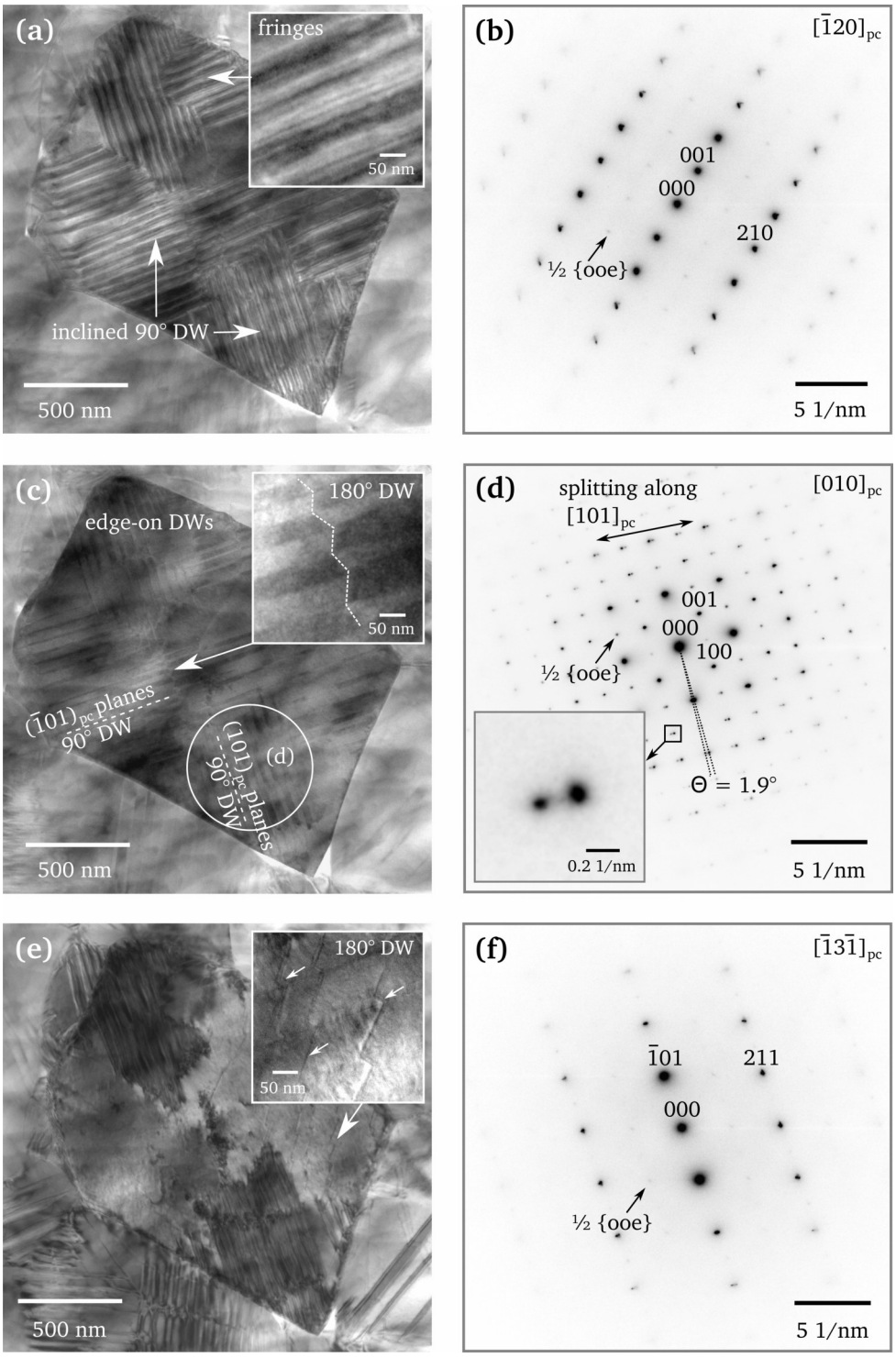

Figure 4.19: TEM micrographs and SAED patterns of a grain in NBT-9BT Q viewed from different zone axes. (a) BF image where fringes (see also the inset) appear along the inclined 90° domain walls (DW). (b) Corresponding $[\bar{1}20]_{pc}$ SAED pattern. (c) The grain viewed from the $[010]_{pc}$ direction, where the 90° domain walls on $(\bar{1}01)_{pc}$ and $(101)_{pc}$ planes (dashed lines) appear edge-on. Their alternating bright and dark contrast and a zigzag 180° domain wall is magnified in the inset. (d) Reflection splitting is visible in the corresponding SAED pattern. The location of the SAED aperture is marked in (c). (e) The grain viewed along $[\bar{1}3\bar{1}]_{pc}$, where inclined 180° domain walls become visible (inset, marked with arrows) and corresponding SAED pattern in (f). Note the pronounced contrast change of the $\frac{1}{2}$ $\{ooe\}$ SRs with respective orientation of the SAED pattern.

4.2.5 Polarization Orientation in Tetragonal Domains

Determining the polarization direction in ferroelectric domains is crucial for understanding the overall domain configuration. Fig. 4.20(a) depicts lamellar needle-shaped 90° domains in NBT-12BT Q, viewed edge-on along the $[010]_{pc}$ zone axis. Splitting of reflections in the corresponding FFT (Fig. 4.20(c)) indicates the rotation of the $[001]_T$ *c* axis when crossing the 90° domain walls. From the reflection splitting it can also be deduced that the polarization vectors lie within the image plane (90° a-a domains, compare also Fig. 2.11 on page 13).

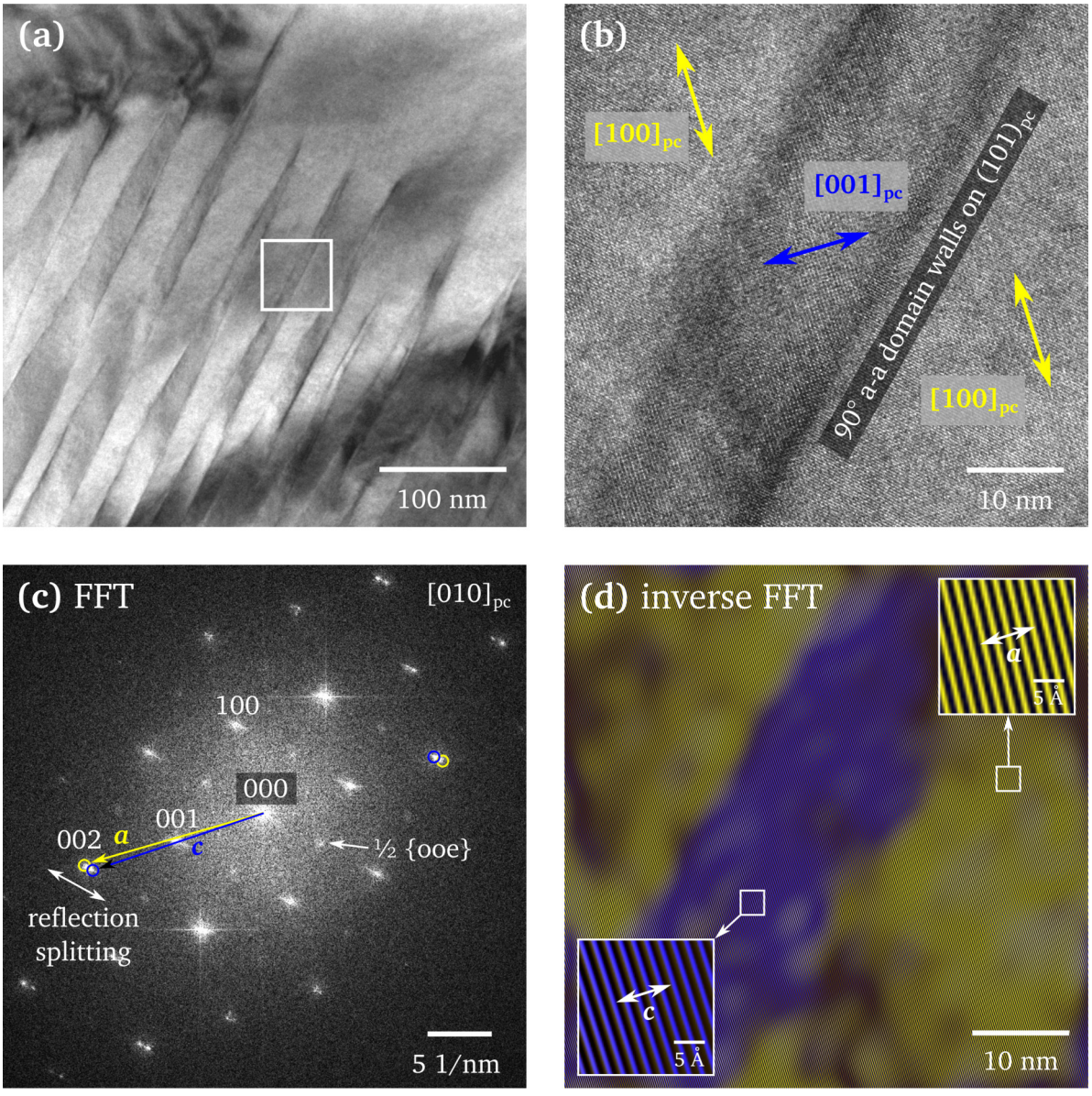

Figure 4.20: (a) TEM-BF image of tetragonal domains in NBT-12BT Q. The inset in (a) is magnified in the HRTEM image in (b). The polarization direction is noted with arrows. (c) Corresponding FFT image, where the split 002 reflection is masked as indicated by the yellow and blue circles. The superimposed inverse FFTs of both masked reflections is depicted in (d). The magnified insets show lattice fringes which are perpendicular to the *c* and *a* axis in the blue and yellow area, respectively.

The approach reported by Moore et al. [270] is followed here, in order to determine the polar axes in the tetragonal domains. A HRTEM image over several domains is recorded (Fig. 4.20(b)) and the FFT is formed (Fig. 4.20(c)). Splitting of diffraction spots along $[101]_{pc}$ direction becomes visible. Regarding the 001 split reflections, the one which is closer to the 000 center of the diffraction pattern corresponds to the *c* axis (smaller reciprocal distance = larger lattice constant). This split reflection is then masked and an inverse FFT is formed. Since the splitting can be better identified the further away from the center of the FFT, here the 002 reflection was masked instead of 001 (Fig. 4.20(c), blue circle). The split reflection further away from 000 corresponds to the *a* axis (yellow circle), which is masked as well. Both inverse FFTs can then be superimposed in one image, depicted in Fig. 4.20(d). The blue area (corresponding to the *c* axis) covers the lamellar domain in the middle of the HRTEM image. The *c* axis is oriented perpendicular to the lattice fringes present in the inverse FFT image (see the inset of the blue area in Fig. 4.20(d)). The polarization axis of the blue domain is thus the $[001]_{pc}$ direction. The *a* axis, oriented along the same pseudocubic direction, corresponds with both domains on the left and right side (yellow in Fig. 4.20(d)). The *c* axis in the yellow domains is thus perpendicular to $[001]_{pc}$ and oriented along $[100]_{pc}$. Both polarization directions are illustrated by the yellow and blue arrows in Fig. 4.20(b). Whether the polar vectors point along $[100]_{pc}$ and $[001]_{pc}$, or are reversed by 180° pointing along $[\bar{1}00]_{pc}$ and $[00\bar{1}]_{pc}$, cannot be specified here. However, their correlation in an alternating head-to-tail configuration across the 90° a-a domain walls is identified.

4.2.6 Domain Configuration Analyzed by PFM

PFM analysis constitutes a further method, which provides information about the ferroelectric polarization. Fig. 4.21 depicts a scanned area in the tetragonal NBT-9BT FC specimen. The images of the vertical and lateral amplitude (Figs. 4.21(a) and (b)) illustrate the lamellar domain pattern. High and low amplitude values relate to the alternating out-of-plane (or in-plane) displacement of the sample surface due to the alternating polarization orientation within the domains. The lamellae exhibit widths of 20-45 nm, which is in accordance with the TEM observations. Apart from the 90° domains, 180° domain walls become visible by PFM, providing additional information about the overall domain structure. Two different configurations for the 180° domain walls exist. On the one hand, they appear as wavy irregular watermarks, where they do not follow any specific crystallographic direction (marked with arrows in Fig. 4.21(a)). On the other hand, they appear as zigzag lines crossing the 90° domains (illustrated in the inset in Fig. 4.21(a)). The second arrangement is equivalent to the TEM observations in Fig. 4.19(e), where the zigzag domain walls lie on $\{001\}_{pc}$ planes. The considerable abundance of 180° domain walls is also illustrated in the corresponding vertical and lateral phase (φ) images (Figs. 4.21(c) and (d)). The vertical (out-of-plane) phase illustrates components of the polarization vectors pointing in and out of the viewing plane, while the lateral (in-plane) phase is especially sensitive to the polarization directions normal to the length of the cantilever needle (the needle is oriented horizontally and scans the image from left to right). In Fig. 4.21(c), where φ is close to 0° (blue color), the polarization vector points downwards (positive c-domains), while it points upwards for φ close to 180° (orange color). An exemplary line profile (red line in Figs. 4.21(c) and (d)) is drawn over several domains and illustrates the vertical and later phase in this specific area. While no change in vertical polarization direction is visible in the line profile in (c), an in-plane alternating polarization direction is present in (d), resulting in a stripe pattern of 180° domains.

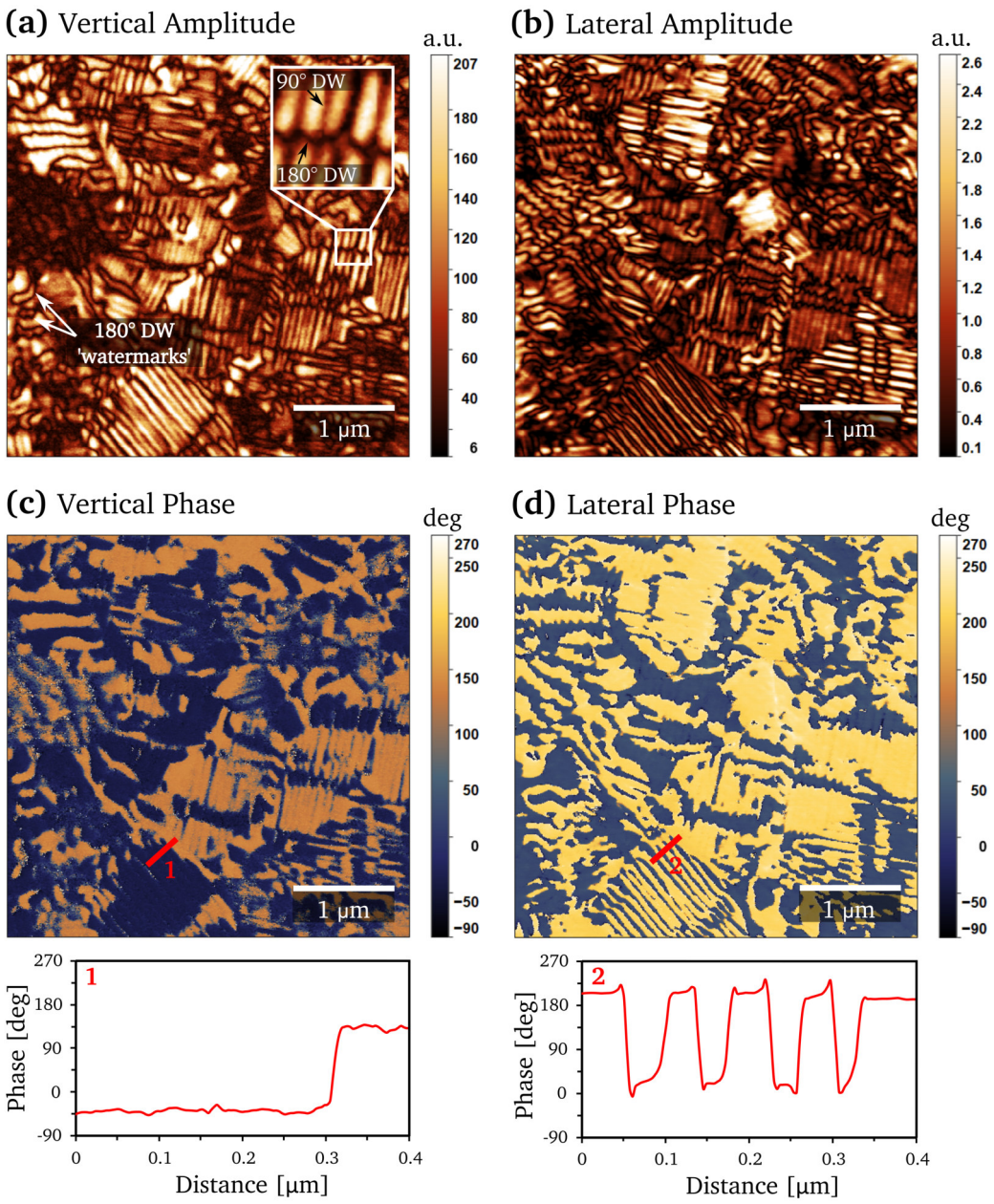

Figure 4.21: PFM analysis of domains in NBT-9BT FC. (a) Vertical amplitude image showing lamellar 90° domain walls (DW), as well as 180° watermarks and zigzag domain walls (inset). (b) Corresponding lateral amplitude image. (c) Vertical phase image and line profile (1) over several domains marked in red. (d) Lateral phase image and corresponding line profile (2).

The domain pattern visualized by PFM in all NBT-BT FC and Q specimens is comparatively illustrated in Fig. 4.22. The information gained from the lateral amplitude is chosen here for comparison. The detailed and largely irregular domain structure of NBT-3BT FC (Fig. 4.22(a)) stands in clear contrast to the lamellar domain formation in NBT-3BT Q (Fig. 4.22(b)). The domain width in the quenched composition shows a large variety, ranging from 20 to 70 nm. The herringbone configuration was not observed via PFM. The NBT-6BT FC specimen shows an indistinct grainy signal and only very few lamellar domains (Fig. 4.22(c)). The grainy morphology can be interpreted as a characteristic of the nanoscale structure. Imaging of structures which are only few nanometers

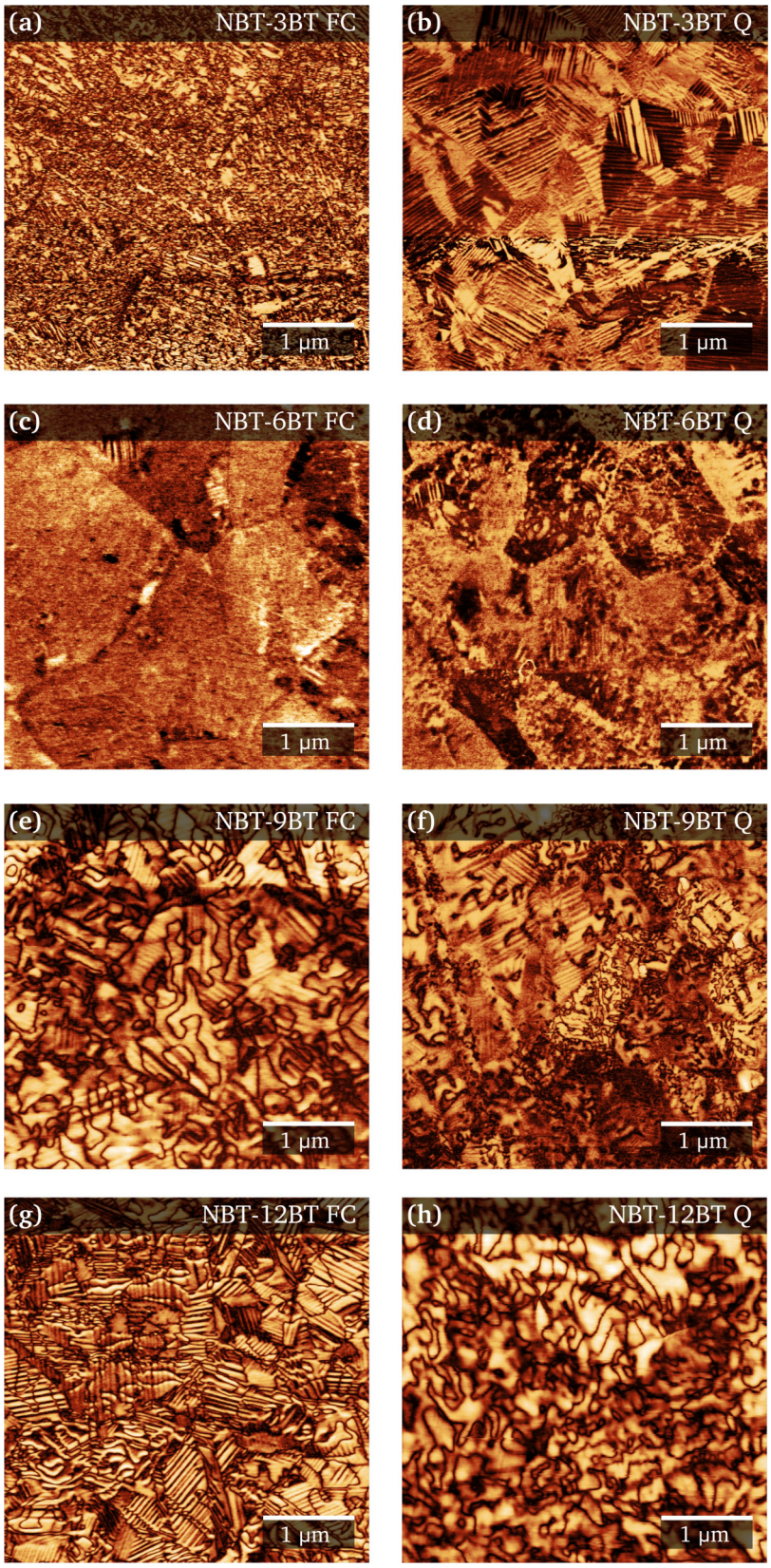

Figure 4.22: Comparative PFM images (lateral amplitude) of the NBT-BT FC and Q specimens. (a) NBT-3BT FC, (b) NBT-3BT Q, (c) NBT-6BT FC, (d) NBT-6BT Q, (e) NBT-9BT FC, (f) NBT-9BT Q, (g) NBT-12BT FC and (h) NBT-12BT Q.

in size is difficult, since the lateral resolution in PFM is limited by the contact area of the cantilever tip and sample surface, which depends on the apex curvature radius of the tip [271] (25 nm for the tip used in the present analyses). However, other factors such as the dielectric properties also highly influence the resolution, which is 20-50 nm for most ferroelectrics, but, e.g., 100-300 nm for $LiNbO_3$ [261]. In PFM dual AC resonance tracking mode, Liu et al. [131] were able to image structures of 50 nm in size in a relaxor ferroelectric, which were interpreted as PNR signatures.

The NBT-6BT Q specimen shows a similar irregular appearance as the FC sample with a slightly increased fraction of lamellar domains (Fig. 4.22(d)). Both FC and Q specimens of NBT-9BT and -12BT are characterized by the abundant appearance of lamellar 90° and wavy 180° domains. Analogous to the TEM observations, no significant differences were observed between FC and Q samples. Lamellar domains in Fig. 4.22(h) are hardly visible, which is not due to their absence, but rather to unfavorable imaging conditions reducing the resolution and image sharpness.

Overall, PFM analysis allows a large-scale imaging of the domain patterns in NBT-BT and complements the findings obtained by TEM. While 180° domain walls are rarely observed in TEM, the PFM analysis supplements the characterization of the domain configuration and illustrates that watermarks are in fact highly abundant in the NBT-9BT and -12BT compositions. Furthermore, PFM allows a direct determination of polarization directions within the domains (compare Fig. 4.21), while indirect methods (as illustrated in Fig. 4.20) and symmetry considerations have to be applied in TEM.

4.2.7 Structure of Poled MPB Compositions

Upon poling, the NBT-6BT composition is transformed from a relaxor to a ferroelectric, which reflects in an enhanced lamellar domain contrast. Compared to the unpoled FC state, where large domains are rather scarce, the poled FC specimen is occupied by ferroelectric lamellar domains (Fig. 4.23(a)). Domain widths are large and up to 100 nm in size. Rhombohedral *R*3*c* regions feature an indistinct irregular domain contrast (Fig. 4.23(b)). Grains which are entirely characterized by such an irregular contrast have been observed as well. Here, the $\frac{1}{2}$ $\{ooo\}$ SRs show an increased intensity and the $\frac{1}{2}$ $\{ooe\}$ SRs are missing, which indicates a predominately rhombohedral symmetry. In

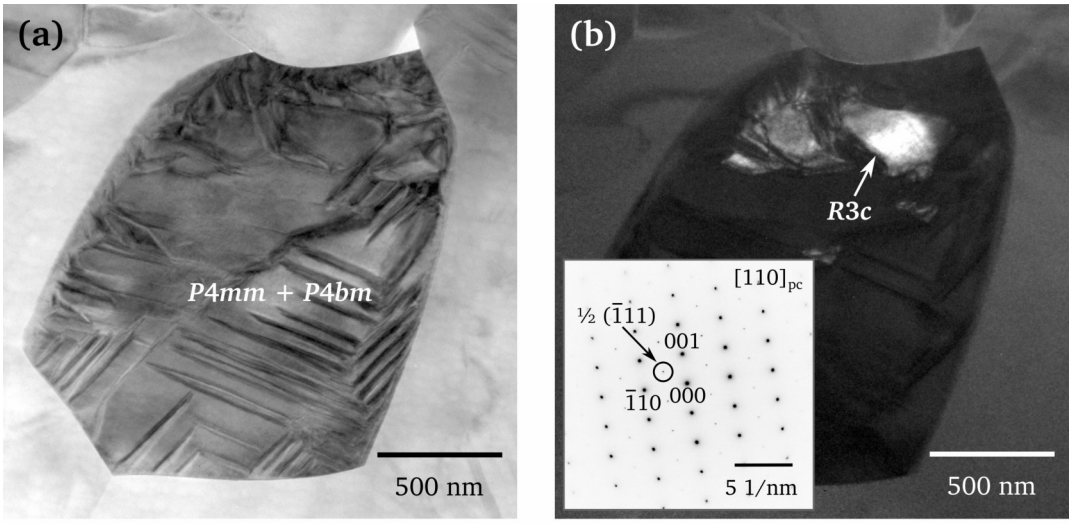

Figure 4.23: TEM micrographs of poled NBT-6BT FC. (a) BF image showing an enhanced lamellar domain contrast. (b) Corresponding DF image obtained from the encircled $\frac{1}{2}$ $(\bar{1}11)$ SR illustrating the *R*3*c* phase (SAED pattern as inset).

lamellar domain regions, only weak $\frac{1}{2}$ $\{ooe\}$ SRs are present. Therefore, a poling induced transition from relaxor *P*4*bm* to a mixture of *P*4*mm* + *P*4*bm* occurs.

The quenched and poled NBT-6BT specimen features lamellar domains in the majority of grains (Fig. 4.24(a)), associated with an increased ferroelectric order and the abundance of *P*4*mm* domains. Weak $\frac{1}{2}$ $\{ooe\}$ SRs occur in these areas, indicating a minor fraction of *P*4*bm* nanodomains. Irregular structured areas of *R*3*c* symmetry are also present (Fig. 4.24(b)). In grains, where the R phase accounts for a larger volume fraction, $\frac{1}{2}$ $\{ooo\}$ SRs are comparably more intense.

Summarizing the TEM observations on poled NBT-6BT, both FC and Q specimens show comparable features regarding lamellar domain formation, domain widths and coexistence of R and T phases. Lamellar domains of neighboring grains usually exhibit independently oriented domain patterns, which are not coherent over grain boundaries.

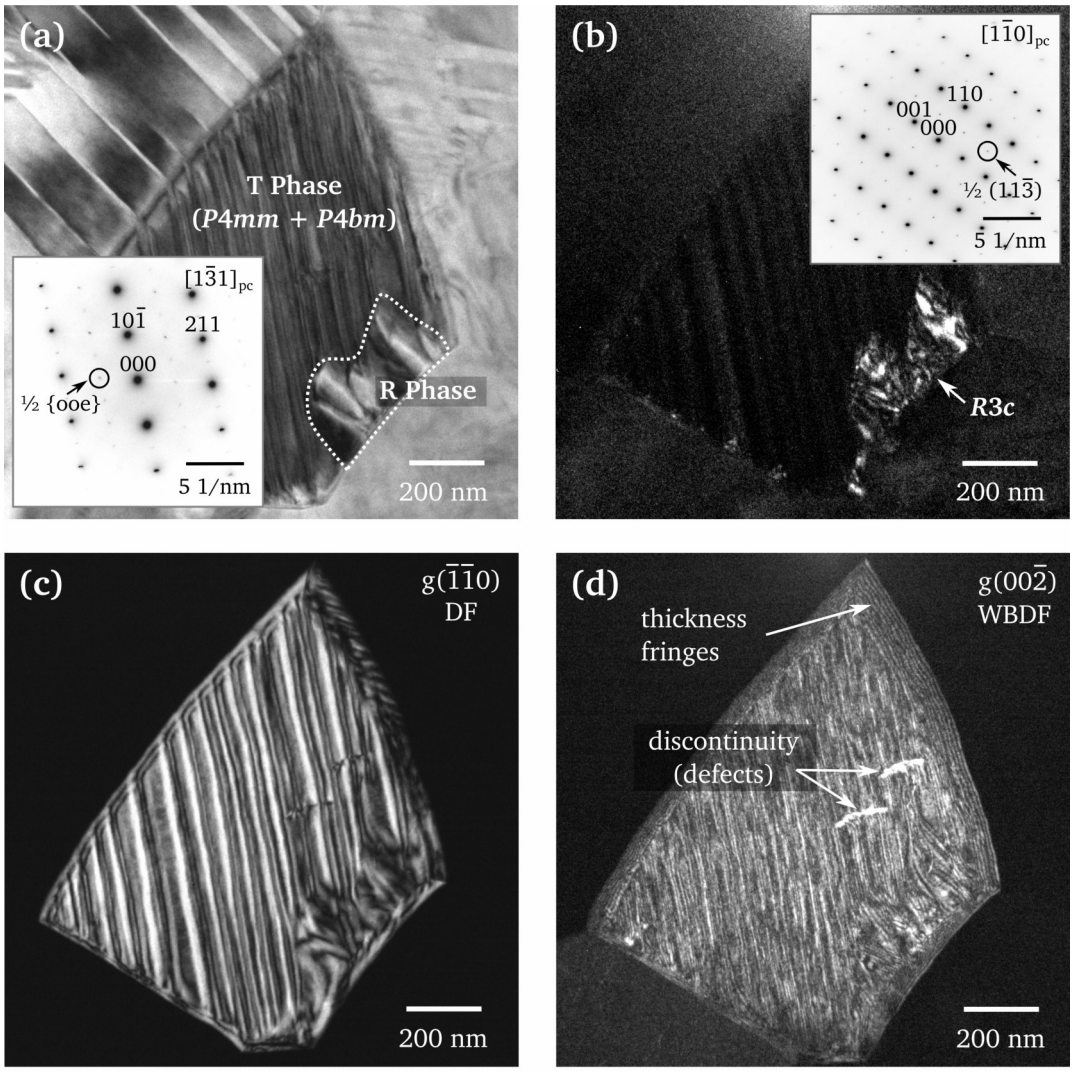

Figure 4.24: TEM micrographs of poled NBT-6BT Q. (a) A grain viewed along the $[1\bar{3}1]_{pc}$ zone axis (SAED pattern as inset) displaying lamellar tetragonal domains. (b) DF image obtained with the encircled $\frac{1}{2}$ $(11\bar{3})$ SR in the SAED pattern (see inset), highlighting an irregular *R*3*c* area. (c) DF image obtained from the $\bar{1}\bar{1}0$ reflection. (d) WBDF image of the $00\bar{2}$ reflection. Bright discontinuities (defects) become visible and domain walls and thickness fringes appear as narrow lines. Note the higher image resolution of the WBDF technique as compared to the regular DF image shown in (c).

The grain in Fig. 4.24 can further be used to visualize the difference between a regular on-axis DF image and a weak beam dark-field (WBDF) image. On-axis DF imaging of SRs has been extensively used throughout the study to illustrate the morphology and location of *P*4*bm* and *R*3*c* phases. A DF image of a main reflection (g) can help to highlight the domain structure (Fig. 4.24(c)). The fringe pattern of the inclined lamellar domain walls exhibits an increased contrast in the DF image. For obtaining a WBDF image, the grain is slightly tilted out of the oriented zone axis, so that the excitation error (s) becomes large. Preferably, 000 and only one further reflection ($2g$ or $3g$) show a high intensity, which is then selected via the objective aperture to obtain the WBDF image. For example, WBDF is often used to image defects, visualizing dislocations as narrow lines and giving the true position of the dislocation core [234]. As the grain is tilted away from the zone axis, only bent regions directly at the dislocation may still fulfill the ideal Bragg condition ($s = 0$) and show a high intensity. This effect is visible in the WBDF image in Fig. 4.24(d), which displays two bright lines running perpendicular to the domains (marked with arrows). These discontinuities are likely defect structures, interrupting the domain walls. Such defects have been found occasionally in both FC and Q samples and are thus believed to be unrelated to the quenching process. Furthermore, contrast fringes appear as rather narrow lines in the WBDF image as compared to the regular DF image shown in Fig. 4.24(c). A detailed contour map of thickness fringes is visible at the grain boundary, where the grain thickness declines.

As for the NBT-9BT composition, both poled FC and Q samples have been examined and display an identical domain structure. Lamellar 90° domain walls are abundantly present in each sample (Fig. 4.25), demonstrating a tetragonal ferroelectric long-range order. Weak $\frac{1}{2}$ $\{ooe\}$ SRs occur throughout both specimens and also very weak $\frac{1}{2}$ $\{ooo\}$ SRs have occasionally been observed, indicating a very minor fraction of rhombohedral phase.

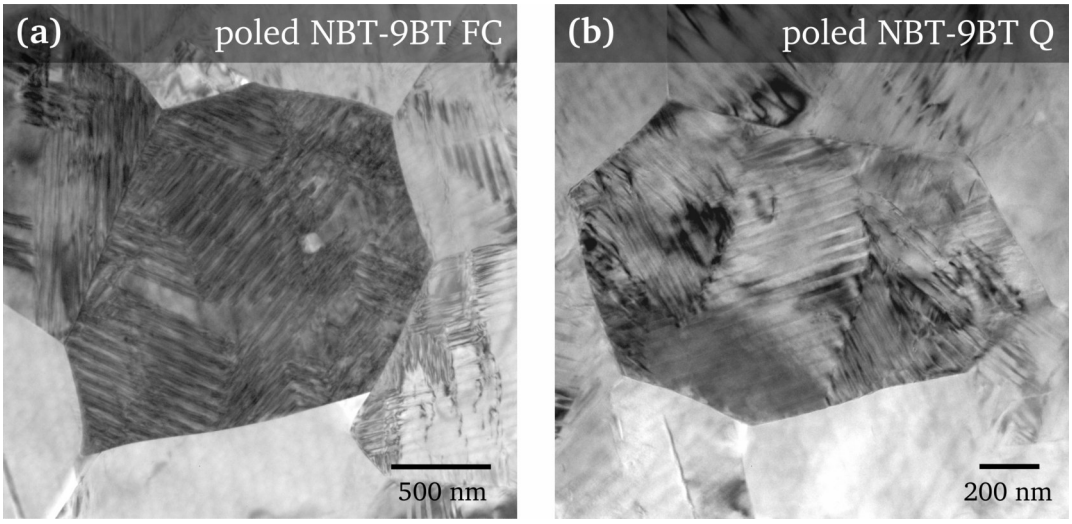

Figure 4.25: TEM-BF images of poled NBT-9BT FC (a) and poled NBT-9BT Q (b), both characterized by abundant tetragonal lamellar domains.

The domain pattern of unpoled and poled NBT-6BT and -9BT specimens was further investigated by SEM on chemically etched sample surfaces (Fig. 4.26). Unpoled NBT-6BT FC is characterized by an irregular small-scale etching structure and the absence of large domains (Fig. 4.26(a)), which is consistent with the TEM observations. The poled specimen displays a similar appearance; however, few lamellar domains occur (indicated with arrows in Fig. 4.26(b)). The unpoled NBT-6BT Q

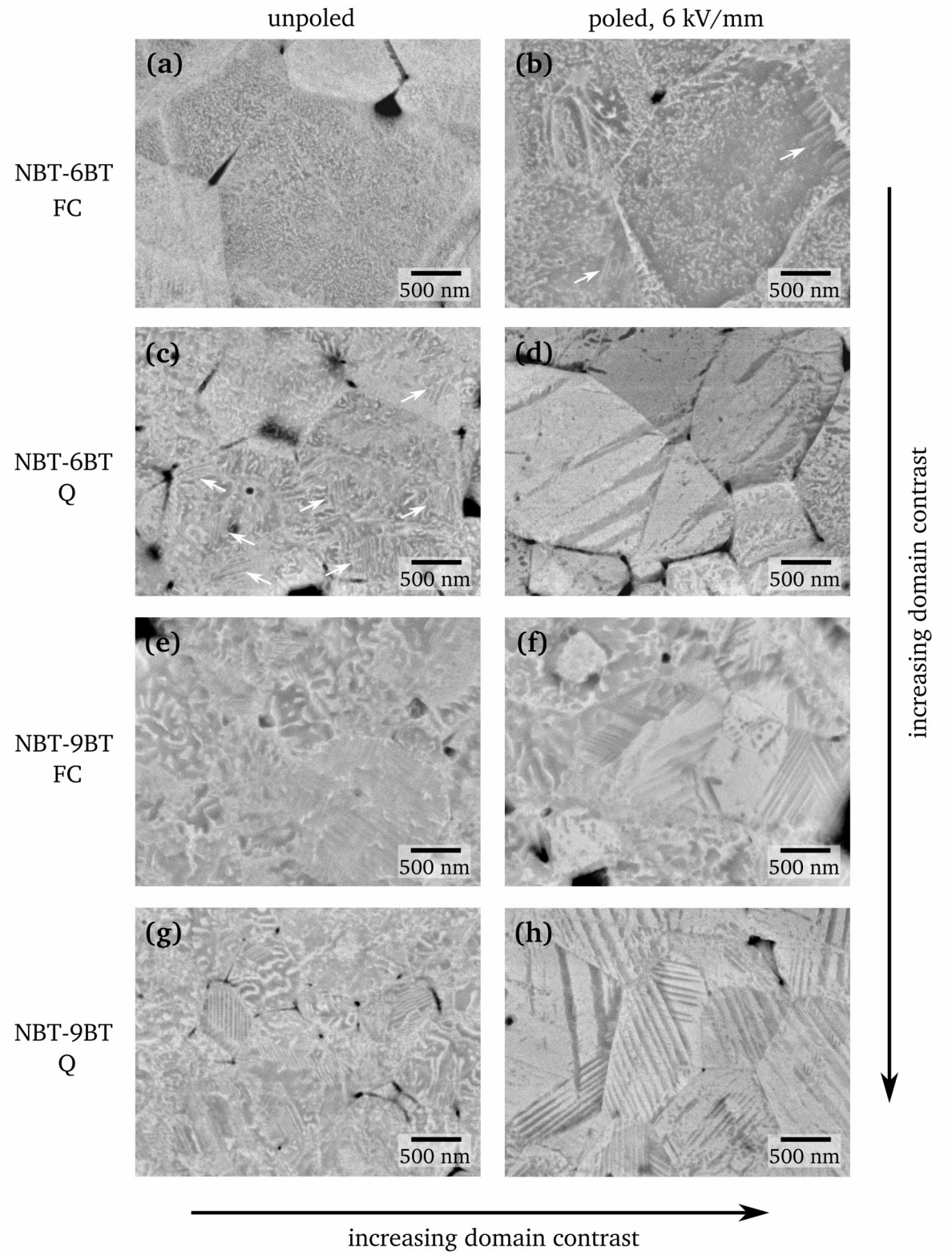

Figure 4.26: SEM micrographs of chemically etched NBT-6BT and -9BT obtained in BSE mode. (a) Unpoled NBT-6BT FC, (b) poled NBT-6BT FC, (c) unpoled NBT-6BT Q, (d) poled NBT-6BT Q, (e) unpoled NBT-9BT FC, (f) poled NBT-9BT FC, (g) unpoled NBT-9BT Q and (h) poled NBT-9BT Q. The white arrows indicate fine lamellar domains in (b) and (c).

specimen features fine lamellar domain structures (indicated with arrows in Fig. 4.26(c)). This supports the TEM findings of an increased lamellar domain contrast upon quenching in unpoled NBT-6BT. More prominent lamellar domains appear in the poled Q state (Fig. 4.26(d)), where they have increased in width and length. Unpoled NBT-9BT FC displays fine lamellar domains with a weak contrast (Fig. 4.26(e)), which are again more pronounced and larger in the poled NBT-9BT FC specimen (Fig. 4.26(f)). The same applies for unpoled NBT-9BT Q (Fig. 4.26(g)) and poled NBT-9BT Q (Fig. 4.26(h)). The SEM investigation demonstrates a trend towards an increasing lamellar domain contrast upon poling and also upon quenching, rendering unpoled NBT-6BT FC as the sample without any obvious domain structures and poled NBT-9BT Q as the sample with the most prominent domain features.

Poled NBT-6BT and -9BT specimens were furthermore investigated by PFM (Fig. 4.27). Compared to the PFM images of the unpoled specimens (Fig. 4.22), the portion of lamellar domains in poled NBT-6BT FC and Q (Figs. 4.27(a) and (b)) has clearly increased. In poled NBT-9BT FC and Q (Figs. 4.27(c) and (d)), long-range domains are even more abundant, which is in agreement with the TEM and SEM results. Compared to the unpoled state, almost no wavy 180° domain walls (watermarks) are present in the poled specimens. Poling thus results in a less complex domain pattern where the amount of 180° domain walls is significantly decreased, while 90° domain walls are still present in great abundance. Within most grains, only two or a single set of lamellar domains is present. On average, domain widths are slightly increased compared to the unpoled specimens.

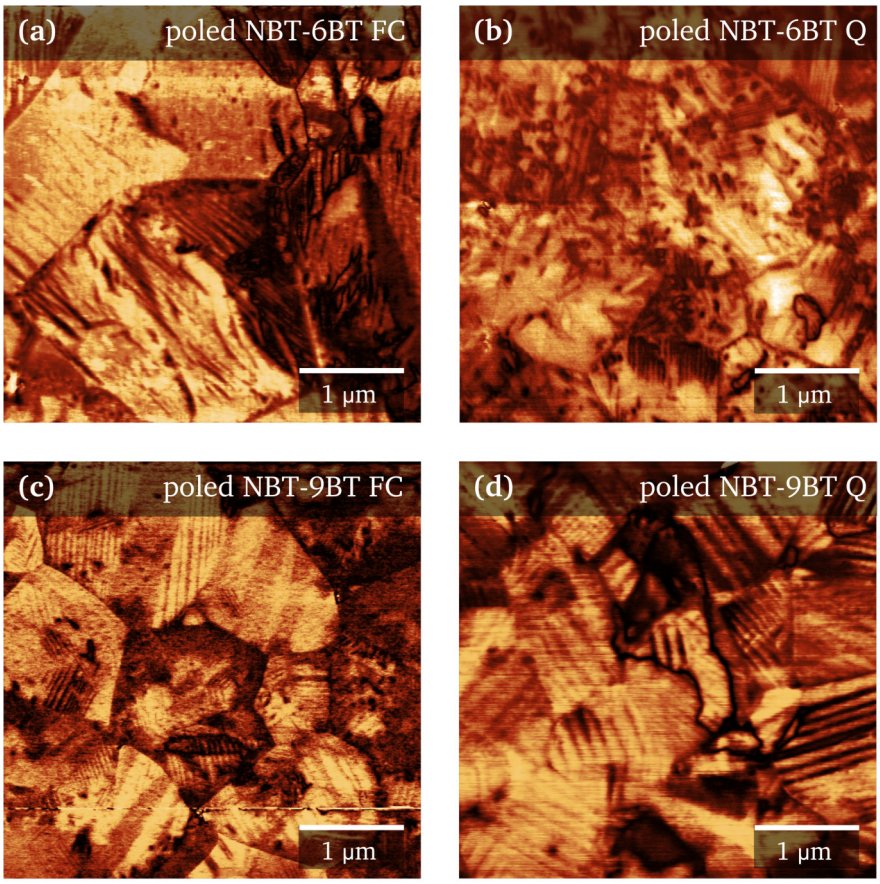

Figure 4.27: PFM images (lateral amplitude) illustrating the domain pattern in poled NBT-6BT and -9BT. (a) Poled NBT-6BT FC, (b) poled NBT-6BT Q, (c) poled NBT-9BT FC and (d) poled NBT-9BT Q. Note that wavy 180° domain walls are absent.

It should be noted that the electric field vector during poling has been applied perpendicular to the sample surface. With the preferential alignment of the polarization vectors in the domains along the electric field, enhanced reversal and domain wall motion for 180° domains leads to the vanishing of watermarks and 180° zigzag domains. Since 180° domain walls are solely ferroelectric and domain wall motion is not associated with any strain, they are believed to respond more easily to switching processes during poling, compared to 90° ferroelastic domains [272]. Due to the spatial constraints of the grains within the ceramic, retaining a high number of 90° domain walls in order to minimize the elastic energy is also required during and after poling. Reorientation of 90° domains upon poling is expected, leading to the slight increase in domain size. The disappearance of 180° watermarks upon poling is a common feature, also observed in other lead-free ferroelectrics [273]. The absence of 180° domain walls is also an indication that the poling induced domain structure of NBT-BT remains stable and does not revert back after the poling process.

4.2.8 Electron Energy-Loss Spectroscopy on NBT-BT

EELS analysis was conducted on all FC and Q specimens, in order to obtain information about the valence state and local electronic environment of titanium in the perovskite structure (Fig. 4.28). For Ti oxides, the ELNES of the Ti L_3- and L_2-edges, arising from $3d$-orbital transitions, provides information about the correlation of Ti with O, impacting the Ti electronic structure and valence state [255]. Equally, the shape of the O K-edge is also influenced by the chemical bonding and coordination of Ti and O, attributed to the hybridization of the O $2p$-orbitals with the Ti $3d$-orbitals. Regarding quenched NBT-BT ceramics, the enhanced formation of oxygen vacancies has been hypothesized [226]. The creation of vacancies ($V_O^{\bullet\bullet}$) on the oxygen lattice site ($O_O^{\times}$) in ferroelectric perovskites produces free electrons (e'), as can be described by the Kröger-Vink notation: $O_O^{\times} \rightleftharpoons V_O^{\bullet\bullet} + 2e' + \frac{1}{2}O_2$ [274]. The electrons can then be bound to titanium according to: $Ti^{4+} + e' \rightleftharpoons Ti^{3+}$ [275]. Formation of oxygen vacancies would consequently lead to a reduction of Ti^{4+} to Ti^{3+}, in order to maintain charge neutrality. The presence of Ti^{3+} is thus expected to change the near-edge signal of the Ti $L_{2,3}$- and O K-edges [276]. In pure Ti^{4+} compounds, a strong splitting of both Ti $L_{2,3}$-edges occurs, which is characteristic for the octahedral coordination of Ti^{4+}. The splitting is ascribed to the crystal-field splitting of Ti $3d$- into t_{2g}- and e_g-orbitals [277]. Likewise, regarding the O K-edge, the peak at lower eV is due to the hybridization of O $2p$ and Ti $3d(t_{2g})$ and the second peak to the hybridization of O $2p$ and Ti $3d(e_g)$ [255]. Decreasing the amount of Ti^{4+} and increasing the amount of Ti^{3+} leads to a distortion of the octahedral coordination and to a less pronounced splitting of the Ti $L_{2,3}$-edges [278]. As an example, the splitting is reduced in synthesized compounds of Ti_3O_5 (with a Ti^{4+}:Ti^{3+} ratio of 1:2) and Ti_2O_3 (with solely Ti^{3+}), while it is absent in the compound TiO, which contains Ti^{2+} [255]. Simultaneously, a shift of Ti $L_{2,3}$-edges to lower energies arises. The shift is reported to be 1.7-2.0 eV per decreased oxidation state [255], while the O K-edge slightly shifts to higher eV values.

Under the above considerations, the EELS spectra of Ti and O edges in NBT-BT FC and Q specimens were compared, in order to gain conclusions about the presence of Ti^{3+}, which would be indicative for a higher number of oxygen vacancies. Fig. 4.28 displays normalized EELS spectra of all four FC and Q compositions. Since the zero loss peak can slightly shift in position during the measurements, the O K-edge was used to calibrate the position of the spectra with respect to the eV axis. All spectra were acquired within one analysis session, assuming a consistent dispersion. Note that the respective FC and Q spectra show an almost identical morphology. Splitting of the Ti $L_{2,3}$- and O K-edges is present to the same degree in all FC and Q specimens. Very slight variations in the

morphology of the near-edge Ti spectra are visible, also occurring within a single sample when comparing several grains (see Fig. A.4 in Appendix on page 146). However, no changes in the Ti $L_{2,3}$-splitting, exceeding the variations that can occur within a single specimen, are present upon quenching. No shift in the Ti $L_{2,3}$-edges is observable for any composition, when comparing FC and Q. Also, variations of the O K-edge are marginal. It can be concluded that no increased amount of Ti^{3+}, relating to an increase in the oxygen vacancy concentration upon quenching, could be observed. The role of oxygen vacancies is further discussed in the following section.

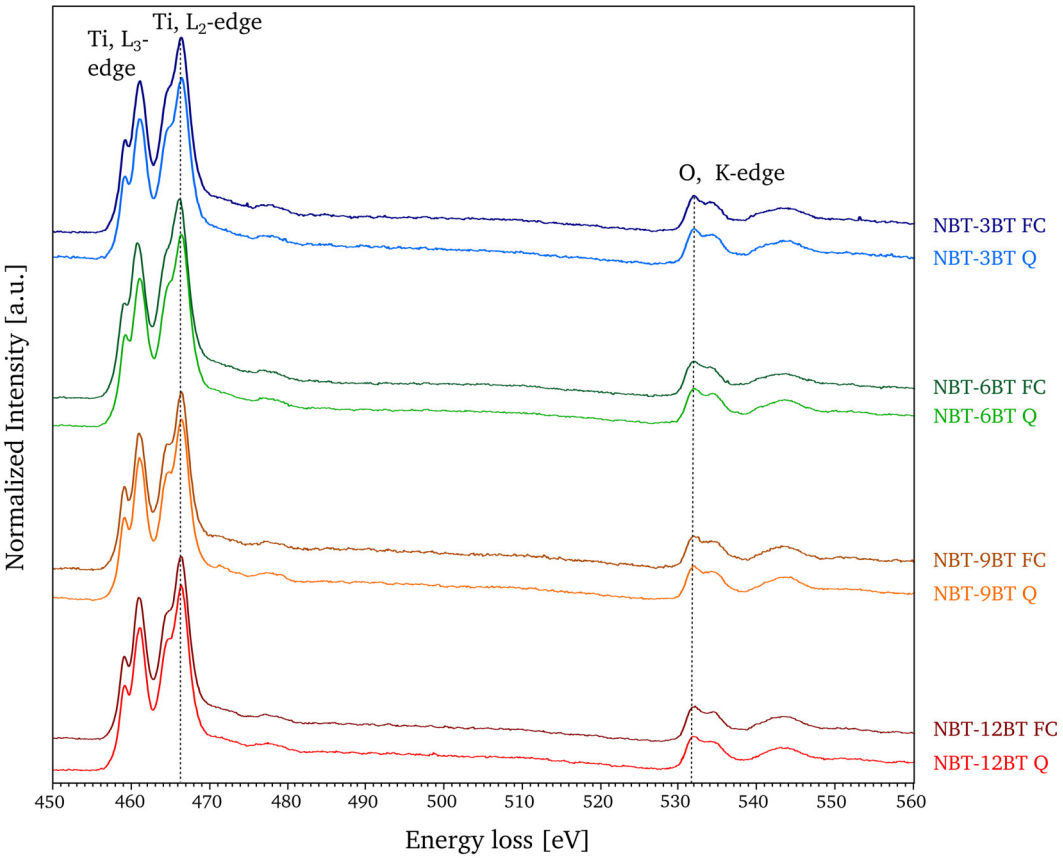

Figure 4.28: EELS spectra of NBT-BT FC and Q specimens, displaying the near-edge structure of the Ti L_3- and L_2-edges and the O K-edge. No changes in peak position and in the fine structure could be discerned between FC and Q specimens, implying that no change in Ti-valency occurred upon quenching.

4.2.9 Discussion of Quenching-Induced Structural Changes

Quenching is generally regarded as a procedure suppressing reactions and transformation processes, which would take place upon slowly cooling the specimen down to ambient temperature. Known from metallurgy, quenching is commonly associated with the hardening of steel, where the metal is heated and successively cooled down quickly (quenched) in a medium such as water, in order to induce a highly strained (thus hardened) martensitic structure [279]. In contrast, the interest in quenching NBT-based ceramics developed under the aspect of increasing T_d. Here, quenching can be viewed as a procedure that allows to alter the materials properties and tailor them in a beneficial way. High cooling rates, which can be achieved by quenching in water, lead to fracturing and microcracking of the ceramics, whose thermal conductivity is generally poor compared to

metals. Quenching in air was established as a method that allows fast cooling, but is not too fast, in order to avoid mechanical degradation of the ceramic materials.

A stabilization of ferroelectric order upon quenching NBT-BT has been hypothesized [15], based on an increased lattice distortion and lower permittivity values upon quenching. Both are characteristic for ferroelectrics rather than for relaxors. The increased lamellar domain contrast observed in TEM evidences the trend from a mere relaxor structure towards a ferroelectric morphology with long-range polar structures. Fig. 4.29 schematically compares the domain patterns in the four FC and Q specimens. A quenching-induced change of the microstructure becomes visible in NBT-3BT and -6BT. The irregular and complex domain structure of NBT-3BT FC is contrasted by the appearance of large lamellar domains in NBT-3BT Q. For the relaxor composition NBT-6BT, the furnace cooled state is characterized by a nanoscale morphology with *P*4*bm* symmetry. Upon quenching, long-range ferroelectric domains of tetragonal and rhombohedral symmetry appear in an increased amount. Areas with no distinct domain contrast are still present, however reduced in favor of a larger fraction of lamellar domains. For the compositions NBT-9BT and -12BT, no distinct changes in the domain structure and phase assemblage upon quenching are apparent. The trend towards an increased lamellar domain fraction does not become visible, since both compositions are already characterized by lamellar *P*4*mm* domains in the FC state. Overall, the TEM observations corroborate the stabilization of ferroelectric order upon quenching, reflected in a consolidated lamellar domain configuration.

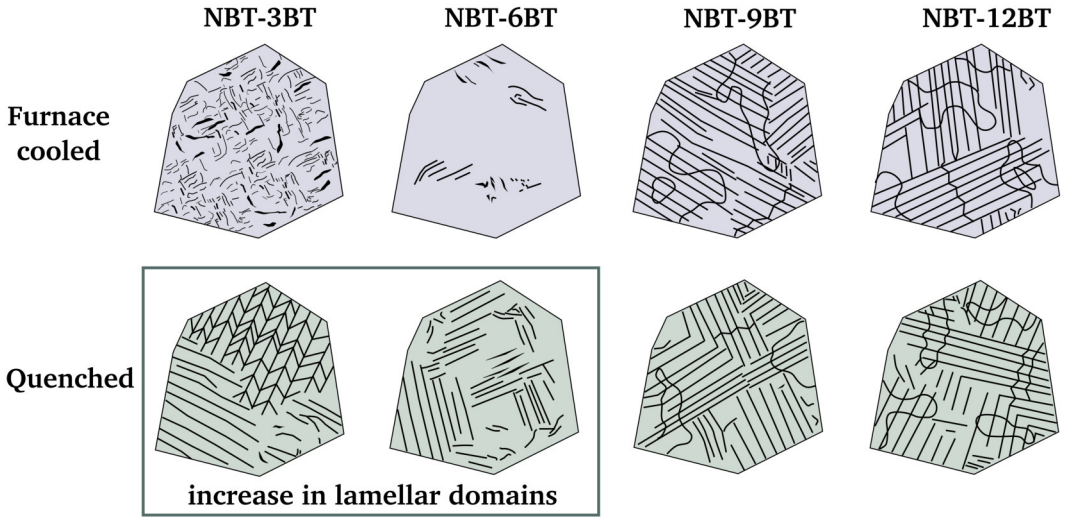

Figure 4.29: Schematic of the domain patterns in the four NBT-BT FC and Q compositions. Significant differences arise for the NBT-3BT and -6BT specimens.

Fig. 4.30 compares the qualitative volume fraction of coexisting phases in NBT-BT FC and Q deduced from the TEM study. An *R*3*m* symmetry appears on the NBT-rich side upon quenching the NBT-3BT composition. Generally, when a rhombohedral distortion from the cubic perovskite structure with cation displacement along the threefold $\langle 111 \rangle_{pc}$ axes is present, the space group *R*3*m* arises [102]. *R*3*c* ($a^-a^-a^-$) is a subgroup of *R*3*m* ($a^0a^0a^0$), where the difference is solely due to the tilting of the oxygen octahedra around the threefold axis and the consequential doubling of the unit cell [280]. Mirror planes in the *R*3*m* space group are replaced by glide planes in *R*3*c*. *R*3*m* is the low temperature rhombohedral phase of BT [281] and was also reported for various other perovskite oxides and their solid solutions, including NBT-KBT [282] and NBT-BT itself [164]. It is therefore conclusive to identify the rhombohedral symmetry of the herringbone-type domains as *R*3*m*. The

phase assemblage between 3 and 6 mol % BT remains speculative. From the investigations here, it cannot be established, whether the *R*3*m* phase stretches towards the MPB, or a transition towards a solely *R*3*c* symmetry exists for $x > 0.03$ as indicated in Fig. 4.30. Especially in NBT-6BT Q, the volume fraction of the relaxor phase *P*4*bm* is reduced in favor of ferroelectric domains of *P*4*mm* and *R*3*c* symmetry. For NBT-9BT and -12BT, it is conceivable that the average phase assemblage slightly shifts towards a higher fraction of *P*4*mm* and slightly lower fractions of *P*4*bm* and *R*3*c*, which not necessarily becomes evident by the highly localized TEM analysis.

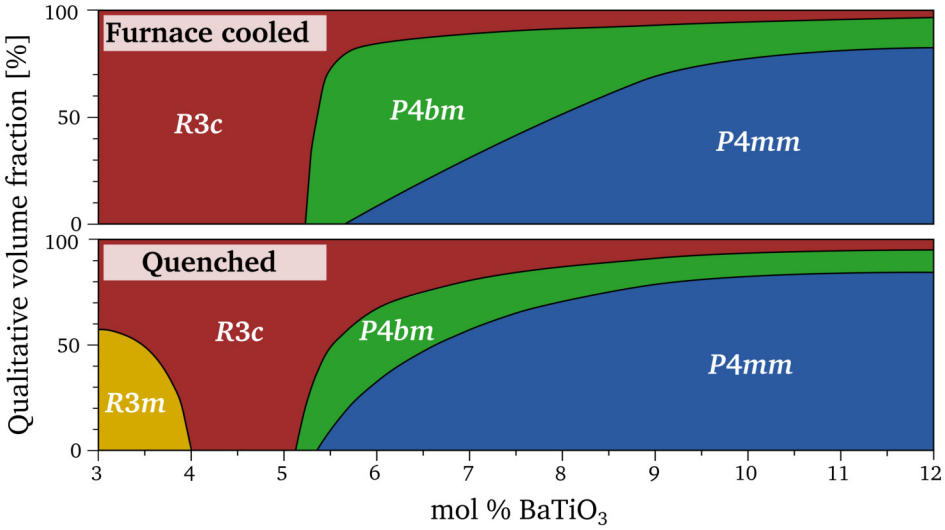

Figure 4.30: Comparison of the qualitative phase volume fractions in the compositional range between 3 and 12 mol % BT in NBT-BT FC and Q specimens.

Quenching is known to increase the lattice distortion of NBT-based ceramics [13–15]. A critical quenching temperature appears to be 800-900 °C. Quenching from below 800 °C does not result in any significant change in lattice distortion and T_d [13], as well as d_{33} and ε' [221] (whereas the Young's modulus is reduced for a quenching temperature of 800 °C). Note that the NBT-BT ceramics in this study were quenched from the sintering temperature 1150 °C, where the change in the unit cell parameters is most pronounced. The lattice distortion obtained by powder X-ray diffraction on FC and Q specimens of the same sample batch as used for the TEM investigation is illustrated in Fig. 4.31 [267]. The rhombohedral distortion is given as $90° - \alpha$ (deviation from the 90° angle of the cubic unit cell). The tetragonal distortion is given in % derived from the ratio of the c and a lattice constant as $(c/a) - 1$.

Conventional XRD analyses, which gives the average crystal symmetry, is not necessarily able to resolve weak deviations from the cubic symmetry. The relaxor NBT-6BT FC composition, where a very low lattice strain is present due to the *P*4*bm* phase, is therefore often described as pseudocubic [121, 267]. This is also evident from Fig. 4.31, where $90° - \alpha$ and $(c/a) - 1$ are both close to zero. A high-resolution XRD study on the same sample batch resulted in 68 % cubic and 32 % rhombohedral phase fraction for NBT-6BT FC [266]. Upon quenching, NBT-6BT Q exhibits a notable increase in rhombohedral (68 %) and tetragonal (32 %) phase fraction [266]. The increase in rhombohedrality relates to the increase of the *R*3*c* volume fraction and its lamellar domain structure observed via TEM (right side in Fig. 4.31). The increased tetragonal distortion correlates well with the occurrence of lamellar domains within the T phase, attributed to *P*4*mm*. It is further plausible to link the enhanced rhombohedral distortion on the NBT-rich side to the appearance of *R*3*m* and

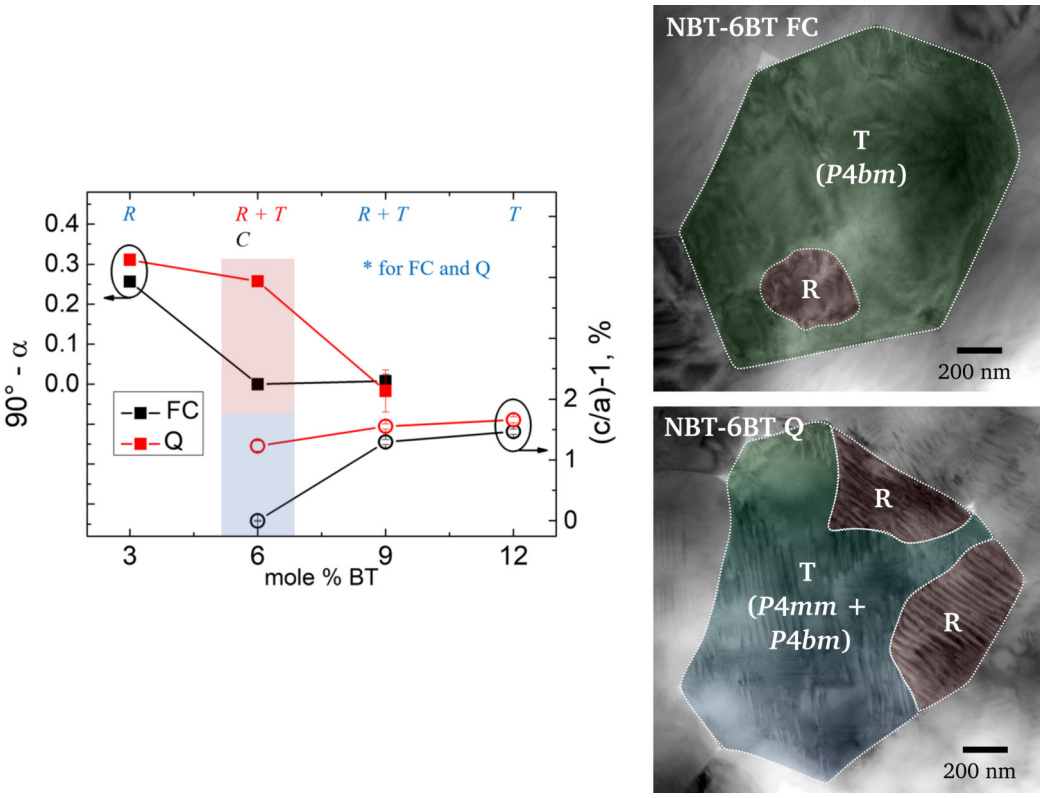

Figure 4.31: Rhombohedral ($90° - \alpha$) and tetragonal ($(c/a) - 1$) lattice distortion of NBT-BT FC and Q as function of the BT content obtained from X-ray powder diffraction (data acquired by A. Wohninsland, graph reproduced from Ref. 267 with permission of AIP Publishing). R, T and C denote a rhombohedral, tetragonal and cubic symmetry. The increase in rhombohedral and tetragonal distortion, especially in NBT-6BT Q, correlates to the increased lamellar domain contrast observed via TEM and shown on the right.

the associated increase in lamellar domains. NBT-9BT Q and -12BT Q also exhibit an increase in tetragonal distortion, indicating a stabilization of the tetragonal *P4mm* phase.

Ferroelastic domains form in order to accommodate the strain which arises from the transition of the cubic to the room temperature ferroelectric phase. The strain is compensated by the formation of predominantly lamellar ferroelastic domains (90° in the tetragonal and 109° and 71° in the rhombohedral phase). The increased lamellar domain contrast upon quenching indicates that the quenched samples have to accommodate a higher degree of deformation strain. This is especially validated for NBT-6BT, showing the most significant change in lattice distortion compared to the pseudocubic FC state. An increased lattice distortion thus results in the enforced formation of long-range lamellar domains.

In NBT-6BT, the transition from the high-temperature cubic phase to *P4bm* spans over a large temperature range [160]. PNRs start to nucleate and grow in number until T_{VF} is reached, where their dynamic behavior ceases and they are frozen-in to the non-ergodic relaxor state. It is likely that the volume fraction of PNRs at elevated temperatures influences the domain formation observed at room temperature. Wohninsland et al. [267] could show that NBT-6BT Q exhibits an increased volume fraction of PNRs by 12 % at 300 °C. A higher fraction of PNRs might facilitate the formation of larger polar domain structures, when further cooling the compositions. Whether PNRs coalesce into larger polar regions, eventually forming domains, or undergo a structural transition is further discussed in section 4.4.6.

The real (ε') and imaginary (ε'') part of the temperature-dependent permittivity of the four unpoled NBT-BT compositions is reproduced in Fig. 4.32 from the supplementary material of Wohninsland et al. [267]. NBT-3BT FC is ferroelectric and does not display a frequency-dependent dispersion of the permittivity in the low temperature regime. However, NBT-3BT Q exhibits a sharper transition at ∼200 °C. The strengthened ferroelectric character of the permittivity curve upon quenching correlates with the enhanced formation of lamellar ferroelectric domains and thus stabilization of ferroelectric order. A shift of the transition to a higher temperature is also visible for ferroelectric NBT-12BT Q. For NBT-9BT FC, it appears difficult to align the dielectric data with the observed domain structure: The composition exhibits a relaxor character indicated by the strong frequency dispersion of ε', whereas a predominantly ferroelectric lamellar domain contrast was observed in TEM and PFM. It can be argued that the volume fraction of PNRs/nanodomains and consequently the *P*4*bm* phase is nevertheless still large enough to result in an overall relaxor behavior that was monitored for this composition. Judging from the strong domain contrast, NBT-9BT FC appears close to the verge of transforming into a ferroelectric. Indeed, the quenching treatment enables

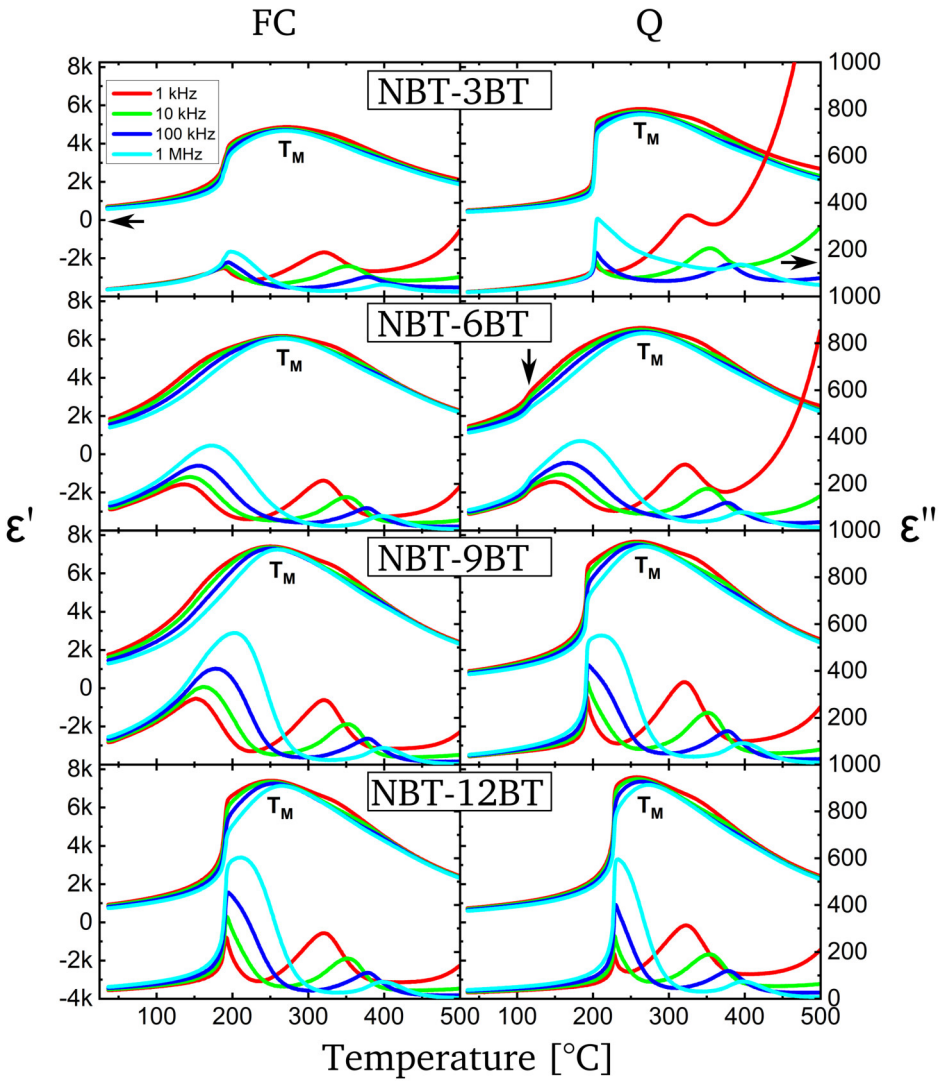

Figure 4.32: Real (ε') and imaginary (ε'') part of the temperature-dependent permittivity of the four unpoled NBT-BT FC and Q compositions (data acquired by A. Wohninsland and reprinted from Ref. 267 with permission of AIP Publishing). Both permittivity and TEM data was obtained from the same sample batch.

to cross this threshold by slightly increasing the tetragonal distortion and ferroelectric domain fraction. A spontaneous transformation into a ferroelectric, where a frequency dispersion at lower temperatures is absent results for NBT-9BT Q. For NBT-6BT, the increase in R and T lamellar domains upon quenching appears to be insufficient for transforming the relaxor composition into a ferroelectric. A frequency dispersion of the permittivity is still visible for the Q sample. However, its permittivity curve depicts a slight kink at ∼115 °C (marked with an arrow in Fig. 4.32), which indicates the onset of a transition towards a more ferroelectric character as a consequence of the consolidated ferroelectric order and domain structure.

Moreover, regarding the effect of an external electric field on the domain structure, poling of NBT-BT ceramics results in a field-induced transition, where tetragonal and rhombohedral lattice distortions are enhanced [203, 204]. Poled NBT-6BT FC and Q exhibit a comparable domain structure, featuring lamellar tetragonal domains and also grains with a large rhombohedral volume fraction. This is mostly in accordance with in-situ field-dependent TEM analyses by Ma et al. [149], where the *R*3*c* + *P*4*bm* assemblage transforms to lamellar domains of *R*3*c* + *P*4*mm* symmetry and eventually to a pure *R*3*c* phase at a poling field of 6 kV/mm (compare Fig. 2.29 on page 31). In the present study, however, abundant tetragonal *P*4*mm* domains are present, although poling was similarly conducted at 6 kV/mm. This difference is likely related to the differing techniques of in-situ biasing and ex-situ poling prior to the TEM sample preparation. Nevertheless, some grains display strong $\frac{1}{2}$ $\{ooo\}$ SRs, which aligns with the trend towards a consolidated rhombohedral structure upon poling, as also observed by others [149, 185]. Weak $\frac{1}{2}$ $\{ooe\}$ SRs in both poled FC and Q specimens illustrate that the relaxor *P*4*bm* phase is not completely transformed upon poling and remains as a subordinate phase.

It becomes apparent that the quenching-induced domain structure and phase assemblage in unpoled NBT-BT shows similarities to the changes observed upon poling: increase of ferroelectric lamellar *P*4*mm* and *R*3*c* domains in NBT-6BT, relative decrease of the *P*4*bm* fraction and enhanced lattice distortion in all compositions. It can be reasoned that the transition towards an increased ferroelectric order upon quenching is further consolidated by the poling process. The quenching treatment may be regarded as a 'booster' for initializing the relaxor-to-ferroelectric transition. The spontaneous onset of ferroelectric order upon quenching also results in less pronounced average structural changes when poled. While NBT-6BT and -9BT FC exhibit a change in volumetric (phase transition) strain when an E-field is applied, no changes in the volumetric strain as a function of the poling field is reported for the quenched specimens, indicating weakened or even absent structural changes during poling [283].

Quenching increases the lattice distortion, which consequently leads to an increase in T_d. Three underlying mechanisms causing these changes have been discussed in literature:

- Residual thermal stress [231]
- Increased oxygen vacancy concentration [15, 226, 230]
- Off-centering of Bi^{3+} cations [14, 219]

When the thermal stress during cooling of the ceramics exceeds the critical stress required for fracturing, crack formation occurs. This is the case for NBT-BT quenched in liquid nitrogen [231] and NBT quenched in water and silicon oil [222], however, not for air quenched samples. Ren et al. [231] argue that thermal stresses nevertheless arise during air quenching of NBT-6BT, leading to significant micro-stress, being responsible for the broadening of XRD profiles and inducing a pseudocubic-to-rhombohedral transition within the grains. Air quenching with a rate of 15 °C/s in

the 1100-800 °C regime reduces the bending strength of NBT ceramics to a quarter of the value of FC samples, likely due to microcrack formation [222]. Zhang et al. [221] measured the surface temperature and modelled the temperature gradient within cylindrical NBT-BT samples of 3 mm thickness when quenched in air from 1100 °C. After 20 s, the surface temperature has decreased to 900 °C (which corresponds to a quenching rate of 10 °C/s), while the temperature in the center of the specimen is ∼920 °C [221]. They concluded that the thermal stress induced by the temperature gradient within the specimens is four times lower than the critical value required for fracture formation. The microstructural investigations on the quenched NBT-BT samples conducted in this work confirm this assumption. No microcracks, whether inter- nor transgranular were observed in the ceramic pellets and TEM specimens. Furthermore, strain contours on grain boundaries, which would indicate the presence of residual stresses within the material, were not observed. Thus, a pronounced influence of residual thermal stress on the lattice distortion seems rather unlikely.

The role of an increased oxygen vacancy concentration in quenched NBT-BT is controversial. Oxygen vacancies form more easily at high temperatures and quenching is known to freeze-in the high defect concentration [227, 228]. It is deduced that oxygen vacancies can provoke the stabilization of ferroelectric order [15]. At a high enough oxygen vacancy concentration, it could be demonstrated on a Pb-based relaxor that an induced ferroelectric phase emerges [284]. Oxygen vacancies can pin the domain walls and are thus believed to result in an increase of T_d [226]. Prolonged annealing of NBT-BT Q in oxygen atmosphere above 800 °C, which promotes annealing of oxygen vacancies, leads to the disappearance of the quenching-induced properties, such as the shift in $T_{F\text{-}R}$ [15]. It could, however, also be demonstrated that annealing NBT-6BT Q in nitrogen atmosphere also reverts $T_{F\text{-}R}$ to its original value [231]. This is contradictory to the assumption that $T_{F\text{-}R}$ and T_d are governed by the oxygen vacancy concentration, which would be expected to increase in nitrogen atmosphere and thus increase T_d.

Since the conductivity of ferroelectric perovskites is predominantly ascribed to the electromigration of oxygen vacancies [284], an increased conductivity observed for NBT-BT Q [220] could in principle be attributed to an increased oxygen vacancy concentration. However, annealing in oxygen atmosphere does not significantly reduce the conductivity, which suggests no or only a weak influence of oxygen vacancies on the quenching-induced characteristics [220]. Also, acceptor doping of NBT-BT with Fe^{3+} on the Ti^{4+} site, which generates oxygen vacancies, was not reported to increase T_d and even decreases T_d for high dopant levels [285]. On the other hand, doping with Zn^{2+} (which is also incorporated on the B site) leads to an increase in T_d and in conductivity [286]. T_d is even further increased when Zn-doped NBT-BT is quenched, while the conductivity remains unchanged, relating the T_d increase to a stabilized tetragonal phase rather than to an increased oxygen vacancy concentration [286].

An increased amount of oxygen vacancies and Ti^{3+} upon quenching NBT-6BT was reported based on X-ray photoelectron spectroscopy (XPS) and electron paramagnetic resonance (EPR) analysis [226]. This can, however, not be confirmed from the EELS analysis of this work. Between FC and Q samples, no shift and change in the morphology of Ti and O ionization edges was observed, exceeding the slight variations that are present within one specimen. As comparison, NBT-BT features a shift of 1.5 eV of the Ti $L_{2,3}$-edges and a well visible decline of the peak splitting when annealed in nitrogen atmosphere [287]. The absence of such features in the EELS spectra of the Q samples indicates that there is no increased amount of Ti^{3+} and consequently no increased amount of oxygen vacancies present. Furthermore, Zhang et al. [230] argue that point defects, such as oxygen vacancies, can have a pinning effect on the domain walls during poling, which results in more irregular domain shapes as observed for quenched and poled NBT-KBT-BT ceramics. In NBT-BT,

however, both poled FC and Q specimens exhibit a comparable regular lamellar domain structure, giving no indication for domain wall pinning by an increased oxygen vacancy concentration. The present findings thus exclude oxygen vacancies as governing mechanism for the enhancement of T_d and increased ferroelectric stability.

It is most likely that the off-centering nature of Bi^{3+} acts as the dominating mechanism, which causes the increased lattice distortion and pronounced domain formation. In NBT-based perovskites, Bi^{3+} shows larger off-centering than the other cations on the *A* site, due to its lone-pair electrons and orbital hybridization [288]. While it has been argued that the depolarization of NBT is dictated by the loss of the Bi-O hybridization through thermal vibrations, allowing for a more cubic environment [54], Moriyoshi et al. [288] showed that Bi^{3+} also exhibits strong off-centering at high temperatures. This suggests that Bi^{3+} also hybridizes with oxygen in the paraelectric cubic phase. Quenching then freezes-in the large off-center positions of Bi^{3+} when rapidly cooled down to room temperature [219]. Furnace cooled and Li-doped NBT ceramics display a disordered structure around the *A* site according to pair distribution function (PDF) analysis, while quenched samples show a more ordered Bi off-centering along $\langle 111 \rangle_{pc}$, which facilitates the larger rhombohedral distortion [219]. The favored displacement of Bi^{3+} along $\langle 100 \rangle$ in the cubic phase [288] may easily facilitate the increased tetragonal distortion observed in NBT-6BT, -9BT and -12BT.

All these observations suggest that the off-centering characteristic of Bi^{3+} can strongly influence the local structure upon quenching, enhancing structural deviations from the cubic/pseudocubic symmetry. Since the present investigations do not support an increase in residual stresses or oxygen vacancy concentration as governing mechanism in NBT-BT, the effect of the Bi^{3+} cation displacement can be deduced as being most influential on the enhanced lattice distortion upon quenching.

Short Summary

Quenching NBT-BT ceramics from sintering temperatures in air leads to a pronounced formation of a lamellar domain contrast. The NBT-3BT Q composition develops a rhombohedral *R*3*m* phase, which exhibits a lamellar herringbone-type domain configuration. The MPB-composition NBT-6BT Q is characterized by a volume fraction increase in lamellar *R*3*c* and *P*4*mm* domains. Similar domain features can be observed upon the poling-induced relaxor-to-ferroelectric transition. The quenched domain structure thus corroborates the hypothesized strengthened ferroelectric character of relaxor compositions. The enhanced lamellar domain formation correlates with the increase in rhombohedral and tetragonal lattice distortion especially noted for NBT-6BT Q. Ferroeleastic domains form in order to accommodate the occurring lattice strain upon quenching. Freezing-in the high-temperature off-center displacement of the Bi^{3+} ions most likely plays a crucial role for the enhanced lattice distortion. Other mechanisms, such as an increased oxygen vacancy concentration or residual thermal stresses could not be confirmed in the present study.

4.3 Temperature-Dependent Domain and Phase Assemblage

4.3.1 Temperature-Dependent Evolution of Furnace Cooled NBT-6BT

The temperature-dependent structural transitions of the MPB composition NBT-6BT were studied in the temperature range from 25 °C to 400 °C. The room temperature *P*4*bm* + *R*3*c* phase coexistence in NBT-6BT FC is illustrated in a grain in Figs. 4.33(a)-(d). The left area of the grain shows a strong *R*3*c* domain contrast (Fig. 4.33(b)), while small bright nanodomains of *P*4*bm* symmetry are present in the rest of the grain (Fig. 4.33(c)). A faint lamellar structure is visible, which relates to a more pronounced cluster of *P*4*bm* nanodomains (marked with an arrow). No $\frac{1}{2}$ {*ooe*} SRs could

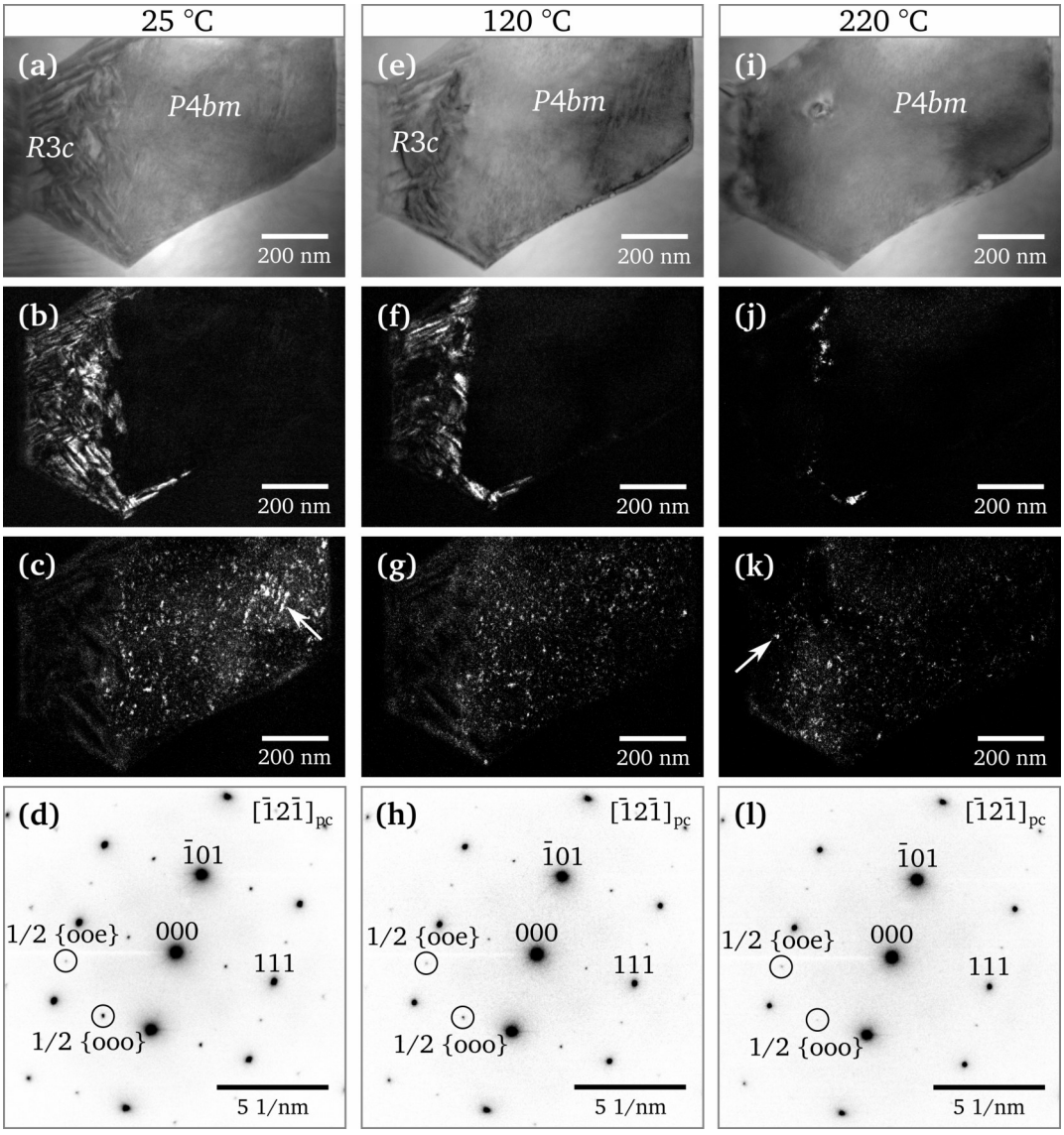

Figure 4.33: Temperature-dependent evolution in NBT-6BT FC. (a) BF image of the grain at 25 °C, depicting *R*3*c* domains and a homogeneous *P*4*bm* area. (b) DF image of the $\frac{1}{2}$ {*ooo*} SR encircled in (d), showing the *R*3*c* phase. (c) DF image of the $\frac{1}{2}$ {*ooe*} SR encircled in (d), showing the *P*4*bm* nanodomains. (d) SAED pattern of the depicted $[\bar{1}2\bar{1}]_{pc}$ zone axis. The same applies for the grain imaged at 120 °C in (e)-(f) and at 220 °C in (i)-(l) (reprinted from Ref. 289 with permission of John Wiley and Sons).

be observed within the *R*3*c* phase, however, a very weak DF intensity of *P*4*bm* also arises from within the *R*3*c* domains. Heating the grain results in the disappearance of the *R*3*c* phase. The *R*3*c* domain contrast starts to diminish between 100 and 120 °C and the $\frac{1}{2}$ {*ooo*} SRs decline in intensity (Figs. 4.33(e), (f) and (h)). The intensity of the $\frac{1}{2}$ {*ooe*} SRs is unchanged and the size of *P*4*bm* nanodomains (∼10 nm) is constant (Fig. 4.33(g)). However, the lamellar cluster has disappeared. At a temperature of 220 °C, the *R*3*c* phase has almost completely vanished (Figs. 4.33(i) and (j)). Likewise, the $\frac{1}{2}$ {*ooo*} SRs are barely visible (Fig. 4.33(l)) and have disappeared at 240 °C. In the former *R*3*c* area, newly formed nanodomains have appeared (indicated by an arrow in Fig. 4.33(k)). The observations illustrate the temperature-dependent transition from the *P*4*bm* + *R*3*c* mixture to a pure *P*4*bm* phase assemblage, which is stable at higher temperatures. The overall nanodomain contrast at 220 °C has slightly decreased and DF imaging becomes increasingly more difficult with higher temperature. A faint nanodomain contrast is still visible at the maximum heating temperature of 400 °C, which indicates a very gradual transition towards the high-temperature cubic phase.

The rhombohedral phase gradually vanishes in a large temperature range between 100 and 220 °C. Although the domain contrast has disappeared, very faint $\frac{1}{2}$ {*ooo*} SRs could be observed at higher temperatures up to 400 °C. The grain in Fig. 4.34(a) features a *R*3*c* domain contrast in its upper right area and $\frac{1}{2}$ {*ooo*} SRs in the corresponding SAED pattern (Fig. 4.34(b)). Heated to 400 °C, the contrast has vanished and the grain appears homogeneous without distinct features (Fig. 4.34(c)). In this temperature range, the NBT-BT system is ascribed to a mixture of *P*4*bm* and cubic *Pm*$\bar{3}$*m* [160]. At first glance, $\frac{1}{2}$ {*ooo*} SRs are absent from the corresponding SAED pattern (Fig. 4.34(d)).

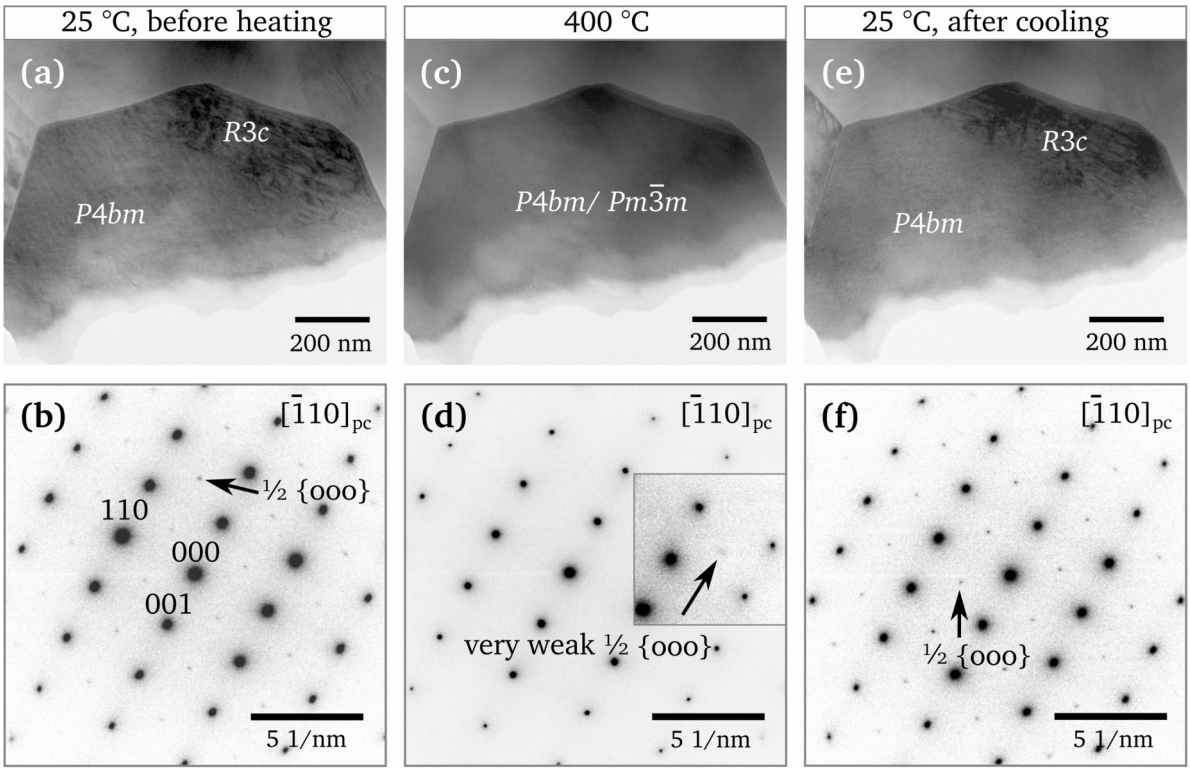

Figure 4.34: Temperature-dependent evolution of a grain in NBT-6BT FC. (a) BF image of the grain at 25 °C and corresponding SAED pattern in (b). The comparing BF image and SAED pattern of the grain at 400 °C is displayed in (c) and (d) and after the experiment when the grain is cooled down again to 25 °C in (e) and (f). Weak $\frac{1}{2}$ {*ooo*} SRs prevail at 400 °C, although the *R*3*c* domain contrast has disappeared.

However, increasing the contrast setting of the image, reveals very faint $\frac{1}{2}$ $\{ooo\}$ SRs, as illustrated in the inset. This indicates that local rhombohedral $a^-a^-a^-$ tilted regions are still present at 400 °C, while a macroscopically visible coherent *R*3*c* phase is absent. It also demonstrates that phase transitions in the NBT-BT system are not sharp, but dispersed over larger temperature ranges. This makes a clear assignment of temperature-dependent stable phase fields more difficult.

When cooling NBT-6BT FC, the *R*3*c* domain contrast starts to reappear in a temperature range from 180 to 140 °C, illustrating the reversibility of the rhombohedral-to-tetragonal transition, however with a slight temperature delay. In Fig. 4.34(e), the *R*3*c* contrast has returned in its former location after the heating experiment and the $\frac{1}{2}$ $\{ooo\}$ SRs are well visible again (Fig. 4.34(f)).

4.3.2 Temperature-Dependent Evolution of Quenched NBT-6BT

In NBT-6BT Q, the *R*3*c*-to-*P4bm* transition temperature is comparable to the FC state. The *R*3*c* domains start to disappear above 80 °C and vanish below 220 °C. Fig. 4.35 depicts a grain along the $[1\bar{2}3]_{pc}$ zone axis, where both sets of SRs are visible (Fig. 4.35(a)). A DF image of the grain area hosting the *R*3*c* domains is illustrated in Fig. 4.35(b) at room temperature (25 °C) before the heating experiment. In Fig. 4.35(c), the very same grain area is illustrated by a DF image of a $\frac{1}{2}$ $\{ooe\}$ SR at 200 °C. Here, the *R*3*c* phase has completely vanished and transformed into a *P4bm* nanodomain contrast.

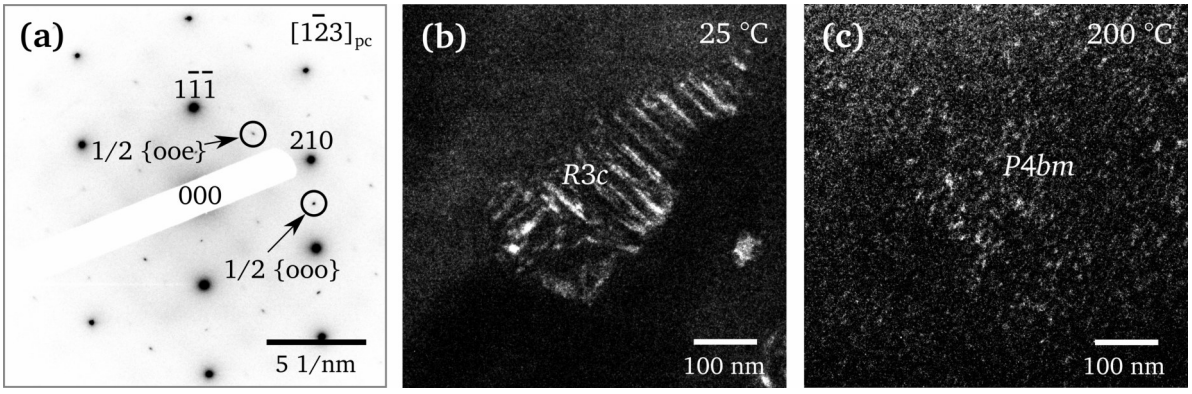

Figure 4.35: (a) SAED pattern of a grain in NBT-6BT Q viewed along the $[1\bar{2}3]_{pc}$ zone axis. (b) DF image at room temperature obtained from the encircled $\frac{1}{2}$ $\{ooo\}$ SR in (a) showing the *R*3*c* phase. (c) DF image at 200 °C obtained from the encircled $\frac{1}{2}$ $\{ooe\}$ SR, illustrating that the area has transformed into *P*4*bm* nanodomains.

Fig. 4.36 illustrates the temperature-dependent intensity change of both $\frac{1}{2}$ $\{ooo\}$ and $\frac{1}{2}$ $\{ooe\}$ SRs in NBT-6BT FC and Q. Note that for the FC sample, the intensity values were obtained from a $[\bar{1}2\bar{1}]_{pc}$ zone axis, while for the Q sample, a $[1\bar{2}3]_{pc}$ zone axis was chosen. However, the common feature to both zone axes is the appearance of both sets of SRs. The trends observed in both specimens are comparable. The $\frac{1}{2}$ $\{ooo\}$ SRs show a high intensity before heating. Their intensity then strongly declines between 80 and 220 °C, indicating the vanishing of the *R*3*c* volume fraction. As illustrated in Fig. 4.34, extremely faint $\frac{1}{2}$ $\{ooo\}$ SRs can persist between 240 and 400 °C, which also holds true for the quenched specimen. For both FC and Q, the *R*3*c* domain contrast starts to reappear at ∼180 °C upon cooling, accompanied by an increasing intensity of $\frac{1}{2}$ $\{ooo\}$ SRs. In both samples, the SR intensity after the experiment does not match the initial intensity. The reappeared *R*3*c* area upon cooling at 25 °C is somewhat smaller in size than before heating. This observation and the temperature delay of approx. 60 °C in the *R*3*c* reappearance indicate a certain sluggishness of

the system and deferred transitions. The intensity of $\frac{1}{2}$ $\{ooe\}$ SRs lies within a consistent range during the experiment, in accordance with the continuous presence of *P*4*bm* during the heating and cooling process. It should be noted that variations in the SR intensity can not only be caused by the relative volume fraction of each phase, but may also be slightly influenced by imaging conditions at each respective temperature and exact orientation of the zone axis with respect to the incident electron beam.

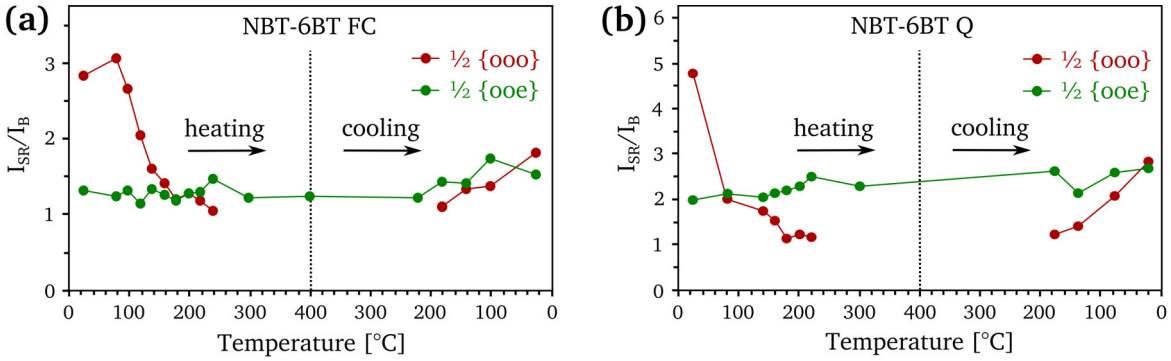

Figure 4.36: Intensity of $\frac{1}{2}$ $\{ooo\}$ and $\frac{1}{2}$ $\{ooe\}$ SRs in a single grain in NBT-6BT FC (a) and Q (b) during the heating and cooling process in the TEM derived from SAED patterns recorded at the specific temperatures. The ratio between the maximum intensity of the SR (I_{SR}) and the mean background intensity (I_B) is depicted.

A difference in the evolution of NBT-6BT FC and Q arises from the temperature-dependent stability of the tetragonal ferroelectric domain fraction, which is significantly higher in the quenched specimen. On average, the tetragonal *P*4*mm* domains are found to be stable up to higher temperatures compared to the *R*3*c* domains. Fig. 4.37(b) displays such tetragonal domains in a grain, viewed along the $[\bar{1}1\bar{1}]_{pc}$ zone axis (Fig. 4.37(a)). Tilting the grain to a $\langle 110 \rangle_{pc}$ zone axis did not reveal any $\frac{1}{2}$ $\{ooo\}$ SRs. The domains can thus with certainty be attributed to *P*4*mm*. At 260 °C, the contrast has slightly declined, but the domains are still well visible (Fig. 4.37(c)). Even at a high temperature of 300 °C, the domains have not yet completely disappeared (Fig. 4.37(d)). Over 340 °C, the contrast then strongly fades out. An interesting observation can be made when cooling the grain. The *P*4*mm* domains only reappear partly. At room temperature directly after the heating experiment, a central area within the grain exhibits few reappeared domains, which are surrounded by an increased grainy nanoscale contrast (Fig. 4.37(e)). However, when examining the grain several days later, the domains have grown in length and more domains have appeared (Fig. 4.37(f)). The grainy nanoscale contrast has transformed back to a lamellar domain structure, which is comparable to the state before the heating experiment.

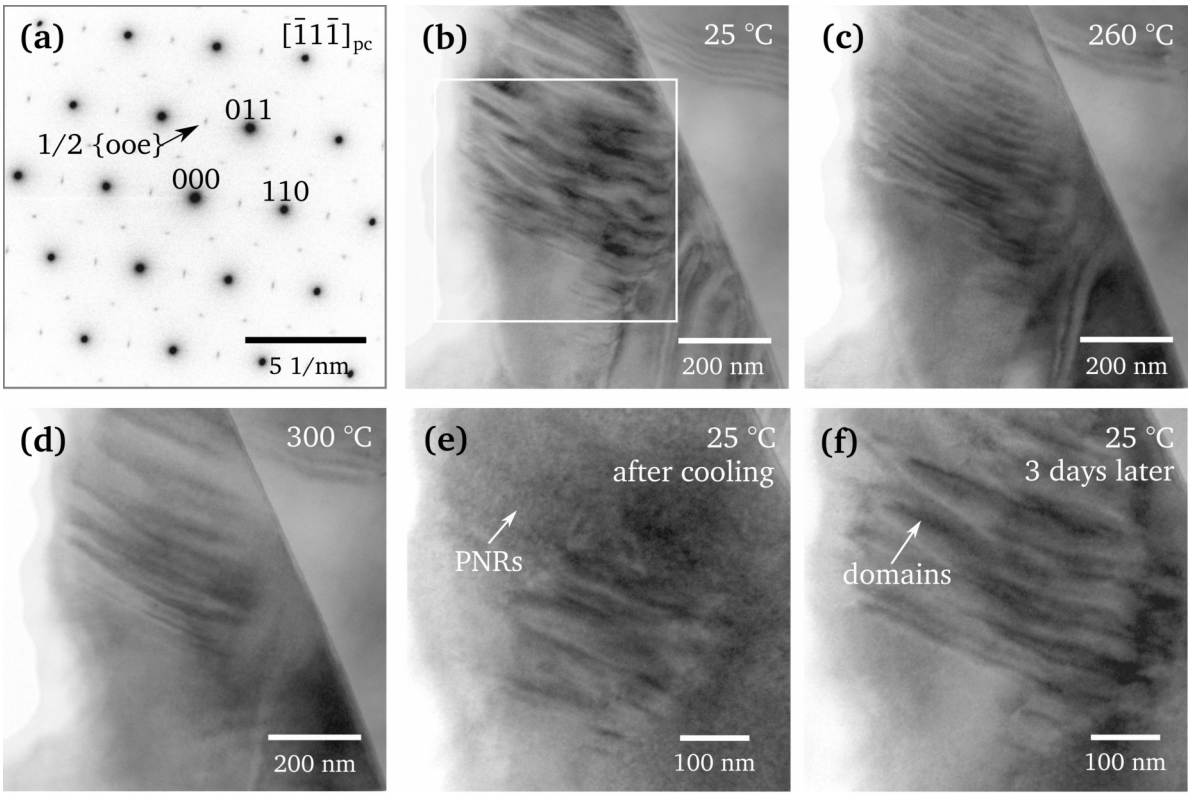

Figure 4.37: A grain in NBT-6BT Q viewed along the $[\bar{1}1\bar{1}]_{pc}$ zone axis. (a) SAED pattern with $\frac{1}{2}$ {*ooe*} SRs. (b) BF image at 25 °C, (c) at 260 °C, (d) at 300 °C, (e) directly after cooling at 25 °C and (f) three days later at 25 °C.

Similar observations can be made in Fig. 4.38. The central and upper grains depict tetragonal domains, while the grain on the left shows rhombohedral domains as noted in Fig. 4.38(b). At 140 °C, the rhombohedral domains have completely disappeared, while the tetragonal *P*4*mm* domains display a higher temperature stability (Fig. 4.38(c)). They start to slowly disintegrate from 120 °C onward and are still visible at 180 °C (Fig. 4.38(d)). Up to 240 °C, few tetragonal domains remain in the central grain (Fig. 4.38(e)). Imaged at 300 °C, the domain contrast in all grains has disappeared (Fig. 4.38(f)). A grainy contrast, characteristic for the relaxor nanostructure, starts to appear upon cooling around 220 °C (Fig. 4.38(g)) and becomes increasingly stronger with further temperature decrease. Lamellar tetragonal domains only start to reappear in the central grain between 140 °C and 100 °C and grow in size until room temperature is reached again (Fig. 4.38(h)). The rhombohedral domains on the left have not reappeared at all. Instead, a strong grainy contrast is visible directly after cooling. Reexamining the grains a couple of weeks later shows that the lamellar domain contrast has returned. Again, rhombohedral domains are present in the grain on the left and tetragonal domains are visible in the upper and central grain (Fig. 4.38(i)).

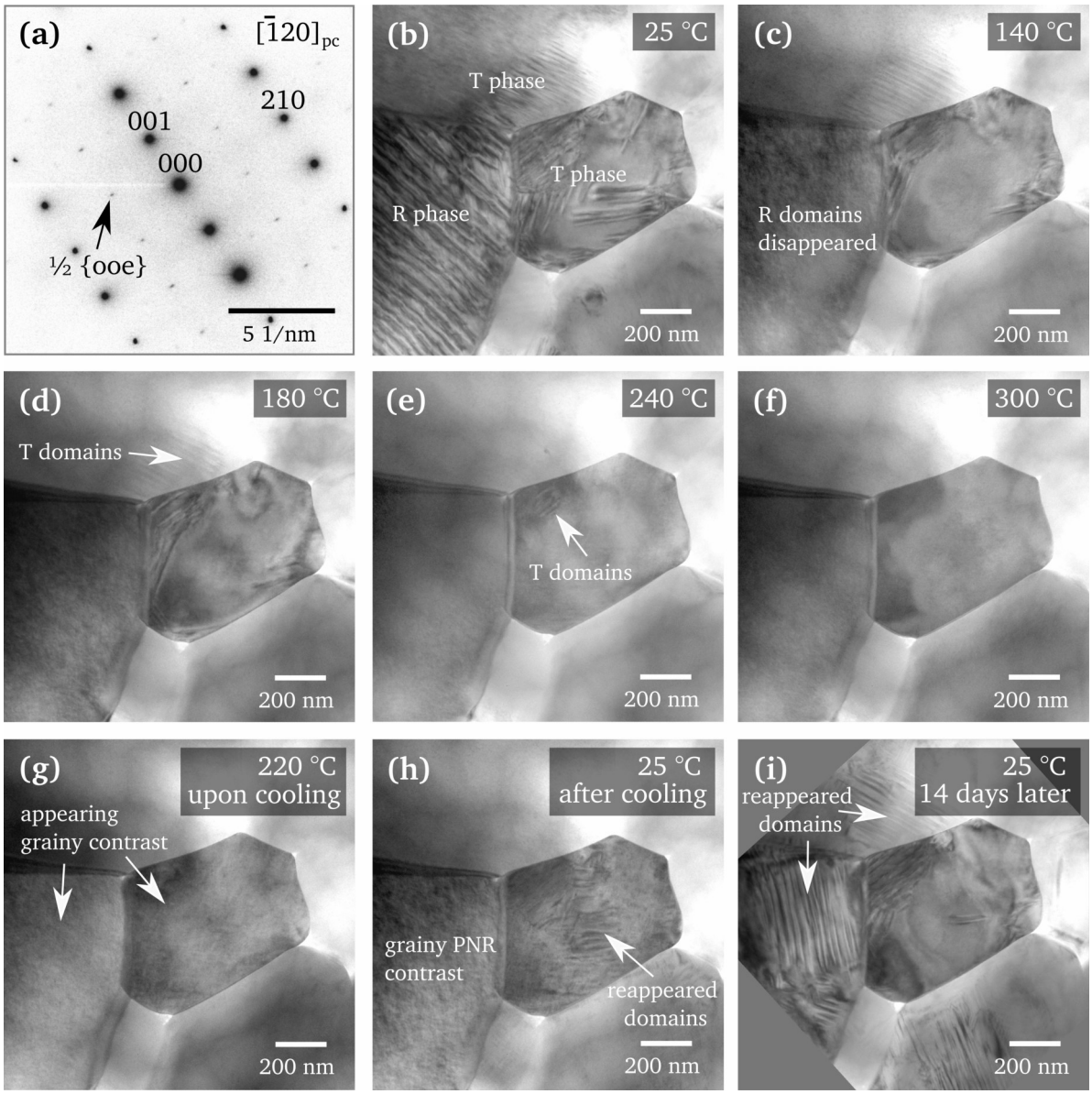

Figure 4.38: Evolution of tetragonal (*P*4*mm*) and rhombohedral (*R*3*c*) domains in NBT-6BT Q. (a) SAED pattern of the central grain, (b) BF image at 25 °C, (c) at 140 °C, (d) at 180 °C, (e) at 240 °C and (f) at 300 °C. (g) The grains upon cooling at 220 °C and at room temperature (h). Only few domains reappear directly after cooling, but have returned in (i), when imaged several days later (image rotation is due to the rotation of the sample in the holder).

4.3.3 Temperature-Dependent Depolarization of Poled NBT-6BT

The temperature-dependent evolution of poled NBT-6BT FC and Q has been examined. T_d, which lies around 100 °C for NBT-6BT FC, can be correlated to the onset of the loss of domain contrast upon heating. Fig. 4.39(b) depicts a grain with strong domain contrast, induced by the relaxor-to-ferroelectric transition upon poling. It can be observed that first few domains start to disappear at 80 °C, indicated with an arrow in Fig. 4.39(c). Interestingly, few new domain walls emerge at 100 °C (indicated with arrows in Fig. 4.39(d)). At 120 °C, the lamellar domain contrast within the grain is strongly reduced (Fig. 4.39(e)). Few remnants of domains are still visible at 160 °C

and have almost disappeared at 200 °C (Figs. 4.39(f) and (g)). Dark irregular structures visible at 200 °C (indicated by the arrow) are assigned to agglomerations of point defects, which are believed to be unrelated to the domain contrast. Upon cooling, a grainy nanodomain contrast emerges (Fig. 4.39(h)), which can be observed the next day as well (Fig. 4.39(i)). The poling-induced ferroelectric domain structure has completely transformed back to the relaxor features, characteristic for unpoled NBT-6BT FC. No delayed reappearance of ferroelectric domains occurred. The observations also verify that the poling-induced domain structure could be preserved during the TEM sample preparation under N_2-cooling in the ion mill. The most pronounced changes in the domain contrast during the depoling process in the TEM take place between 80 and 120 °C. This confirms that T_d (∼100 °C) is strongly linked to the disintegration of ferroelectric domains.

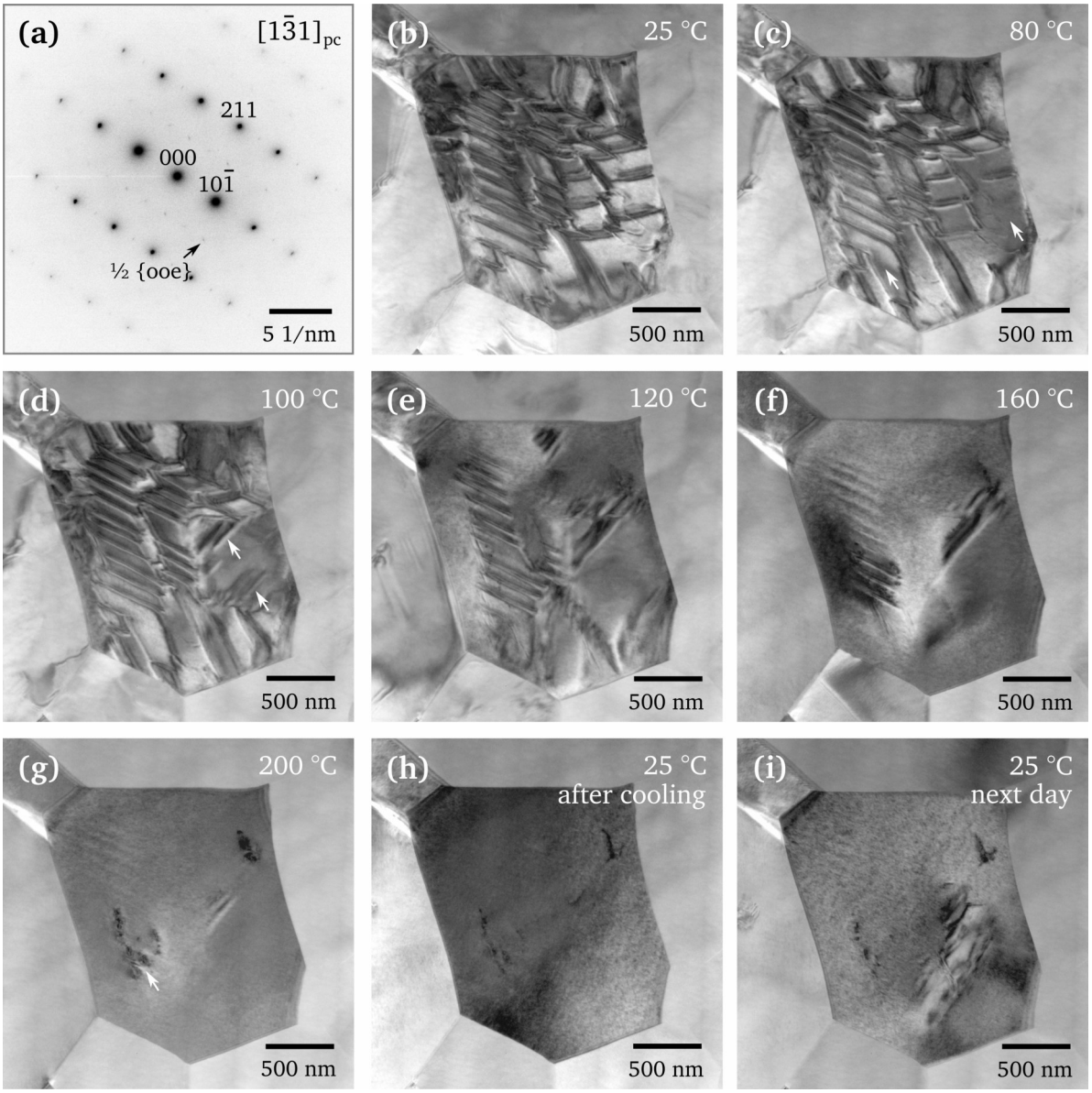

Figure 4.39: Temperature-dependent depolarization of a grain in poled NBT-6BT FC. (a) $[1\bar{3}1]_{pc}$ SAED pattern and (b) BF image at 25 °C before heating. (c) Domains start to disappear at 80 °C and further vanish at 100 °C (d), 120 °C (e), 160 °C (f) and up to 200 °C (g). (h) The grain at 25 °C directly after cooling, exhibiting a grainy nanoscale contrast. (i) No domains have reappeared the next day, indicating that the relaxor state is stable upon annealing.

Poling has been reported to stabilize the rhombohedral phase in NBT-6BT [185]. This can be visualized in Fig. 4.40, depicting DF images of the rhombohedral phase within a grain at different temperatures. Before heating, the poled grain exhibits a rhombohedral volume fraction on its left side (Fig. 4.40(a)). It is reduced at 100 °C (Fig. 4.40(b)) and mostly gone at 120 °C (Fig. 4.40(c)). Upon cooling, the rhombohedral volume fraction does not reappear. Reviewing the grain the next day shows only very small irregular rhombohedral areas of less than 50 nm in size (indicated with arrows in Fig. 34.40(d)). Accordingly, the SAED pattern before the depolarization features strong $\frac{1}{2}$ $\{ooo\}$ SRs (Fig. 4.40(e)), while they are almost not visible after the heating experiment (Fig. 4.40(f)). These observations indicate that the *R*3*c* fraction has formed upon the poling process. Once the grain is transferred to its unpoled state, the poling-induced large *R*3*c* phase fraction disappeared.

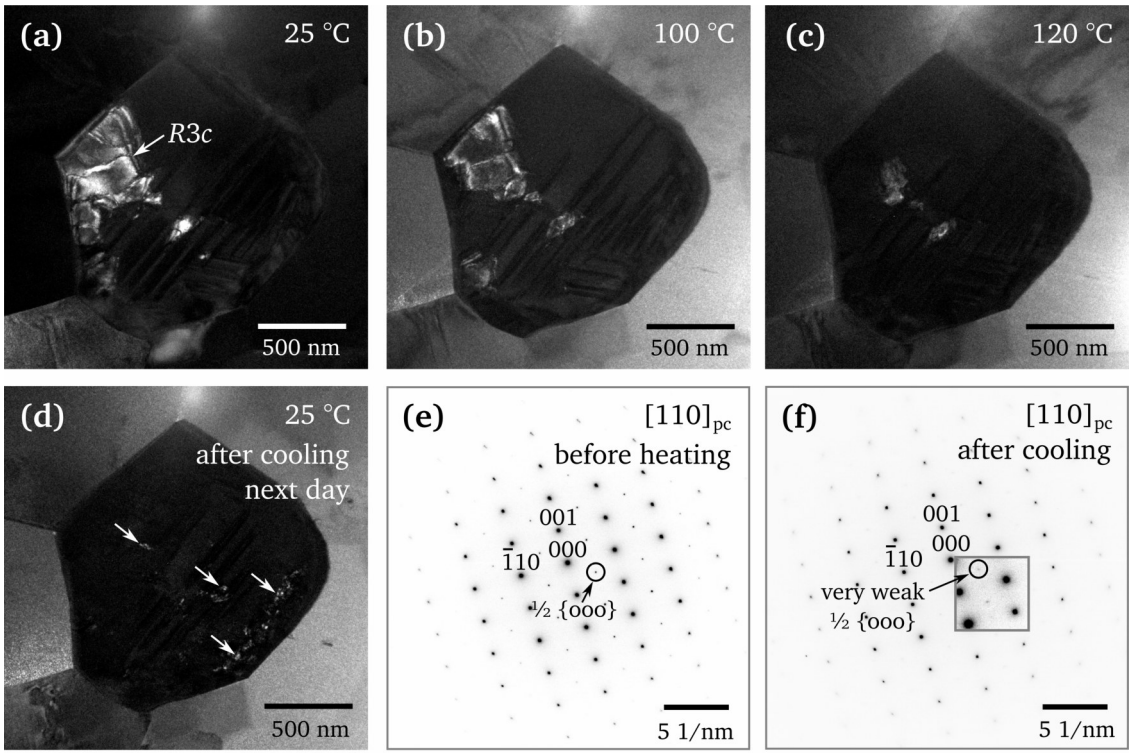

Figure 4.40: DF images illustrating the evolution of the *R*3*c* phase in poled NBT-6BT FC. (a) The large *R*3*c* volume fraction at 25 °C becomes smaller when heated to 100 °C (b) and has almost disappeared at 120 °C (c). Only very small rhombohedral areas (indicated with arrows) reappear after cooling (d). Accordingly, $\frac{1}{2}$ $\{ooo\}$ SRs feature a high intensity before heating (e) and are almost gone upon cooling (f).

In poled NBT-6BT Q, the disintegration of the lamellar domains sets in at a higher temperature compared to the poled FC specimen. Fig. 4.41(b) displays a grain with pronounced tetragonal lamellar domains. At 130 °C, the domain contrast is practically unchanged (Fig. 4.41(c)). Note that at this temperature, most of the domains in the poled NBT-6BT FC sample have already disappeared (compare Fig. 4.39). At around 150 °C, the onset of disintegration of the domains can be observed (indicated with an arrow in Fig. 4.41(d)). Lamellar domains are still visible at 170 °C (Fig. 4.41(e)), while they have almost disappeared at 200 °C (Fig. 4.41(f)). Unlike the FC sample, lamellar domains do reappear upon cooling (Figs. 4.41(h) and (i)). This is expected and shows that the unpoled quenched state is restored, which is characterized by a pronounced lamellar domain contrast. The reappeared domains are consistent in orientation with the poled state in (b).

A highly irregular contrast emerged throughout the entire grain at high temperature (Figs. 4.41(f) and (g)). Its origin is unclear, but it can be assumed that it is unrelated to the domain structure and is most likely caused by clusters of point defects. Within such clusters, a 'coffee-bean'-like contrast can occasionally be observed, indicating the presence of local strain fields. Coffee-bean defects are usually related to the local incorporation of elemental impurities or precipitates, but can in principle also be caused by agglomerations of vacancies, small fluid inclusions or local dislocations and stacking faults [290, 291]. Whether these defects have an influence on the domain reorientation during poling, cannot be excluded.

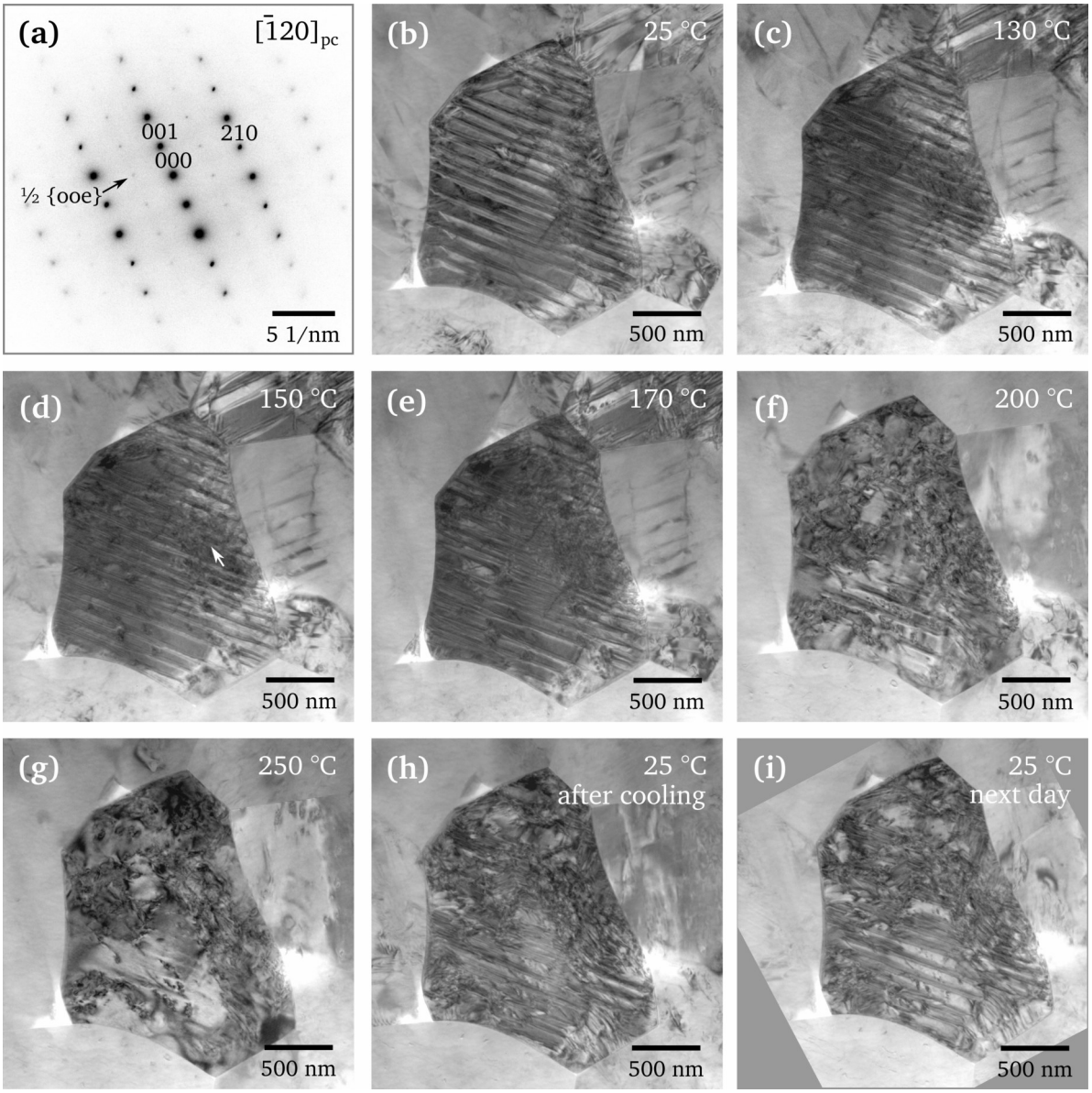

Figure 4.41: Temperature-dependent depolarization of a grain in poled NBT-6BT Q. (a) $[\bar{1}20]_{pc}$ SAED pattern, (b) BF image at 25 °C with strong lamellar domain contrast, which is still present at 130 °C (c) and 150 °C (d). Domains start to disintegrate visibly at 170 °C (e), which continues through 200 °C (f) to 250 °C (g). Domains reappear upon cooling (h) and are visible the next day (i).

4.3.4 Discussion of Temperature-Dependent Domain and Phase Evolution

The in-situ TEM investigations illustrate that temperature-dependent transitions in NBT-BT stretch over a wide temperature range and occur rather gradual. The start and end points of the transitions obtained from the heating experiments thus bear a certain subjectivity. Transition temperatures can also slightly vary between examined grains, depending, e.g., on the volume fraction of the different phases. It should be noted that the reproduced temperatures reflect the furnace temperature of the TEM heating holder, in which the specimen is situated. An exact temperature determination of the investigated area on the specimen is not possible. Considering the volatile character of Na^{+} and Bi^{3+}, the heating experiments were limited to a maximum temperature of 400 °C. EDS analysis conducted before and after heating on the same sample region did not indicate any elemental loss.

The *R*3*c*-to-*P*4*bm* transition occurs in the same temperature range for unpoled NBT-6BT FC and Q, starting at 80-100 °C and continuing to 200-220 °C. In this range, which spans more than 100 °C, the *R*3*c* domains gradually disappear and transform to *P*4*bm* nanodomains. Tetragonal *P*4*mm* domains, which are abundant in NBT-6BT Q, but hardly present in NBT-6BT FC, persist up to higher temperatures than the R domains. The observations are summarized in Fig. 4.42, illustrating the temperature-dependent changes of the qualitatively estimated phase fractions of *R*3*c*, *P*4*bm* and *P*4*mm*. Deduced from the marginal changes of $\frac{1}{2}$ $\{ooe\}$ SR intensities, the *P*4*bm* volume fraction is still large at the maximum heating temperature of 400 °C. With regard to another study [160], a coexistence with the paraelectric cubic phase can be assumed for the high-temperature range.

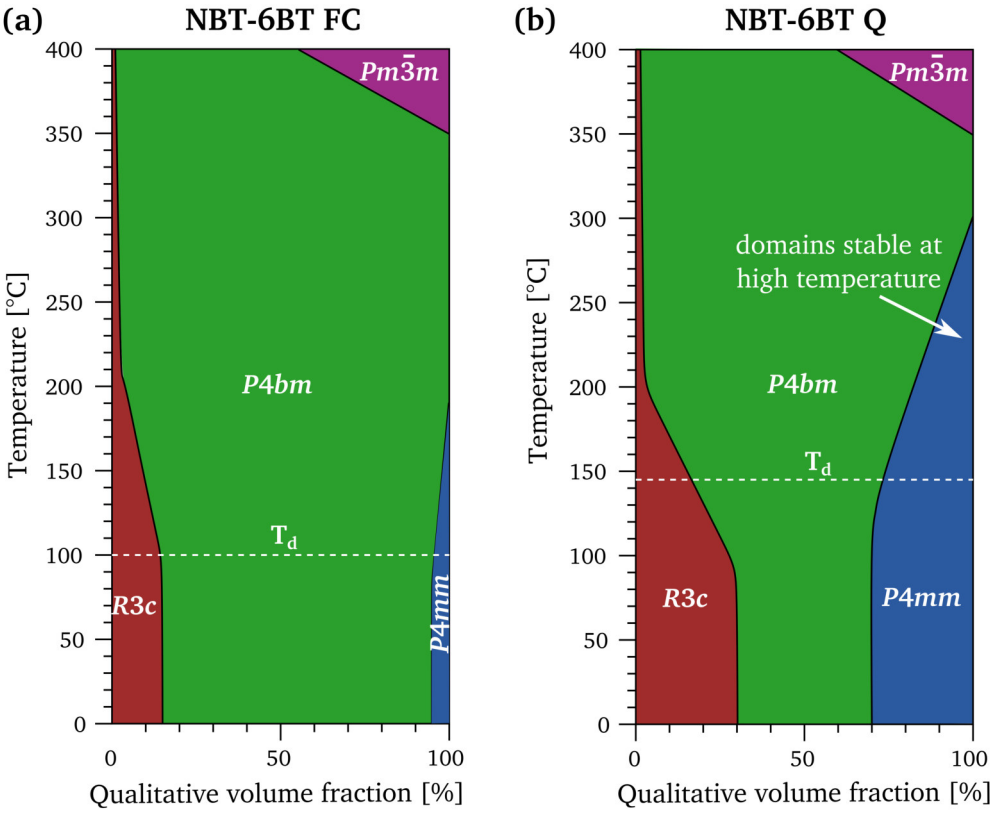

Figure 4.42: Schematic illustrating the temperature-dependent evolution of estimated phase fractions in unpoled NBT-6BT FC (a) and NBT-6BT Q (b), deduced from the TEM heating experiments. Tetragonal *P*4*mm* domains are abundant in NBT-6BT Q and stable at high temperatures, enhancing T_d (dashed white line).

It could further be emphasized that $\frac{1}{2}$ $\{ooo\}$ SRs of very low intensity persist up to 400 °C. The high-temperature range is thus not a mere $P4bm + Pm\overline{3}m$ mixture as previously reported [150, 160], but entails rhombohedral $a^-a^-a^-$ tilted regions as well. These presumably local rhombohedral areas can facilitate growth of larger rhombohedral volume fractions upon cooling, which explains the reappearance of the *R*3*c* domain contrast in the very same location as before the heating experiment. A temperature hysteresis for the reoccurring *R*3*c* phase exists, indicating a kinetically delayed retransformation of *P*4*bm* to *R*3*c*. During the experiments, identical heating and cooling rates were adhered, with waiting periods of ∼10 min at temperatures of interest before image acquisition. Supposing the system is allowed to equilibrate longer at certain temperature intervals, a more consistent temperature range for the dis- and reappearance of the domains can be assumed. Considerably larger waiting periods would, however, compromise the feasibility of the conducted heating experiments.

Temperature ranges for the disappearance of the R and T domains upon heating and their respective reappearance upon cooling are summarized in Table 4.2. In the quenched specimen, a wide temperature variety for the disintegration of the T domains was observed. In some grains, they disappear between 120 and 240 °C, while several grains showed a persisting domain contrast even above 300 °C. This can be rationalized by assuming a certain degree of structural differences between examined grains. As noted for NBT-6BT Q, the overall tetragonality is increased by the quenching process. The local tetragonal distortion may slightly vary between grains. A high tetragonal deviation from the cubic symmetry can imply a superior solidification of tetragonal domains, which in turn may exhibit a larger temperature-dependent stability by dissipating only at elevated temperatures. It is therefore conclusive to assume that the high-temperature stability of the *P*4*mm* domains benefits the overall increase in T_d (and $T_{F\text{-}R}$) from 100 °C in NBT-6BT FC to 140 °C in NBT-6BT Q. The persistence of tetragonal domains indicates a prolonged stability of the ferroelectric order at higher temperatures. This aligns with findings of a stabilized tetragonal phase in Zn-doped NBT-6BT and -9BT, which rationalizes an enhanced temperature-dependent stability of piezoelectric properties [286]. In NBT-6BT FC, *P*4*mm* domains are almost absent and the depolarization is rather dictated by the disintegration of the *R*3*c* domains, which takes place at a lower temperature range.

Table 4.2: Temperature ranges for the disappearance and reappearance of domain structures in unpoled and poled NBT-6BT FC and Q, deduced from the TEM-heating experiments.

	***R*3*c* domains disappear**	***R*3*c* domains reappear**	***P*4*mm* domains disappear**	***P*4*mm* domains reappear**	***P*4*bm* $\frac{1}{2}$ $\{ooe\}$ SRs present**
NBT-6BT FC	100-220 °C	180-25 °C	almost none present	almost none present	throughout
NBT-6BT Q	80-200 °C	180-25 °C	120-300 °C	140-25 °C	throughout
NBT-6BT FC poled	80-140 °C	almost none	80-200 °C	almost none	throughout
NBT-6BT Q poled	80-130 °C	partly	140-250 °C	partly	throughout

Upon poling, *P*4*mm* domains appear in both NBT-6BT FC and Q specimens. Still, in poled NBT-6BT Q, they start to disappear at higher temperatures compared to poled NBT-6BT FC. This likely originates from a close correlation between the strengthened tetragonal distortion and higher temperature-dependent domain stability in the quenched composition. It is, e.g., also reported that *P*4*mm* domains in a BT-rich composition (NBT-11BT), where the tetragonal distortion is very pronounced, only start to disappear at a high temperature of 170 °C [160]. The TEM observations in this work illustrate that T_d is strongly linked to the onset of the ferroelectric domain disintegration. In poled NBT-6BT FC, the R and T domains start to disappear around 80 °C, which then progresses significantly between 100 °C and 120 °C. T_d and $T_{F\text{-}R}$ (∼100 °C) are thus dictated by the temperature range, in which the largest portion of ferroelectric domains is transformed back to the relaxor state. Fig. 4.43(a) illustrates this correlation by superimposing the temperature range in which the domain contrast disappears with the development of the temperature-dependent permittivity curve. In poled NBT-6BT Q, according to an increased T_d, the onset of tetragonal domain disappearance was observed to start at a higher temperature of 140 °C. Therefore, T_d and $T_{F\text{-}R}$ seem to be mainly influenced by the onset of the vanishing *P*4*mm* domain contrast (Fig. 4.43(b)), which in turn is dictated by the enhanced degree of tetragonal distortion upon quenching. Previous reports on NBT-based ceramics linked the increase in T_d and the stabilization of ferroelectric order upon quenching to the stabilization of a ferroelectric rhombohedral phase [13, 230, 231]. A poling-induced increase in the rhombohedral fraction, which disappears upon depolarization and does not (or only partly) return upon cooling, could be confirmed by the TEM investigations. However, no significant differences in the temperature dependence of the *R*3*c* phase was observed for FC and Q. Deduced from the TEM study here, the major differences in the temperature-dependent evolution of NBT-BT FC and Q (unpoled and poled) relate to the tetragonal phase and the ferroelectric *P*4*mm* domain contrast. This demonstrates that not only the increase in rhombohedrality, but also the increase in tetragonal distortion and the subsequent stabilization of long-range T domains is highly influential for retaining the ferroelectric order at elevated temperatures.

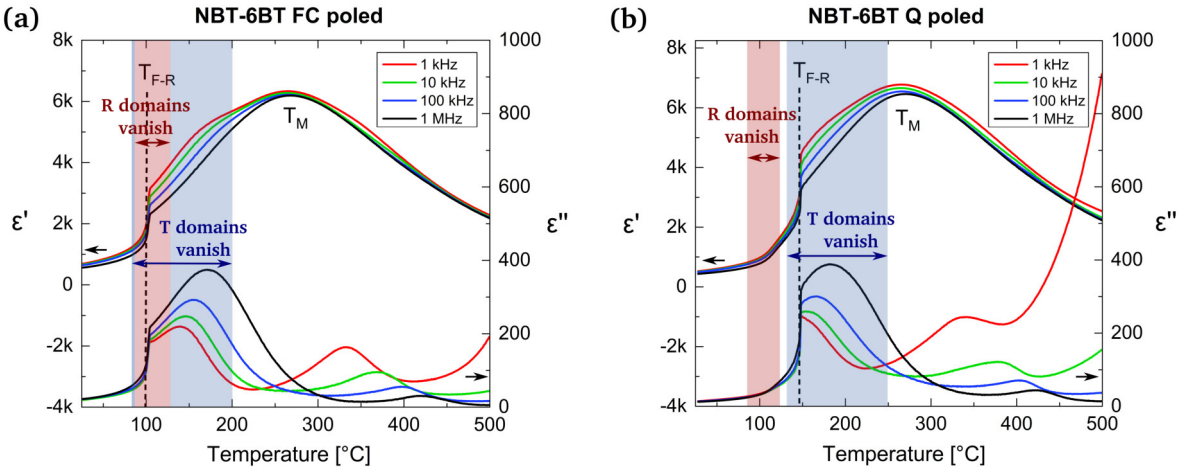

Figure 4.43: Temperature-dependent real (ε') and imaginary (ε'') part of the permittivity in poled NBT-6BT FC (a) and Q (b). The temperature ranges where R and T domains disappear are noted in both graphs (permittivity data acquired by A. Wohninsland).

Investigating the cooling process via TEM gives further insights about the dynamics of NBT-BT ceramics. Domains do not directly reappear upon cooling; instead, a grainy nanodomain contrast manifests itself between 220 °C and room temperature. This phenomenon was predominantly

observed in NBT-6BT Q due to the high fraction of lamellar domains before heating. However, it is also present in NBT-6BT FC, where it is less prominent due to fewer domains in the furnace cooled state. Hence, this characteristic appears to be a feature of NBT-BT in general and is not necessarily a consequence of quenching. While PNRs start to develop below T_B (∼700-750 °C for NBT-BT [292]) as dynamic polarization fluctuations with a short lifespan, the characteristic relaxor behavior becomes visible in the temperature regime below T_M (∼260 °C). Here, the relaxor typical frequency dispersion of the permittivity is related to the thermal evolution of the PNR dynamics. Their lifespan increases and local strain fields can develop, which can stabilize the existence of permanent PNRs (or nanodomains) [293]. With decreasing temperature, the portion of static PNRs increases [294] until the freezing temperature, T_{VF}, is reached and PNRs are not dynamic any longer. The onset of the appearing grainy contrast during cooling (∼220 °C) correlates well with the onset of the strong frequency dispersion of the permittivity. The increasing nanoscale contrast thus reflects the manifestation of a growing fraction of static PNRs/nanodomains during cooling.

The grainy contrast remains prominent directly after cooling and only partly transforms back into a lamellar domain structure. After some time (observed the next day), more lamellar domains reappear and the initial state as before the experiment is restored. The kinetically delayed retransformation of nanodomains into larger domains implies that a metastable state exists directly after the heating experiment and a certain amount of relaxation time is required in order to return to the original domain structure. Regarding relaxor ferroelectrics in the light of the random-field model, it is argued that the slowing down and freezing of PNR dynamics results from constraints of internal random electric fields, also preventing the formation of large scale ferroelectric structures [106, 125]. The random distribution of the heterovalent cations in relaxors results in structural and chemical charge disorder, causing the formation of such local random electric fields [125, 295], which energetically favor the formation of polar nanoregions [296]. It is conceivable that the presence of such random electric fields in the bulk of NBT-6BT may hinder an immediate and large-scale domain formation upon cooling. Instead, a slow relaxation and kinetically delayed formation of a long-range domain structure is promoted.

Short Summary

In-situ heating experiments on the NBT-6BT FC and Q composition illustrate that phase transitions occur gradually over wide temperature ranges. The *R*3*c*-to-*P*4*bm* transition takes place between 80 °C and 220 °C, deduced from the declining *R*3*c* domain contrast in favor of newly formed *P*4*bm* nanodomains. However, very weak $\frac{1}{2}\{ooo\}$ SRs also persist up to 400 °C, accounting for the reversibility of the transition. The pronounced lamellar *P*4*mm* domain contrast in the quenched sample partially persists up to 300 °C. The initial domain structure in both FC and Q samples can be restored upon cooling, however, is kinetically delayed. In poled NBT-6BT FC, the temperature-dependent depolarization is reflected in the disintegration of the domain contrast, starting at 80-100 °C, which correlates with a T_d of 100 °C. Poled NBT-6BT Q exhibits a later onset of tetragonal domain disappearance (∼140 °C), according to an increase in T_d. The differences in the temperature-dependent stability of the tetragonal domain structure are likely correlated to the more pronounced tetragonal lattice distortions in the quenched composition.

4.4 The Nanoscale Structure of NBT-BT

4.4.1 Ferroelectric Domains and Nanodomains in HRTEM

HRTEM allows to comparatively image the typical ferroelectric structure (lamellar domains) and the nanoscale relaxor structure (nanodomains) at high magnification (Fig. 4.44). Ferroelectric domains are well visible in TEM-BF at low magnifications (Fig. 4.44(a)). In HRTEM, the domain-wall contrast becomes less pronounced. Nevertheless, a blurred dark line is visible in Fig. 4.44(b), representing a 90° domain wall. The width of the domain wall amounts to 1.5 nm (edge-on view). It corresponds to approx. 4 unit cells, over which the $[001]_T$ polarization direction changes by 90°. This is consistent with observations made by HAADF imaging (compare Fig. 4.55 on page 113), where the polar displacement of the Ti^{4+} cation gradually changes direction over several unit cells. On the left side of the domain wall in Fig. 4.44(b), lattice fringes are well visible, while they are less pronounced on the right side. The varying contrast can be rationalized by the slightly different diffraction conditions within each domain, causing a difference in phase shift. The phase contrast is also highly influenced by slight thickness variations in the specimen.

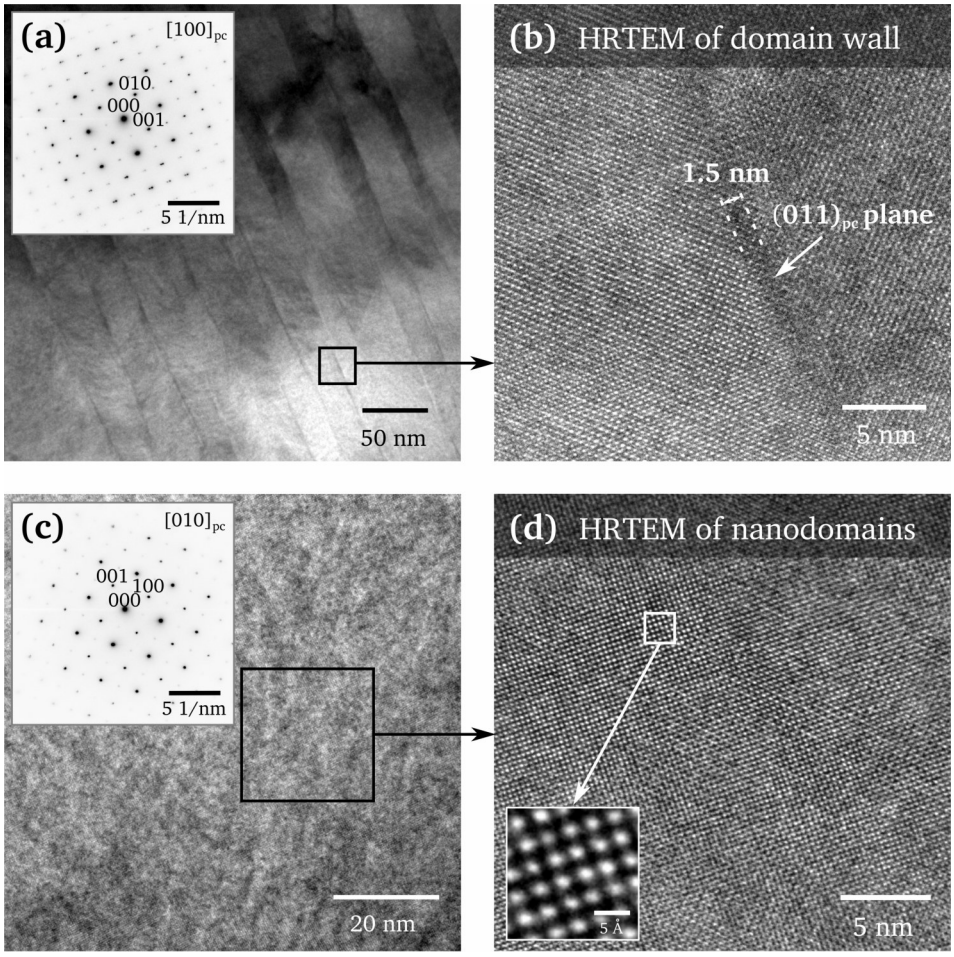

Figure 4.44: Comparison of the ferroelectric and relaxor structure. (a) TEM-BF image of ferroelectric domains in NBT-9BT Q, viewed along $[100]_{pc}$ (SAED pattern as inset). (b) Domain wall in HRTEM with a width of 1.5 nm. (c) TEM-BF image of the grainy nanoscale relaxor structure in NBT-6BT Q, viewed along $[010]_{pc}$ (SAED pattern as inset). (d) Corresponding area in HRTEM showing no distinct features. The inset illustrates a magnified view of the HRTEM image.

In contrast to the ferroelectric domains, the relaxor structure is characterized by a grainy appearance at low magnifications (Fig. 4.44(c)). However, no distinct features appear in the HRTEM image (Fig. 4.44(d)). This is largely comparable to another TEM study on NBT-BT by Zhou et al. [200], showing a grainy contrast (interpreted as PNRs), but no distinct characteristics in HRTEM. The inset in Fig. 4.44(d) illustrates a magnified area of the image. Lattice spacings can generally be deduced from HRTEM images. Whether the image shows bright atoms on a dark background (negative contrast) or dark atoms on a bright background (positive contrast) is not directly interpretable. In order to specify the atomic positions and interpret the contrast correctly, image simulations can be conducted. For obtaining a simulated image which is comparable to the imaged HRTEM micrograph, parameters such as the specimen thickness, the alignment of the specimen with respect to the optical axis, the defocus and aberration values need to be known [234].

4.4.2 Nanodomains in Relaxor NBT-6BT

As already illustrated in the previous chapters, TEM-DF imaging acts as a viable tool to directly visualize the nanodomains in the relaxor compositions. The *P4bm* nanodomains are characterized by a plate-like morphology. These platelets lie in the $(100)_{pc}$, $(010)_{pc}$ and $(001)_{pc}$ planes of the pseudocubic crystal lattice. All three orientation variants occur in the same grain region, as illustrated in Fig. 4.45. The BF image shows a grainy nanoscale contrast (Fig. 4.45(a)). The corresponding SAED pattern features three variants of the $\frac{1}{2}$ $\{ooe\}$ SRs: $\frac{1}{2}$ (oeo), $\frac{1}{2}$ (eoo) and $\frac{1}{2}$ (ooe) (Fig. 4.45(b)).

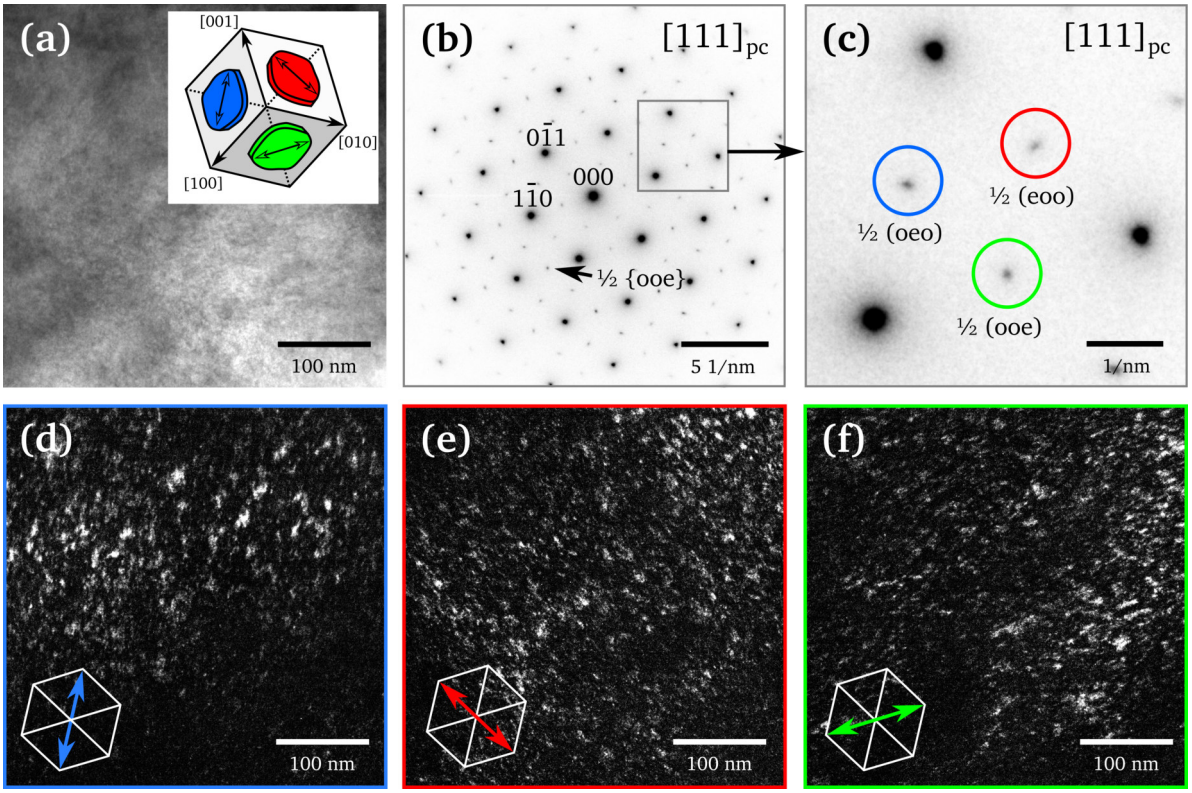

Figure 4.45: Plate-like *P4bm* nanodomains in NBT-6BT FC. (a) BF image with grainy nanoscale contrast. The inset illustrates the location of the three $\{001\}_{pc}$ platelet variants within the unit cell. (b) Corresponding $[111]_{pc}$ SAED pattern. (c) Enlarged region indicating the three SR variants: $\frac{1}{2}$ (oeo), $\frac{1}{2}$ (eoo) and $\frac{1}{2}$ (ooe). (d)-(f) DF images obtained from each SR variant, noted with the respective color. The elongation direction of the nanodomains projected on the viewing plane is indicated by the colored arrows and corresponds to the arrows in the schematic in (a).

The SR variants show a slight elongation in three different reciprocal directions as illustrated in the magnified section of the diffraction pattern in Fig. 4.45(c). From each variant, a DF image is obtained, reflecting the same grain area as depicted in the BF image. Corresponding DF images and encircled SR are noted with the same color. In each DF image, the bright nanodomains show a slight elongation direction projected on the viewing plane, which is indicated by colored arrows (Figs. 4.45(d)-(f)). The three variants arise from *P*4*bm* nanodomains lying in $\{001\}_{pc}$ planes and corresponding SRs stretching along $\langle 001\rangle_{pc}$. The location of the *P*4*bm* platelets in the pseudocubic unit cell in real space is illustrated in the schematic in Fig. 4.45(a) with the respective color. Note that the platelets are inclined towards the viewing direction, when imaged along $\langle 111\rangle_{pc}$. A comparable configuration was also noted for pure NBT, where *P*4*bm* platelets were found to be dispersed within the rhombohedral matrix [84, 175].

The presence of three nanodomain variants within a grain region can also be illustrated by masking a FFT obtained from a HRTEM image and forming an inverse FFT. Fig. 4.46(a) shows a HRTEM micrograph viewed along $[111]_{pc}$. In the corresponding FFT (Fig. 4.46(b)), the three different $\frac{1}{2}$ $\{ooe\}$ SR variants are selected and masked (red, green and blue circles). From each variant, an inverse FFT image is formed, containing the image information which corresponds to the selected SRs. The three inverse FFTs can then be merged into one single image as illustrated in Fig. 4.46(c). The regions corresponding to the three SR variants are displayed in the respective color. A close network of differently oriented nanodomains becomes visible.

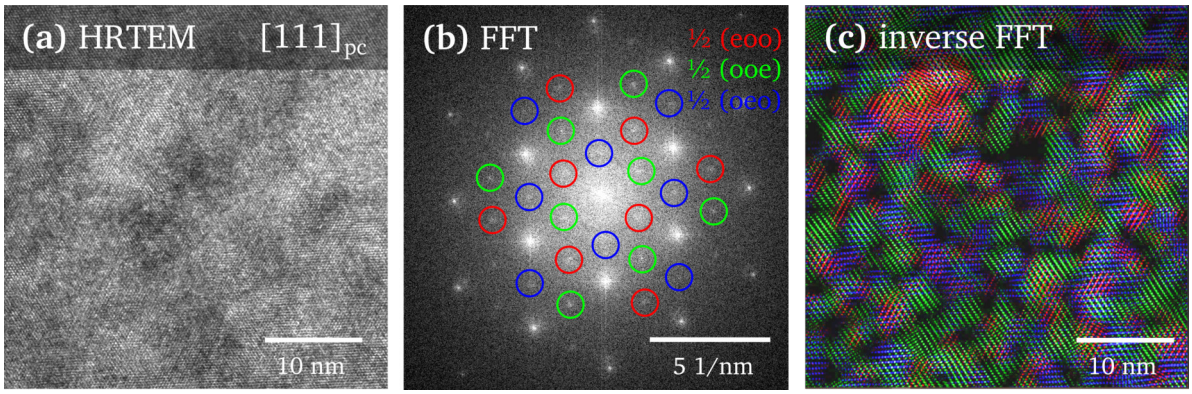

Figure 4.46: (a) HRTEM image of a grain in NBT-6BT FC viewed along the $[111]_{pc}$ zone axis. (b) Corresponding FFT, where the three SR variants, $\frac{1}{2}$ (oeo), $\frac{1}{2}$ (eoo) and $\frac{1}{2}$ (ooe) are masked. (c) Overlay of the three inverse FFTs obtained from the masked SRs. Nanoregions corresponding to the SR variants are displayed in the respective color.

The plate-like morphology of the nanodomains becomes especially visible when viewed along the $[013]_{pc}$ direction as in Fig. 4.47. The $\frac{1}{2}$ (eoo) SR variant visible in the SAED pattern stretches along the $[100]_{pc}$ direction (Fig. 4.47(a)) and corresponds to *P*4*bm* nanodomains, which lie in $(100)_{pc}$ planes (Fig. 4.47(b)). Here, the $(100)_{pc}$ plane and the platelets are oriented parallel to the viewing direction (edge-on). The platelets exhibit a maximum thickness of 3.5 nm and a lateral expansion of up to 35 nm. Taking a closer look at the SAED pattern also reveals very weak $\frac{1}{2}$ $\{ooo\}$ SRs. A DF image obtained from such an SR, the $\frac{1}{2}$ $(\bar{1}3\bar{1})$ reflection, reveals small *R*3*c* nanodomains (4.47(c)). Both DF images of the *P*4*bm* and *R*3*c* phase were obtained from the exact same grain regions. The *R*3*c* nanodomains are fewer in number and exhibit a less pronounced contrast in DF imaging, which corresponds to the very weak $\frac{1}{2}$ $\{ooo\}$ SR intensity. Furthermore, the rhombohedral nanodomains do not exhibit a plate-like morphology. Their size ranges from approx. 1 nm up to 5 nm.

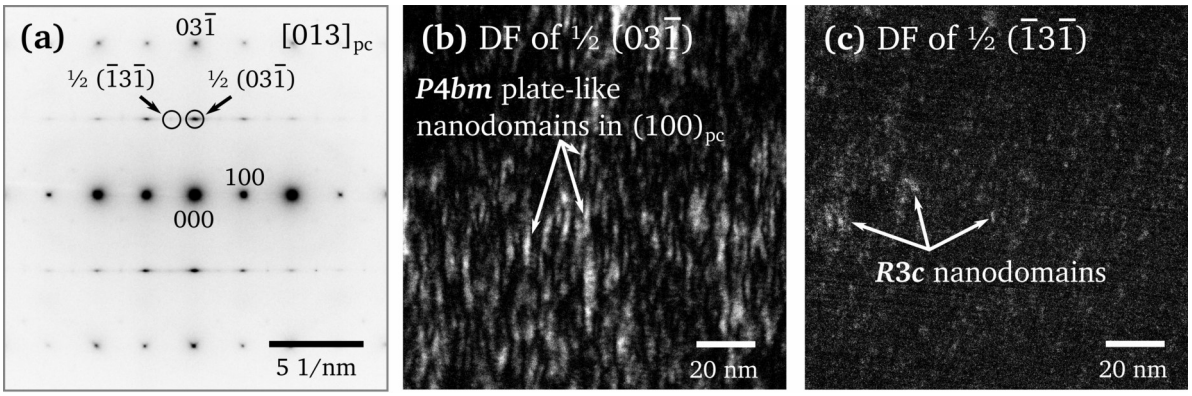

Figure 4.47: (a) SAED pattern of NBT-6BT FC viewed along the $[013]_{pc}$ zone axis. A $\frac{1}{2}$ (eoo) SR, the $\frac{1}{2}$ $(03\bar{1})$ reflection, and a $\frac{1}{2}$ $\{ooo\}$ SR, the $\frac{1}{2}$ $(\bar{1}3\bar{1})$ reflection, are encircled and corresponding DF images are displayed in (b) and (c), respectively. Among the plate-like *P*4*bm* nanodomains, a minor fraction of *R*3*c* nanodomains is present, depicted in (c).

4.4.3 Association of Nanodomains and Ferroelectric Domains

In the compositions NBT-9BT and -12BT, the ferroelectric domain contrast is increased, however, $\frac{1}{2}$ $\{ooe\}$ SRs still indicate the presence of *P*4*bm* nanodomains. NBT-9BT marks a transition between relaxor and ferroelectric state. Deduced from the strong frequency dispersion of the permittivity, the composition exhibits relaxor behavior, while the domain structure is already characterized by abundant ferroelectric *P*4*mm* domains. A grain is illustrated in Fig. 4.48(a), displaying lamellar domains, which completely occupy the right half of the grain. The left half is characterized by both lamellar domains and areas without domain contrast. An SAED pattern obtained from the latter region (Fig. 4.48(b)) exhibits well visible $\frac{1}{2}$ $\{ooe\}$ SRs, while the lamellar domain area shows no obvious SRs (Fig. 4.48(c)). Drawing an intensity profile over the main and the superlattice reflections, however, reveals weakly intense remnants of $\frac{1}{2}$ $\{ooe\}$ SRs also for the lamellar domain region. A corresponding DF image in Fig. 4.48(d) illustrates the location of the *P*4*bm* nanodomains. They are abundant in regions, where a lamellar domain contrast is absent. An intergrown structure of nanodomains and lamellar domain bands results, which is visualized in Fig. 4.48(e) by a color map. Furthermore, it can be observed that a very weak nanodomain signal also arises from within the lamellar domains (Fig. 4.48(d) as indicated), which corresponds to the weak SRs observed in the SAED pattern. Therefore, a significantly reduced population of nanodomains exists within the lamellar ferroelectric domains. This demonstrates a highly complex structure, where nanoscale polar areas and long-range domains are closely associated within the same grain region.

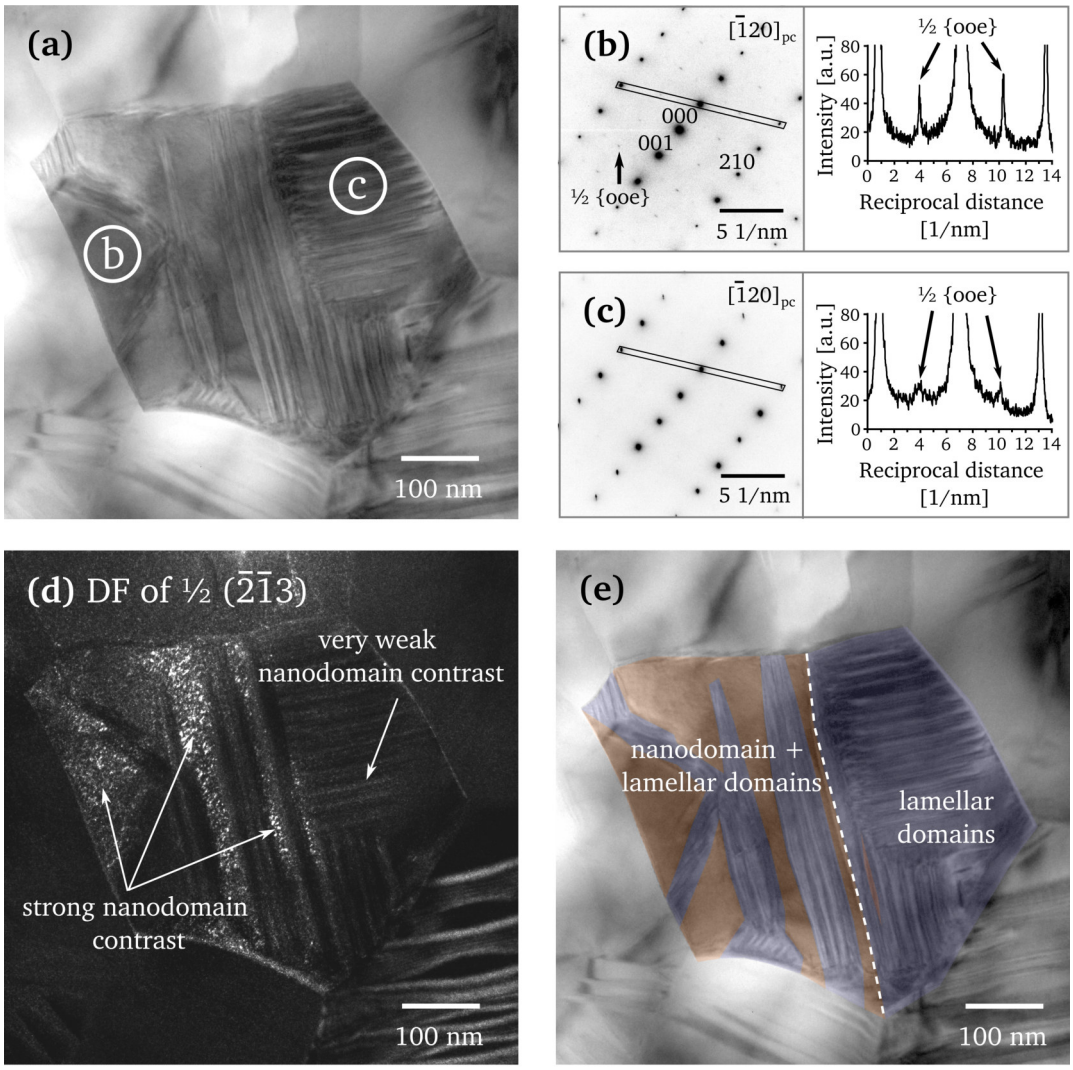

Figure 4.48: (a) BF image of a grain in NBT-9BT FC. The location of the SAED aperture for obtaining the SAED patterns in (b) and (c) is noted. In (b), $\frac{1}{2}\{ooe\}$ SRs are clearly visible in the diffraction pattern and the intensity profile (location marked by the rectangle in the SAED pattern). In (c), very weak SRs only become visible in the intensity profile. (d) DF image obtained from a $\frac{1}{2}\{ooe\}$ SR. (e) Color overlay emphasizing the intergrowth of nanodomains and lamellar domains (reproduced from Ref. 297 with permission of the American Physical Society).

The same feature can also be observed in NBT-12BT. The tetragonal composition exhibits a ferroelectric character and lamellar *P*4*mm* domains, while *P*4*bm* and *R*3*c* only occur in minor phase fractions. However, $\frac{1}{2}\{ooe\}$ SRs were also observed within areas, which are occupied by long-range *P*4*mm* domains (Fig. 4.49(a)). The DF image obtained from the encircled SR reveals nanodomains embedded within the ferroelectric domain structure (Fig. 4.49(b)). This illustrates a complex hierarchical configuration of nanodomains and lamellar domains. Such an observation can only be made by combining BF, DF and SAED methods and cannot be inferred from BF imaging alone.

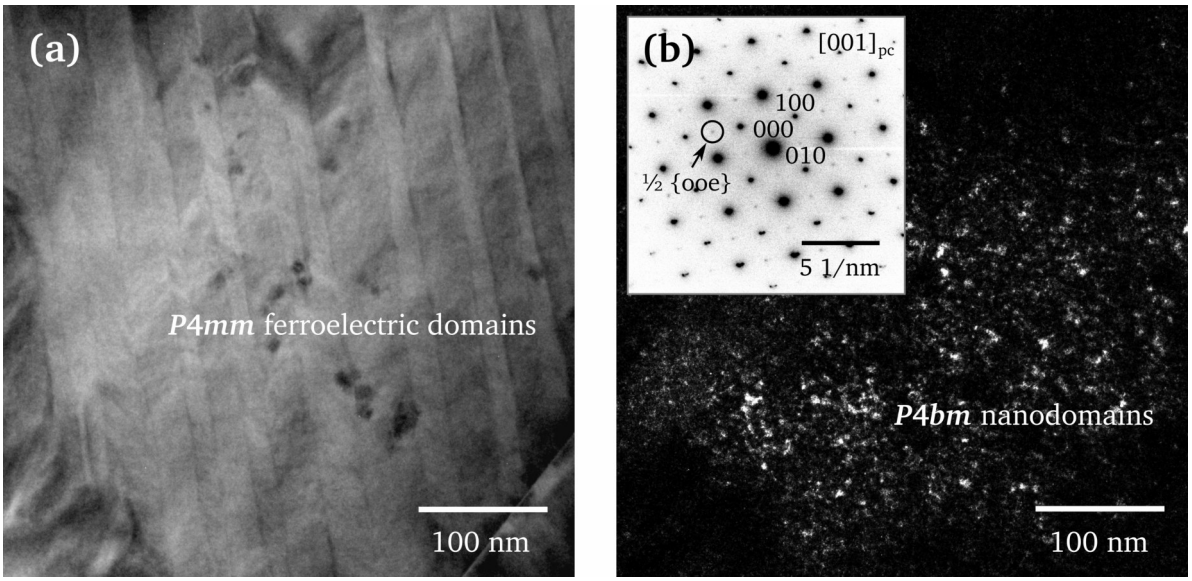

Figure 4.49: (a) A grain in NBT-12BT FC displaying lamellar ferroelectric *P*4*mm* domains. (b) Corresponding DF image of the same area obtained from the encircled $\frac{1}{2}$ $\{ooe\}$ SR, visible in the $[001]_{pc}$ SAED pattern (inset). The image reveals *P*4*bm* nanodomains embedded within the lamellar *P*4*mm* domains.

In the NBT-12BT composition, the *P*4*bm* nanodomains also display a plate-like character as illustrated in Fig. 4.50, when viewed along the $[013]_{pc}$ direction. However, their size is reduced compared to NBT-6BT and is now in the range of 3-15 nm. It can further be observed that the nanodomains are partly absent or strongly reduced in size and number within specific domain bands. Fig. 4.50(a) shows a BF image, where lamellar domains are visible in the lower half of the image. The location of the domain walls in the corresponding DF images is indicated with dashed lines. The displayed *P*4*bm* nanodomain variant is absent from a domain band, but present in the neighboring domain (Fig. 4.50(b)). While all three variants occur within the same region where large domains are absent, it can be concluded that this is not necessarily the case for nanodomains embedded within the lamellar domains. The number of present variants can be reduced to two or only one, which is further discussed in section 4.4.6. Interestingly, *R*3*c* nanodomains are also present in NBT-12BT as illustrated in the DF image in Fig. 4.50(c). Here, they occur throughout the displayed grain region, also within the lamellar domains. This demonstrates that local rhombohedral distorted regions still prevail in NBT-BT compositions with such a high BT content. The same could also be observed for the quenched composition (Figs. 4.50(d)-(f)). Although the average tetragonality is increased upon quenching, *R*3*c* nanodomains still prevail in NBT-12BT Q (Fig. 4.50(f)). Therefore, quenching does not necessarily change the phase assemblage on a local level, but shifts the proportional phase fractions on an average scale. Regarding the association of nanodomains and lamellar domains, an alternating appearance can be observed. In the domain bands where the *P*4*bm* nanodomains are less prominent (Fig. 4.50(e)), more *R*3*c* nanodomains occur (Fig. 4.50(f)).

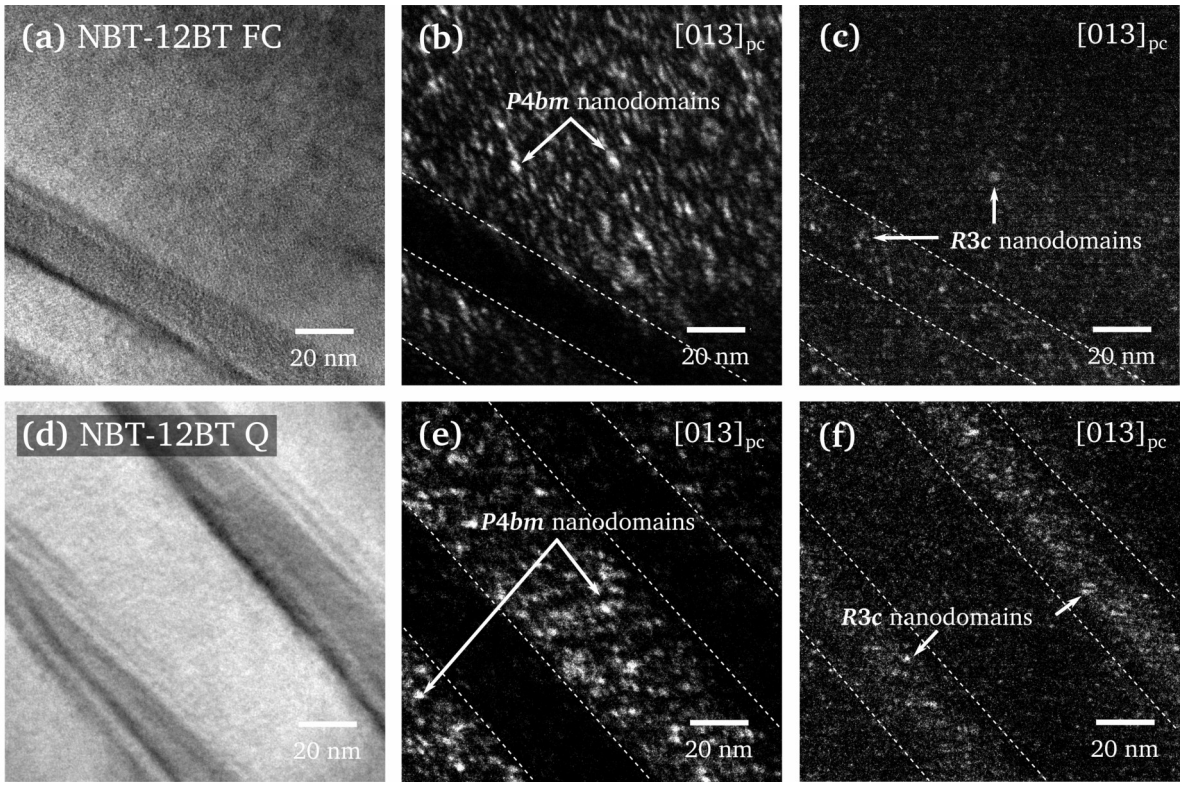

Figure 4.50: *P4bm* and *R3c* nanodomains in NBT-12BT. (a) BF image of a grain in NBT-12BT FC. (b) Corresponding DF image showing the *P4bm* nanodomains. The location of the domain walls is indicated with dashed lines. (c) Corresponding DF image of the *R3c* nanodomains. The same description applies for NBT-12BT Q in (d)-(f).

4.4.4 High-Resolution STEM and Chemical Disorder

The atomic positions in the lattice can be imaged by HRSTEM. Fig. 4.51 comparatively displays a HAADF, BF and ABF image of NBT-BT. The structural model indicates the location of the *A*-site (Na^+, Bi^{3+}, Ba^{2+}) and *B*-site (Ti^{4+}) atoms and the oxygen octahedra. In the HAADF image, which is sensitive to the atomic number (Z), the *A*-site atoms appear brighter than Ti^{4+} (Fig. 4.51(a)). The corresponding BF image shows a reversed image contrast (Fig. 4.51(b)). Light atoms, such as oxygen, contribute weakly to HAADF and BF images. They can be visualized by ABF, where the

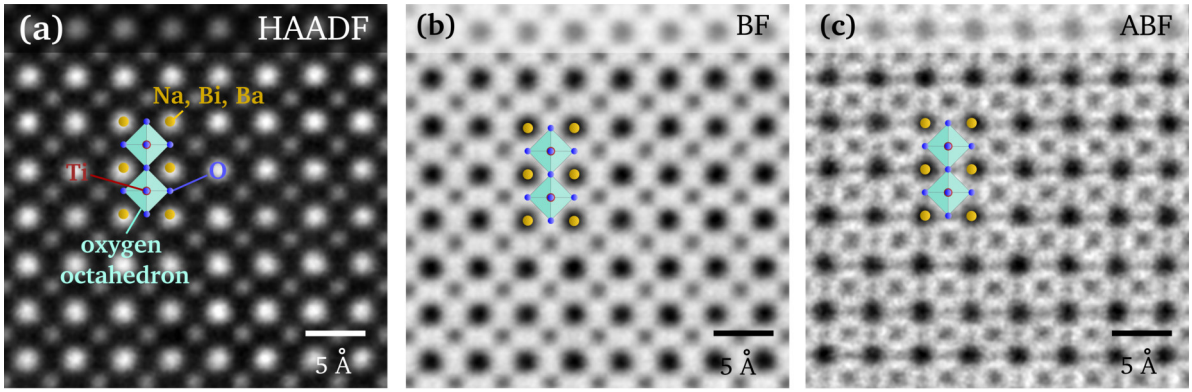

Figure 4.51: HRSTEM imaging of a NBT-6BT ceramic. (a) HAADF image, (b) BF image and (c) ABF image. The structural schematic illustrates the positions of the respective atoms.

location of the oxygen columns becomes visible (Fig. 4.51(c)).

Chemical ordering on the *A* site in NBT and NBT-based solid solutions is debatable. No direct evidence for long-range chemical ordering could be detected [175]. However, ordering on very local and short length scales, playing a role in the formation of PNRs, is hypothesized [180, 182]. The *Z*-sensitive HAADF image contrast in STEM can give indications, whether an ordered or random distribution of the *A*-site cations is present, since Bi^{3+} ($Z = 83$) and Ba^{2+} ($Z = 56$) are much heavier than Na^{+} ($Z = 11$). Fig. 4.52(a) and (b) show unfiltered HAADF images viewed along the $[001]_{pc}$ zone axis of NBT-6BT FC and Q, respectively. Slight contrast variations on the *A* site are visible in both specimens. Line profiles of the intensity distribution on the *A* site in vertical and horizontal direction are displayed in Fig. 4.52(c). Their position within the HAADF images is marked with the respective color. Intensity variations from column to column are present in both specimens, suggesting a heterogeneous distribution on the *A* site. No obvious ordering patterns, such as alternating bright and dark columns, are visible. This holds true for both the FC and Q specimen. However, the intensity range, which is indicated by the dashed lines in the intensity profiles, is slightly more narrow for the quenched specimen. This suggests a more homogeneous distribution of the cations, which can be expected when quenching the high-temperature state. The

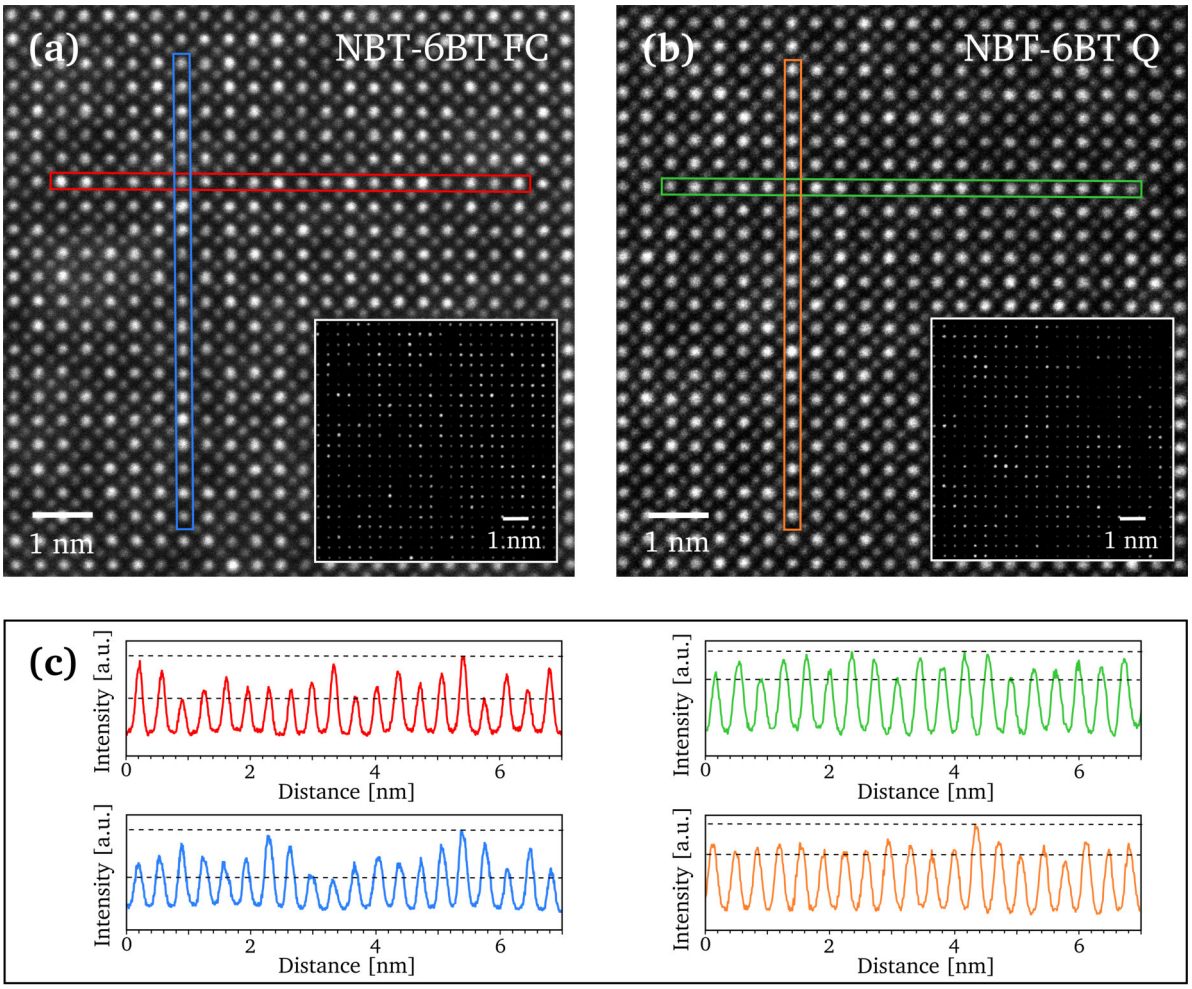

Figure 4.52: HAADF images of NBT-6BT FC (a) and Q (b). The inset on the bottom right depicts the respective same image with increased contrast. Colored rectangles illustrate positions of intensity line profiles, which are displayed in (c). No chemical ordering pattern is visible.

insets in Figs. 4.52(a) and (b) display the respective same HAADF image, however, with largely exaggerated contrast settings, in order to better visualize the positions of bright and dark atom columns. A random and heterogeneous distribution with rows and patches spanning several unit cells comprising more of heavier (brighter) or lighter (darker) *A*-site atoms is present. A well-defined ordering effect cannot be determined, also not for short correlation lengths of few unit cells in size. The absence of chemical ordering on the *A* site observed here is in agreement with a previous TEM study on NBT-6BT, where experimental and simulated images were compared [195]. It should further be noted that due to a certain thickness of the TEM foil, HAADF images usually do not show a single atom layer, but stacks of several unit cells. The intensity of each position is thus influenced by the elemental distribution within the atomic column, which makes it more difficult to chemically interpret the image.

4.4.5 Polar Displacement

Advanced imaging analysis allows to gain multiple information about the materials structure from atomically resolved C_s-corrected STEM images. Characteristics of the local structure can be deduced from measuring atomic positions and distances with a picometer accuracy [298]. Thus, the local polar displacement of ions in high-resolution HAADF images can be mapped. The applied image analysis tool [251, 252] was firstly tested on a tetragonal PZT specimen, in order to verify the feasibility of the method. The *B*-site displacement of Ti^{4+}/Zr^{4+} in PZT is reported to be about 0.3 Å [299, 300] which is somewhat large than the Ti^{4+} displacement of 0.1-0.15 Å reported for BT and NBT-BT [301, 302]. Fig. 4.53(b) shows the polarization mapping in tetragonal PZT over a domain wall, viewed edge-on along the $[001]_{pc}$ direction. The grain contains numerous tetragonal ferroelectric 90° domain walls, as displayed in the STEM-BF image in (a). The polarization vectors are displayed as yellow arrows and the location of the domain walls is indicated with dashed lines. The direction of the polarization vectors rotates by 90° when crossing the domain wall. The magnitude of polar displacement within each domain, indicated by the vector length, is highly

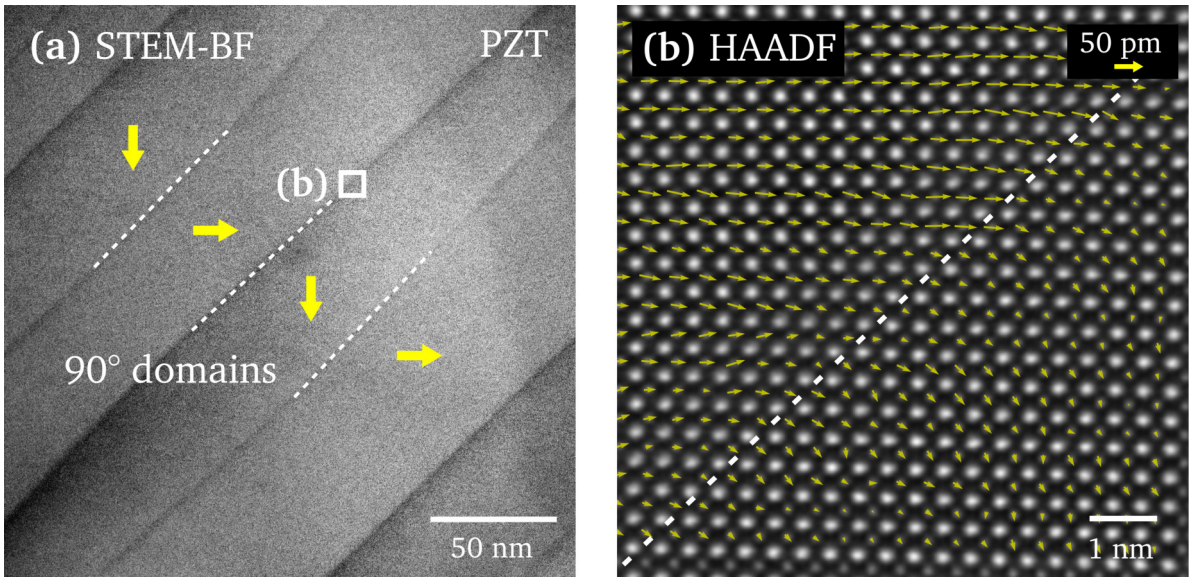

Figure 4.53: (a) STEM-BF image of tetragonal PZT with lamellar 90° domains. The boxed area indicates the position of the HAADF image displayed in (b). The polar displacement of Ti^{4+}/Zr^{4+} with reference to the *A*-site lattice is given as yellow arrows. The polarization vectors change by 90° when crossing the domain wall (dashed line).

uniform. These results illustrate that the applied method can be used to map the polar displacement in HAADF images of ferroelectric perovskites.

In order to image the local polarization in the nanodomain-containing compositions (NBT-6BT, -9BT and -12BT), the method was uniformly adopted to respective atomically resolved HAADF images. The relative displacement of Ti^{4+} with respect to the *A*-site positions of Na^{+}, Bi^{3+} and Ba^{2+} is illustrated in Fig. 4.54. The nanoscale polar structure of the relaxor composition NBT-6BT reflects in short-range fluctuations of the polarization direction and magnitude (Figs. 4.54(a)-(c)).

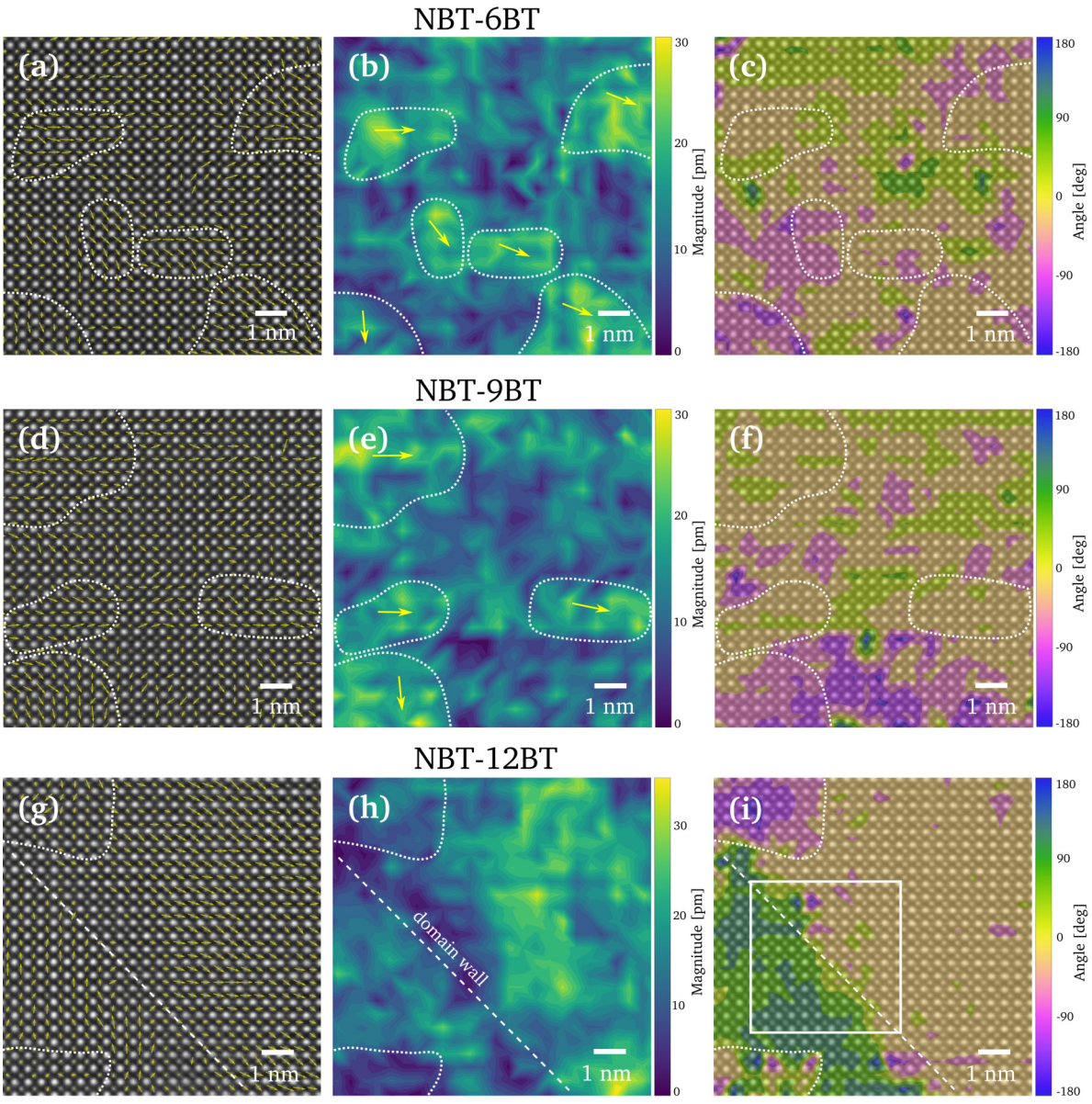

Figure 4.54: Mapping of the polar displacement in NBT-6BT, -9BT and -12BT FC. (a) High-resolution HAADF image of NBT-6BT viewed along $[010]_{pc}$, illustrating the relative displacement of Ti^{4+} with reference to the *A*-site lattice (yellow arrows). Island-like regions (PNRs) with a pronounced polarization are highlighted with dotted white lines. (b) Magnitude of the polar displacement. (c) Angle color map emphasizing the direction changes of the polar displacement. The same description applies for NBT-9BT in (d)-(f) and for NBT-12BT in (g)-(i). The boxed area in (i) is magnified in Fig. 4.55 (reprinted from Ref. 297 with permission of the American Physical Society).

Here, these fluctuations are denoted as PNRs. The polarization vectors show variations in the polar displacement on the nanoscale length (Fig. 4.54(a)). Small PNRs, up to 4 nm in size, display a coherent polarization direction. They are indicated with dotted white lines. Within those island-like regions, the magnitude of polarization is more pronounced than in the surrounding area, as illustrated in Fig. 4.54(b). The relative Ti^{4+} displacement reaches values of up to 0.3 Å. Those PNRs, however, are not clearly separated from each other. The transition between the PNRs is smooth and the magnitude and direction of polarization changes gradually. Significant areas, where the magnitude is close to zero, are absent. The variations in the polarization direction are emphasized by a color map in Fig. 4.54(c). The deviation from an average polarization direction amounts to approx. ± 90°. Across only a few unit cells, the direction of polarization can change, which leads to an overall heterogeneous polar structure. A similar configuration is visible in NBT-9BT (Figs. 4.54(d)-(f)). The analysis was conducted on an area dominated by nanodomains. Here as well, a disordered polar structure is present, which manifests in changes of the displacement direction and magnitude comparable to NBT-6BT.

A difference becomes visible when imaging a region in NBT-12BT FC, occupied by long-range ferroelectric domains. Figs. 4.54(g)-(i) display the polarization in an area near a 90° domain wall, which is indicated by the dashed white line. In contrast to the HAADF images obtained from NBT-6BT and -9BT, a more homogeneous and ordered polar structure is present. The polarization direction on each side of the domain wall is largely coherent (Fig. 4.54(g)). The magnitude of polarization within the domains is slightly increased up to 0.35 Å (Fig. 4.54(h)). Directly at the domain wall, the magnitude is the lowest and close to zero. Although the overall polarization in NBT-12BT appears to be more homogeneous compared to the MPB-close compositions, small regions are still present, which differ from the average polarization (marked with dotted white lines in Figs. 4.54(g)-(i)). This illustrates that within the ferroelectric domains, nanoscale regions with a deviating polarization direction still exist, however, in reduced number. The findings align with the fact that both *R*3*c* and *P*4*bm* nanodomains could be imaged via TEM-DF embedded within the ferroelectric domains of NBT-12BT (compare Fig. 4.50).

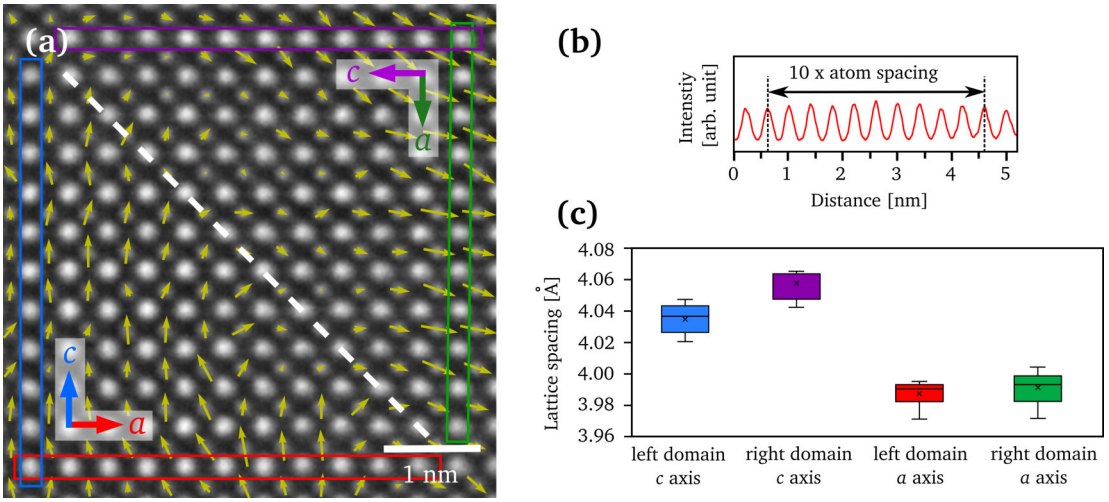

Figure 4.55: (a) HAADF image of a 90° domain wall in NBT-12BT FC (inset in Fig. 4.54(i)). The polarization direction is given as yellow arrows and the domain wall is indicated by the dashed line. The *c* and *a* axes are denoted in each domain. The colored rectangles indicate intensity profiles, exemplary depicted in (b). The plot in (c) illustrates the differences in lattice spacing along the *a* and *c* axes in both domains. Values were obtained from ten intensity profiles each.

The boxed area in Fig. 4.54(i) marks a region, in which no PNRs are present. It is magnified in Fig. 4.55(a), showing the change of polarization direction over the ferroelectric 90° domain wall (dashed line). The image is viewed along the $[010]_{pc}$ direction and the polar displacement changes from $[100]_{pc}$ to $[001]_{pc}$ when crossing the $(101)_{pc}$ domain wall. By measuring atomic distances in the HAADF image, the lattice parameters on both sides of the domain wall can be determined and assigned to the *a* and *c* axes, respectively. Profiles over ten atom spacings along the main axes in both domains where drawn, indicated by colored rectangles in Fig. 4.55(a). An exemplary profile is illustrated in Fig. 4.55(b). For each direction, ten profiles where obtained and analyzed. The boxplot in Fig. 4.55(c) depicts the measured values of the lattice spacing in the respective color. A clear difference in lattice parameters between *a* and *c* directions within each domain arises. The *c* lattice constants amount to approx. 4.04-4.06 Å while the *a* lattice constants amount to approx. 3.99 Å, which accounts for ∼2-3 % deviation from the cubic lattice setting. In the neighboring domain, the *a* and *c* axes are reversed, illustrating the 90° rotation over the domain wall.

The heterogeneous local structure in the MPB composition can also be observed upon quenching. Fig. 4.56(a) and (b) compares HAADF images of the NBT-6BT FC and Q specimen. Both samples display a short-ranged variation in the polar displacement direction and magnitude similar to the PNR regions shown in Figs. 4.54(a)-(c). This agrees with the observation that a high fraction of nanodomains can still be observed upon quenching (compare Fig. 4.17 on page 68). The difference between the two specimens may not necessarily reflect in the local nanoscale structure but rather in the overall proportion of nanodomains and long-range ferroelectric domains.

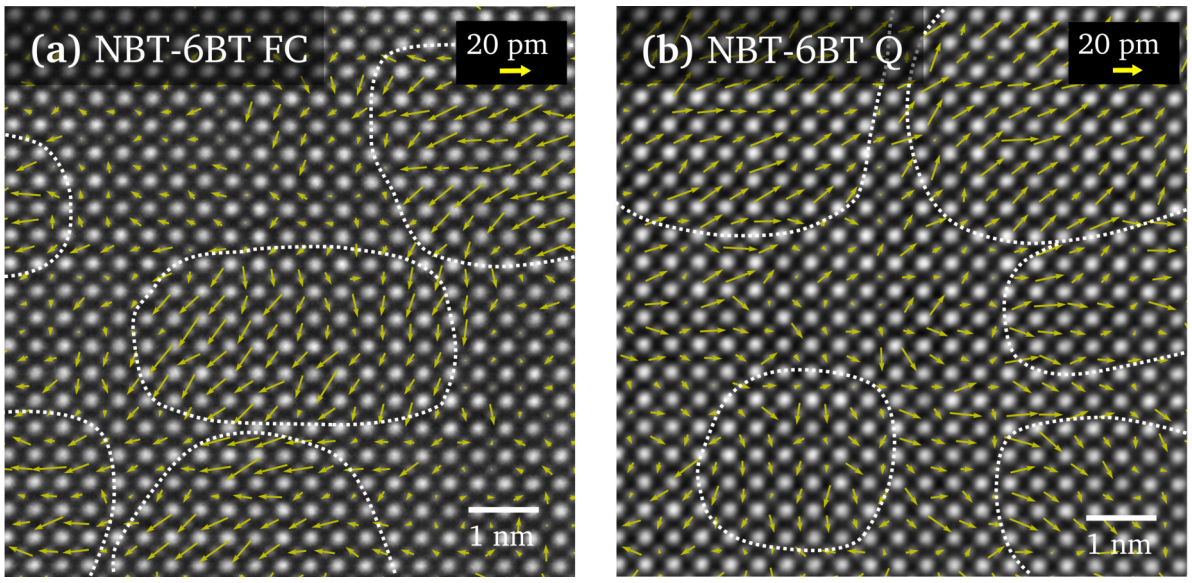

Figure 4.56: High-resolution HAADF images of NBT-6BT FC (a) and Q (b) viewed along $[001]_{pc}$ with comparable heterogeneous polar displacements (yellow arrows). PNRs with a pronounced displacement are noted with dotted lines.

Determining the location of HAADF images in STEM mode with respect to the nanodomains imaged in TEM-DF mode, in order to correlate both imaging techniques, is challenging. Fig. 4.57(a) shows a DF image of an area within a NBT-6BT grain, where *P4bm* nanodomains appear. Bright clusters of approx. 25 nm in size are visible. Within one cluster (defined as one nanodomain) variations in the brightness arise. Boundaries of the nanodomain clusters are not well defined and appear rather diffuse. This suggest a certain heterogeneity within a single nanodomain. A HAADF image was recorded from the very same grain area and is displayed in Fig. 4.57(b). Its location with respect to

the DF image is indicated by the yellow box in (a). Variances in the polar displacement direction and magnitude become visible in (b). Areas with pronounced polar displacement are indicated with dashed lines. This implies that within the boundaries of a single *P4bm* nanodomain, small fluctuations in the local polar displacement are present, which can be denoted as PNRs. On average, the displacement of the PNRs fluctuates around a consistent tetragonal $[001]_T$ direction. The image suggests that nanodomains can be composed of multiple PNRs. Following this interpretation would add another level to the already existing complexity of the relaxor structure.

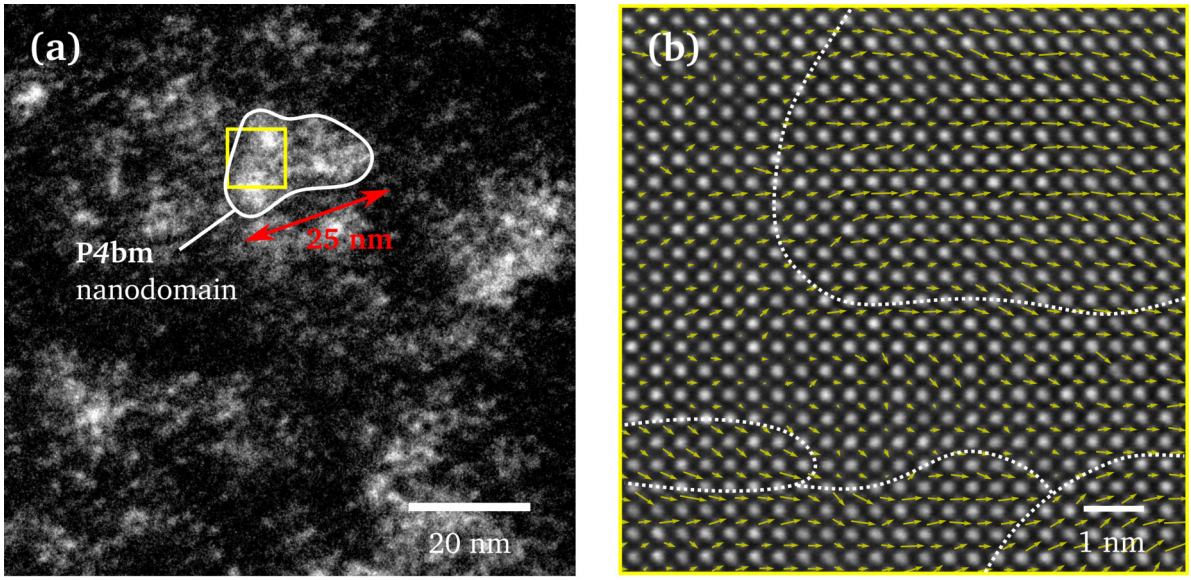

Figure 4.57: (a) TEM-DF image of a grain in NBT-6BT FC showing *P4bm* nanodomains (obtained from a $\frac{1}{2}$ $\{ooe\}$ SR). Bright clusters as indicated of approx. 25 nm in size appear. (b) HAADF image of the yellow boxed region marked in (a), which illustrates that variances in the polar displacement occur within a nanodomain.

4.4.6 Discussion of Nanoscale Structure in NBT-BT

The TEM and STEM observations emphasize the complexity of the NBT-BT nanoscale structure. It could be illustrated that the bulk of NBT-6BT is build up by three variants of plate-like *P4bm* nanodomains lying in $\{001\}_{pc}$ planes. Between these densely packed tetragonal nanodomains, nanometer-sized rhombohedral domains of *R3c* symmetry occur. It can be concluded that the *R3c* phase within the MPB compositions exhibits two different morphologies. It is present as large volume fractions with a large-scale domain contrast and as nanoscale regions dispersed within the *P4bm* nanodomains. The coexistence of both *R3c* and *P4bm* nanodomains has previously been deduced for NBT-6BT from the appearance of both types of SRs in electron diffraction [157]. The results here consolidate this picture. The TEM-DF images provide visual evidence about the nanodomain morphology and distribution. With nanoscale regions of R + T symmetry, the polar vector can potentially fluctuate among equivalent eight $\langle 111\rangle_{pc}$ and six $\langle 001\rangle_{pc}$ directions. It is assumed that rhombohedral PNRs can easily convert into tetragonal PNRs and vice versa, due to low energy barriers between both symmetries [157] (note that the nanoscale R + T regions are termed 'nanodomains' in this work, while others refer to them as 'PNRs'). The relaxor behavior of NBT-BT can thus be explained by the existence and thermal evolution of the PNRs [147]. Within the temperature range of frequency dispersion, a conversion of *R3c* to *P4bm* nanoregions is expected with increasing temperature [157]. The observed very weak $\frac{1}{2}$ $\{ooo\}$ SRs at 400 °C, however,

suggest that *R*3*c* nanodomains also prevail in a reduced population alongside *P*4*bm* at elevated temperatures. MPB regions have been associated with the flattening of Gibbs free energy profiles, which allows an easy conversion and polarization reversal between different symmetries [36]. The formation of nanodomains at the MPB is thus associated with only a minimal energetic effort. This can explain why the nanodomains in off-MPB compositions are reduced in size by ∼10 nm compared to the nanodomains at the MPB, where they can form and grow more easily.

It was further proposed that the *P*4*bm* nanodomains are dispersed within a non-polar cubic phase [130, 158], which would correspond to the dark area in the DF images. This picture, however, may appear too simplified. As illustrated, only one type of SR variant can be imaged in a single DF image. The dark matrix therefore also contains the other SR variants. Here, the controversial models for the local structure of relaxors should be emphasized. The early picture of island-like PNRs embedded within a cubic matrix is widely adopted. On the other hand, the volume of the relaxor structure can also be seen as being ferroelectric, composed of nanometer-sized domains, where a cubic phase is absent [127]. Investigations on PMN-based materials illustrate a gradual change in polar displacement between different nanodomains [108]. A model with a high density of nanometer-sized domains, compared to a slush-like state, and the absence of a polar matrix was proposed [137]. In NBT-BT, the observed nanodomains are not necessarily discrete units. In the DF images, their boundaries appear rather undefined and ragged. This does not indicate well-defined domain walls following specific orientations, but rather gradual transitions between differently orientated areas. A dense arrangement of R + T nanodomains can be assumed. This is more in agreement with the modeled tilt disorder in NBT-5BT, where plate-like T regions are dispersed within R nanodomains [303]. Whether a non-polar matrix is present or not, cannot be established with certainty from the TEM/STEM investigations in this work.

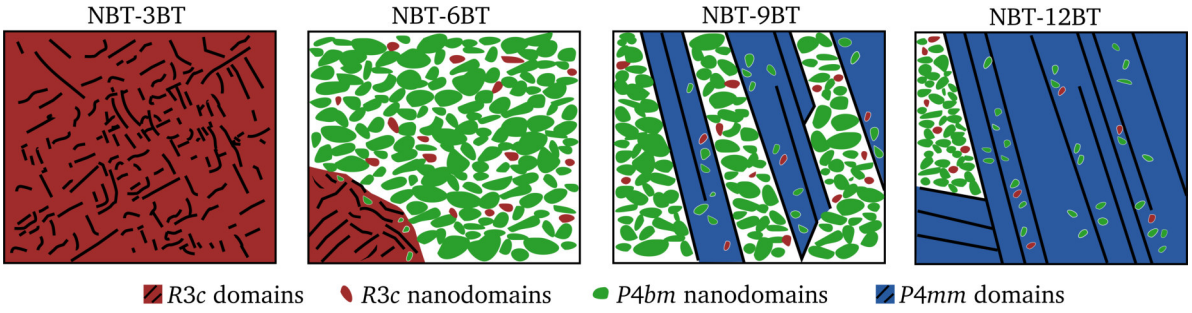

Figure 4.58: Schematic of the evolution of the nanoscale structure in NBT-BT with increasing BT content. Nanodomains of *P*4*bm* and *R*3*c* symmetry exist at the MPB and are embedded within ferroelectric *P*4*mm* domains in BT-rich compositions.

Fig. 4.58 schematically summarizes the evolution of the local structure with increasing BT content. Within the NBT-3BT specimens, only rhombohedral $\frac{1}{2}\{ooo\}$ SRs were observed. The absence of $\frac{1}{2}\{ooe\}$ SRs or any other superlattice reflections indicates that there is no other phase present. Other studies, however, observed plate-like tetragonal regions within the R domains in pure NBT [84] and even local orthorhombic domains are reported [175]. In the specimens examined in this work, the local nanodomain structure only emerges in NBT-6BT, -9BT and -12BT.

Increasing the BT content leads to an intergrown structure of lamellar *P*4*mm* domains and areas dominated by nanodomains. Even in the BT-rich NBT-12BT composition, *P*4*bm* and *R*3*c* nanodomains are found to be embedded within the ferroelectric *P*4*mm* domain structure in a reduced volume fraction. Although having a largely ferroelectric character, the tilt disorder of the local structure shows that NB-12BT clearly differentiates from a long-range ordered purely ferroelectric material.

This also reflects in the minor, but still existing frequency dispersion of permittivity observed for this composition [297].

It should be emphasized that the transition towards a ferroelectric structure is not accompanied by a growth of the nanodomains. This contradicts previous assumptions, which expected an increase in size and coherence length of PNRs/nanodomains when forming a ferroelectric long-range order [130] either by poling or by an increase in BT content. The transition towards a long-range *P4mm* structure can rather be viewed as a recrystallization process. Looking at the three phases, the distinction merely arises from differently tilted oxygen octahedra. Fig. 4.59 illustrates the mode of tilting in the pseudocubic perovskite structure of *R3c* and *P4bm*. In *P4mm*, tilting of oxygen octahedra is absent. In order to transform to *P4mm*, the oxygen octahedra have to revert back to the untilted state (a *R3c*-to-*P4mm* transition additionally requires a change in cation displacement form $\langle 111 \rangle_{pc}$ to $\langle 001 \rangle_{pc}$). Comparing both tetragonal phases, tilting of the oxygen octahedra causes the occurrence of mirror glide planes in *P4bm* as illustrated in Fig. 4.59.

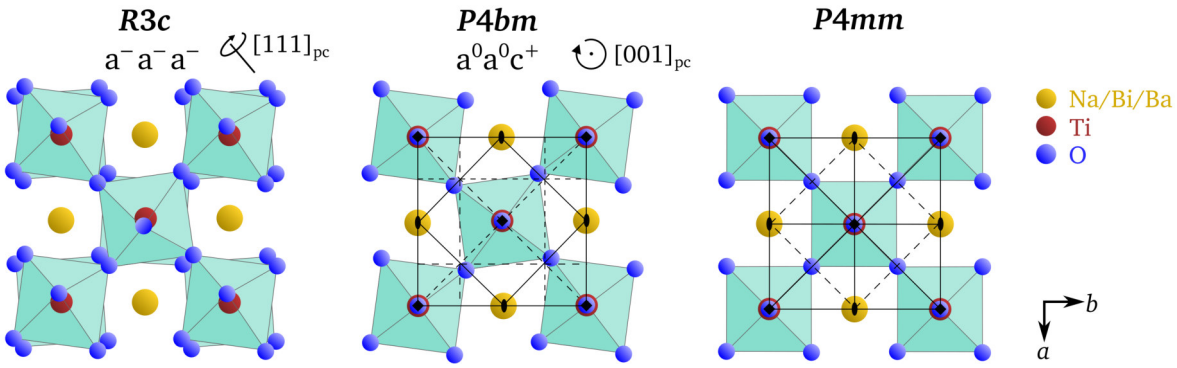

Figure 4.59: Schematics of the *R3c*, *P4bm* and *P4mm* crystal structure. The tilt axis in *R3c* and *P4bm* is noted. Differences in the symmetry operations in *P4bm* and *P4mm* are displayed (solid lines = mirror planes, dashed lines = glide planes).

In perovskite oxides, tilting of oxygen octahedra is a common phenomenon due to an easy substitution of the cations. By tilting the oxygen octahedra, the volume of the *A*-site interstice is reduced, which allows for a more stable structural configuration, once small cations occupy the *A* site [100]. The ionic radius of Ba^{2+} is relatively large, so pure BT exhibits a *P4mm* structure where tilting is absent. In comparison, Na^{+} and Bi^{3+} possess rather small ionic radii. Tilting in NBT is thus expected [165]. Continuously increasing the Ba^{2+} fraction on the *A* site thus drives the transition to a structure where tilting is reduced and finally absent. In NBT-12BT, 12 % of the *A*-site ions are Ba^{2+}, while 88 % are still occupied by Na^{+} and Bi^{3+}. Viewed from this perspective, it does not seem surprising that an abundant tilt disorder persists in the composition. It can be assumed that local chemical heterogeneities determine the local structure and present tilt system. Notably, these small tilted nanodomains are embedded within a ferroelectric *P4mm* matrix. However, not necessarily all three $\{001\}_{pc}$ variants of *P4bm* nanodomains occur within the *P4mm* domains. This implies that certain variants transform more easily. It can be assumed that variants in which the polar $[001]_T$ axis is aligned with the polar $[001]_T$ axis of the *P4mm* matrix will transform more easily by simply reverting back the oxygen octahedra to the non-tilted state. This is energetically less costly than changing the direction of the polar axis in addition to losing the octahedral tilting. While a variant is absent in one domain, it is present in the neighboring domain, since the 90° rotation of polarization favors another $\{001\}_{pc}$ nanodomain variant to be absent. The same effect is less prominent for the *R3c* nanodomains, where no distinction between different variants can be made.

HAADF imaging revealed a strongly heterogeneous local polar displacement in the MPB composition NBT-6BT (compare 4.56 on page 114). The polarization is deduced from the displacement of the *B*-site atoms (Ti^{4+}). NBT and its solid solutions, however, not solely exhibit displacement of Ti^{4+}, but also of *A*-site cations [165]. The calculated polarization vectors thus represent the relative Ti^{4+} displacement with respect to the *A*-site sublattice. For clarification, mapping the displacement of the *A*-site cations results in exactly the same image information, only with the polarization vectors being reversed in direction. The net polarization of a material is usually determined by the relative location of the cations and anions (O^{2-}) in the structure. Oxygen atoms, however, are not visible in HAADF imaging. Nevertheless, it can be inferred that the polar displacement in the HAADF images should be consistent with the local net polarization. Referring again to Fig. 4.59, the oxygen octahedra in *P*4*bm* are tilted around the *c* axis. When viewed along one of the $\langle 001 \rangle_{pc}$ directions, the plane in which the oxygen atoms are tilted either lies parallel to the image plane (as in Fig. 4.59), or perpendicular to it. So theoretically, the center of mass for the O^{2-} anions does not change when viewed along $\langle 001 \rangle_{pc}$. For the $a^-a^-a^-$ tilt system, this consideration is more difficult, since the octahedra are rotated around $\langle 111 \rangle_{pc}$ and adjacent octahedra layers are tilted in opposite sense (compare Fig. 4.59). As soon as more than one octahedra layer is regarded, the offset in the center of mass for O^{2-}, when viewed along $\langle 001 \rangle_{pc}$, is balanced by the offset of the adjacent layer. The net polarization in both structures should thus be very similar to the polar displacement determined from the cation positions.

In Figs. 4.54(a)-(f), the polar vector fluctuates with ± 90° around an average $[001]_{pc}$ direction. Variances in the polar displacement within the vicinity of a nanodomain cluster could also be imaged (compare Fig. 4.57). It can therefore be assumed that the fluctuations on the atomic scale (PNRs) are possibly present within one *P*4*bm* nanodomain. The difference in size between those PNRs, which only span few nanometers and the nanodomains, which can be up to 35 nm in diameter, corroborates this assumption. This would imply that within a nanodomain, the polarization vector can fluctuate around an average direction, which corresponds to the $[001]_T$ direction of the *P*4*bm* variant. It should, however, be noted that superimposition of different polarization directions along the viewing direction can complicate the interpretation of the projected HAADF image. Nevertheless, a promotion of the relaxational behavior in MPB compositions by such a configuration is conclusive.

The overall more ordered local structure of NBT-12BT still entails small PNRs in HAADF imaging (compare Figs. 4.54(g)-(i)), which aligns with the observed reduced population of nanodomains. PNRs located within a ferroelectric matrix have been observed for other relaxor-ferroelectric systems as well, such as PMN-PT [304]. Here, it could be demonstrated that the presence of nanoscale PNRs can induce an easy polarization reversal of large-scale domains upon poling. According to Li et al. [304], PNRs account for 50-80 % of the measurable piezoelectricity in the PMN-PT solid solutions. A hierarchical association of nanodomains and large-scale domains could not only be observed in the unpoled NBT-BT FC and Q, but also in the poled specimens (see Fig A.5 in Appendix on page 147). Thus, it can be inferred that the PNRs/nanodomains within the long-range *P*4*mm* structure in NBT-BT also significantly contribute to the piezoelectric and dielectric properties upon poling. The close association of short- and long-range polar structures, positively affecting the piezoelectric performance of relaxor ferroelectrics, can also explain the good piezoelectric properties of the NBT-9BT composition, which shows a pronounced intergrown configuration of ferroelectric domains and nanodomains already in the unpoled state.

The formation of PNRs has been attributed to a locally correlated displacement of Bi^{3+} [191]. As previously noted, Bi^{3+} can exhibit a large off-centering due to its lone pair character [288]. Bi^{3+} displacement along $\langle 001 \rangle_{pc}$ is believed to induce PNR formation in pure NBT and a correlation

of a changing displacement direction and BT content could be observed [191]. Off-centering of Bi^{3+} over short correlation lengths can thus promote the relaxational behavior. With an increasing amount of Ba^{2+} and likewise decrease in Bi^{3+}, an overall reduction in the *A*-site displacement can be expected. This aligns with the reduced, but still present population of nanodomains in BT-rich compositions.

The possibility of chemical ordering on the *A* site in FC and Q samples was examined via HAADF imaging. An early work on the relaxor $PbSc_{1/2}Ta_{1/2}O_3$ related an increase in ferroelectric character to the chemical long-range ordering of Sc^{3+} and Ta^{5+} [305]. For NBT-BT FC, a random distribution of Na^+, Bi^{3+} and Ba^{2+} was expected and no chemical ordering could be found in previous studies [195, 196]. Here as well, no indications for a chemical ordering on the *A* site could be observed in FC and Q specimens. It can be concluded that quenching is not related to any chemical ordering effect. Comparing both NBT-6BT FC and Q specimens furthermore revealed a similar heterogeneous local structure with fluctuations (PNRs) on the atomic scale. The quenching-induced structural change (increase in lamellar domains) is only visible on a larger scale. Quenching shifts the proportions between nanodomains and lamellar domains from a merely nanodomain-dominated structure in FC towards a structure with increased long-range domains and an overall slightly reduced nanodomain population. Both structural features are closely associated in a hierarchical configuration of nanodomains embedded within lamellar domains, where the ferroelectric matrix compensates for the enhanced lattice strain that arises upon quenching.

Short Summary

TEM-DF imaging revealed that the NBT-6BT composition not only consists of plate-like *P*4*bm* nanodomains lying in the three $\langle 001 \rangle_{pc}$ planes, but also of a minor fraction of *R*3*c* nanodomains. The coexistence of tetragonal and rhombohedral nanodomains and an easy conversion between the increased number of possible polar directions can explain the enhanced polarizability at the MPB. Nanometer-sized fluctuation in the direction and magnitude of the polar cation displacement, denoted as PNRs, show a heterogeneous local relaxor structure. When increasing the BT content and crossing the composition-dependent relaxor-to-ferroelectric transition, lamellar long-range *P*4*mm* domains emerge. However, nanodomains of both symmetries are still embedded within these lamellar domains, resulting in a complex hierarchical domain arrangement. Here, the nanodomain size and number is reduced and a conversion within the polar *P*4*mm* matrix can be assumed, induced by the increasing Ba^{2+} amount on the A site and thus an overall reduction in oxygen octahedral tilting.

5 Conclusions & Outlook

The present work investigated the domain structure and phase evolution in furnace cooled and quenched relaxor ferroelectric $(1-x)(Na_{1/2}Bi_{1/2})TiO_3$-$xBaTiO_3$ ceramics using TEM, STEM, PFM and SEM. A locally resolved analysis, which was possible by TEM and STEM techniques, gave insight about the actual local distribution and morphology of present phases, thus complementing other techniques focusing on long-range and average structural descriptions. This allowed not only to investigate on structural changes upon quenching, but also to closely examine the relaxor-ferroelectric nanostructure and obtain a more holistic picture of this promising lead-free material system.

The compositional range of $x = 0.03$, 0.06, 0.09 and 0.12 was examined. The NBT-BT system changed from a rhombohedral structure on the NBT-rich side to a pseudocubic structure of *R*3*c* + *P*4*bm* symmetries at the MPB, primarily dominated by nanodomains. With increasing BT content, the system exhibited a more lamellar domain structure of tetragonal *P*4*mm* symmetry with minor amounts of *P*4*bm* and *R*3*c* phases embedded. This illustrated a very wide compositional range of phase coexistence, opposed to more narrow MPB regions reported before.

The strengthened rhombohedral and tetragonal character of the quenched specimens could be correlated to an increased lamellar domain formation visualized by TEM, SEM and PFM analyses. In NBT-3BT, this manifested in the formation of a second rhombohedral phase (*R*3*m*), in which oxygen octahedral tilting was absent and which featured a herringbone-type domain configuration. In the MPB composition NBT-6BT, pronounced lamellar domains of both rhombohedral (*R*3*c*) and tetragonal (*P*4*mm*) symmetry emerged upon quenching, accommodating the strain arising with the rhombohedral and tetragonal distortions. A similar trend was not visible in quenched NBT-9BT and -12BT, since both compositions already displayed lamellar domains in the furnace cooled state. The increased long-range polar structures in quenched MPB compositions showed resemblance to the structure observed upon the relaxor-to-ferroelectric transition in poled NBT-6BT. Thus, it could be inferred that quenching promotes a transition in relaxor compositions towards an increased ferroelectric order.

In-situ experiments on NBT-6BT investigated the thermal evolution of the domain structure and phase assemblage. The *R*3*c* domains disappeared in a comparable range for FC and Q specimens (∼100 to 200 °C) and transformed to *P*4*bm* nanodomains. Very weak superlattice reflections, however, prevailed even up to 400 °C, indicating the persistence of small rhombohedral regions. In the quenched specimen, the tetragonal *P*4*mm* domains were stable up to high temperatures of ∼300 °C. Their persistence shifts the overall stability of the ferroelectric order to higher temperatures and thus benefits a delayed depolarization. In the poled NBT-6BT Q specimen, the lamellar tetragonal domain contrast started to disappear at ∼140 °C, compared to ∼100 °C in the poled FC state. T_d and the vanishing of piezoelectric properties thus appears to be strongly linked to the onset of the tetragonal domain disintegration. The temperature-dependent stability of the ferroelectric domain structure up to ∼140 °C accounts for the increase in T_d in the quenched composition.

Underlying mechanisms for the quenching-induced structural changes, such as residual thermal stresses, an increased oxygen vacancy concentration and an enhanced off-centering of Bi^{3+} ions were discussed. No increase in Ti^{3+}, which would in turn indicate an increase in oxygen vacancies, could be detected in quenched NBT-BT via EELS analysis of the near-edge fine structure. No indications for large residual thermal stresses, such as microcracks, could be observed. Freezing-in the off-center positions of Bi^{3+} ions from the high-temperature cubic phase most likely benefits the occurrence of non-cubic lattice distortions and thus ferroelastic lamellar domains.

A detailed investigation on the nanoscale relaxor structure via TEM-DF imaging and HRSTEM revealed that the *P*4*bm* phase is composed of three variants of plate-like nanodomains of up to 35 nm in size, lying in $\{001\}_{pc}$ planes. Among them, a minor fraction of *R*3*c* nanodomains (up to 10 nm in size) is dispersed. While the presence of nanoscale *P*4*bm* and *R*3*c* symmetries was inferred before, the TEM results here provide a clear visual evidence of their coexistence. Their association implies the presence of multiple equivalent polarization states and accounts for the increased polarizability of relaxor compositions, leading to the enhanced piezoelectric response and high permittivity values. HRSTEM analysis demonstrated a heterogeneous local polar displacement in the MPB composition with short-ranged fluctuations (PNRs) in the direction and magnitude of the polar displacement. Within lamellar *P*4*mm* domains in BT-rich compositions, a more homogeneous polar displacement was present, while small regions still deviated from the average polarization direction. DF imaging illustrated a hierarchical association of both *P*4*bm* and *R*3*c* nanodomains embedded within the lamellar ferroelectric domains. Here, nanodomains are reduced in size and number, which emphasizes that they do not coalescence into larger polar structure when crossing the relaxor-to-ferroelectric compositional threshold. The structural transition can rather be regarded as a recrystallization process from a tilted to a non-tilted oxygen sublattice.

With respect to future studies, high-resolution STEM can offer further techniques to characterize perovskite oxides and can elaborate on the tilt and displacement characteristics in such materials. It becomes apparent that short-range variances in oxygen octahedral tilting is a key element to the complex relaxor nanostructure. Oxygen atoms can be imaged via high-resolution ABF and tilts can be quantitatively measured [306], giving insight into the local short-range tilt disorder. This might further allow to image the interaction of ionic displacement and tilt orientation.

Application-wise, a lasting stability of the quenching-induced structural changes is desirable. Thus, studies on NBT-BT ceramics need to be expanded to the fatigue behavior of the quenching-induced properties. Investigations on the di- and piezoelectric properties and microstructural characteristic after a prolonged cycling process could give insights in improving and tailoring the quenching procedure. In addition to in-situ heating experiments, E-field dependent TEM analysis can provide further information on poling-induced structural changes. A complementary in-situ electrical biasing study can shed light on the domain growth during the relaxor-to-ferroelectric transition and elucidate on the role of nanodomains/PNRs within the polar long-range order. Furthermore, taking into account that many applications operate under elevated temperatures, such as ultrasonic cleaning devices, a simultaneous heating and electrical biasing TEM investigation could elaborate on the evolution of the domain structure and phase assemblage under conditions resembling a practical application.

As illustrated, the formation of lamellar domains is crucial for improving the temperature-dependent performance of relaxor NBT-BT compositions. T_d is commonly lowest at the MPB, while here the piezoelectric properties are maximized (Fig. 5.1). This also holds true for other solid solutions formed with NBT, such as NBT-KBT or NBT-KBT-BT [307, 308]. Shifting T_d to higher temperature is only desirable, as long as the piezoelectric and mechanical properties are not significantly impaired.

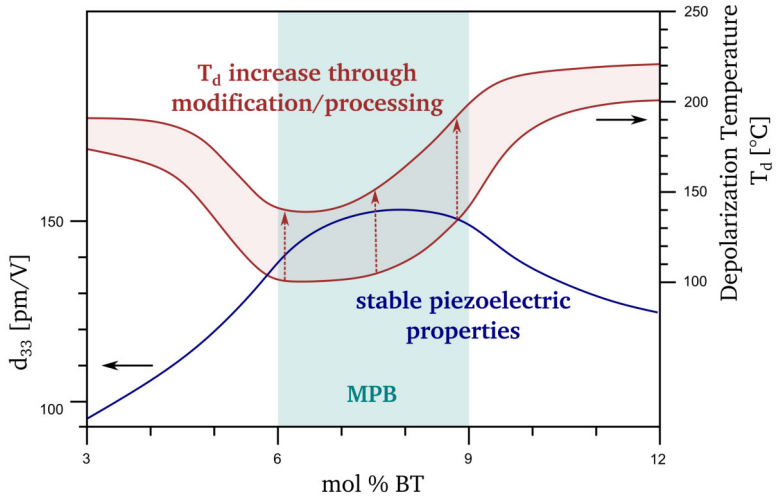

Figure 5.1: Schematic illustrating that the depolarization temperature (T_d) is lowest for MPB compositions, while the piezoelectric properties (exemplary d_{33}) are maximized. Increasing T_d in order to improve the temperature-dependent performance without deteriorating the piezoelectric properties can be achieved via chemical modification (doping, composite formation) or an alternative processing such as quenching.

It could be demonstrated that an increase in T_d can be achieved by enhancing the ferroelectric order at the MPB. Increasing lattice distortions and thus inducing the formation of long-range ferroelectric domains appears to be a key element in engineering the functional properties of such relaxor ferroelectric materials. Quenching serves as a rather easy applicable tool to alter the microstructure accordingly. However, other methods are likewise promising. So did doping NBT-BT with Zn^{2+}, as well as the formation of composites with ZnO inclusions, also enhance the rhombohedral and tetragonal lattice distortion, resulting in an increase in T_d [214, 309]. Here, it would be insightful to look into the nanostructure and examine whether a similar interplay of nanodomains and lamellar domains of different symmetries is prevalent, as observed upon quenching. This could further consolidate the importance of an enhanced ferroelectric domain structure in deferring the thermal depolarization, independently from the applied procedure (quenching, doping, composite formation).

The detailed visualization of nanodomains and their association with large ferroelectric domains illustrates the complexity of this particular relaxor ferroelectric solid solution. The high-resolution TEM and STEM techniques utilized here can also be applied to other lead-free systems. A better understanding of the micro- and nanostructural features in lead-free relaxor ferroelectrics in general can help to more effectively influence the functionality and performance of the material of interest in the future.

Bibliography

[1] Scott, J. F. Application of Modern Ferroelectrics. *Science* **315,** 954–959 (2007).

[2] Uchino, K. *Ferroelectric Devices,* 2nd edition (CRC Press, Boca Raton, 2008).

[3] Rabe, K. M., Dawber, M., Lichtensteiger, C., Ahn, C. H. & Triscone, J.-M. Modern Physics of Ferroelectrics: Essential Background. In *Physics of Ferroelectrics - A Moderne Perspective* (eds. Rabe, K., Ahn, C. H. & Triscone, J.-M.) 1–30 (Springer, Berlin, 2007).

[4] Setter, N., Damjanovic, D., Eng, L., Fox, G., Gevorgian, S., Hong, S., Kingon, A., Kohlstedt, H., Park, N. Y., Stephenson, G. B., Stolitchnov, I., Taganstev, A. K., Taylor, D. V., Yamada, T. & Streiffer, S. Ferroelectric thin films: Review of materials, properties, and applications. *J. Appl. Phys.* **100,** 051606 (2006).

[5] Rödel, J., Webber, K. G., Dittmer, R., Jo, W., Kimura, M. & Damjanovic, D. Transferring lead-free piezoelectric ceramics into application. *J. Eur. Ceram. Soc.* **35,** 1659–1681 (2015).

[6] Cowley, R. A., Gvasaliya, S. N., Lushnikov, S. G., Roessli, B. & Rotaru, G. M. Relaxing with relaxors: a review of relaxor ferroelectrics. *Adv. Phys.* **60,** 229–327 (2011).

[7] Bokov, A. A. & Ye, Z.-G. Recent progress in relaxor ferroelectrics with perovskite structure. *J. Mater. Sci.* **41,** 31–52 (2006).

[8] Shvartsman, V. V. & Lupascu, D. C. Lead-Free Relaxor Ferroelectrics. *J. Am. Ceram. Soc.* **95,** 1–26 (2012).

[9] Uchino, K. Relaxor ferroelectric devices. *Ferroelectrics* **151,** 321–330 (1994).

[10] Takenaka, T., Maruyama, K. & Sakata, K. $(Bi_{1/2}Na_{1/2})TiO_3$-$BaTiO_3$ System of Lead-Free Piezoelectric Ceramics. *Jpn. J. Appl. Phys.* **30,** 2236–2239 (1991).

[11] Tou, T., Hamaguti, Y., Maida, Y., Yamamori, H., Takahashi, K. & Terashima, Y. Properties of $(Bi_{0.5}Na_{0.5})TiO_3$-$BaTiO_3$-$(Bi_{0.5}Na_{0.5})(Mn_{1/3}Nb_{2/3})O_3$ Lead-Free Piezoelectric Ceramics and Its Application to Ultrasonic Cleaner. *Jpn. J. Appl. Phys.* **48,** 07GM03 (2009).

[12] Chu, B.-J., Chen, D.-R., Li, G.-R. & Yin, Q.-R. Electrical properties of $Na_{1/2}Bi_{1/2}TiO_3$-$BaTiO_3$ ceramics. *J. Eur. Ceram. Soc.* **22,** 2115–2121 (2002).

[13] Muramatsu, H., Nagata, H. & Takenaka, T. Quenching effects for piezoelectric properties on lead-free $(Bi_{1/2}Na_{1/2})TiO_3$ ceramics. *Jpn. J. Appl. Phys.* **55,** 10TB07 (2016).

[14] Miura, T., Nagata, H. & Takenaka, T. Quenching effects on piezoelectric properties and depolarization temperatures of $(Bi_{0.5}Na_{0.5})TiO_3$-based solid solution systems. *Jpn. J. Appl. Phys.* **56,** 10PD05 (2017).

[15] K. V., Lalitha, Koruza, J. & Rödel, J. Propensity for spontaneous relaxor-ferroelectric transition in quenched $(Na_{1/2}Bi_{1/2})TiO_3$-$BaTiO_3$ compositions. *Appl. Phys. Lett.* **113,** 252902 (2018).

[16] Känzig, W. Ferroelectrics and antiferroeletrics. *Solid State Phys.* **4,** 1–197 (1957).

[17] Waser, R., Böttger, U. & Tiedke, S. *Polar Oxides: Properties, Characterization, and Imaging* (WILEY-VCH Verlag, Weinheim, 2005).

[18] Moulson, A. J. & Herbert, J. M. *Electroceramics: Materials, Properties, Applications,* 2nd edition (John Wiley & Sons, Chichester, 2003).

[19] Hunklinger, S. *Festkörperphysik,* 5th edition (Walter de Gruyter GmbH, Berlin, 2018).

[20] Craciun, F. Dielectric, Ferroelectric, Antiferroelectric, Relaxor, Piezoelectric Ceramics: Definitions and Main Applications. In *Encyclopedia of Materials: Technical Ceramics and Glasses* (ed. Pomeroy, M.) 281–294 (Elsevier, Amsterdam, 2021).

[21] Damjanovic, D. Ferroelectric, dielectric and piezoelectric properties of ferroelectric thin films and ceramics. *Rep. Prog. Phys.* **61,** 1267–1324 (1998).

[22] Jaffe, B., Cook, W. R. & Jaffe, H. *Piezoelectric Ceramics* (Academic Press, Cambridge, 1971).

[23] Nye, J. F. *Physical Properties of Crystals: Their Representation by Tensors and Matrices* (Oxford University Press, Oxford, 1985).

[24] Cohen, R. E. Origin of ferroelectricity in perovskite oxides. *Nature* **358,** 136–138 (1992).

[25] Kay, H. F. & Vousden, P. XCV. Symmetry Changes in Barium Titanate at Low Temperatures and their Relation to its Ferroelectric Properties. *The London, Edinburgh, and Dublin Philosophical Magazine and Journal of Science* **40,** 1019–1040 (1949).

[26] Wieder, H. H. Electrical Behavior of Barium Titanate Single Crystals at Low Temperatures. *Phys. Rev.* **99,** 1161–1165 (1955).

[27] Ravel, B., Stern, E. A., Vedrinskii, R. I. & Kraizman, V. Local structure and the phase transitions of $BaTiO_3$. *Ferroelectrics* **206,** 407–430 (1998).

[28] Darlington, C. N. W., David, W. I. F. & Knight, K. S. Structural study of barium titanate between 150 and 425 K. *Ph. Transit.* **48,** 217–236 (1994).

[29] Samara, G. A. Ferroelectricity Revisited - Advances in Materials and Physics. *Solid State Phys.* **56,** 239–458 (2001).

[30] Schultheiss, J. E. *Polarization reversal dynamics in polycrystalline ferroelectric/ferroelastic ceramic materials* (PhD thesis, Technical University of Darmstadt, Darmstadt, 2018).

[31] Kittel, C. Theory of Antiferroelectric Crystals. *Phys. Rev.* **82,** 729–732 (1951).

[32] Vopson, M. M., Caruntu, G. & Tan, X. Polarization reversal and memory effect in antiferroelectric materials. *Scr. Mater.* **128,** 61–64 (2017).

[33] Zhang, S., Xia, R. & Shrout, T. R. Lead-free piezoelectric ceramics vs. PZT? *J. Electroceramics* **19,** 251–257 (2007).

[34] Noheda, B., Gonzalo, J., Cross, L., Guo, R., Park, S.-E., Cox, D. & Shirane, G. Tetragonal-to-monoclinic phase transition in a ferroelectric perovskite: The structure of $PbZr_{0.52}Ti_{0.48}O_3$. *Phys. Rev. B* **61,** 8687–8695 (2000).

[35] Ragini, Ranjan, R., Mishra, S. K. & Pandey, D. Room temperature structure of $Pb(Zr_xTi_{1-x}O_3)$ around the morphotropic phase boundary region: A Rietveld study. *J. Appl. Phys.* **92,** 3266–3274 (2002).

[36] Damjanovic, D. A morphotropic phase boundary system based on polarization rotation and polarization extension. *Appl. Phys. Lett.* **97,** 062906 (2010).

[37] Fu, H. & Cohen, R. E. Polarization rotation mechanism for ultrahigh electromechanical response in single-crystal piezoelectrics. *Nature* **403,** 281–283 (2000).

[38] Schmitt, L. A., Schönau, K. A., Theissmann, R., Fuess, H., Kungl, H. & Hoffmann, M. J. Composition dependence of the domain configuration and size in $Pb(Zr_{1-x}Ti_x)O_3$ ceramics. *J. Appl. Phys.* **101,** 074107 (2007).

[39] Schönau, K. A., Schmitt, L. A., Knapp, M., Fuess, H., Eichel, R.-A., Kungl, H. & Hoffmann, M. J. Nanodomain structure of $Pb[Zr_{1-x}Ti_x]O_3$ at its morphotropic phase boundary: Investigations from local to average structure. *Phys. Rev. B* **75,** 184117 (2007).

[40] Damjanovic, D., Klein, N., Li, J. & Porokhonskyy, V. What can be expected from lead-free piezoelectric materials? *Funct. Mater. Lett.* **3,** 5–13 (2010).

[41] World Health Organization. *Exposure to lead: a major public health concern,* 2nd edition (report, Department of Environment, Climate Change and Health, WHO, Geneva, 2021).

[42] Bell, A. J. & Deubzer, O. Lead-free piezoelectrics - The environmental and regulatory issues. *MRS Bull.* **43,** 581–587 (2018).

[43] Rödel, J., Jo, W., Seifert, K. T. P., Anton, E.-M., Granzow, T. & Damjanovic, D. Perspective on the Development of Lead-free Piezoceramics. *J. Am. Ceram. Soc.* **92,** 1153–1177 (2009).

[44] Ibn-Mohammed, T., Koh, S. C. L., Reaney, I. M., Acquaye, A., Wang, D., Taylor, S. & Genovese, A. Integrated hybrid life cycle assessment and supply chain environmental profile evaluations of lead-based (lead zirconate titanate) *versus* lead-free (potassium sodium niobate) piezoelectric ceramics. *Energy Environ. Sci.* **9,** 3495–3520 (2016).

[45] Buzek, J. & Györi, E. Directive 2011/65/EU of the European parliament and of the council of 8 June 2011 on the restriction of the use of certain hazardous substances in electrical and electronic equipment. *Official Journal of the European Union* **L 174,** 88–110 (2011).

[46] Baron, Y., Gensch, C.-O., Koehler, A., Liu, R., Loew, C. & Moch, K. *Study to assess requests for a renewal of nine (-9-) exemptions 6(a), 6(a)-I, 6(b), 6(b)-I, 6(b)-II, 6(c), 7(a), 7(c)-I and 7 (c)-II of Annex III of Directive 2011/65/EU (Pack 22) - Final Report* (Oeko-Institut e.V., Freiburg, 2021).

[47] Malič, B., Otoničar, M., Radan, K. & Koruza, J. Lead-Free Piezoelectric Ceramics. In *Encyclopedia of Materials: Technical Ceramics and Glasses* (ed. Pomeroy, M.) 358–368 (Elsevier, Amsterdam, 2021).

[48] Zheng, T., Wu, J., Xiao, D. & Zhu, J. Recent development in lead-free perovskite piezoelectric bulk materials. *Prog. Mater. Sci.* **98,** 552–624 (2018).

[49] Rödel, J. & Li, J.-F. Lead-free piezoceramics: Status and perspectives. *MRS Bull.* **43,** 576–580 (2018).

[50] Koruza, J., Bell, A. J., Frömling, T., Webber, K. G., Wang, K. & Rödel, J. Requirements for the transfer of lead-free piezoceramics into application. *J. Materiomics* **4,** 13–26 (2018).

[51] Hong, C.-H., Kim, H.-P., Choi, B.-Y., Han, H.-S., Son, J. S., Ahn, C. W. & Jo, W. Lead-free piezoceramics - Where to move on? *J. Materiomics* **2,** 1–24 (2016).

[52] Kumari, P., Rai, R., Sharma, S., Shandilya, M. & Tiwari, A. State-of-the-art of lead free ferroelectrics: A critical review. *Adv. Mater. Lett.* **6,** 453–484 (2015).

[53] Pitike, K. C., Parker, W. D., Louis, L. & Nakhmanson, S. M. First-principles studies of lone-pair-induced distortions in epitaxial phases of perovskite $SnTiO_3$ and $PbTiO_3$. *Phys. Rev. B* **91,** 035112 (2015).

[54] Schütz, D., Deluca, M., Krauss, W., Feteira, A., Jackson, T. & Reichmann, K. Lone-Pair-Induced Covalency as the Cause of Temperature- and Field-Induced Instabilities in Bismuth Sodium Titanate. *Adv. Funct. Mater.* **22,** 2285–2294 (2012).

[55] Seshadri, R. & Hill, N. A. Visualizing the Role of Bi 6s 'Lone Pairs' in the Off-Center Distortion in Ferromagnetic $BiMnO_3$. *Chem. Mater.* **13,** 2892–2899 (2001).

[56] Zhang, S.-T., Kounga, A. B., Aulbach, E., Granzow, T., Jo, W., Kleebe, H.-J. & Rödel, J. Lead-free piezoceramics with giant strain in the system $Bi_{0.5}Na_{0.5}TiO_3$-$BaTiO_3$-$K_{0.5}Na_{0.5}NbO_3$. I. Structure and room temperature properties. *J. Appl. Phys.* **103,** 034107 (2008).

[57] Demartin Maeder, M., Damjanovic, D. & Setter, N. Lead Free Piezoelectric Materials. *J. Electroceramics* **13,** 385–392 (2004).

[58] Saito, Y., Takao, H., Tani, T., Nonoyama, T., Takatori, K., Homma, T., Nagaya, T. & Nakamura, M. High performance lead-free piezoelectric material. *R&D Review of Toyota CRDL* **41,** 22–28 (2004).

[59] Liu, W. & Ren, X. Large piezoelectric effect in Pb-free ceramics. *Phys. Rev. Lett.* **103,** 257602 (2009).

[60] Lee, M. H., Kim, D. J., Park, J. S., Kim, S. W., Song, T. K., Kim, M. H., Kim, W.-J., Do, D. & Jeong, I.-K. High-Performance Lead-Free Piezoceramics with High Curie Temperatures. *Adv. Mater.* **27,** 6976–6982 (2015).

[61] Gao, L., Ko, S. W., Guo, H., Hennig, E., Randall, C. A. & Jones, J. L. Demonstration of Copper Co-Fired (Na, K)NbO_3 Multilayer Structures for Piezoelectric Applications. *J. Am. Ceram. Soc.* **99,** 2017–2023 (2016).

[62] Ditas, P., Hennig, E. & Kynast, A. Lead-Free Piezoceramic Materials for Ultrasonic Applications. *Sensoren und Messsysteme, ITG/GMA Symposium, VDE Verlag,* 1–4 (2014).

[63] Shibata, K., Wang, R., Tou, T. & Koruza, J. Applications of lead-free piezoelectric materials. *MRS Bull.* **43,** 612–616 (2018).

[64] Shur, V. Y. Fast Polarization Reversal Process: Evolution of Ferroelectric Domain Structure in Thin Films. In *Ferroelectric Thin Films: Synthesis and Basic Properties* (eds. Araujo, C. P. D., Scott, J. F. & Taylor, G. W.) 153–192 (Gordon & Breach Science Publishers Ltd., Philadelphia, 1996).

[65] Lines, M. E. & Glass, A. M. *Principles and Applications of Ferroelectrics and Related Materials* (Oxford University Press, Oxford, 2001).

[66] Arlt, G. Twinning in ferroelectric and ferroelastic ceramics: stress relief. *J. Mater. Sci.* **25,** 2655–2666 (1990).

[67] Arlt, G. & Sasko, P. Domain configuration and equilibrium size of domains in $BaTiO_3$ ceramics. *J. Appl. Phys.* **51,** 4956–4960 (1980).

[68] Sapriel, J. Domain-wall orientations in ferroelastics. *Phys. Rev. B* **12,** 5128–5140 (1975).

[69] Fousek, J. & Janovec, V. The Orientation of Domain Walls in Twinned Ferroelectric Crystals. *J. Appl. Phys.* **40,** 135–142 (1969).

[70] Hu, Y. H., Chang, H. M., Wen, Z. X. & Harmer, M. P. Scanning Electron Microscopy and Transmission Electron Microscopy Study of Ferroelectric Domains in Doped $BaTi0_3$. *J. Am. Ceram. Soc.* **69,** 594–602 (1986).

[71] Tanaka, M. & Honjo, G. Electron optical studies of barium titanite single crystal films. *J. Phys. Soc. Japan* **19,** 954–970 (1964).

[72] Cheng, S.-Y., Ho, N.-J. & Lu, H.-Y. Transformation-Induced Twinning: The 90° and 180° Ferroelectric Domains in Tetragonal Barium Titanate. *J. Am. Ceram. Soc.* **89,** 2177–2187 (2006).

[73] López-Juárez, R., Novelo-Peralta, O., González-García, F., Rubio-Marcos, F. & Villafuerte-Castrejón, M.-E. Ferroelectric domain structure of lead-free potassium-sodium niobate ceramics. *J. Eur. Ceram. Soc.* **31,** 1861–1864 (2011).

[74] Remaut, G., Gevers, R. & Amelinckx, S. Wavy Fringes at Domain Boundaries in Barium Titanate Observed in the Electron Microscope. *Phy. Stat. Sol.* **20,** 613–621 (1967).

[75] Gureev, M. Y., Tagantsev, A. K. & Setter, N. Head-to-head and tail-to-tail 180° domain walls in an isolated ferroelectric. *Phys. Rev. B* **83,** 184104 (2011).

[76] Ricote, J., Whatmore, R. W. & Barber, D. J. Studies of the ferroelectric domain configuration and polarization of rhombohedral PZT ceramics. *J. Phys.: Condens. Matter* **12,** 323–337 (2000).

[77] Erhart, J. & Cao, W. Permissible symmetries of multi-domain configurations in perovskite ferroelectric crystals. *J. Appl. Phys.* **94,** 3436–3445 (2003).

[78] Randall, C. A., Barber, D. J. & Whatmore, R. W. Ferroelectric domain configurations in a modified-PZT ceramic. *J. Mater. Sci.* **22,** 925–931 (1987).

[79] Schierholz, R. *Konvergente Elektronenbeugung an $PbZr_{1-x}Ti_xO_3$-Keramiken* (PhD thesis, Technical University of Darmstadt, Darmstadt, 2010).

[80] Wang, H., Zhu, J., Zhang, X. W., Tang, Y. X. & Luo, H. S. Hierarchical Domain Structure of Adaptive M_B Phase in $Pb(Mg_{1/3}Nb_{2/3})O_3$-32 %$PbTiO_3$ Single Crystal. *J. Am. Ceram. Soc.* **91,** 2382–2384 (2008).

[81] Wiesendanger, E. Domain structures in orthorhombic $KNbO_3$ and characterisation of single domain crystals. *Czech. J. Phys. B* **23,** 91–99 (1973).

[82] Lu, N., Yu, R., Cheng, Z., Dai, Y., Zhang, X. & Zhu, J. Ferroelectric polarization and domain walls in orthorhombic $(K_{1-x}Na_x)NbO_3$ lead-free ferroelectric ceramics. *Appl. Phys. Lett.* **96,** 221905 (2010).

[83] Otoničar, M., Škapin, S. D. & Jančar, B. TEM Analyses of the Local Crystal and Domain Structures in $(Na_{1-x}K_x)_{0.5}Bi_{0.5}TiO_3$ Perovskite Ceramics. *IEEE Transactions on Ultrasonics, Ferroelectrics, and Frequency Control* **58,** 1928–1938 (2011).

[84] Dorcet, V. & Trolliard, G. A transmission electron microscopy study of the A-site disordered perovskite $Na_{0.5}Bi_{0.5}TiO_3$. *Acta Mater.* **56,** 1753–1761 (2008).

[85] Asada, T. & Koyama, Y. Ferroelectric domain structures around the morphotropic phase boundary of the piezoelectric material $PbZr_{1-x}Ti_xO_3$. *Phys. Rev. B* **75,** 214111 (2007).

[86] Zhang, L. X. & Ren, X. *In situ* observation of reversible domain switching in aged Mn-doped $BaTiO_3$ single crystals. *Phys. Rev. B* **71,** 174108 (2005).

[87] Kuroda, A., Kurimura, S. & Uesu, Y. Domain inversion in ferroelectric MgO:$LiNbO_3$ by applying electric fields. *Appl. Phys. Lett.* **69,** 1565–1567 (1996).

[88] Shur, V. Y. & Rumyantsev, E. L. Kinetics of ferroelectric domain structure during switching: Theory and experiment. *Ferroelectrics* **151,** 171–180 (1994).

[89] Hong, S., Colla, E. L., Kim, E., Taylor, D. V., Tagantsev, A. K., Muralt, P., No, K. & Setter, N. High resolution study of domain nucleation and growth during polarization switching in Pb(Zr,Ti)O_3 ferroelectric thin film capacitors. *J. Appl. Phys.* **86,** 607–613 (1999).

[90] Stadler, H. L. & Zachmanidis, P. J. Nucleation and Growth of Ferroelectric Domains in $BaTiO_3$ at Fields from 2 to 450 kV/cm. *J. Appl. Phys.* **34,** 3255–3260 (1963).

[91] Miller, R. C. & Savage, A. Velocity of Sidewise 180° Domain-Wall Motion in $BaTiO_3$ as a Function of the Applied Electric Field. *Phys. Rev.* **112,** 755–762 (1958).

[92] Salje, E. K. H. Ferroelastic Materials. *Annu. Rev. Mater. Res.* **42,** 1.1–1.19 (2012).

[93] Mendiola, J., Alemany, C., Jimenez, B. & Maurer, E. Poling strategy of PLZT ceramics. *Ferroelectrics* **54,** 195–198 (2011).

[94] Bartel, C. J., Sutton, C., Goldsmith, B. R., Ouyang, R., Musgrave, C. B., Ghiringhelli, L. M. & Scheffler, M. New tolerance factor to predict the stability of perovskite oxides and halides. *Sci. Adv.* **5,** 1–9 (2019).

[95] Goldschmidt, V. M. Die Gesetze der Krystallochemie. *Naturwissenschaften* **14,** 477–485 (1926).

[96] Woodward, P. M. Octahedral tilting in perovskites. I. Geometrical considerations. *Acta Crystallogr. B* **53,** 32–43 (1997).

[97] Momma, K. & Izumi, F. VESTA: a three-dimensional visualization system for electronic and structural analysis. *J. Appl. Crystallogr.* **41,** 653–658 (2008).

[98] Howard, C. J. & Stokes, H. T. Group-theoretical analysis of octahedral tilting in perovskites. *Acta Cryst. B* **54,** 782–789 (1998).

[99] Woodward, P. M. Octahedral tilting in perovskites. II. Structure stabilizing forces. *Acta Crystallogr. B* **53,** 44–66 (1997).

[100] Woodward, D. I. & Reaney, I. M. Electron diffraction of tilted perovskites. *Acta Cryst. B* **61,** 387–99 (2005).

[101] Glazer, A. M. The Classification of Tilted Octahedra in Perovskites. *Acta Cryst. B* **28,** 3384–3392 (1972).

[102] Glazer, A. M. Simple Ways of Determining Perovskite Structures. *Acta Cryst. A* **31,** 756–762 (1975).

[103] Stokes, H. T., Kisi, E. H., Hatch, D. M. & Howard, C. J. Group-theoretical analysis of octahedral tilting in ferroelectric perovskites. *Acta Cryst. B* **58,** 934–938 (2002).

[104] Park, S.-E. & Shrout, T. R. Ultrahigh strain and piezoelectric behavior in relaxor based ferroelectric single crystals. *J. Appl. Phys.* **82,** 1804–1811 (1997).

[105] Cross, L. E. Relaxor ferroelectrics. *Ferroelectrics* **76,** 241–267 (1987).

[106] Fu, D., Taniguchi, H., Itoh, M., Koshihara, S. Y., Yamamoto, N. & Mori, S. Relaxor Pb($Mg_{1/3}Nb_{2/3}$)O_3: A Ferroelectric with Multiple Inhomogeneities. *Phys. Rev. Lett.* **103,** 207601 (2009).

[107] Ravez, J. & Simon, A. Some Solid State Chemistry Aspects of Lead-Free Relaxor Ferroelectrics. *J. Solid State Chem.* **162,** 260–265 (2001).

[108] Eremenko, M., Krayzman, V., Bosak, A., Playford, H. Y., Chapman, K. W., Woicik, J. C., Ravel, B. & Levin, I. Local atomic order and hierarchical polar nanoregions in a classical relaxor ferroelectric. *Nat. Commun.* **10,** 1–9 (2019).

[109] Cohen, R. E. Relaxors go critical. *Nature* **441,** 941–942 (2006).

[110] Samara, G. A. The relaxational properties of compositionally disordered ABO_3 perovskites. *J. Phys.: Condens. Matter* **15,** 367–411 (2003).

[111] Bokov, A. A. & Ye, Z.-G. Dielectric Relaxation in Relaxor Ferroelectrics. *J. Adv. Dielectr.* **2,** 1241010 (2012).

[112] Bokov, A. A., Rodriguez, B. J., Zhao, X., Ko, J.-H., Jesse, S., Long, X., Qu, W., Kim, T. H., Budai, J. D., Morozovska, A. N., Kojima, S., Tan, X., Kalinin, S. V. & Ye, Z.-G. Compositional disorder, polar nanoregions and dipole dynamics in $Pb(Mg_{1/3}Nb_{2/3})O_3$-based relaxor ferroelectrics. *Z. Kristallogr.* **226,** 99–107 (2011).

[113] Viehland, D., Jang, S. J., Cross, L. E. & Wuttig, M. Freezing of the polarization fluctuations in lead magnesium niobate relaxors. *J. Appl. Phys.* **68,** 2916–2921 (1990).

[114] Maier, B. J. *Phase transitions in advanced relaxor-ferroelectric materials with a perovskite-type structure* (PhD thesis, University of Hamburg, Hamburg, 2010).

[115] Viehland, D., Li, J. F., Jang, S. J., Cross, L. E. & Wuttig, M. Dipolar-glass model for lead magnesium niobate. *Phys. Rev. B* **43,** 8316–8320 (1991).

[116] Ye, Z.-G. & Schmid, H. Optical, dielectric and polarization studies of the electric field-induced phase transition in $Pb(Mg_{1/3}Nb_{2/3})O_3$ [PMN]. *Ferroelectrics* **145,** 83–108 (1993).

[117] Glaum, J., Simons, H., Hudspeth, J., Acosta, M. & Daniels, J. E. Temperature dependent polarization reversal mechanism in $0.94(Bi_{1/2}Na_{1/2})TiO_3$-$0.06Ba(Zr_{0.02}Ti_{0.98})O_3$ relaxor ceramics. *Appl. Phys. Lett.* **107,** 232906 (2015).

[118] Jo, W., Daniels, J., Damjanovic, D., Kleemann, W. & Rödel, J. Two-stage processes of electrically induced-ferroelectric to relaxor transition in $0.94(Bi_{1/2}Na_{1/2})TiO_3$-$0.06BaTiO_3$. *Appl. Phys. Lett.* **102,** 192903 (2013).

[119] Bobnar, V., Kutnjak, Z., Pirc, R. & Levstik, A. Electric-field-temperature phase diagram of the relaxor ferroelectric lanthanum-modified lead zirconate titanate. *Phy. Rev. B* **60,** 6420–6427 (1999).

[120] Glazounov, A. E. & Tagantsev, A. K. Direct evidence for Vögel-Fulcher freezing in relaxor ferroelectrics. *Appl. Phys. Lett.* **73,** 856–858 (1998).

[121] Garg, R., Rao, B. N., Senyshyn, A., Krishna, P. S. R. & Ranjan, R. Lead-free piezoelectric system $(Na_{0.5}Bi_{0.5})TiO_3$-$BaTiO_3$: Equilibrium structures and irreversible structural transformations driven by electric field and mechanical impact. *Phy. Rev. B* **88,** 014103 (2013).

[122] Ahn, C. W., Hong, C.-H., Choi, B.-Y., Kim, H.-P., Han, H.-S., Hwang, Y., Jo, W., Wang, K., Li, J.-F., Lee, J.-S. & Kim, I. W. A brief review on relaxor ferroelectrics and selected issues in lead-free relaxors. *J. Korean Phys. Soc.* **68,** 1481–1494 (2016).

[123] Blinc, R., Gregorovi, A., Zalar, B., Pirc, R., Laguta, V. V. & Glinchuk, M. D. ^{207}Pb NMR study of the relaxor behavior in $PbMg_{1/3}Nb_{2/3}O_3$. *Phys. Rev. B* **63,** 024104 (2000).

[124] Glinchuk, M. & Farhi, R. A random field theory based model for ferroelectric relaxors. *J. Condens. Matter Phys.* **8,** 6985–6996 (1996).

[125] Westphal, V., Kleemann, W. & Glinchuk, M. D. Diffuse Phase Transitions and Random-Field-Induced Domain States of the "Relaxor" Ferroelectric $PbMg_{1/3}Nb_{2/3}O_3$. *Phys. Rev. Lett.* **68,** 847–850 (1992).

[126] Kleemann, W. Random-field induced antiferromagnetic, ferroelectric and structural domain states. *Int. J. Mod. Phys. B* **7,** 2469–2507 (1993).

[127] Hlinka, J. Do We Need the Ether of Polar Nanoregions? *J. Adv. Dielectr.* **2,** 1241006 (2012).

[128] Gehring, P. M., Hiraka, H., Stock, C., Lee, S. H., Chen, W., Ye, Z. G., Vakhrushev, S. B. & Chowdhuri, Z. Reassessment of the Burns temperature and its relationship to the diffuse scattering, lattice dynamics, and thermal expansion in relaxor $Pb(Mg_{1/3}Nb_{2/3})O_3$. *Phys. Rev. B* **79,** 224109 (2009).

[129] Jeong, I. K., Darling, T. W., Lee, J. K., Proffen, T., Heffner, R. H., Park, J. S., Hong, K. S., Dmowski, W. & Egami, T. Direct observation of the formation of polar nanoregions in $Pb(Mg_{1/3}Nb_{2/3})O_3$ using neutron pair distribution function analysis. *Phys. Rev. Lett.* **94,** 147602 (2005).

[130] Groszewicz, P. B., Breitzke, H., Dittmer, R., Sapper, E., Jo, W., Buntkowsky, G. & Rödel, J. Nanoscale phase quantification in lead-free$(Bi_{1/2}Na_{1/2})TiO_3$-$BaTiO_3$ relaxor ferroelectrics by means of ^{23}Na NMR. *Phys. Rev. B* **90,** 220104 (2014).

[131] Liu, N., Dittmer, R., Stark, R. W. & Dietz, C. Visualization of polar nanoregions in lead-free relaxors *via* piezoresponse force microscopy in torsional dual AC resonance tracking mode. *Nanoscale* **7,** 11787–96 (2015).

[132] Yoshida, M., Mori, S., Yamamoto, N., Uesu, Y. & Kiat, J. M. TEM observation of polar domains in relaxor ferroelectric $Pb(Mg_{1/3}Nb_{2/3})O_3$. *Ferroelectrics* **217,** 327–333 (1998).

[133] Tao, H., Wu, H., Liu, Y., Zhang, Y., Wu, J., Li, F., Lyu, X., Zhao, C., Xiao, D., Zhu, J. & Pennycook, S. J. Ultrahigh Performance in Lead-Free Piezoceramics Utilizing a Relaxor Slush Polar State with Multiphase Coexistence. *J. Am. Chem. Soc.* **141,** 13987–13994 (2019).

[134] Burns, G. & Dacol, F. Glassy polarization behavior in ferroelectric compounds $Pb(Mg_{1/3}Nb_{2/3})O_3$ and $Pb(Zn_{1/3}Nb_{2/3})O_3$. *Solid State Commun.* **48,** 853–856 (1983).

[135] Randall, C. A. & Bhalla, A. S. Nanostructural-property relations in complex lead perovskites. *Jpn. J. Appl. Phys.* **29,** 327–333 (1990).

[136] Liu, Y., Withers, R. L., Nguyen, B. & Elliott, K. Structurally frustrated polar nanoregions in $BaTiO_3$-based relaxor ferroelectric systems. *Appl. Phys. Lett.* **91,** 152907 (2007).

[137] Takenaka, H., Grinberg, I., Liu, S. & Rappe, A. M. Slush-like polar structures in single-crystal relaxors. *Nature* **546,** 391–395 (2017).

[138] Bosak, A., Chernyshov, D., Vakhrushev, S. & Krisch, M. Diffuse scattering in relaxor ferroelectrics: true three-dimensional mapping, experimental artefacts and modelling. *Acta Crystallogr. A* **68,** 117–23 (2012).

[139] Manley, M. E., Lynn, J. W., Abernathy, D. L., Specht, E. D., Delaire, O., Bishop, A. R., Sahul, R. & Budai, J. D. Phonon localization drives polar nanoregions in a relaxor ferroelectric. *Nat. Commun.* **5,** 1–9 (2014).

[140] Kim, J. S., Choi, B. C., Jeong, J. H., Lee, K.-S. & Cho, S.-B. Ferroelectric Properties of La Doped $Na_{1/2}Bi_{1/2}TiO_3$ (NBT) Lead-Free Ferroelectric Ceramics. *Ferroelectrics* **384,** 120–125 (2009).

[141] Guo, Y., Liu, Y., Withers, R. L., Brink, F. & Chen, H. Large Electric Field-Induced Strain and Antiferroelectric Behavior in $(1-x)(Na_{0.5}Bi_{0.5})TiO_3$-$xBaTiO_3$ Ceramics. *Chem. Mater.* **23,** 219–228 (2011).

[142] McQuade, R. R. & Dolgos, M. R. A review of the structure-property relationships in lead-free piezoelectric $(1-x)Na_{0.5}Bi_{0.5}TiO_3$-$(x)BaTiO_3$. *J. Solid State Chem.* **242,** 140–147 (2016).

[143] Zhang, S.-T., Kounga, A. B., Aulbach, E. & Deng, Y. Temperature-Dependent Electrical Properties of $0.94Bi_{0.5}Na_{0.5}TiO_3$-$0.06BaTiO_3$ Ceramics. *J. Am. Ceram. Soc.* **91,** 3950–3954 (2008).

[144] Doshida, Y., Shimizu, H., Mizuno, Y. & Tamura, H. Investigation of High-Power Properties of (Bi,Na,Ba)TiO_3 and $(Sr,Ca)_2NaNb_5O_{15}$ Piezoelectric Ceramics. *Jpn. J. Appl. Phys.* **52,** 07HE01 (2013).

[145] Foronda, H., Deluca, M., Aksel, E., Forrester, J. S. & Jones, J. L. Thermally-induced loss of piezoelectricity in ferroelectric $Na_{0.5}Bi_{0.5}TiO_3$-$BaTiO_3$. *Mater. Lett.* **115,** 132–135 (2014).

[146] Hiruma, Y., Watanabe, Y., Nagata, H. & Takenaka, T. Phase Transition Temperatures of Divalent and Trivalent Ions Substituted $(Bi_{1/2}Na_{1/2})TiO_3$ Ceramics. *Key Eng. Mater.* **350,** 93–96 (2007).

[147] Craciun, F., Galassi, C. & Birjega, R. Electric-field-induced and spontaneous relaxor-ferroelectric phase transitions in $(Na_{1/2}Bi_{1/2})_{1-x}Ba_xTiO_3$. *J. Appl. Phys.* **112,** 124106 (2012).

[148] Ma, C. & Tan, X. Phase diagram of unpoled lead-free $(1-x)(Bi_{1/2}Na_{1/2})TiO_3$-$x$$BaTiO_3$ ceramics. *Solid State Commun.* **150,** 1497–1500 (2010).

[149] Ma, C., Guo, H., Beckman, S. P. & Tan, X. Creation and Destruction of Morphotropic Phase Boundaries through Electrical Poling: A Case Study of Lead-Free $(Bi_{1/2}Na_{1/2})TiO_3$-$BaTiO_3$ Piezoelectrics. *Phys. Rev. Lett.* **109,** 107602 (2012).

[150] Adhikary, G. D., Mahale, B., Rao, B. N., Senyshyn, A. & Ranjan, R. Depoling phenomena in $Na_{0.5}Bi_{0.5}TiO_3$-$BaTiO_3$: A structural perspective. *Phy. Rev. B* **103,** 184106 (2021).

[151] Dai, Y. J., Pan, J. S. & Zhang, X. W. Composition Range of Morphotropic Phase Boundary and Electrical Properties of NBT-BT System. *Key Eng. Mater.* **336,** 206–209 (2007).

[152] Chen, M., Xu, Q., Kim, B. H., Ahn, B. K., Ko, J. H., Kang, W. J. & Nam, J. Structure and electrical properties of $(Na_{0.5}Bi_{0.5})_{1-x}Ba_xTiO_3$ piezoelectric ceramics. *J. Eur. Ceram. Soc.* **28,** 843–849 (2008).

[153] Swain, S., Kar, S. K. & Kumar, P. Dielectric, optical, piezoelectric and ferroelectric studies of NBT-BT ceramics near MPB. *Ceram. Int.* **41,** 10710–10717 (2015).

[154] Xu, C., Lin, D. & Kwok, K. W. Structure, electrical properties and depolarization temperature of $(Bi_{0.5}Na_{0.5})TiO_3$-$BaTiO_3$ lead-free piezoelectric ceramics. *Solid State Sci.* **10,** 934–940 (2008).

[155] Anton, E.-M., Jo, W., Damjanovic, D. & Rödel, J. Determination of depolarization temperature of $(Bi_{1/2}Na_{1/2})TiO_3$-based lead-free piezoceramics. *J. Appl. Phys.* **110,** 094108 (2011).

[156] Sung, Y. S., Kim, J. M., Cho, J. H., Song, T. K., Kim, M. H. & Park, T. G. Roles of lattice distortion in $(1-x)(Bi_{0.5}Na_{0.5})TiO_3$-$x$$BaTiO_3$ ceramics. *Appl. Phys. Lett.* **96,** 202901 (2010).

[157] Jo, W., Schaab, S., Sapper, E., Schmitt, L. A., Kleebe, H.-J., Bell, A. J. & Rödel, J. On the phase identity and its thermal evolution of lead free $(Bi_{1/2}Na_{1/2})TiO_3$-6mol% $BaTiO_3$. *J. Appl. Phys.* **110,** 074106 (2011).

[158] Ma, C., Tan, X., Dul'kin, E. & Roth, M. Domain structure-dielectric property relationship in lead-free $(1-x)(Bi_{1/2}Na_{1/2})TiO_3$-$x$$BaTiO_3$ ceramics. *J. Appl. Phys.* **108,** 104105 (2010).

[159] Aksel, E., Forrester, J. S., Kowalski, B., Deluca, M., Damjanovic, D. & Jones, J. L. Structure and properties of Fe-modified $Na_{0.5}Bi_{0.5}TiO_3$ at ambient and elevated temperature. *Phys. Rev. B* **85,** 024121 (2012).

[160] Ma, C. & Tan, X. *In situ* Transmission Electron Microscopy Study on the Phase Transitions in Lead-Free $(1-x)(Bi_{1/2}Na_{1/2})TiO_3$-$xBaTiO_3$ Ceramics. *J. Am. Ceram. Soc.* **94,** 4040–4044 (2011).

[161] Wylie-van Eerd, B., Damjanovic, D., Klein, N., Setter, N. & Trodahl, J. Structural complexity of $(Na_{0.5}Bi_{0.5})TiO_3$-$BaTiO_3$ as revealed by Raman spectroscopy. *Phys. Rev. B* **82,** 104112 (2010).

[162] Rout, D., Moon, K.-S., Rao, V. S. & Kang, S.-J. L. Study of the morphotropic phase boundary in the lead-free $Na_{1/2}Bi_{1/2}TiO_3$-$BaTiO_3$ system by Raman spectroscopy. *J. Ceram. Soc. Japan* **117,** 797–800 (2009).

[163] Ma, C., Guo, H. & Tan, X. A New Phase Boundary in $(Bi_{1/2}Na_{1/2})TiO_3$-$BaTiO_3$ Revealed via a Novel Method of Electron Diffraction Analysis. *Adv. Funct. Mater.* **23,** 5261–5266 (2013).

[164] Jo, W., Daniels, J. E., Jones, J. L., Tan, X., Thomas, P. A., Damjanovic, D. & Rödel, J. Evolving morphotropic phase boundary in lead-free $(Bi_{1/2}Na_{1/2})TiO_3$-$BaTiO_3$ piezoceramics. *J. Appl. Phys.* **109,** 014110 (2011).

[165] Jones, G. O. & Thomans, P. A. Investigation of the structure and phase transitions in the novel A-site substituted distorted perovskite compound $Na_{0.5}Bi_{0.5}TiO_3$. *Acta Cryst. B* **58,** 16–178 (2002).

[166] Jones, G. O. & Thomas, P. A. The tetragonal phase of $Na_{0.5}Bi_{0.5}TiO_3$ - a new variant of the perovskite structure. *Acta Cryst. B* **56,** 426–430 (2000).

[167] Paterson, A. R., Nagata, H., Tan, X., Daniels, J. E., Hinterstein, M., Ranjan, R., Groszewicz, P. B., Jo, W. & Jones, J. L. Relaxor-ferroelectric transitions: Sodium bismuth titanate derivatives. *MRS Bull.* **43,** 600–606 (2018).

[168] Aksel, E., Forrester, J. S., Jones, J. L., Thomas, P. A., Page, K. & Suchomel, M. R. Monoclinic crystal structure of polycrystalline $Na_{0.5}Bi_{0.5}TiO_3$. *Appl. Phys. Lett.* **98,** 152901 (2011).

[169] Gorfman, S. & Thomas, P. A. Evidence for a non-rhombohedral average structure in the lead-free piezoelectric material $Na_{0.5}Bi_{0.5}TiO_3$. *J. Appl. Crystallogr.* **43,** 1409–1414 (2010).

[170] Rao, B. N., Fitch, A. N. & Ranjan, R. Ferroelectric-ferroelectric phase coexistence in $Na_{1/2}Bi_{1/2}TiO_3$. *Phys. Rev. B* **87,** 060102 (2013).

[171] Rao, B. N., Avdeev, M., Kennedy, B. & Ranjan, R. Phase boundary at $x = 0.03$ and its anomalous influence on the structure and properties in the lead-free piezoelectric $(1-x)Na_{1/2}Bi_{1/2}TiO_3$-$(x)BaTiO_3$. *Phys. Rev. B* **92,** 214107 (2015).

[172] Usher, T.-M., Levin, I., Daniels, J. E. & Jones, J. L. Electric-field-induced local and mesoscale structural changes in polycrystalline dielectrics and ferroelectrics. *Sci. Rep.* **5,** 1–10 (2015).

[173] Soukhojak, A. N., Wang, H., Farrey, G. W. & Chiang, Y.-M. Superlattice in single crystal barium-doped sodium bismuth titanite. *J. Phys. Chem. Solids* **61,** 301–304 (2000).

[174] Yao, J., Ge, W., Yang, Y., Luo, L., Li, J., Viehland, D., Bhattacharyya, S., Zhang, Q. & Luo, H. Observation of partially incoherent 110 boundaries between polar nanodomains in $Na_{1/2}Bi_{1/2}TiO_3$ single crystals. *J. Appl. Phys.* **108,** 064114 (2010).

[175] Levin, I. & Reaney, I. M. Nano- and Mesoscale Structure of $Na_{1/2}Bi_{1/2}TiO_3$: A TEM Perspective. *Adv. Funct. Mater.* **22,** 3445–3452 (2012).

[176] Meyer, K.-C., Gröting, M. & Albe, K. Octahedral tilt transitions in the relaxor ferroelectric $Na_{1/2}Bi_{1/2}TiO_3$. *J. Solid State Chem.* **227,** 117–122 (2015).

[177] Dorcet, V., Trolliard, G. & Boullay, P. Reinvestigation of Phase Transitions in $Na_{0.5}Bi_{0.5}TiO_3$ by TEM. Part I: First Order Rhombohedral to Orthorhombic Phase Transition. *Chem. Mater.* **20,** 5061–5073 (2008).

[178] Dorcet, V., Trolliard, G. & Boullay, P. The structural origin of the antiferroelectric properties and relaxor behavior of $Na_{0.5}Bi_{0.5}TiO_3$. *J. Magn. Magn. Mater.* **321,** 1758–1761 (2009).

[179] Maurya, D., Murayama, M., Pramanick, A., Reynolds, W. T., An, K. & Priya, S. Origin of high piezoelectric response in A-site disordered morphotropic phase boundary composition of *lead-free* piezoelectric $0.93(Na_{0.5}Bi_{0.5})TiO_3$-$0.07BaTiO_3$. *J. Appl. Phy.* **113,** 114101 (2013).

[180] Petzelt, J., Kamba, S., Fábry, J., Noujni, D., Porokhonskyy, V., Pashkin, A., Franke, I., Roleder, K., Suchanicz, J., Klein, R. & Kugel, G. E. Infrared, Raman and high-frequency dielectric spectroscopy and the phase transitions in $Na_{1/2}Bi_{1/2}TiO_3$. *J. Condens. Matter Phys.* **16,** 2719–2731 (2004).

[181] Park, S. E., Chung, S. J., Kim, I. T. & Hong, K. S. Nonstoichiometry and the longrange cation ordering in crystals of $(Na_{1/2}Bi_{1/2})TiO_3$. *J. Am. Ceram. Soc.* **77,** 2641–2647 (1994).

[182] Gröting, M., Hayn, S. & Albe, K. Chemical order and local structure of the lead-free relaxor ferroelectric $Na_{1/2}Bi_{1/2}TiO_3$. *J. Solid State Chem.* **184,** 2041–2046 (2011).

[183] Buttner, R. H. & Maslen, E. N. Structural Parameters and Electron Difference Density in $BaTiO_3$. *Acta Cryst.* **B48,** 764–769 (1992).

[184] Ranjan, R. & Dviwedi, A. Structure and dielectric properties of $(Na_{0.50}Bi_{0.50})_{1-x}Ba_xTiO_3$: $0 \leq x \leq 0.10$. *Solid State Commun.* **135,** 394–399 (2005).

[185] Simons, H., Daniels, J., Jo, W., Dittmer, R., Studer, A., Avdeev, M., Rödel, J. & Hoffman, M. Electric-field-induced strain mechanisms in lead-free $94\%(Bi_{1/2}Na_{1/2})TiO_3$-$6\%BaTiO_3$. *Appl. Phys. Lett.* **98,** 082901 (2011).

[186] Mohanty, H. S., Dam, T., Borkar, H., Pradhan, D. K., Mishra, K. K., Kumar, A., Sahoo, B., P. K. Kulriya, C. C., Scott, J. F. & Pradhan, D. K. Structural transformations and physical properties of $(1-x)Na_{0.5}Bi_{0.5}TiO_3$-$xBaTiO_3$ solid solutions near a morphotropic phase boundary. *J. Condens. Matter Phys.* **31,** 075401 (2019).

[187] Cordero, F., Craciun, F., Trequattrini, F., Mercadelli, E. & Galassi, C. Phase transitions and phase diagram of the ferroelectric perovskite $(Na_{0.5}Bi_{0.5})_{1-x}Ba_xTiO_3$ by anelastic and dielectric measurements. *Phy. Rev. B* **81,** 144124 (2010).

[188] Ge, W., Luo, C., Zhang, Q., Ren, Y., Li, J. & et al., H. L. Evolution of structure in $Na_{0.5}Bi_{0.5}TiO_3$ single crystals with $BaTiO_3$. *Appl. Phys. Lett.* **105,** 162913 (2014).

[189] Daniels, J. E., Jo, W., Rödel, J., Rytz, D. & Donner, W. Structural origins of relaxor behavior in a $0.96(Bi_{1/2}Na_{1/2})TiO_3$-$0.04BaTiO_3$ single crystal under electric field. *Appl. Phys. Lett.* **98,** 252904 (2011).

[190] Pforr, F., Major, M., Donner, W., Stuhr, U. & Roessli, B. Influence of tetragonal platelets on the dielectric permittivity of $0.964Na_{1/2}Bi_{1/2}TiO_3$-$0.036BaTiO_3$. *Phys. Rev. B* **94,** 014105 (2016).

[191] Zhang, H., Deng, G., Studer, A. J., Li, X., Zhao, X. & Luo, H. Neutron diffuse scattering of $(1-x)(Na_{0.5}Bi_{0.5})TiO_3$-$xBaTiO_3$ relaxor ferroelectric single crystals. *Scr. Mater.* **86,** 5–8 (2014).

[192] Ge, W., Luo, C., Devreugd, C. P., Zhang, Q., Ren, Y., Li, J., Luo, H. & Viehland, D. Direct evidence of correlations between relaxor behavior and polar nano-regions in relaxor ferroelectrics: A case study of lead-free piezoelectrics $Na_{0.5}Bi_{0.5}TiO_3$-x%$BaTiO_3$. *Appl. Phys. Lett.* **103,** 241914 (2013).

[193] Xu, Y.-N. & Ching, W. Y. Electronic structure of $(Na_{1/2}Bi_{1/2})TiO_3$ and its solid solution with $BaTiO_3$. *Philos. Mag. B* **80,** 1141–1151 (2000).

[194] Chiang, Y.-M., Farrey, G. W. & Soukhojak, A. N. Lead-free high-strain single-crystal piezoelectrics in the alkaline-bismuth-titanate perovskite family. *Appl. Phys. Lett.* **73,** 3683–3685 (1998).

[195] Kling, J., Hayn, S., Schmitt, L. A., Gröting, M., Kleebe, H.-J. & Albe, K. A-site occupancy in the lead-free $(Bi_{1/2}Na_{1/2}TiO_3)_{0.94}$-$(BaTiO_3)_{0.06}$ piezoceramic: Combining first-principles study and TEM. *J. Appl. Phys.* **107,** 114113 (2010).

[196] Shanmuga Sundari, S., Kumar, B. & Dhanasekaran, R. Synthesis, dielectric and relaxation behavior of lead free NBT-BT ceramics. *Ceram. Int.* **39,** 555–561 (2013).

[197] Schmitt, L. A., Kling, J., Hinterstein, M., Hoelzel, M., Jo, W., Kleebe, H.-J. & Fuss, H. Structural investigations on lead-free $Bi_{1/2}Na_{1/2}TiO_3$-based piezoceramics. *J. Mater. Sci.* **46,** 4368–4376 (2011).

[198] Hinterstein, M., Schmitt, L. A., Hoelzel, M., Jo, W., Rödel, J., Kleebe, H.-J. & Hoffman, M. Cyclic electric field response of morphotropic $Bi_{1/2}Na_{1/2}TiO_3$-$BaTiO_3$ piezoceramics. *Appl. Phys. Lett.* **106,** 222904 (2015).

[199] Schmitt, L. A. & Kleebe, H.-J. Single Grains Hosting Two Space Groups - A Transmission Electron Microscopy Study of a Lead-Free Ferroelectric. *Funct. Mater. Lett.* **3,** 55–58 (2011).

[200] Zhou, X., Jiang, C., Luo, H., Chen, C., Zhou, K. & Zhang, D. Enhanced piezoresponse and electric field induced relaxor-ferroelectric phase transition in NBT-0.06BT ceramic prepared from hydrothermally synthesized nanoparticles. *Ceram. Int.* **42,** 18631–18640 (2016).

[201] Chen, C.-S., Chen, P.-Y. & Tu, C.-S. Polar nanoregions and dielectric properties in high-strain lead-free $0.93(Bi_{1/2}Na_{1/2})TiO_3$-$0.07BaTiO_3$ piezoelectric single crystals. *J. Appl. Phys.* **115,** 014105 (2014).

[202] Yao, J., Monsegue, N., Murayama, M., Leng, W., Reynolds, W. T., Zhang, Q., Luo, H., Li, J., Ge, W. & Viehland, D. Role of coexisting tetragonal regions in the rhombohedral phase of $Na_{0.5}Bi_{0.5}TiO_3$-xat.%$BaTiO_3$ crystals on enhanced piezoelectric properties on approaching the morphotropic phase boundary. *Appl. Phys. Lett.* **100,** 012901 (2012).

[203] Picht, G., Töpfer, J. & Hennig, E. Structural properties of $(Bi_{0.5}Na_{0.5})_{1-x}Ba_xTiO_3$ lead-free piezoelectric ceramics. *J. Eur. Ceram. Soc.* **30,** 3445–3453 (2010).

[204] Daniels, J. E., Jo, W., Rödel, J. & Jones, J. L. Electric-field-induced phase transformation at a lead-free morphotropic phase boundary: Case study in a 93% $(Bi_{0.5}Na_{0.5})TiO_3$-7% $BaTiO_3$ piezoelectric ceramic. *Appl. Phys. Lett.* **95,** 032904 (2009).

[205] Ge, W., Devreugd, C. P., Phelan, D., Zhang, Q., Ahart, M., Li, J., Luo, H., Boatner, L. A., Viehland, D. & Gehring, P. M. Lead-free and lead-based ABO_3 perovskite relaxors with mixed-valence *A*-site and *B*-site disorder: Comparative neutron scattering structural study of $(Na_{1/2}Bi_{1/2})TiO_3$ and $Pb(Mg_{1/3}Nb_{2/3})O_3$. *Phys. Rev. B* **88,** 174115 (2013).

[206] Yao, J., Yan, L., Ge, W., Luo, L., Li, J., Viehland, D., Zhang, Q. & Luo, H. Evolution of domain structures in $Na_{1/2}Bi_{1/2}TiO_3$ single crystals with $BaTiO_3$. *Phys. Rev. B* **83,** 054107 (2011).

[207] Li, X., Nie, S., Wang, F., Zhao, X., Zhang, H., Luo, H., Li, G., Ko, J.-H., Guo, Z., Jiang, Z. & Tai, R. Local-structure evidence for a phase transition in a lead-free single crystal of $(Na_{1/2}Bi_{1/2})TiO_3$-0.06$BaTiO_3$ by absorption fine-structure spectroscopy with synchrotron x-ray radiation. *Phys. Rev. B* **101,** 104105 (2020).

[208] Kling, J., Tan, X., Jo, W., Kleebe, H.-J., Fuess, H. & Rödel, J. *In Situ* Transmission Electron Microscopy of Electric Field-Triggered Reversible Domain Formation in Bi-Based Lead-Free Piezoceramics. *J. Am. Ceram. Soc.* **93,** 2452–2455 (2010).

[209] Zhang, J., Pan, Z., Guo, F. F., Liu, W. C., Ning, H., Chen, Y. B., Lu, M.-H., Yang, B., Chen, J., Zhang, S.-T., Xing, X., Rödel, J., Cao, W. & Chen, Y.-F. Semiconductor/relaxor 0-3 type composites without thermal depolarization in $Bi_{0.5}Na_{0.5}TiO_3$-based lead-free piezoceramics. *Nat. Commun.* **6,** 1–10 (2015).

[210] K.V., Lalitha, Riemer, L. M., Koruza, J. & Rödel, J. Hardening of electromechanical properties in piezoceramics using a composite approach. *Appl. Phys. Lett.* **111,** 022905 (2017).

[211] Fan, Z., Zhou, L., Kim, T.-H., Zhang, J., Zhang, S.-T. & Tan, X. Mechanisms of enhanced thermal stability of polarization in lead-free $(Bi_{1/2}Na_{1/2})_{0.94}Ba_{0.06}TiO_3$/ZnO ceramic composites. *Phys. Rev. Mater.* **3,** 024402 (2019).

[212] Yin, J., Wang, Y., Zhang, Y., Wu, B. & Wu, J. Thermal depolarization regulation by oxides selection in lead-free BNT/oxides piezoelectric composites. *Acta Mater.* **158,** 269–277 (2018).

[213] K.V., Lalitha, Koruza, J. & Rödel, J. Mechanical versus electromechanical hardening in relaxor ferroelectric $Na_{1/2}Bi_{1/2}TiO_3$-$BaTiO_3$ with ZnO inclusions. *Scr. Mater.* **169,** 92–95 (2019).

[214] Riemer, L. M., K. V., Lalitha, Jiang, X., Liu, N., Dietz, C., Stark, R. W., Groszewicz, P. B., Buntkowsky, G., Chen, J., Zhang, S.-T. & Rödel, J. Stress-induced phase transition in lead-free relaxor ferroelectric composites. *Acta Mater.* **136,** 271–280 (2017).

[215] Ren, P., Wang, Y., Waidha, A. I., Clemens, O. & K. V., Lalitha. Compositionally driven relaxor to ferroelectric crossover in $(1-x)Na_{0.5}Bi_{0.5}TiO_3$-$xBiFeO_3$ $(0 \leq x \leq 0.60)$. *J. Mater. Chem. C* **8,** 8613–8621 (2020).

[216] Luo, H., Liu, H., Deng, S., Hu, S., Wang, L., Gao, B., Sun, S., Ren, Y., Qiao, L. & Chen, J. Simultaneously enhancing piezoelectric performance and thermal depolarization in lead-free (Bi,Na)TiO_3-$BaTiO_3$ via introducing oxygen-defect perovskites. *Acta Mater.* **208,** 116711 (2021).

[217] Zang, J., Jo, W. & Rödel, J. Quenching-induced circumvention of integrated aging effect of relaxor lead lanthanum zirconate titanate and $(Bi_{1/2}Na_{1/2})TiO_3$-$BaTiO_3$. *Appl. Phys. Lett.* **102,** 032901 (2013).

[218] Takagi, Y., Ochiai, Y. & Nagata, H. Temperature dependence of dielectric properties and phase transition behavior in quenched $(Bi_{0.5}Na_{0.5})TiO_3$ ceramics. *Jpn. J. Appl. Phys.* **60,** SFFD02 (2021).

[219] Nagata, H., Takagi, Y., Yoneda, Y. & Takenaka, T. Correlation between depolarization temperature and lattice distortion in quenched $(Bi_{1/2}Na_{1/2})TiO_3$-based ceramics. *App. Phys. Express.* **13,** 061002 (2020).

[220] Kodumudi Venkataraman, L. Influence of Quenching and Subsequent Annealing on the Conductivity and Electromechanical Properties of $Na_{1/2}Bi_{1/2}TiO_3$-$BaTiO_3$. *Materials* **14,** 2149 (2021).

[221] Zhang, M.-H., Breckner, P., Frömling, T., Rödel, J. & K.V., Lalitha. Role of thermal gradients on the depolarization and conductivity in quenched $Na_{1/2}Bi_{1/2}TiO_3$-$BaTiO_3$. *Appl. Phys. Lett.* **116,** 262902 (2020).

[222] Takagi, Y., Nagata, H. & Takenaka, T. Effects of quenching on bending strength and piezoelectric properties of $(Bi_{0.5}Na_{0.5})TiO_3$ ceramics. *J. Asian Ceram. Soc.* **8,** 277–283 (2020).

[223] K.V., Lalitha, Wang, B., Ren, P., Hall, D. A. & Rojac, T. Quenching effects and mechanisms in bismuth-based perovskite ferroelectrics. *Open Ceramics* **10,** 100259 (2022).

[224] Li, Q., Wei, J., Tu, T., Cheng, J. & Chen, J. Remarkable piezoelectricity and stable high-temperature dielectric properties of quenched $BiFeO_3$-$BaTiO_3$ ceramics. *J. Am. Ceram. Soc.* **100,** 5573–5583 (2017).

[225] Hua, Q., Ren, P., Wang, J., Wang, Y., Liu, L., K. V., Lalitha, Hua, D. & Zhao, G. Quenching-induced nonergodicity in ergodic $Na_{1/2}Bi_{1/2}TiO_3$-$BaTiO_3$-$AgNbO_3$ ceramics. *J. Mater. Sci.* **56,** 18430–18439 (2021).

[226] Li, Z.-T., Liu, H., Thong, H.-C., Xu, Z., Zhang, M.-H., Yin, J., Li, J.-F., Wang, K. & Chen, J. Enhanced Temperature Stability and Defect Mechanism of BNT-Based Lead-Free Piezoceramics Investigated by a Quenching Process. *Adv. Electron. Mater.* **5,** 1800756 (2019).

[227] Morrison, F. D., Sinclair, D. C. & West, A. R. Characterization of Lanthanum-Doped Barium Titanate Ceramics Using Impedance Spectroscopy. *J. Am. Ceram. Soc.* **84,** 531–538 (2001).

[228] Wang, X., Ren, P., Tian, H., Fan, H., Cai, C. & Liu, W. Enhanced gas sensing properties of SnO_2: The role of the oxygen defects induced by quenching. *J. Alloys Compd.* **669,** 29–37 (2016).

[229] Noguchi, Y., Miwa, I., Goshima, Y. & Miyayama, M. Defect Control for Large Remanent Polarization in Bismuth Titanate Ferroelectrics - Doping Effect of Higher-Valent Cations. *Jpn. J. Appl. Phys.* **39,** 1259–1262 (2000).

[230] Zhang, J., Wang, R.-X., Li, L., Wu, J.-Y., Cui, Y.-S., Gu, Z.-B., Zhang, H., Zhu, M.-W., Zhang, S.-T. & Yang, B. Highly enhanced thermal stability in quenched $Na_{0.5}Bi_{0.5}TiO_3$-based lead-free piezoceramics. *J. Eur. Ceram. Soc.* **39,** 4705–4711 (2019).

[231] Ren, P., Wang, J., Wang, Y., V., L. K. & Zhao, G. Origin of enhanced depolarization temperature in quenched $Na_{0.5}Bi_{0.5}TiO_3$-$BaTiO_3$ ceramics. *J. Eur. Ceram. Soc.* **40,** 2964–2969 (2020).

[232] Miehe, G. *Program for Interpreting Electron Diffraction Patterns (PIEP), Version 7.12* (Department of Materials Science, Technical University of Darmstadt, 2002).

[233] Fetzer, A.-K., Trapp, M., Lauterbach, S. & Kleebe, H.-J. Introduction to Transmission Electron Microscopy; The Basics. In *Encyclopedia of Materials: Technical Ceramics and Glasses* (ed. Pomeroy, M.) 578–599 (Elsevier, Amsterdam, 2021).

[234] Williams, D. B. & Carter, C. B. *Transmission Electron Microscopy: A Textbook for Materials Science* (Springer, New York, 2009).

[235] Thomas, J. & Gemming, T. *Analytische Transmissionselektronenmikroskopie - Eine Einführung für den Praktiker* (Springer, Wien, 2013).

[236] De Graef, M. *Introduction to Conventional Transmission Electron Microscopy* (Cambridge University Press, Cambridge, 2003).

[237] Scherzer, O. The Theoretical Resolution Limit of the Electron Microscope. *J. Appl. Phys.* **20,** 20–29 (1949).

[238] Scherzer, O. Sphärische und chromatische Korrektur von Elektronen-Linsen. *Optik* **2,** 114–132 (1947).

[239] Bleloch, A. & Ramasse, Q. Lens Aberrations: Diagnosis and Correction. In *Aberration-Corrected Analytical Transmission Electron Microscopy* (ed. Brydson, R.) 163–210 (John Wiley & Sons Ltd., Chichester, 2011).

[240] Reimer, L. *Transmission Electron Microscopy: Physics of Image Formation and Microanalysis* (Springer, Berlin, 1984).

[241] McLaren, A. C. *Transmission Electron Microscopy of Minerals and Rocks* (Cambridge Univerity Press, Cambridge, 1991).

[242] Spence, J. C. H. *High-Resolution Electron Microscopy* (Oxford University Press, Oxford, 2013).

[243] Chou, J.-F., Lin, M.-H. & Lu, H.-Y. Ferroelectric Domains in Pressureless-Sintered Barium Titanate. *Acta Mater.* **48,** 3569–3579 (2000).

[244] Gevers, R., Delavignette, P., Blank, H., Van Landuyt, J. & Amelinckx, S. Electron Microscope Transmission Images of Coherent Domain Boundaries II. Observations. *Phys. Status Solidi B* **5,** 595–633 (1964).

[245] Verwerft, M., Van Tendeloo, G., Van Landuyt, J. & Amelinckx, S. Electron microscopy of domain structures. *Ferroelectrics* **97,** 5–17 (1989).

[246] Serneels, R., Snykers, M., Delavignette, P., Gevers, R. & Amelinckx, S. Friedel's Law in Electron Diffraction as Applied to the Study of Domain Structures in Non-Centrosymmetrical Crystals. *Phys. Stat. Sol. B* **58,** 277–292 (1973).

[247] Rothmann, M. U., Li, W., Zhu, Y., Bach, U., Spiccia, L., Etheridge, J. & Cheng, Y.-B. Direct observation of intrinsic twin domains in tetragonal $CH_3NH_3PbI_3$. *Nat. Commun.* **8,** 1–8 (2017).

[248] Pennycook, S. J. & Nellist, P. D. *Scanning Transmission Electron Microscopy: Imaging and Analysis* (Springer, New York, 2011).

[249] Craven, A. Details of STEM. In *Aberration-Corrected Analytical Transmission Electron Microscopy* (ed. Brydson, R.) 111–161 (John Wiley & Sons Ltd., Chichester, 2011).

[250] Findlay, S. D., Shibata, N., Sawada, H., Okunishi, E., Kondo, Y., Yamamoto, T. & Ikuhara, Y. Robust atomic resolution imaging of light elements using scanning transmission electron microscopy. *Appl. Phys. Lett.* **95,** 191913 (2009).

[251] Nord, M., Vullum, P. E., MacLaren, I., Tybell, T. & Holmestad, R. Atomap: a new software tool for the automated analysis of atomic resolution images using two-dimensional Gaussian fitting. *Adv. Struct. Chem. Imag.* **3,** 1–12 (2017).

[252] O'Connell, E. *TEMUL Toolkit* (https://temul-toolkit.readthedocs.io/en/latest/, 2020).

[253] Brydson, R. & Hondow, N. Electron Energy Loss Spectrometry and Energy Dispersive X-ray Analysis. In *Aberration-Corrected Analytical Transmission Electron Microscopy* (ed. Brydson, R.) 163–210 (John Wiley & Sons Ltd., Chichester, 2011).

[254] Egerton, R. F. & Malac, M. EELS in the TEM. *J. Electron Spectrosc. Relat. Phenom.* **143,** 43–50 (2005).

[255] Stoyanov, E., Langenhorst, F. & Steinle-Neumann, G. The effect of valence state and site geometry on Ti $L_{3,2}$ and O K electron energy-loss spectra of Ti_xO_y phases. *Am. Mineral.* **92,** 577–586 (2007).

[256] Goldstein, J. I., Newbury, D. E., Michael, J. R., Ritchie, N. W., Scott, J. H. J. & Joy, D. C. *Scanning electron microscopy and X-ray microanalysis,* 4th edition (Springer, New York, 2017).

[257] Zhou, W., Apkarian, R. P., Wang, Z. L. & Joy, D. Fundamentals of Scanning Electron Microscopy. In *Scanning Microscopy for Nanotechnology* (eds. Zhou, W. & Wang, Z. L.) 1–40 (Springer, New York, 2006).

[258] Balke, N., Bdikin, I., Kalinin, S. V. & Kholkin, A. L. Electromechanical Imaging and Spectroscopy of Ferroelectric and Piezoelectric Materials: State of the Art and Prospects for the Future. *J. Am. Ceram. Soc.* **92,** 1629–1647 (2009).

[259] Soergel, E. Piezoresponse force microscopy (PFM). *J. Phys. D: Appl. Phys.* **44,** 1–17 (2011).

[260] Gruverman, A. & Kalinin, S. V. Piezoresponse force microscopy and recent advances in nanoscale studies of ferroelectrics. *J. Mater. Sci.* **41,** 107–116 (2006).

[261] Proksch, R. & Kalinin, S. Piezoresponse Force Microscopy. *Microscopy Today* **17,** 10–15 (2009).

[262] Kholkin, A. L., Kiselev, D. K. & Heredia, A. Piezoresponse Force Microscopy. In *Encyclopedia of Materials: Science and Technology* (eds. Buschow, K. H. J., Cahn, R. W., Flemings, M. C., Ilschner, B., Kramer, E. J., Mahajan, S. & Veyssière, P.) 1–8 (Elsevier, Oxford, 2011).

[263] Cinibulk, M. K., Kleebe, H.-J. & Rühle, M. Quantitative Comparison of TEM Techniques for Determining Amorphous Intergranular Film Thickness. *J. Am. Ceram. Soc.* **76,** 426–432 (1993).

[264] Siegelin, F., Kleebe, H.-J. & Sigl, L. S. Interface characteristics affecting electrical properties of Y-doped SiC. *J. Mater. Res.* **18,** 2608 (2003).

[265] Schäfer, F. N. *Experimentelle Bestimmung der Benetzungswinkel silikatischer Schmelzen auf Mineraloberflächen in Abhängigkeit von der kristallographischen Orientierung* (PhD thesis, Georg-August-Universität zu Göttingen, Göttingen, 2000).

[266] Fetzer, A.-K., Wohninsland, A., Hofmann, K., Clemens, O., Kodumudi Venkataraman, L. & Kleebe, H.-J. Domain structure and phase evolution in quenched and furnace cooled lead-free $Na_{1/2}Bi_{1/2}TiO_3$-$BaTiO_3$ ceramics. *Open Ceramics* **5,** 100077 (2021).

[267] Wohninsland, A., Fetzer, A.-K., Riaz, A., Kleebe, H.-J., Rödel, J. & Venkataraman, L. K. Correlation between enhanced lattice distortion and volume fraction of polar nanoregions in quenched $Na_{1/2}Bi_{1/2}TiO_3$-$BaTiO_3$ ceramics. *Appl. Phys. Lett.* **118,** 072903 (2021).

[268] Howard, C. J. & Stokes, H. T. Structures and phase transitions in perovskites - a group-theoretical approach. *Acta Cryst. A* **61,** 93–111 (2005).

[269] Gevers, R., Delavignette, P., Blank, H. & Amelinckx, S. Electron Microscope Transmission Images of Coherent Domain Boundaries I. Dynamical Theory. *Phys. Status Solidi B* **4,** 383–410 (1964).

[270] Moore, K., Conroy, M. & Bangert, U. Rapid polarization mapping in ferroelectrics using Fourier masking. *J. Microsc.* **279,** 222–228 (2020).

[271] Gruverman, A., Alexe, M. & Meier, D. Piezoresponse force microscopy and nanoferroic phenomena. *Nat. Commun.* **10,** 1–9 (2019).

[272] Zhang, J., Tian, X., Gao, Y., Yao, W., Qin, Y. & Su, W. Domain Structure of Poled $(K_{0.50}Na_{0.50})_{1-x}Li_xNbO_3$ Ceramics with Different Stabilities. *J. Am. Ceram. Soc.* **98,** 990–995 (2015).

[273] Qin, Y., Zhang, J., Yao, W., Lu, C. & Zhang, S. Domain Configuration and Thermal Stability of $(K_{0.48}Na_{0.52})(Nb_{0.96}Sb_{0.04})_3$-$Bi_{0.50}(Na_{0.82}K_{0.18})_{0.50}ZrO_3$ Piezoceramics with High d_{33} Coefficient. *ACS Appl. Mater. Interfaces* **8,** 7257–7265 (2016).

[274] Das, T., Nicholas, J. D. & Qi, Y. Long-range charge transfer and oxygen vacancy interactions in strontium ferrite. *J. Mater. Chem. A* **5,** 4493–4506 (2017).

[275] Ang, C., Yu, Z. & Cross, L. E. Oxygen-vacancy-related low-frequency dielectric relaxation and electrical conduction in Bi:$SrTiO_3$. *Phy. Rev. B* **62,** 228–236 (2000).

[276] Höche, T., Kleebe, H.-J. & Brydson, R. Can fresnoite ($Ba_2TiSi_2O_8$) incorporate Ti^{3+} when crystallizing from highly reduced melts? *Philos. Mag. A* **81,** 825–839 (2001).

[277] Stemmer, S., Höche, T., Keding, R., Rüssel, C., Schneider, R., Browning, N. D., Streiffer, S. K. & Kleebe, H.-J. Oxidation states of titanium in bulk barium titanates and in (100) fiber-textured $(Ba_xSr_{1-x})Ti_{1+y}O_{3+z}$ thin films. *Appl. Phys. Lett.* **79,** 3149–3151 (2001).

[278] Muller, D. A., Nakagawa, N., Ohtomo, A., Grazul, J. L. & Hwang, H. Y. Atomic-scale imaging of nanoengineered oxygen vacancy profiles in $SrTiO_3$. *Nature* **430,** 657–661 (2004).

[279] Ohring, M. How Engineering Materials are Strengthened and Toughened. In *Engineering Material Science* (ed. Ohring, M.) 431–500 (Academic Press, San Diego, 1995).

[280] Frantti, J., Ivanov, S., Eriksson, S., Rundlöf, H., Lantto, V., Lappalainen, J. & Kakihana, M. Phase transitions of $Pb(Zr_xTi_{1-x})O_3$ ceramics. *Phys. Rev. B* **66,** 064108 (2002).

[281] Forsbergh, P. W. Domain Structures and Phase Transitions in Barium Titanate. *Phys. Rev.* **76,** 1187–1201 (1949).

[282] Jones, G. O., Kreisel, J. & Thomas, P. A. A structural study of the $(Na_{1-x}K_x)_{0.5}Bi_{0.5}TiO_3$ perovskite series as a function of substitution (x) and temperature. *Powder Diffr.* **17,** 301–319 (2012).

[283] Wohninsland, A., Fetzer, A.-K., Broughton, R., Jones, J. L. & K. V., Lalitha. Structural and microstructural description of relaxor-ferroelectric transition in quenched $Na_{1/2}Bi_{1/2}TiO_3$-$BaTiO_3$. *J. Materiomics* **8,** 823–832 (2022).

[284] Glinchuk, M. D., Eliseev, E. A., Li, G., Zeng, J., Kalinin, S. V. & Morozovska, A. N. Ferroelectricity induced by oxygen vacancies in relaxors with perovskite structure. *Phys. Rev. B* **98,** 094102 (2018).

[285] Shi, J., Tian, W., Liu, X. & Fan, H. Electric-field induced phase transition and fatigue behaviors of $(Bi_{0.5+x/2}Na_{0.5-x/2})_{0.94}Ba_{0.06}Ti_{1-x}Fe_xO_3$ ferroelectrics. *J. Am. Ceram. Soc.* **100,** 1080–1090 (2017).

[286] Kodumudi Venkataraman, L., Zhu, T., Salazar, M. P., Hoffman, K., Waidha, A. I., Jaud, J. C., Groszewicz, P. B. & Rödel, J. Thermal depolarization and electromechanical hardening in Zn^{2+}-doped $Na_{1/2}Bi_{1/2}TiO_3$-$BaTiO_3$. *J. Am. Ceram. Soc.* **104,** 2201–2212 (2021).

[287] Babu, J. B., Madeswaran, G., Chen, X. L. & Dhanasekaran, R. Effect of oxygen vacancies on ferroelectric behavior of $Na_{1/2}Bi_{1/2}TiO_3$-$BaTiO_3$ single crystals. *Mater. Sci. Eng. B* **156,** 36–41 (2009).

[288] Moriyoshi, C., Takeda, S., Kuroiwa, Y. & Goto, M. Off-centering of a Bi ion in cubic phase of $(Bi_{1/2}Na_{1/2})TiO_3$. *Jpn. J. Appl. Phys.* **53,** 09PD02 (2014).

[289] Fetzer, A.-K., Wohninsland, A., K.V., Lalitha & Kleebe, H.-J. In situ hot-stage TEM of the phase and domain evolution in quenched $Na_{1/2}Bi_{1/2}TiO_3$-$BaTiO_3$. *J. Am. Ceram. Soc.* **105,** 2878–2888 (2022).

[290] Necke, T., Trapp, M., Lauterbach, S., Amthauer, G. & Kleebe, H.-J. Electron microscopy investigations on the mineral lorándite ($TlAsS_2$) from Allchar in Macedonia. *Z. Kristallogr.* **236,** 51–60 (2021).

[291] Litvinov, D., Rosenauer, A., Gerthsen, D., Preis, H., Bauer, S. & Kurtz, E. On the origin of the 'coffee-bean' contrast in transmission electron microscopy images of CdSe/ZnSe quantum dot structures. *J. Appl. Phys.* **89,** 4150–4155 (2001).

[292] Wohninsland, A. *personal correspondance* (Department of Materials Science, Technical University of Darmstadt, 2021).

[293] Toulouse, J. The Three Characteristic Temperatures of Relaxor Dynamics and Their Meaning. *Ferroelectrics* **369,** 203–213 (2008).

[294] Gobeljic, D., Dittmer, R., Rödel, J., Shvartsman, V. V., Lupascu, D. C. & Zhang, S. Macroscopic and Nanoscopic Polarization Relaxation Kinetics in Lead-Free Relaxors $Bi_{1/2}Na_{1/2}TiO_3$-$Bi_{1/2}K_{1/2}TiO_3$-$BiZn_{1/2}Ti_{1/2}O_3$. *J. Am. Ceram. Soc.* **97,** 3904–3912 (2014).

[295] Phelan, D., Stock, C., Rodriguez-Rivera, J. A., Chi, S., Leao, J., Long, X., Xie, Y., Bokov, A. A., Ye, Z.-G., Ganesh, P. & Gehring, P. M. Role of random electric fields in relaxors. *Proceedings of the National Academy of Sciences* **111,** 1754–1759 (2014).

[296] Kleemann, W. The relaxor enigma - charge disorder and random fields in ferroelectrics. *J. Mater. Sci.* **41,** 129–136 (2006).

[297] Fetzer, A.-K., Wohninsland, A., K.V., Lalitha & Kleebe, H.-J. Nanoscale polar regions embedded within ferroelectric domains in $Na_{1/2}Bi_{1/2}TiO_3$-$BaTiO_3$. *Phys. Rev. Mater.* **6,** 064409 (2022).

[298] Gao, P., Kumamoto, A., Ishikawa, R., Lugg, N., Shibata, N. & Ikuhara, Y. Picometer-scale atom position analysis in annular bright-field STEM imaging. *Ultramicroscopy* **184,** 177–187 (2018).

[299] Cao, D., Jeong, I. K., Heffner, R. H., Darling, T., Lee, J. K., Bridges, F., Park, J.-S. & Hong, K.-S. Local structure study of the off-center displacement of Ti and Zr across the morphotropic phase boundary of $PbZr_{1-x}Ti_xO_3$ ($x = 0.40, 0.47, 0.49, 0.55$). *Phys. Rev. B* **70,** 224102 (2004).

[300] Grinberg, I., Cooper, V. R. & Rappe, A. M. Relationship between local structure and phase transitions of a disordered solid solution. *Nature* **419,** 909–911 (2002).

[301] Datta, K., Roleder, K. & Thomas, P. A. Enhanced tetragonality in lead-free piezoelectric $(1-x)BaTiO_3$-$xNa_{12}Bi_{12}TiO_3$ solid solutions where x=0.05-0.40. *J. Appl. Phys.* **106,** 123512 (2009).

[302] Buscaglia, V., Buscaglia, M. T. & Canu, G. $BaTiO_3$-Based Ceramics: Fundamentals, Properties and Applications. In *Encyclopedia of Materials: Technical Ceramics and Glasses* (ed. Pomeroy, M.) 311–344 (Elsevier, Oxford, 2021).

[303] Neagu, A. & Tai, C.-W. Investigation of local structural phase transitions in $95Na_{0.5}Bi_{0.5}TiO_3$-$5BaTiO_3$ piezoceramics by means of *in-situ* transmission electron microscopy. *J. Appl. Phys.* **123,** 244105 (2018).

[304] Li, F., Zhang, S., Yang, T., Xu, Z., Zhang, N., Liu, G., Wang, J., Wang, J., Cheng, Z., Ye, Z.-G., Luo, J., Shrout, T. R. & Chen, L.-Q. The origin of ultrahigh piezoelectricity in relaxor-ferroelectric solid solution crystals. *Nat. Commun.* **7,** 1–9 (2016).

[305] Stenger, C. G. F., Scholten, F. L. & Burggraaf, A. J. Ordering and diffuse phase transitions in $Pb(Sc_{0.5}Ta_{0.5})O_3$ ceramics. *Solid State Commun.* **32,** 989–992 (1979).

[306] He, Q., Ishikawa, R., Lupini, A. R., Qiao, L., Moon, E. J., Ovchinnikov, O., May, S. J., Biegalski, M. D. & Borisevich, A. Y. Towards 3D Mapping of BO_6 Octahedron Rotations at Perovskite Heterointerfaces, Unit Cell by Unit Cell. *Acs Nano* **9,** 8412–8419 (2015).

[307] Yoshii, K., Hiruma, Y., Nagata, H. & Takenaka, T. Electrical Properties and Depolarization Temperature of $(Bi_{1/2}Na_{1/2})TiO_3$-$(Bi_{1/2}K_{1/2})TiO_3$ Lead-free Piezoelectric Ceramics. *Jpn. J. Appl. Phys.* **45,** 4493–4496 (2006).

[308] Takenaka, T., Nagata, H., Hiruma, Y., Yoshii, Y. & Matumoto, K. Lead-free piezoelectric ceramics based on perovskite structures. *J. Electroceram.* **19,** 259–265 (2007).

[309] Slabki, M., Kodumudi Venkataraman, L., Rojac, T., Rödel, J. & Koruza, J. Thermal stability of the electromechanical properties in acceptor-doped and composite-hardened $(Na_{1/2}Bi_{1/2})TiO_3$-$BaTiO_3$ ferroelectrics. *J. Appl. Phys.* **130,** 014101 (2021).

Appendix

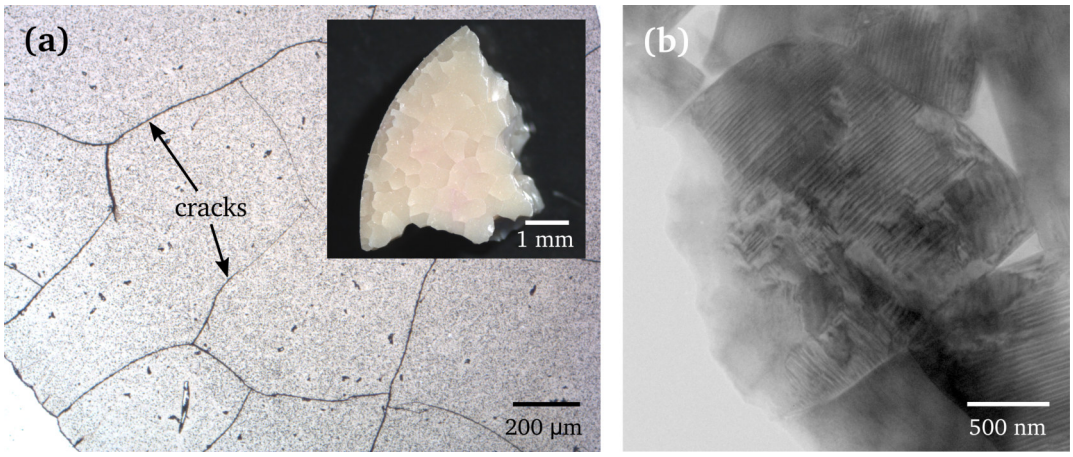

Figure A.1: Water-quenched NBT-6BT specimen. (a) Micrograph of the polished TEM specimen displaying microcracks. A piece of the fractured ceramic pellet is displayed in the inset. (b) TEM-BF micrograph of the water-quenched specimen showing an enhanced lamellar domain contrast.

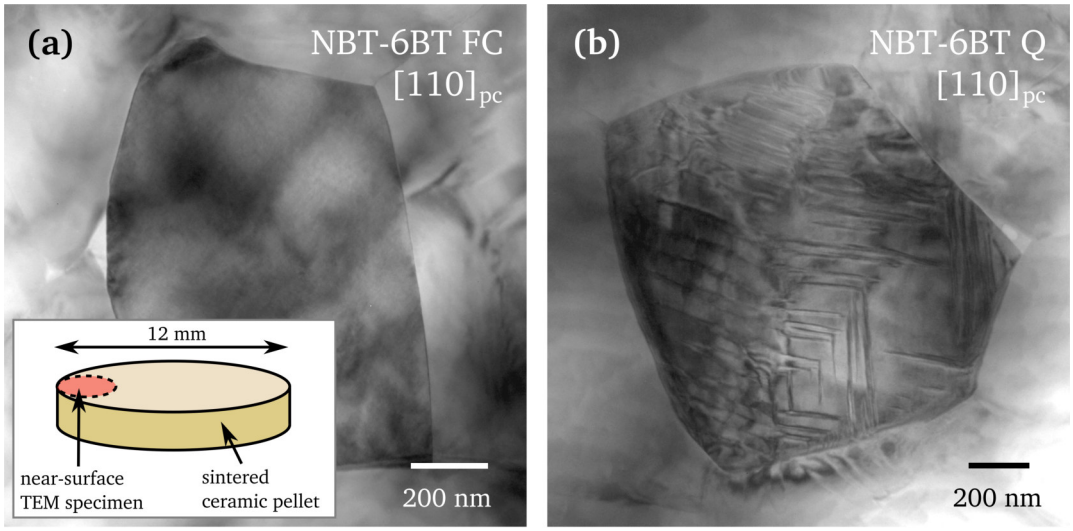

Figure A.2: TEM micrographs of NBT-6BT FC (a) and Q (b), obtained from the near-surface area of the sintered pellet (see inset in (a)). The FC specimen displays no strong domain contrast as expected for the relaxor composition, while abundant lamellar domains occur in the Q specimen. This matches with the observations made on the conventionally obtained NBT-6BT FC and Q specimens from the center of the ceramic pellet.

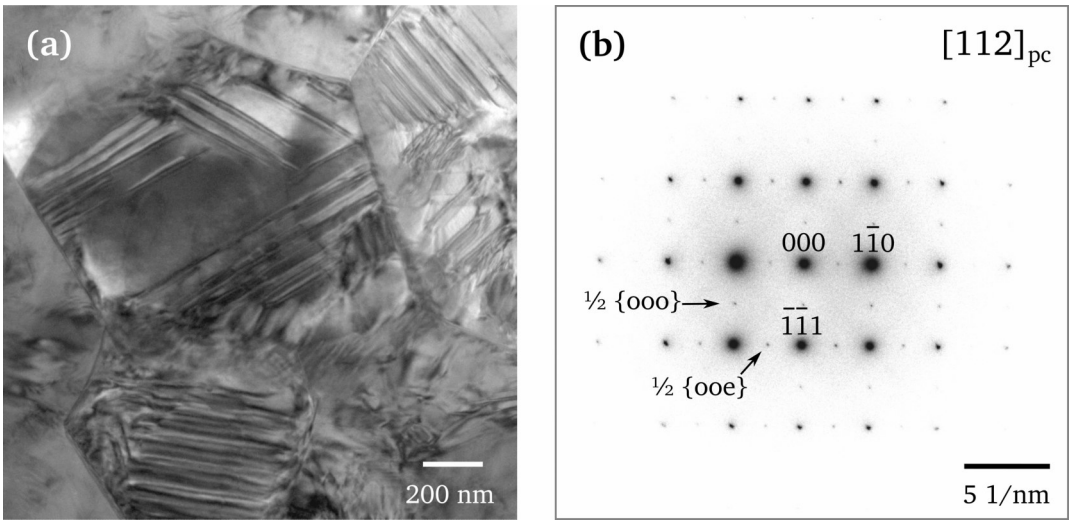

Figure A.3: (a) TEM micrograph of NBT-6BT Q, where annealing at 400 °C was omitted during sample preparation. A strong lamellar domain contrast is visible as observed in specimens, which were annealed. Equally, a phase coexistence of *R3c* and *P4bm* is present, deduced from the occurrence of $\frac{1}{2}$ {*ooo*} and $\frac{1}{2}$ {*ooe*} SRs (b). This indicates no significant influence of the annealing step onto the morphology of the domain structure and the phase assemblage.

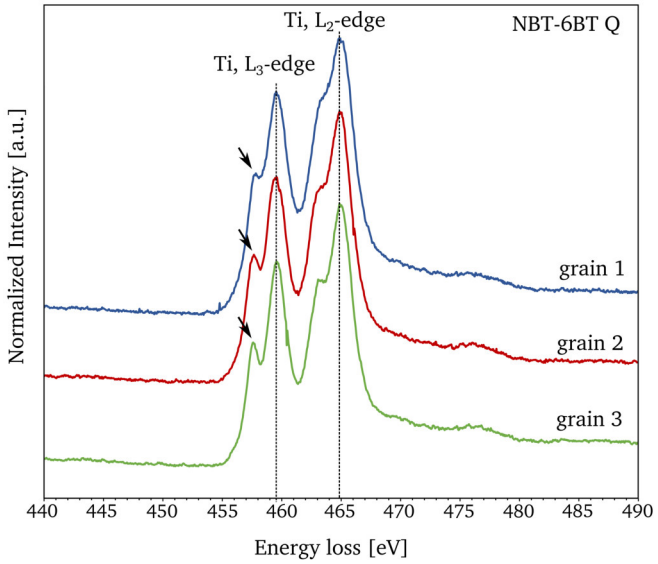

Figure A.4: EELS spectra obtained from three different grains within the same NBT-6BT Q specimen, displaying the near-edge structure of the Ti L_3- and L_2-edges. Slight variances in the peak shape are present, when comparing the different spectra (indicated with arrows).

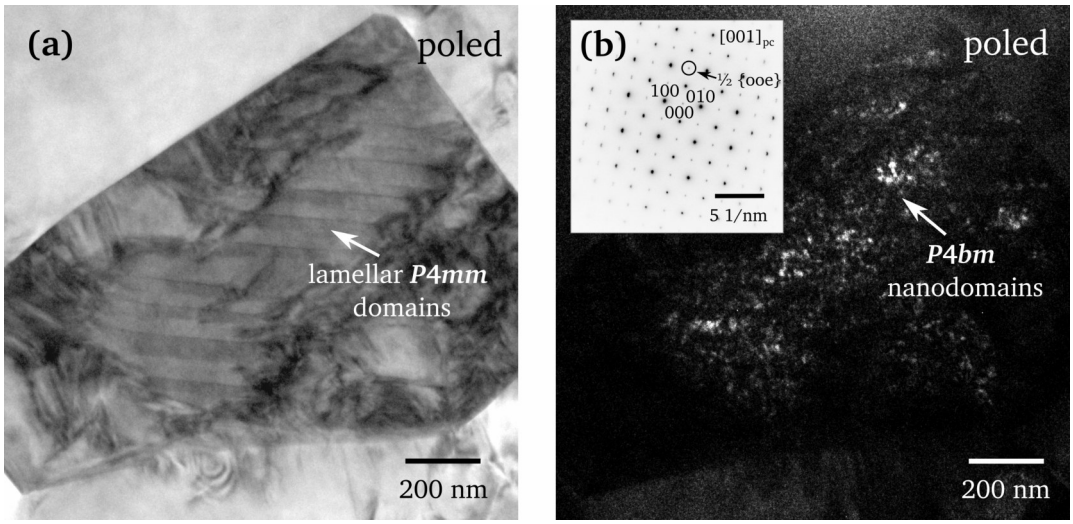

Figure A.5: (a) TEM-BF image of a grain in poled NBT-6BT Q, where lamellar *P4mm* domains appear. (b) The corresponding DF image obtained from the encircled $\frac{1}{2}$ $\{ooe\}$ SR in the SAED pattern (inset) illustrates that *P4bm* nanodomains are embedded within the poled ferroelectric domain structure.

List of Figures

List of Tables

Acknowledgments

I am very grateful that I was given the opportunity to write this dissertation in the research group Geomaterial Science at the TU Darmstadt under the supervision of Prof. Dr. Hans-Joachim Kleebe. I would like to thank him for enabling me to write my PhD thesis and guiding me along the way this past years. I highly valued his support, encouragement and constructive advice. I very much appreciated the opportunity to pursue own research ideas in a pleasant environment, where doors and ears where always open for scientific discussions.

I would like to express my gratitude to Prof. Dr. Jürgen Rödel for being the second reviewer of this work. Likewise, I would like to thank the committee members Prof. Dr. Christoph Schüth and Prof. Dr. Oliver Clemens for their time and interest.

I am especially thankful to Dr. Lalitha Kodumudi Venkataraman, who guided the project and who was always supportive and took time for my concerns. I highly appreciated her scientific input and feedback and I am glad that I could learn from her knowledge and experience.

I would like to thank my project colleague Andreas Wohninsland for the scientific exchange, the great cooperation and his help in many things. Thanks for providing me with ceramic samples and keeping me connected to the NAW group.

I would like to especially thank Dr. Stefan Lauterbach for taking the time and introducing me to the world of TEM. I highly appreciated his continuous support and help, whenever technical problems occurred.

I would like to thank Ulrike Kunz for her insightful advice at the SEM.

I am very thankful to Dr. Fangping Zhuo, who took the time and effort to introduce me to PFM, assisted the analyses and gave advice in sample preparation and data interpretation.

Now, I am glad to say that I enjoyed working in the Geomaterial Science group, thanks to my great colleagues. First of all, I am very thankful to Maximilian Trapp, who especially assisted me when I was new to the group, introduced me to the sample preparation techniques with a lot of patience and who was always helpful and enthusiastic in discussing TEM-related topics. I thank all my PhD fellows, Max, Johannes, Hui, Emilia, Kerstin, Mathis, Tobias and Nathalie for the pleasant time together, the scientific and non-scientific conversations and the occasional activities outside of work.

I also thank Prof. Dr. Ute Kolb for her enthusiastic engagement and Angelika Willführ for her administrative support.

I would like to thank my family, my parents and my brother, for their everlasting support and love not only during the PhD, but in all circumstances in life.

Finally, I thank my partner Robert for his unlimited moral support during all the ups and downs and for always being there for me.

Publications & Conference Contributions

Publications

1. **Fetzer, A.-K.**, Wohninsland, A., K.V., Lalitha & Kleebe, H.-J. Nanoscale polar regions embedded within ferroelectric domains in $Na_{1/2}Bi_{1/2}TiO_3$-$BaTiO_3$. *Phys. Rev. Mater.* **6**, 064409 (2022).
2. Wohninsland, A., **Fetzer, A.-K.**, Broughton, R., Jones, J. L. & K.V., Lalitha. Structural and microstructural description of relaxor-ferroelectric transition in quenched $Na_{1/2}Bi_{1/2}TiO_3$-$BaTiO_3$. *J. Materiomics* **8**, 823-832 (2022).
3. **Fetzer, A.-K.**, Wohninsland, A., K.V., Lalitha & Kleebe, H.-J. In situ hot-stage TEM of the phase and domain evolution in quenched $Na_{1/2}Bi_{1/2}TiO_3$-$BaTiO_3$. *J. Am. Ceram. Soc.* **105**, 2878-2888 (2022).
4. **Fetzer, A.-K.**, Wohninsland, A., Hofmann, K., Clemens, O., Kodumudi Venkataraman, L. & Kleebe, H.-J. Domain structure and phase evolution in quenched and furnace cooled lead-free $Na_{1/2}Bi_{1/2}TiO_3$-$BaTiO_3$ ceramics. *Open Ceramics* **5**, 100077 (2021).
5. **Fetzer, A.-K.**,Trapp, M., Lauterbach, S. & Kleebe, H.-J. Introduction to Transmission Electron Microscopy; The Basics. In *Encyclopedia of Materials: Technical Ceramics and Glasses* (ed. Pomeroy, M.) 578-599 (Elsevier, Amsterdam, 2021).
6. Wohninsland, A., **Fetzer, A.-K.**, Riaz, A., Kleebe, H.-J., Rödel, J. & Kodumudi Venkataraman, L. Correlation between enhanced lattice distortion and volume fraction of polar nanoregions in quenched $Na_{1/2}Bi_{1/2}TiO_3$-$BaTiO_3$ ceramics. *Appl. Phys. Lett.* **118**, 072903 (2021).
7. Feng, B., **Fetzer, A.-K.**, Ulrich, A. S., Galetz, M. C., Kleebe, H.-J. & Ionescu, E. Monolithic ZrB_2-based UHTCs using polymer-derived Si(Zr,B)CN as sintering aid. *J. Am. Ceram. Soc.* **105**, 99-110 (2021).

Conference Contributions

1. **Fetzer, A.-K.**, Wohninsland, A., Kodumudi Venkataraman, L. & Kleebe, H.-J. Transmission electron microscopy study of the local structure in $Na_{1/2}Bi_{1/2}TiO_3$-$BaTiO_3$ ceramics. *Ceramics in Europe*, Krakow, Poland, 07/2022 (invited talk).
2. **Fetzer, A.-K.**, Wohninsland, A., Kodumudi Venkataraman, L. & Kleebe, H.-J. Evolution of domain morphology in quenched $Na_{1/2}Bi_{1/2}TiO_3$-$BaTiO_3$ ceramics by in situ transmission electron microscopy. *6th International Conference on Advanced Electromaterials*, Jeju, South Korea, 11/2021 (oral presentation).
3. **Fetzer, A.-K.**, Wohninsland, A., Kodumudi Venkataraman, L. & Kleebe, H.-J. Transmission electron microscopy study on quenching-induced domain structure and phase assemblage in $Na_{1/2}Bi_{1/2}TiO_3$-$BaTiO_3$ ceramics. *Microscopy Conference*, Vienna, Austria, 08/2021 (oral

presentation).

4. **Fetzer, A.-K.**, Wohninsland, A., Kodumudi Venkataraman, L. & Kleebe, H.-J. A transmission electron microscopy study of the domain morphology and phase assemblage in quenched versus furnace cooled lead-free $Na_{1/2}Bi_{1/2}TiO_3$-$BaTiO_3$. *MSE Congress*, Darmstadt, Germany, 09/2020 (oral presentation).
5. **Fetzer, A.-K.**, Wohninsland, A., Kodumudi Venkataraman, L. & Kleebe, H.-J. Comparison of domain morphology and phase evolution in quenched and furnace cooled lead-free $Na_{1/2}Bi_{1/2}TiO_3$-$BaTiO_3$ ceramics. *Electroceramics XVII Conference*, Darmstadt, Germany, 08/2020 (oral presentation).